Comportement électrochimique vis-à-vis de l'intercalation de l'oxygène de quelques ferrites déficitaires en oxygène et propriétés physiques de la perovskite Sr2LaFe3O8.95 préparée par oxydation électrochimique

Fang Zhou

To cite this version:

Fang Zhou. Comportement électrochimique vis-à-vis de l'intercalation de l'oxygène de quelques ferrites déficitaires en oxygène et propriétés physiques de la perovskite Sr2LaFe3O8.95 préparée par oxydation électrochimique. Matériaux. Université Sciences et Technologies - Bordeaux I, 1997. Français. NNT : . tel-00833236

HAL Id: tel-00833236

https://theses.hal.science/tel-00833236v1

Submitted on 12 Jun 2013

N° of order : 1709

THESIS

PRESENTED AT

UNIVERSITY BORDEAUX I

DOCTORAL SCHOOL OF SCIENCES OF CHEMISTRY

by Mr. **ZHOU Fang** （周放）

FOR OBTAINING THE DEGREE OF

DOCTOR

SPECIALITY : MATERIAL SCIENCE

THE BEHAVIORS OF ELECTROCHEMICAL OXYGEN INTERCALATION OF SOME OXYGEN-DEFICIENT FERRITES AND PHYSICAL PROPERTIES OF PEROVSKITE $Sr_2LaFe_3O_{8.95}$ PREPARED BY ELECTROCHEMICAL OXIDATION

Defended at June 12, 1997

With the opinion of : **Mr. M. DRILLON** *Reviewers*
Mr. P. MAESTRO

Before the commission of examination formed by :

Mr. M. POUCHARD	**(Professor of University Bordeaux I)**	***President***
Mr. J. ETOURNEAU	**(Professor of University Bordeaux I)**	***Reviewer***
Mr. A. BOUZDINE	**(Professor of University Bordeaux I)**	***Examiners***
Mr. M. DRILLON	**(Directeur de Recherche of CNRS)**	
Mr. J.-C. GRENIER	**(Directeur de Recherche of CNRS)**	
Mr. P. MAESTRO	**(Engineer, Rhône-Poulenc)**	

1997

献给我的父母。

A mes parents.

A Monsieur le Professeur P. HAGENMULLER

Hommage
de ma sincère et respectueuse reconnaissance

天行健，君子以自强不息。

世上无难事，只要肯登攀。

毛泽东（1893 - 1976）

Aucune montagne n'est suffisamment haute
pour celui qui veut l'escalader.

Nothing in the world is difficult
for one who is willing to climb upwards.

MAO Zedong (1893 - 1976)

学海无涯。

L'océan de la connaissance est sans limite.

The ocean of learning is without limit.

Ce travail a été réalisé à l'Institut de Chimie de la Matière Condensée de Bordeaux du CNRS et de l'Université Bordeaux I.

J'exprime toute ma sincère et respectueuse reconnaissance à Monsieur le Professeur J. ETOURNEAU, Directeur du Laboratoire, pour l'honneur qu'il m'a fait en participant au Jury de cette thèse et pour m'avoir accueilli dans son laboratoire.

Je tiens à remercier Monsieur le Professeur M. POUCHARD pour m'avoir fait l'honneur de présider le Jury de thèse. J'ai pu bénéficier de ses grandes compétences et de ses conseils. Je lui adresse ma sincère et respectueuse reconnaissance.

Monsieur M. DRILLON, Directeur de Recherche au CNRS, a bien voulu examiner et juger ce travail. Je lui exprime mes sincères remerciements.

Monsieur P. MAESTRO, Ingénieur à Rhône-Poulenc, a bien voulu consacrer de son temps pour examiner et juger ce travail de thèse. Qu'il trouve ici le témoignage de mes sincères remerciements.

Je tiens à remercier sincèrement Monsieur le Professeur A. BOUZDINE pour avoir accepté de participer au Jury de thèse.

Monsieur J.-C. GRENIER, Directeur de Recherche au CNRS, a dirigé ce travail en me faisant bénéficier de son expérience. Qu'il veuille bien trouver ici l'expression de ma gratitude.

Ma gratitude va également à Monsieur A. WATTIAUX, Ingénieur de Recherche au CNRS, qui a apporté toutes ses compétences et ses qualités humaines pour m'aider à réaliser une partie de ce travail. Pour sa sincérité et gentillesse, je lui adresse mes vifs remerciements.

J'exprime mes sincères et respectueux remerciements à Monsieur J.-P. DOUMERC, Directeur de Recherche au CNRS, pour les discussions fructueuses sur les propriétés de transport et le temps qu'il a bien voulu accorder à la correction d'une partie de ce manuscrit.

Mes remerciements s'adressent également à Messieurs A. Villesuzanne, L. Fournès, L. Rabardel et H. Kachkachi pour leurs discussions et collaborations fructueuses.

Je remercie aussi tous ceux qui m'ont aidé pendant ces années de travail, en particulier : E. Marquestaut, J.-P. Chaminade, M. Dupeyron, F. Castex, J. Villot, P. Durand, J.-M. Bassat, P. Dordor, tous les membres du groupe des RX, Hong-Jie Zhang, Ming Dong, Hui Wang, Hai Zhang, P. Bezdicka, S. Petit, M. Coutanceau, R. Von der Mühll, B. Lestienne et les étudiants de l'équipe "Physico-Chimie des Oxydes Conducteurs".

Table of Contents

Introduction

Introduction in English* : *Page 4

Introduction

Les recherches concernant les oxydes de métaux de transition constituent un domaine très important de la chimie et de la physique du solide, notamment depuis la découverte de cuprates supraconducteurs à hauts T_C. Parmi ces oxydes les ferrites forment aussi une classe très importante dont les propriétés physiques ont été étudiées en relation avec les caractéristiques structurales, notamment les phénomènes de non-stoechiométrie anionique ou cationique.

Ce travail de thèse est consacré à l'étude de l'intercalation de l'oxygène par voie électrochimique dans quelques ferrites déficitaires en oxygène appartenant à la série $AMO_{3-1/n}$ ($n = 2, 3, \cdots$, ou ∞), où A représente un cation volumineux (A = Ca, Sr, La) et M le métal de transition, en l'occurrence le fer.

La non-stoechiométrie est un phénomène assez habituel dans ces oxydes ; il implique des changements structuraux parfois importants pouvant entraîner des évolutions notables des propriétés physiques. Un modèle structural a été proposé pour les ferrites, nous le décrirons dans le ***Chapitre I***.

Le ***Chapitre II*** est consacré à la description de la préparation des produits de départ, les brownmillerite $SrFeO_{2.5}$ et $CaFeO_{2.5}$ (termes n = 2) et les phases de type G $Sr_2LaFe_3O_8$ et $Ca_2LaFe_3O_8$ (termes n = 3) qui sont ensuite utilisées pour nos études.

Habituellement l'intercalation d'oxygène dans ces matériaux est réalisée à température assez élevée ($t \geq 300$ à 400°C), parfois sous pression d'oxygène. Dans ce travail nous utiliserons une méthode électrochimique à température ambiante qui s'est révélée très efficace pour oxyder certains matériaux : La_2CuO_4 en est le plus bel exemple. ***La 1^{ième} partie du chapitre III*** est un rappel des principaux résultats obtenus antérieurement dans notre groupe de recherche et quelques laboratoires étrangers. Cette méthode de ***Chimie Douce*** encore récente nécessite des études pour permettre de mieux comprendre les paramètres régissant l'intercalation de l'oxygène. Nous nous sommes intéressés à la faisabilité de l'oxydation électrochimique des matériaux préparés précédemment. Les résultats sont reportés dans ***la 2^{ième} partie du chapitre III***.

Il est alors apparu que l'oxydation électrochimique permettait effectivement d'oxyder les composés du Strontium tandis que ceux contenant du Calcium ne l'étaient pas. Les causes de ce phénomène sont analysées et des explications données dans le ***Chapitre IV*** sur la base des données cristallographiques disponibles et d'un modèle ionique.

L'ensemble du ***Chapitre V*** est consacré aux investigations des propriétés physiques de l'un des composés préparés par la méthode décrite précédemment, $Sr_2LaFe_3O_{8.95}$. Les aspects suivants sont décrits :

- caractérisations structurales de 300 à 80 K par diffraction X (XRD) : examen des distorsions structurales, de la symétrie et du désordre cationique.

- étude des propriétés magnétiques en fonction de la température et du champ appliqué (aimantation et susceptibilité magnétique) : description de la structure magnétique et modélisation des interactions d'échanges (*Annexe I*).

- étude des propriétés de transport (conductivité, effet Seebeck) en relation notamment avec la dismutation du fer tétravalent étudiée par résonance Mössbauer. Un mécanisme de conduction sera proposé.

- propriétés thermodynamiques : l'anomalie de chaleur spécifique due à la transition électronique sera étudiée (changement d'entropie et d'énergie interne).

- la transition de phase électronique sera examinée d'un point de vue thermodynamique : influence des interactions de type non-Heisenberg sur les propriétés magnétiques, influence des interactions magnétiques et de type Pauli sur les liaisons chimiques.

Introduction

The research on transition metal oxides has long been an important field in solid-state chemistry, solid-state physics and material science, and it has recently been emphasized with the discovery of high T_C superconductivity in copper oxides.

Ferrites form an important branch of transition metal oxides, and comprise a broad research area. The main respects involve : oxygen or cation non-stoichiometry and its influences on the structure and properties, electron transport properties (in both localized and extended regimes), electronic spin interactions and resulting magnetic structures and properties, magnetic and metal-insulator transitions, charge disproportionations, spectroscopic properties, and so on.

The work of this thesis is focused on some perovskite-related ferrites belonging to the series generally formulated as $AMO_{3-1/n}$ (n = 2, 3,···, or ∞). The A-site cations concerned here are Sr^{2+}, Ca^{2+} or (Sr^{2+}, La^{3+}) and (Ca^{2+}, La^{3+}), and M = Fe.

Oxygen non-stoichiometry is an usual phenomenon in this series and it often involves important changes in the crystal structures and physical properties of the ferrites. Due to the close relationship between oxygen content and structure, the structures of different terms in this series (associated with different n values) can be described by an unified model, as it is presented in ***Chapter I***.

Relative to their parent perovskites (the n = ∞ terms in the series), brownmillerite phases of $SrFeO_{2.5}$, $CaFeO_{2.5}$ (the n = 2 terms) and G-type phases of $Sr_2LaFe_3O_8$, $Ca_2LaFe_3O_8$ (the n = 3 terms) are oxygen-deficient ones. In the oxygen intercalation studies of this thesis, these ferrites are used as precursors, and their preparations are described in ***Chapter II***.

The oxygen vacancies in these oxygen-deficient ferrites are ordered in rows, so that oxygen atoms may be intercalated into their structures under some conditions, with a simultaneous increase in the oxidation state of iron and a possible change in the crystal structure.

Conventionally, the oxygen intercalation (or the oxidation of the irons) is done at certain temperatures in oxygen atmosphere or even under high oxygen pressures (may be up to 10^9 Pa). In this work, however, a quite different recently developed method, ***the electrochemical oxidation***, has been used for this purpose.

The method of electrochemical oxidation has been successful in obtaining high oxidation state of some transition metals in compounds such as perovskites $SrFeO_3$,

$SrCoO_3$ and $SrFe_{0.5}Co_{0.5}O_3$, and K_2NiF_4-type superconducting phase $La_2CuO_{4+\delta}$ (δ up to 0.08 ~ 0.09) and overoxidized phase $La_2NiO_{4+\delta}$ (δ up to 0.25), etc. A review of previous works in this area is given in ***the first part of Chapter III.***

By contrast to the conventional method usually using extreme conditions, the electrochemical oxidation is carried out under mild conditions, such as room temperature and air atmosphere. It therefore belongs to the so called "Chimie Douce (soft chemistry)", and provides a new route for preparing some compounds. Studies on the electrochemical oxidation are thus important for the synthetic chemistry.

Hence, one of the main purposes of this thesis work has been a systematic examination of the oxygen intercalation capabilities under electrochemical conditions of the above-mentioned oxygen-deficient ferrites. These results are reported in ***the second part of Chapter III.***

It turns out that the electrochemical method is quite effective in oxidizing the Sr-containing ferrites into their related perovskite phases, but not for the Ca-containing ones. The cause for this phenomenon is analyzed and explained in details in ***Chapter IV*** based on available crystallographic data and ionic model. We will see that some simple principles and considerations presented there can give an insight into the factors which influence the oxygen intercalation in these ionic precursors.

The whole ***Chapter V*** is devoted to the investigations and discussions of some physical properties of perovskite phase $Sr_2LaFe_3O_{8.95}$, which is prepared by means of electrochemical oxidation. Following respects are involved:

- Structural characterization (from 300 K down to 80 K) using XRD method; examination of structural distortion and symmetry ; cationic disorder in the structure.
- Studies on magnetic properties based on temperature and field dependencies of the susceptibility ; the magnetic structure and its origin (superexchange interactions) ; spin configuration ; spin polarizations ; anisotropy.
- Electron transport properties and charge disproportionation : information from conductivity data, Seebeck coefficient, and Mössbauer spectra ; mechanisms of electron hopping (VRH and small polaron) and electron localization (Anderson localization, etc.).

- Thermodynamic properties : anomaly in the specific heat due to electron phase transition ; the entropy and internal energy changes during the transition (both the experimental ones and theoretical ones).
- The electronic phase transition : examination of the transition from thermodynamic point of view; the influence of non-Heisenberg interactions on the magnetic properties below and during the transition ; the influence of magnetic and Pauli interactions on the chemical bonds.

In addition, in a cooperative work, some magnetic and thermodynamic properties of perovskite $Sr_2LaFe_3O_9$ are studied theoretically in the mean field approximation, in order to obtain more knowledge of the magnetic interactions. The results are reported in ***Appendix I***.

Chapter I

Structural Features of the Phases in the $A_nM_nO_{3n-1}$ Series ($n \geq 2$)

Many perovskite compounds, AMO_{3-y}, exhibit oxygen non-stoichiometric over a wide range and the oxygen vacancy concentration can reach values as high as y = 1, which often involves vacancy order-disorder phenomena. Various systems have been intensively investigated, such as manganites, ferrites, nickelates and cuprates, and many structural models have been proposed for describing the structures resulting from the oxygen vacancy ordering [1-4].

The ferrites have been more especially studied in our research group and a series of orthorhombic phases formulated $A_nM_nO_{3n-1}$ ($n \geq 2$) have been identified. A structural model based on the description of the brownmillerite-like structure of the dicalcium ferrite $Ca_2Fe_2O_5$ was proposed for the first time in 1976 [5].

I-1. Description of the Perovskite Structure

There are two basic ways for describing the structure of the perovskites AMO_3 : the first one represented in Fig 1a consists in an infinite succession along the *c*-direction (for instance) of layers of corner-sharing MO_6 octahedra (M being usually a smaller cation with $r_M \leq 0.70$Å); the bigger cation A occupies the central site with a 12-fold coordination (a cuboctahedron).

It is also usually depicted as a stacking of compact hexagonal AO_3 layers along $[111]_C$ direction of the cubic perovskite cell in which 1/4 of the octahedral sites are occupied by M cations (Fig 1b). A succession of three layers is necessary for describing completely a unit cell of the cubic perovskite (so-called 3C). Such a representation was proposed by Katz and Ward [6] for introducing all the perovskite polytypes (namely 2H, 6H, 3R .... polytypes) which correspond to various more or less complex sequences of AO_3 layers (***a***, ***b*** or *c*-type).

I-2. Description of the Brownmillerite-Type Structure

The general formulation of these compounds is $A_2M_2O_5$: they can be considered as non-stoichiometric perovskites AMO_{3-y} with y = 0.50. Their structure (Fig. 2) is easily derived from the cubic perovskite structure AMO_3 assuming that the oxygen vacancies (1/6 anionic sites) are ordered in rows along $[101]_C$ direction in each second (0k0) planes (Fig. 2, 3) [7]. A slight shifts of the anions and cations in those planes lead to this structure with alternating sheets of MO_6 octahedra and MO_4 tetrahedra perpendicular to the *y*-axis. One should point out that the tetrahedral chains

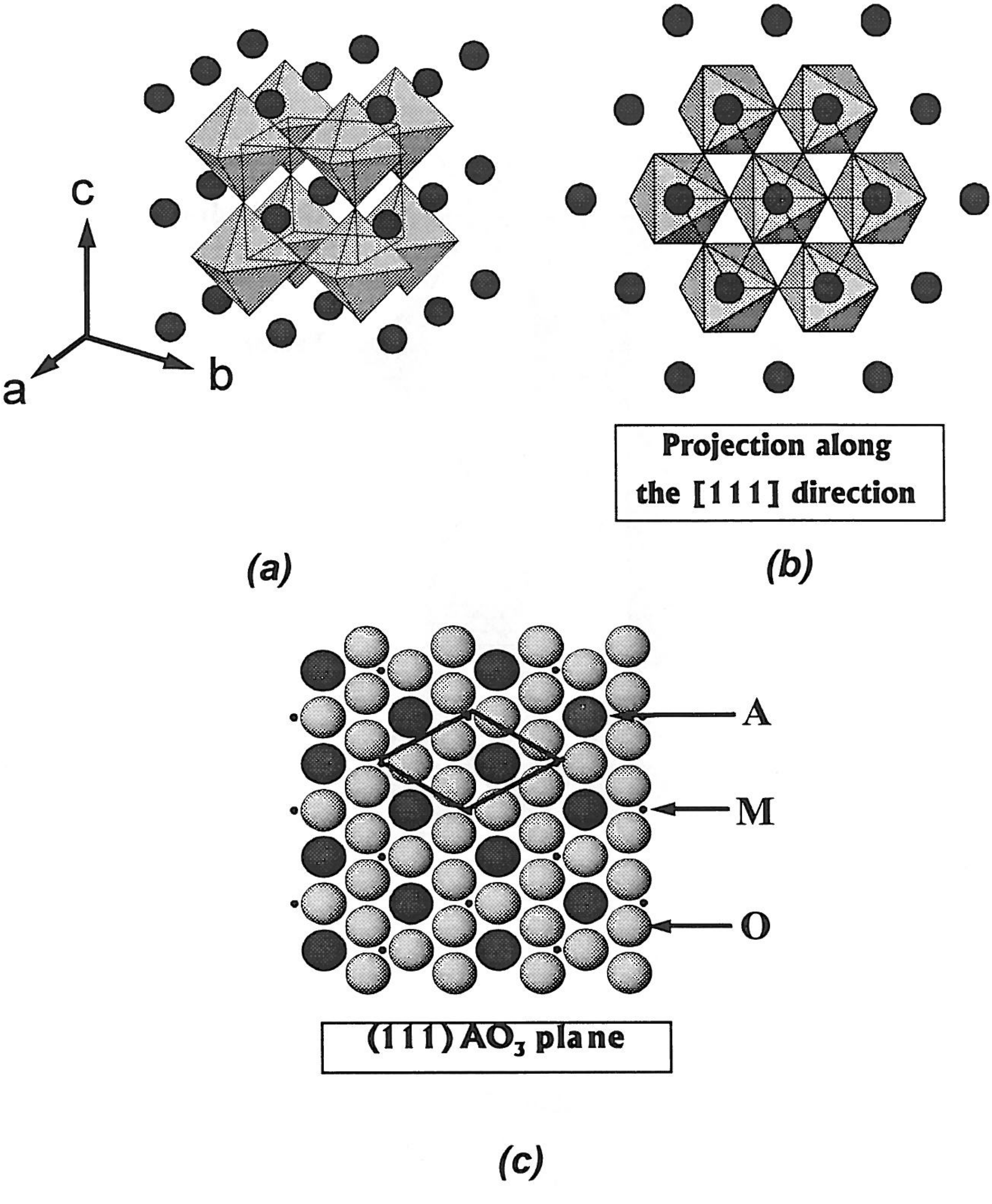

Figure 1

Idealized representation of the perovskite structure :

(a) cubic unit cell (b) projection along the [111] direction

(c) AO_3 (111) plane.

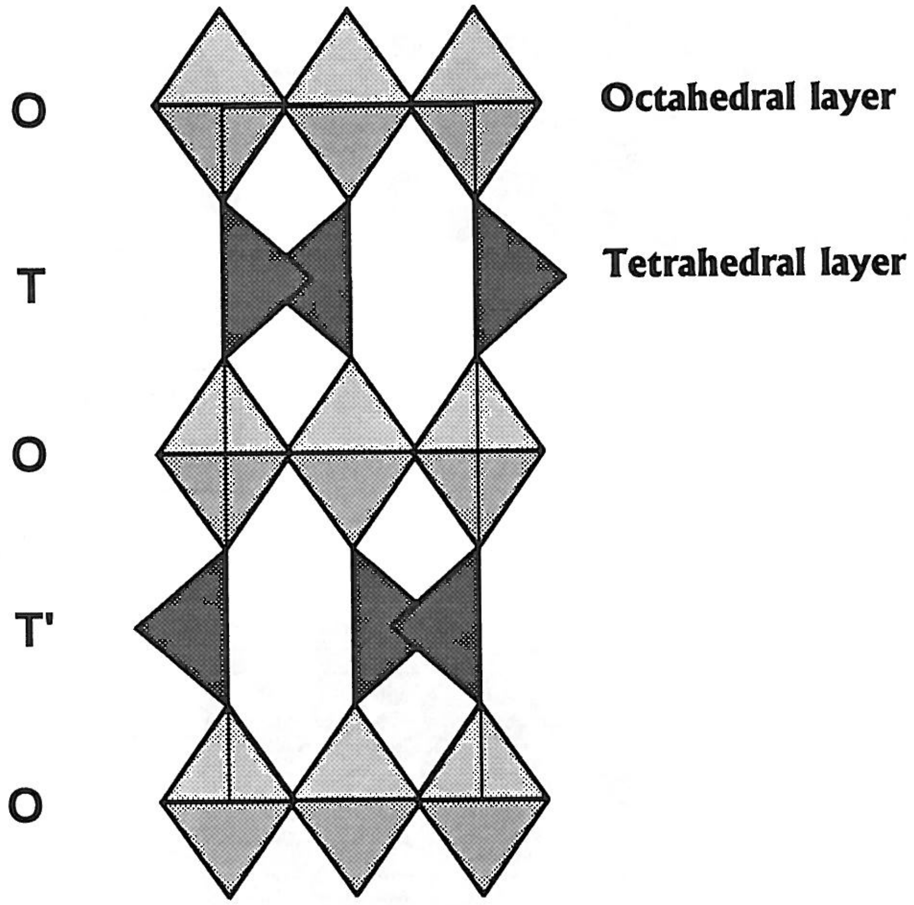

Figure 2

Idealized structure of the brownmillerite compounds $A_2M_2O_5$.

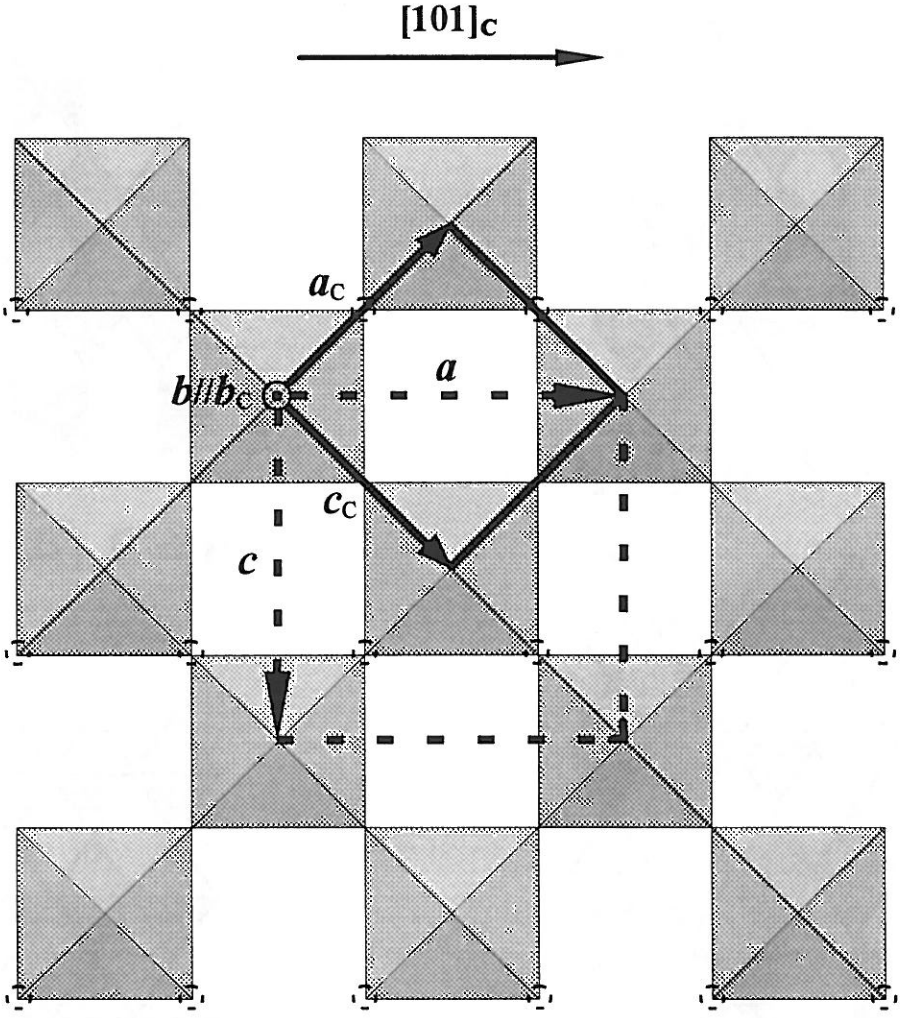

Figure 3

Relative orientations of the brownmillerite-type and the G-type orthorhombic lattices with their related cubic perovskite lattice

The lattice vectors $\boldsymbol{a}_C$, $\boldsymbol{b}_C$ and $\boldsymbol{c}_C$ refer to the cubic cell. The brownmillerite-type and G-type cells are represented by lattice vectors $\boldsymbol{a}$, $\boldsymbol{b}$ and $\boldsymbol{c}$ with $\boldsymbol{b}//\boldsymbol{b}_C$; when a G-type lattice is under consideration, $\boldsymbol{b} \approx 3 \cdot \boldsymbol{b}_C$, and for a Brownmillerite-type cell a relation of $\boldsymbol{b} \approx 4 \cdot \boldsymbol{b}_C$ is observed. It is also shown in the figure one of the corner-sharing metal-oxygen octahedral layers in the perovskite structure which is projected on *xz*-plane. A tetrahedral layer in brownmillerite-type, or G-type, structure (see Chap. IV) is formed when the alternative oxygen chains are missing, which are indicated by dashed open circles in the figure and are along $[101]_C$ direction of the cubic lattice.

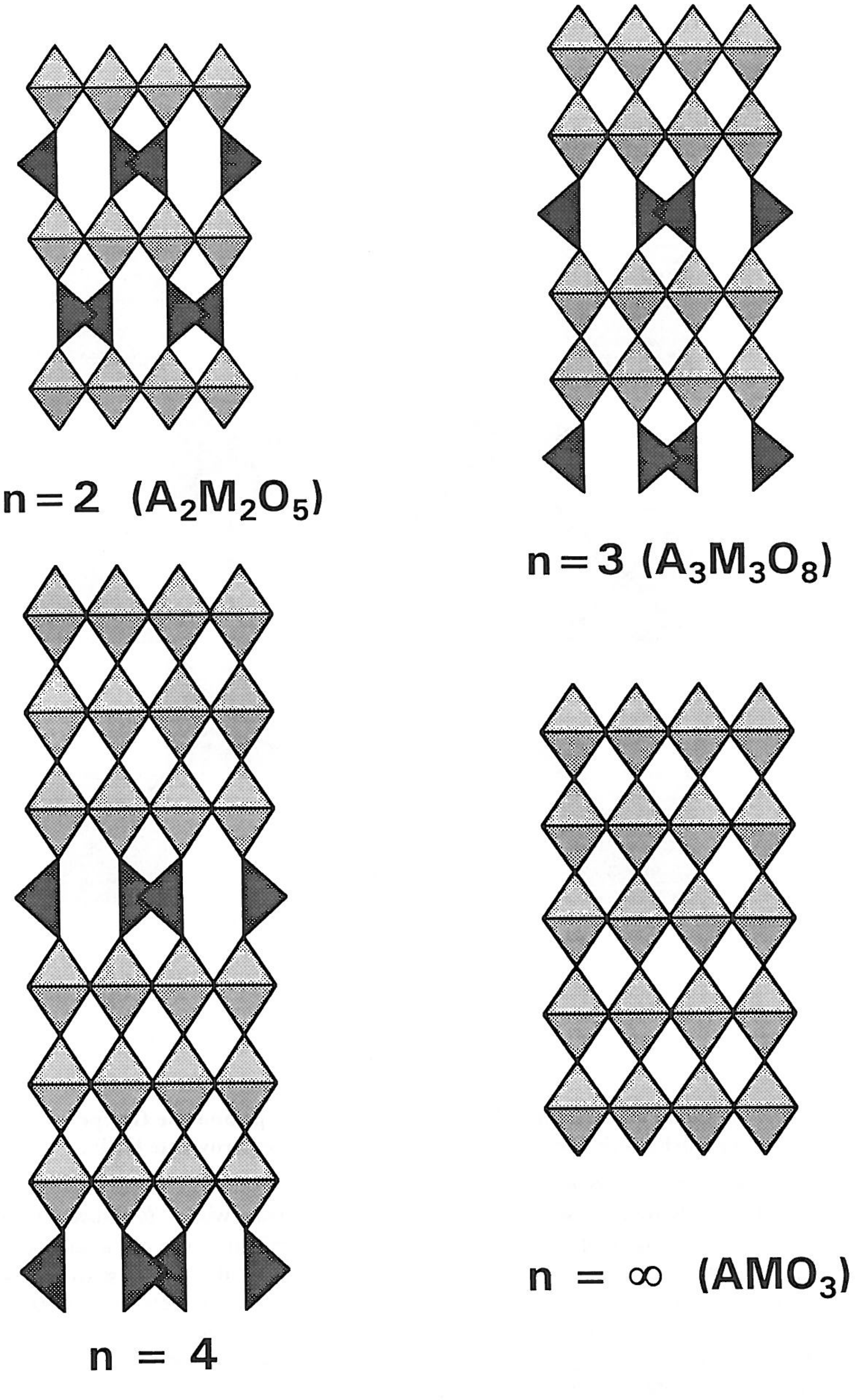

$n=2$ $(A_2M_2O_5)$

$n=3$ $(A_3M_3O_8)$

$n=4$

$n=\infty$ (AMO_3)

Figure 4

Idealized structures of the $A_nM_nO_{3n-1}$ series.

are oriented in each layer in such a way that the sequence of layers along the *b*-direction is ...OTOT'OTOT'... A complete description of this structure is given in Chap. IV.

I-3. Structural Model of the $A_nM_nO_{3n-1}$ Phases.

From this relationship between the two structures of perovskite and brownmillerite, a general structural model for the AMO_{3-y} phases with intermediate compositions ($0 < y < 0.50$, with $y = 1/n$) was suggested. It supposes a sequence of (n-1) perovskite-like sheets of MO_6 octahedra alternating with one sheet consisting of parallel chains of MO_4 tetrahedra. The general formulation of such phases may be alternatively written as $A_nM_nO_{3n-1}$ (with $n \geq 2$), and the idealized structures for $n = 2, 3, 4$ and ∞ are shown in Fig 4. Assuming an orthorhombic symmetry similar to that of the brownmillerite, the theoretical cell parameters are related to that of the perovskite a_c by the following relations :

$$a_n \approx \sqrt{2}\, a_c, \qquad b_n \approx n a_c, \qquad c_n \approx \sqrt{2} a_c$$

The complete study of various systems such as, for instance, $Ca_2Fe_2O_5$-$CaTiO_3$ or $Ca_2Fe_2O_5$-$LaFeO_3$ have definitively shown that the $n = 3$ (general formula $A_3M_3O_8$) is the most stable intermediate term of the series, other terms have been prepared and characterized, for example, $Ca_4Fe_2Ti_2O_{11}$ ($n = 4$) and $Ca_4LaFe_5O_{13}$ ($n = 5/2$); more complex terms have also been identified using electron microscopy [8].

I-4. Description of the G-Type Structure of $A_3M_3O_8$.

As shown in Fig. 4, the anion-deficient G-type structure of $A_3M_3O_8$ phase is built up by double layers of MO_6 octahedra (O) separated by one layer of MO_4 tetrahedra (T), that is, the polyhedral layers, which are perpendicular to the *b*-direction of the G-type lattice and parallel to *xz*-plane, are stacked in a OOTOOT sequence, which differs from the sequence observed in the brownmillerite structure. Examples will be given in Chap. IV.

I-5. Conclusion.

Common features of these oxygen-deficient structures are that all the M–O coordination polyhedra are linked to one another by shared-corners and that the oxygen vacancies in the tetrahedral layers are ordered in rows along $[101]_C$ direction of their related cubic perovskite cell. As a consequence, while the parent perovskite structure may be sketched by three-dimensional succession of MO_6 octahedra, in the oxygen-deficient brownmillerite and the G-type structures, the octahedral succession is only two-dimensional, together with one-dimensional succession of tetrahedra resulting from the ordered oxygen vacancy rows.

The relationship between the structure and composition in this series is demonstrated by the influence of the relative oxygen content on the ratio of the tetrahedral layers to the octahedral ones.

References

[1] A. Reller, J.M. Thomas, D.A. Jefferson and M.K. Uppal,
Proc. Roy. Soc. A, **394**, 223 (1984)
[2] J-C. Grenier, M. Pouchard and P. Hagenmuller,
Structure and Bonding, Springer, **47**, 1 (1981)
[3] C.N.R. Rao, J. Gopalakrishnan and K. Vidyasagar,
Ind. J. Chem., **23A**, 275 (1984)
[4] C. Michel, L. Er Rakho, and B. Raveau
Mat. Res. Bull., **20**, 667 (1985)
[5] J-C. Grenier, J. Darriet, M. Pouchard and P. Hagenmuller,
Mat. Res. Bull., **11**, 1279 (1976)
[6] L. Katz and R. Ward,
Inorg. Chem., **3**, 205 (1964)
[7] P. Hagenmuller, M. Pouchard and J-C. Grenier,
J. Mater. Educ., **12**, 297 (1990)
[8] Y. Bando, Y. Sekikawa, H. Nakamara and Y. Matsui,
Acta Crystallogr. , **A37**, 723 (1981)

Chapter II

Some Brownmillerite and G-type Oxygen-Deficient Ferrites : Preparation and Phase Identification

In the following, by oxygen-deficient phases, are meant brownmillerite-type or G-type phases like $A_2Fe_2O_5$ or $A_2LaFe_3O_8$ (A = Sr or Ca) in which 1/6 or 1/9 oxygen atoms are missing compared to their parent perovskite phases $A_2Fe_2O_6$ or $A_2LaFe_3O_9$.

The purpose of the preparation of those phases is to obtain starting materials (the precursors), in form of ceramic pellets, used for electrochemical experiments (Chapter III) in order to examine their oxygen intercalation capabilities under conditions of "*Chimie Douce*" (soft chemistry) and, if possible, to obtain their related stoichiometric perovskite phases.

The structural characterization of the phases was mainly done by X-ray powder diffraction(XRD). Contents of Fe^{4+} ions were determined by chemical analysis using solutions of Mohr salt (N/10) and potassium dichromate $K_2Cr_2O_7$ (N/10) in the presence of barium diphenylamine sulfonate (0.2%) as indicator. The oxygen content of the phases were then obtained by assuming that the oxygen species are O^{2-}. For the details of the experimental techniques see Appendix III.

II-1. The Brownmillerite-Type Ferrites

II-1-1. The Starting Powders

The raw materials used for preparing $Sr_2Fe_2O_5$ and $Ca_2Fe_2O_5$ phases were $SrCO_3$, $CaCO_3$, and $Fe(NO_3)_3 \cdot 9H_2O$ or Fe_2O_3 with the purity greater than 99 wt%. The carbonates, $SrCO_3$ and $CaCO_3$, were dried at 120 °C overnight in an oven and the lanthanum oxide La_2O_3 was heated at 850 °C for 4 hours just before weighing.

When iron nitrate $Fe(NO_3)_3 \cdot 9H_2O$ was used as the source of iron, the mixtures of accurately weighed, stoichiometric amounts of the raw materials according to the chemical formula of $Sr_2Fe_2O_5$ or $Ca_2Fe_2O_5$ were dissolved in nitric solution (volumetric ratio HNO_3 (65wt %) : H_2O = 1:2) and slowly dehydrated overnight over a sand-bath. The obtained precipitates were preliminarily denitrified over flame and then well ground to avoid inhomogeneity, before heated at 900~1000 °C in air for 6~10 hours.

When iron oxide Fe_2O_3 was used as the source of iron, the mixtures were ground and heated at 1000~1100 °C in air for 10~15 hours.

The obtained products were ground and used as starting powders for the treatments in the following steps.

II-1-2. Preparation and Identification of $Sr_2Fe_2O_5$ Phase

- The Preparation Procedures

The starting powder prepared in previous steps was pelleted and heated in air at 1250~1300 °C for 48 hours before quenched in air. The product, black in color, has a composition of $Sr_2Fe_2O_{5+\delta}$ with $\delta = 0.40 \sim 0.46$ according to chemical analysis.

The non-stoichiometric phase, $Sr_2Fe_2O_{5+\delta}$, was then ground into powder and reduced in a stream of argon gas (U degree, with oxygen partial pressure $P_{O_2} < 10^{-4}$ atm) at 1250 °C for 15~18 hours and slowly cooled in furnace. To obtain ceramic pellets, the sample was ground and pressed into pellets with a size of $\phi 8\times2$ mm under a pressure of 1 T held for 1 minute and then heated under the same conditions.

The relative density of the ceramic pellets is $D_r \approx 80\%$, here $D_r = D_{exp}/D_{th}$, and D_{exp} and D_{th} are the experimental density and calculated density (from X-ray data) of the pellets, respectively.

- The Phase Identification

Following features shown by the finally obtained ceramic sample characterize the Brownmillerite phase of $Sr_2Fe_2O_5$:

(a) Chemical analysis of the ceramic sample (having a brown colour) gave a value of $\varepsilon = 0$ for the formula $Sr_2Fe_2O_{5+\varepsilon}$;

(b) Its XRD pattern can be indexed in an orthorhombic unit cell having characteristic brownmillerite-type cell parameters as

$$a = 5.530(3)\ \text{Å}, \qquad b = 15.578(5)\ \text{Å}, \qquad c = 5.674(3)\ \text{Å};$$

(c) The reflection conditions of the XRD pattern agree with the I2mb space group previously proposed for the brownmillerite structure of $Sr_2Fe_2O_5$ by Harder *et al.* [1].

II-1-3. Preparation and Identification of $Ca_2Fe_2O_5$ Phase

- The Preparation Procedures

Because of its stability with respect to a large range of oxygen pressure, the brownmillerite compound $Ca_2Fe_2O_5$ can be synthesized in air. The starting powder (*cf.* II-1-2-1) was heated at 1200 °C for 20~24 hours before quenched in air. The sample was then ground and pressed into pellets of ϕ 8×2 mm in size under a pressure of 1 T held for 1 minute and heated again at 1200 °C for 24 hours before quenched in air.

- The Phase Identification

The ceramic pellets were brown in colour after their black surfaces were polished. Chemical analysis indicated a value of $\varepsilon = 0$ in the formula of $Ca_2Fe_2O_{5+\varepsilon}$. XRD experiments characterize a brownmillerite-type orthorhombic unit cell having following cell parameters,

$$a = 5.416(4)\ \text{Å}, \qquad b = 14.78(1)\ \text{Å}, \qquad c = 5.588(3)\ \text{Å}.$$

The reflection conditions of the XRD pattern are consistent with the space group Pnma reported for the brownmillerite structure of $Ca_2Fe_2O_5$ by Colville [2].

II-2. The G-type Ferrites

II-2-1. Preparation and Identification of $Sr_2LaFe_3O_8$ Phase

- The Preparation Procedures

The sample of $Sr_2LaFe_3O_8$ was synthesized starting from accurately weighed, stoichiometric amounts of $SrCO_3$, La_2O_3, and $Fe(NO_3)_3{\cdot}9H_2O$ with the purity greater than 99 wt%. The $SrCO_3$ powder was dried at 120 °C overnight in an oven and La_2O_3 powder was heated at 850 °C for 4 hours just before weighing. The stoichiometric mixture was first dissolved in nitric solution and slowly dehydrated overnight over a sand-bath. The obtained precipitates were then preliminarily denitrified over flame and well ground to avoid inhomogeneity before heated at 600~850 °C for several hours. The obtained mixture was ground again and pelleted, and then fired in a platinum crucible at 1250 °C for two days with an intermediate grinding.

According to XRD examination (Fig. 1), the as-prepared black sample is considered to be a mixture of cubic and tetragonal phases and the composition obtained by chemical analysis is $Sr_2LaFe_3O_{8.58}$ ($\delta = 0.58$).

To obtain the orthorhombic G-type phase, the previously prepared sample was well ground and reduced at 900 °C for 36 hours in a stream of purified argon gas and then rapidly cooled in the stream to avoid extra oxygen uptake.

<u>Note</u>: The "rapid cooling" at the end of the reduction was done by quickly pushing the sample out of the heating zone toward the cold end of the long furnace tube without stopping the argon flow. The argon gas used for the reduction had been purified just before it entered the furnace, by its passing through a separately heated steel tube tightly stuffed with very fine iron fibers heated at 350~500 °C. Such a purification which

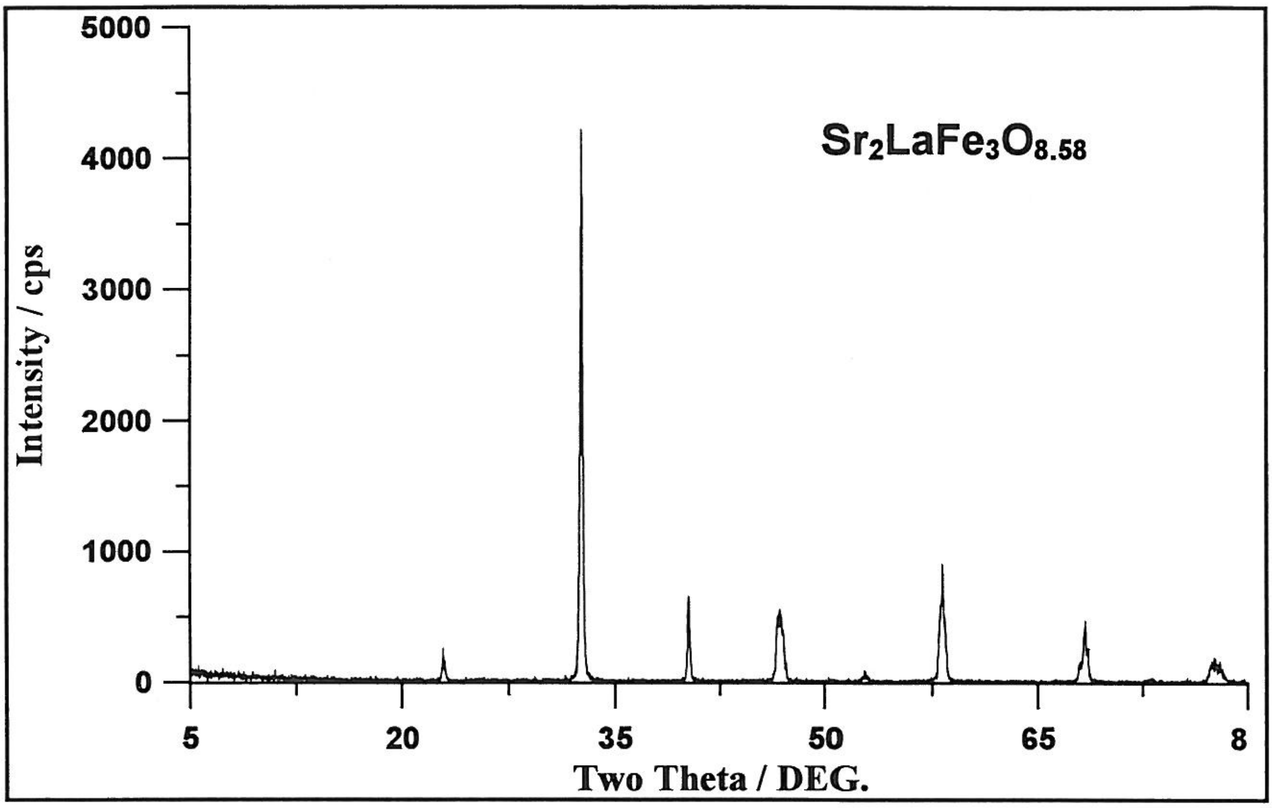

Fig. 1 X-ray powder diffraction pattern of $Sr_2LaFe_3O_{8.58}$.

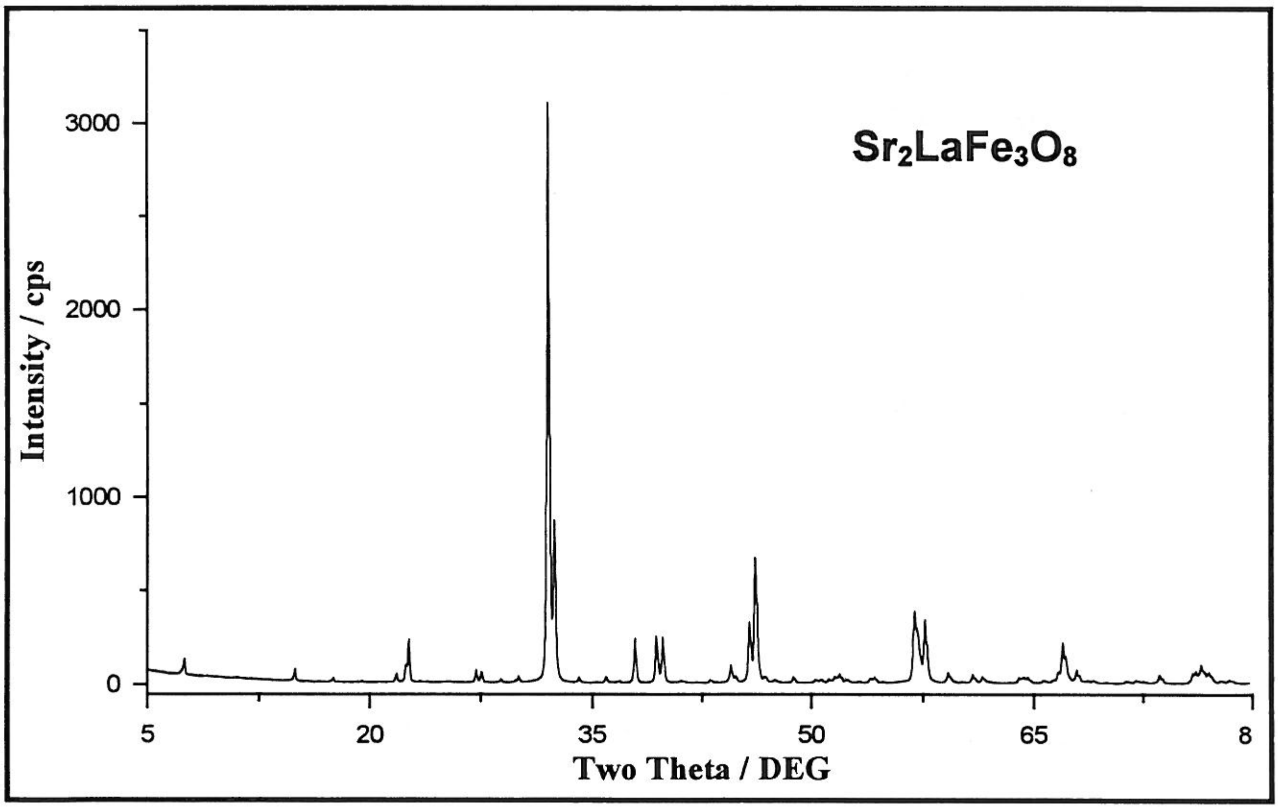

Fig. 2 X-ray powder diffraction pattern of $Sr_2LaFe_3O_8$.

Table 1

X-ray Powder Diffraction Data for $Sr_2LaFe_3O_{8.00\pm0.03}$ (at 25°C)

h k l	d_{calc}	d_{obs}	I/I_0	h k l	d_{calc}	d_{obs}	I/I_0
0 1 0	11.896	11.887	2	2 3 2	1.7611	1.7606	2
0 2 0	5.948	5.950	2	3 0 1	1.7467	1.7471	1
0 1 1	5.071	5.073	<1	1 5 2	1.7230	1.7226	<1
0 2 1	4.080	4.081	1	0 7 0	1.6994	1.6990	1
0 3 0	3.965	3.966	3	0 3 3	1.6903	1.6898	1
1 0 1	3.931	3.929	6	1 3 3	1.6161	1.6159	25
1 2 1	3.2796	3.2800	2	3 3 1	1.5985	1.5983	17
0 3 1	3.2373	3.2368	2	1 7 1	1.5599	1.5598	3
		3.0928	<1	1 4 3	1.5209	1.5212	2
0 4 0	2.9740	2.9731	1	3 4 1	1.5061	1.5061	2
0 0 2	2.8029	2.8026	26 *a*	0 7 2	1.4532	1.4528	1
1 3 1	2.7918	2.7915	100	2 7 0	1.4467	1.4472	1
2 0 0	2.7573	2.7577	30	2 3 3	1.4411	1.4416	1
0 4 1	2.6272	2.6269	<1	1 5 3	1.4200	1.4201	<1
1 0 2	2.4987	2.4984	1	2 6 2	1.3959	1.3958	12
1 4 1	2.3718	2.3720	8	4 0 0	1.3786	1.3787	4
0 3 2	2.2888	2.2885	9	3 4 2	1.3655	1.3649	<1
2 3 0	2.2638	2.2640	8	0 2 4	1.3641		
0 5 1	2.1901	2.1920	<1	1 0 4	1.3583	1.3587	<1
2 3 1	2.0991	2.0992	<1	1 6 3	1.3203	1.3203	<1
1 5 1	2.0355	2.0365	4	3 6 1	1.3106	1.3108	<1
2 4 0	2.0220	2.0224	1	3 0 3	1.3104		
0 6 0	1.9827	1.9824	14	4 3 0	1.3022	1.3015	<1
2 0 2	1.9656	1.9651	28	2 7 2	1.2856	1.2854	2
2 1 2	1.9393	1.9378	2	1 3 4	1.2850		
1 4 2	1.9131	1.9125	<1	1 9 1	1.2529	1.2529	2
2 2 2	1.8664	1.8669	1	2 0 4	1.2493	1.2493	2
0 5 2	1.8139	1.8130	<1	3 3 3	1.2442	1.2438	6
2 5 0	1.8013	1.7998	1	4 0 2	1.2371	1.2368	4
0 2 3	1.7827	1.7822	<1	1 7 3	1.2258	1.2257	<1
1 6 1	1.7703	1.7702	1	3 7 1	1.2180	1.2178	1

a This peak was resolved using a peak decomposition program DESOMPV based on Pseudo-Voigt profiles written by B. Lestienne and R. Von Der Mühll in this Institute.

G-type orthorhombic unit cell: a = 5.5146(4) Å; V = 367.75 Å^3;
b = 11.896(1) Å; Z = 2;
c = 5.6058(6) Å; D_x=5.506 (g /cm^3).

Space group: Pmma; Smith-Snyder figure of merit: F_{30} = 56(0.0111, 48).

lowers the oxygen partial pressure down to ~10^{-12} atm is necessary for obtaining the well-defined G-type phase.

Pellets of ϕ 8×2 mm in size were obtained by pressing the reduced powder (ground) under a pressure of 2 T held for 2 minutes. They were at first sintered at 1150 °C for 2 hours in argon (U) gas, then, after decreasing slowly the temperature (50 ~ 100 °C/hr), annealed at 900 °C for 15 hours in purified argon flow, before rapidly cooled in this inert atmosphere to prevent extra oxidation. The relative density of the ceramic pellets is D_r = 70~80%.

- The Phase Identification

According to chemical analysis, the final sample, brown in colour, has an $|\varepsilon| \leq 0.03$ for the formula of $Sr_2LaFe_3O_{8+\varepsilon}$.

The XRD analysis for this phase ($Sr_2LaFe_3O_{8.00\pm0.03}$) showed an orthorhombic G-type unit cell having

a = 5.5146(4) Å,	b = 11.896(1) Å,	c = 5.6058(6) Å,
and V = 367.75 Å^3,	Z = 2,	D_x=5.506 (g /cm^3).

The reflection conditions of the XRD pattern agree with the space group Pmma proposed for the G-type structure of $Sr_2LaFe_3O_8$ [3]. The XRD pattern and its indexing are shown in Fig. 2 and Table 1. The Smith-Snyder figure of merit [4] for the indexing is F_{30} = 56(0.0111, 48).

II-2-2. Preparation and Identification of $Ca_2LaFe_3O_8$ Phase

- The Preparation Procedures

The first steps of the procedure for preparing $Ca_2LaFe_3O_8$ were the same as those described for $Sr_2LaFe_3O_8$, starting from a mixture of $CaCO_3$, La_2O_3, and $Fe(NO_3)_3{\cdot}9H_2O$. The preliminarily denitrified precipitates of nitric solution were ground and heated at 950 °C for 10 hours in air. The product was again ground and heated at 1300 °C for 15~20 hours before quenched in air, which gave a composition of $Ca_2LaFe_3O_{8+\delta}$ with $\delta = 0.17$ according to chemical analysis.

The as-prepared non-stoichiometric sample was ground and reduced in a stream of Ar+1%H_2 mixed gases at 1050 °C for 22 hours and slowly cooled in furnace. Ceramic pellets were heated at 1300 °C for 15 hours in air, then at 1050 °C for 30 hours in a flow of argon (U degree). The relative density of the ceramic pellets was $D_r \approx 90\%$.

- *The Phase Identification*

An $\varepsilon = 0.02$ in the formula of $Ca_2LaFe_3O_{8+\varepsilon}$ was determined by chemical analysis for the final ceramic sample.

XRD experiment led to an orthorhombic unit cell with characteristic G-type cell parameters as follows :

$a = 5.495(5)$ Å, $b = 11.291(5)$ Å, $c = 5.564(2)$ Å $V = 345.21$ Å^3

The XRD pattern is consistent with those previously reported for the G-type phase of $Ca_2LaFe_3O_8$ [5].

II-3. Some Remarks

The brownmillerite-type phases, $Sr_2Fe_2O_5$ and $Ca_2Fe_2O_5$, and G-type phases, $Sr_2LaFe_3O_8$ and $Ca_2LaFe_3O_8$, were prepared by means of solid-state reaction with several steps.

As it has been previously quoted, brownmillerite-type and G-type structures are characteristic of continuous oxygen vacancy rows in their tetrahedral layers, which may act as channels for oxygen diffusing into or out of the structures under certain conditions.

Usually, increasing the oxygen partial pressure P_{O_2} will make oxygen atoms to diffuse into the structures at appropriate temperature T; and the diffused oxygen may re-escape from the structures when P_{O_2} is decreased and/or T is increased. Therefore, it is a usual routine for the synthesis of those phases through solid-state reaction that samples are at first heated in air atmosphere ($P_{O_2} = 0.2$ atm) at a temperature appropriate for completing solid-state reactions, which usually produces non-stoichiometric phases like $A_2Fe_2O_{5+\delta}$ or $A_2LaFe_3O_{8+\delta}$ (here A = Sr^{2+} or Ca^{2+} and $\delta > 0$). Then they are reduced in inert atmosphere ($P_{O_2} <$ or $<< 10^{-4}$ atm) at a given temperature T and for a given time t, for obtaining the desired "stoichiometric" phases of $A_2Fe_2O_5$ or $A_2LaFe_3O_8$. Such a reduction process can be expressed as follows :

$$A_2Fe^{3+}_{2-2\delta}Fe^{4+}_{2\delta}O_{5+\delta} \xrightarrow{P_{O_2}\sim 0,\,T,\,t} A_2Fe^{3+}_{2-2\varepsilon}Fe^{4+}_{2\varepsilon}O_{5+\varepsilon} + (\delta\text{-}\varepsilon)/2\ O_2\nearrow,$$

$$\text{or}\quad A_2LaFe^{3+}_{3-2\delta}Fe^{4+}_{2\delta}O_{8+\delta} \xrightarrow{P_{O_2}\sim 0,\,T,\,t} A_2LaFe^{3+}_{3-2\varepsilon}Fe^{4+}_{2\varepsilon}O_{8+\varepsilon} + (\delta\text{-}\varepsilon)/2\ O_2\nearrow,$$

with $\delta > \varepsilon \approx 0$.

For some phases, the reduction process can not be easily controlled and a small negative ε value may occur as was observed in $Sr_2LaFe_3O_{8+\varepsilon}$, indicating that a small quantity of oxygen vacancies may exist in its octahedral layers. Anyway, an ε-value of $|\varepsilon| \leq 0.02 \sim 0.03$ can usually be reached.

As the "stability" of the tetrahedral layers is different from phase to phase, preparation conditions such as atmosphere (P_{O_2}) and temperature differ. For example, to obtain brownmillerite phase $Sr_2Fe_2O_5$ starting from non-stoichiometric phase $Sr_2Fe_2O_{5+\delta}$ ($\delta > 0$), an inert atmosphere is necessary, and it was achieved by heating the sample in a flow of argon (U degree) with oxygen partial pressure $P_{O_2} < 10^{-4}$ atm; but for preparing G-type phase $Sr_2LaFe_3O_8$ through similar reduction procedure, a purified argon gas with much lower oxygen partial pressure should be used in order to obtain samples with desired composition. Conversely, the brownmillerite phase $Ca_2Fe_2O_5$ can be synthesized by heating in air, indicating a higher "stability" of its tetrahedral layers, and such a "stability" is also demonstrated by the difficulty in intercalating oxygen into its structure.

References

[1] Harder, Von M. and H. Müller-Buschbaum (1980). *Z. Anorg. Allg. Chem.* **464**, 169

[2] Colville, A.A. (1970). *Acta Crystallogr.* **B26**, 1469

[3] Battle, P.D., Gibb, T.C., and Lightfoot, P. (1990). *J. Solid State Chem.* **84**, 237.

[4] Smith, G.S. and Snyder, R.L. (1979). *J. Appl. Crystallogr.* **12**, 60

[5] Grenier, J.G. (1976). Ph.D. Thesis, University Bordeaux I

Chapter III

Electrochemical Oxidation:
General Considerations on the Oxygen Intercalation into Oxides Networks
and
Electrochemical Behaviors of Some Oxygen-Deficient Ferrites Under Oxidation Conditions.

III-1. Electrochemical Oxidation : General Considerations on the Oxygen Intercalation into Oxides Networks. A Review of Previous Works.

III-1-1. Introduction

In the synthetic chemistry of oxides, the key parameters governing their oxygen stoichiometry are the annealing temperature and the oxygen pressure p_{O_2}. Obtaining high oxidation states of cations requires high oxygen pressures and annealing at rather low temperatures, typically 400 to 700 °C. From a thermodynamic viewpoint, such oxides are usually in a stable state.

In the last two decades, other ways belonging to the field of the so-called 'Chimie Douce' have been investigated for preparing metastable forms of highly oxidized materials. The first one that can be quoted is the chemical oxidation, which implies either to use a strong oxidizing agent in solution at room temperature or to achieve a solid-gas reaction at moderate temperature (typically $t < 400°C$).

In solution, using MnO_4^-, BrO^- or ClO^- species has been fruitful for oxidizing some cuprates such as, for instance, $La_2CuO_{4+\delta}$ (δ up to 0.08) or $LaCuO_{2+\delta}$ (δ up to 0.63) [1, 2]. For solid-gas reactions, F_2, Cl_2 or NO_2 gases have been successfully used at moderate temperatures. Intercalation of fluorine has been achieved at about 150-200 °C in $(La,Sr)_2CuO_4$ or YBCO compounds leading to the formation of trivalent copper [3, 4]. With Cl_2, a partial decomposition of the starting material is observed, followed by an auto-oxidation [5]. Very recent works have given evidence of promising results with NO_2 gas : the reaction is based on the *in situ* destruction of ammonium ions in oxide lattices by NO_2 in a rather large range of temperatures (20 to 400 °C) [6]. Thus oxides with new structures or textures have been prepared by this topotactic reaction, such as h-WO_3 or V_2O_5 [6].

Another important field of the 'Chimie Douce' is concerned with electrochemical processes, the electric potential being an interesting 'driving force' instead of chemical agents. As a matter of fact, intercalation chemistry has been widely developed especially for battery researches ; it is now clearly established that intercalating cations such as H^+, Li^+ or Na^+ whose ionic size are rather small, can be easily achieved [7] thanks to an expansion of the host lattice resulting from its reduction. On the other hand, oxidizing materials requires to insert (or add) oxygen anions in the host lattice. While the material is oxidized, its lattice simultaneously collapses. The size of the O^{2-} anions being rather big ($r_{O2-} \approx 1.40$ Å), this reaction appears quite doubtful and therefore would be likely to occur provided that high oxygen activity could be reached.

This was achieved using the following reaction in alkaline solution (KOH 1M):

$4\,OH^- \rightarrow O_2^{\nearrow} + 2\,H_2O + 4e^-$; $E_{th} = 0.303$ V/Hg/HgO. *[1]*

According to the Nernst relation ($E = E_{th} + (RT/4F)\ln(a_{O_2}/[OH^-]^4)$), the oxygen activity can be estimated for usual anodic overpotentials ($\eta = E - E_{th} \approx +150$ mV), equivalent to oxygen pressures of about 10^{15} Pa, at room temperature. Such an activity of oxygen leads to the formation of oxide thin films when the working electrode is a metal. These thin films can be either conducting as for Ni or Ru, or insulating and passivating as for Al or Ti. A similar reaction was successfully achieved for the first time by A. Wattiaux et al. [8], on oxide ceramics of La_2CuO_4 for which, surprisingly, oxygen overstoichiometry and superconductivity were observed [9].

Such experiments have been then repeated by several groups and the most significant results are reported below. The experimental procedure has been described in detail in ref. [10] : experiments are carried out at room temperature, in a two compartment cell filled with an alkaline solution (KOH or NaOH 1M), under air or nitrogen flow. The oxidation is performed using either the potentiostatic mode or the galvanostatic one. The working electrode is usually a ceramic.

III-1-2. Oxygen Intercalation or Not ?

All these experiments being performed in concentrated $[OH^-]$ solution immediately raised the question concerning the nature of the intercalated species, the formation of oxyhydroxides being the most obvious assumption. Early works using T.G.A., ^{H}N.M.R. as well as I.R. spectroscopy clearly demonstrated the absence of (OH) species in the final material [11]. However R. Schöllhorn et al. [12] contesting these results, proposed the anodic oxidation to be described as an electron/proton transfer process involving some lanthanum deficiency, the reaction being :

$La_{1.95}CuO_{3.85}(OH)_{0.15} \Leftrightarrow La_{1.95}Cu^{2.15+}O_4 + 0.15H^+ + 0.15e^-$.

These conclusions were based on the facts that the structure of La_2CuO_4 is densely packed with apparently no diffusion pathway of lower energy and the oxygen transport unbelievable in an oxide network. These controversies lasted a few years and various intercalated species such as O_2^{2-}, O_2^- or O^- were suggested for explaining the overstoichiometry of $La_2CuO_{4+\delta}$ [13].

Soon after, oxygen intercalation by means of this electrochemical process was definitively established with the oxidation of the brownmillerite-type compound $Sr_2Fe_2O_5$ into $SrFeO_3$, followed by the preparation of $SrCoO_3$ and Sr_2FeCoO_6 [14 -16]. Similar experiments are described in details in the following sections.

In the same way, recently the rhombohedral perovskite $NdNiO_{2.95}$ and a cubic form of $LaMnO_{3+\delta}$ were also prepared [17].

Thus the following general electrochemical reaction can be proposed :

$$A_xMO_y + 2\delta\, OH^- \Rightarrow A_xMO_{y+\delta} + \delta\, H_2O + 2\,\delta e^- \quad \textit{[2]},$$

which was extensively discussed and supported by galvanostatic experiments of Chou et al. [18]. In fact, it is interesting to notice that this reaction occurs in the range of potentials preceding the oxygen evolution (according to eq. *[1]*) and can be directly evidenced by a plateau on the voltammogram (Fig. 1). However it appears that in most cases, even for low values of the current intensity, a mixed process involving both the oxidation of the electrode (eq. *[2]*) and the oxygen evolution takes place, which avoids to quantify accurately the value of δ, a part of the transferred electrons being used for reaction *[1]*.

Very recently, studying the electrochemical reduction of $La_2Cu_{1-x}Ni_xO_{4+\delta}$ ($0 \leq x \leq 1$) samples prepared in air, C. Monroux et al. [19] could determine the δ values by coulometry. They found a very good agreement with the data of the iodometric titration of these samples, which comes from the fact that the reduction of the sample takes place in a range of potentials far from the hydrogen evolution ($E \approx -1.1$ V /Hg/HgO). Such experiments confirmed also the complete reversibility of the oxygen intercalation as noticed by several groups [12, 20, 21].

III-1-3. Intercalation of Oxygen into La_2MO_4-Type Compounds.

The most intense researches were devoted to the intercalation of oxygen into La_2CuO_4 and related compounds due to the great interest of this material for understanding superconductivity.

Earliest experiments were carried out using a steady potential ($450 < E < 900$ mV) and various polarization times [20, 22 - 25]. The oxidation reaction was followed by measuring as a function of time, the Cu^{3+} content that was directly correlated to the

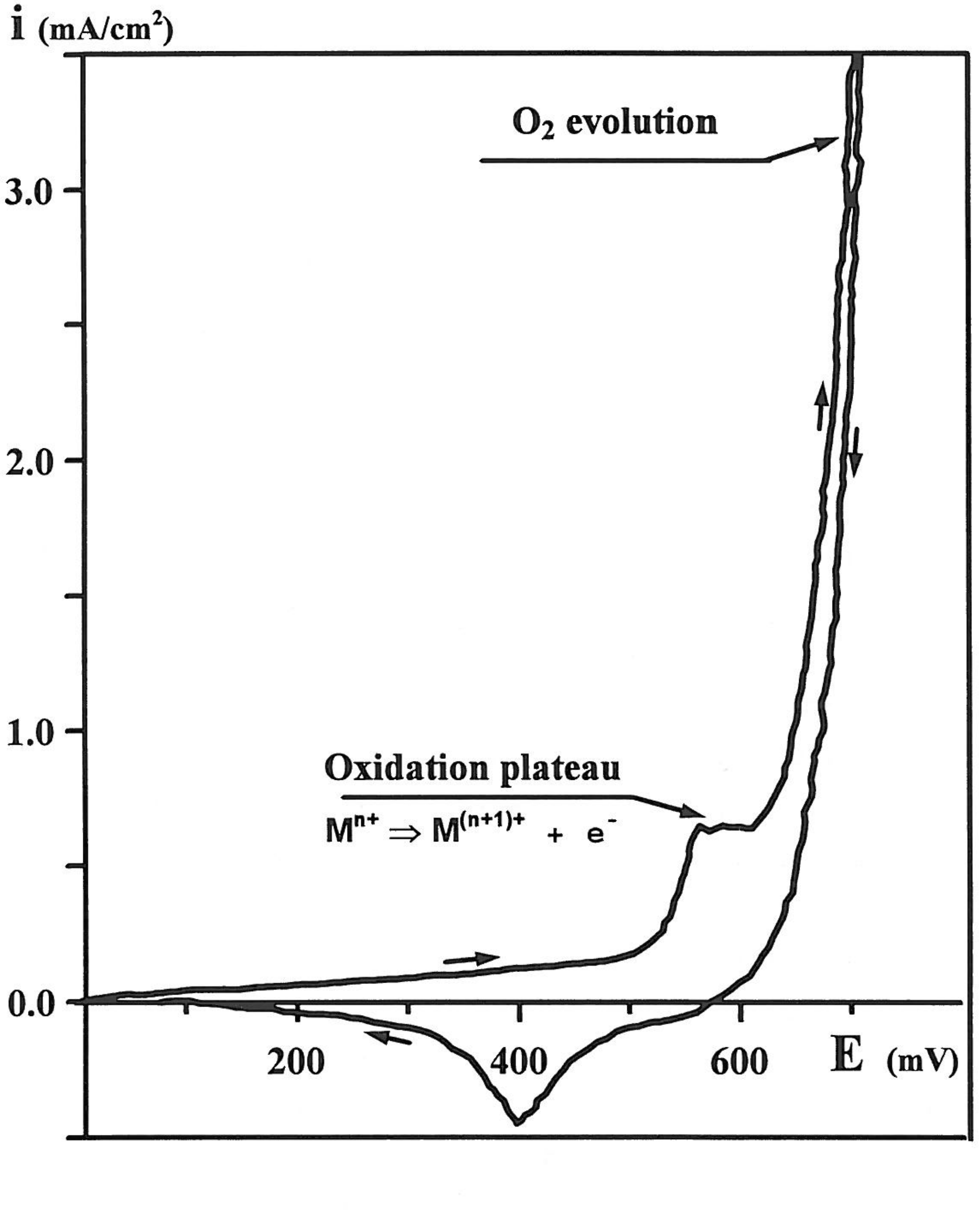

Fig. 1
Typical cyclic voltammogram of an oxide showing the oxidation plateau.

open circuit voltage (O.C.V. potential) [22]. Samples with different oxygen stoichiometry composition were prepared and, whatever the value of $\delta \geq 0.05$, two distinct superconducting transitions always appear, which was finally assigned to the existence of two superconducting phases :

- the first one with $T_C = 32$ K and a reduced orthorhombic distortion (almost tetragonal symmetry), δ being close to 0.03-0.05 depending on authors.

- the second one with $T_C = 44$ K, value significantly enhanced compared to materials prepared under high oxygen pressures [26]. Its composition seems also to correspond to the maximum value of created holes ([p] ≈ 0.16-0.18 holes/*f.u.*, $\delta \approx$ 0.08--0.09). An enhanced orthorhombic distortion as well as a significant increase of the c parameter are also noticed, which confirms the intercalation process.

A further step was reached with galvanostatic experiments which led to control the kinetics of the electrochemical reaction. This method was successfully used by several authors and the existence of those two superconducting phases was clearly corroborated [18, 21, 27 -31]. More recently C. Monroux et al. oxidizing ceramics in galvanostatic conditions very close to the thermodynamical equilibrium ($i = 2\mu A$ for about 100 days), definitively established the compositions of these phases ($\delta = 0.04$ and $\delta = 0.09$) and their electrochemical conditions of preparation and stability [32]. Fig. 2 shows the variation of the potential obtained in these conditions and the two steps corresponding to the formation of line-phases.

Galvanostatic experiments were also used by F.C. Chou et al. [33] for oxidizing single crystalline La_2CuO_4 materials. These authors observed very slow kinetics depending upon the quality of the crystals (*i.e.* the density of microcracks). These experiments were repeated in our group using the potentiostatic method [30]. The oxidation leads to superconducting materials with T_C similar to those observed for ceramics (32 K and 40--44 K), however, the superconducting Meissner fraction appears always rather low.

On the other hand, nice results were reported by the group of J-P. Locquet in I.B.M. (Zürich) concerning the electrochemical oxygen intercalation into *c*-axis La_2CuO_4 thin films grown by Molecular Beam Epitaxy [30 ,35 - 36]. Fig. 3 shows typical thermal variations of the electrical resistivity before and after electrochemical oxidation. The increase of the *c* parameter as well as the occurrence of additional (00l) diffraction peaks nicely confirms the previous results on ceramics [30, 36].

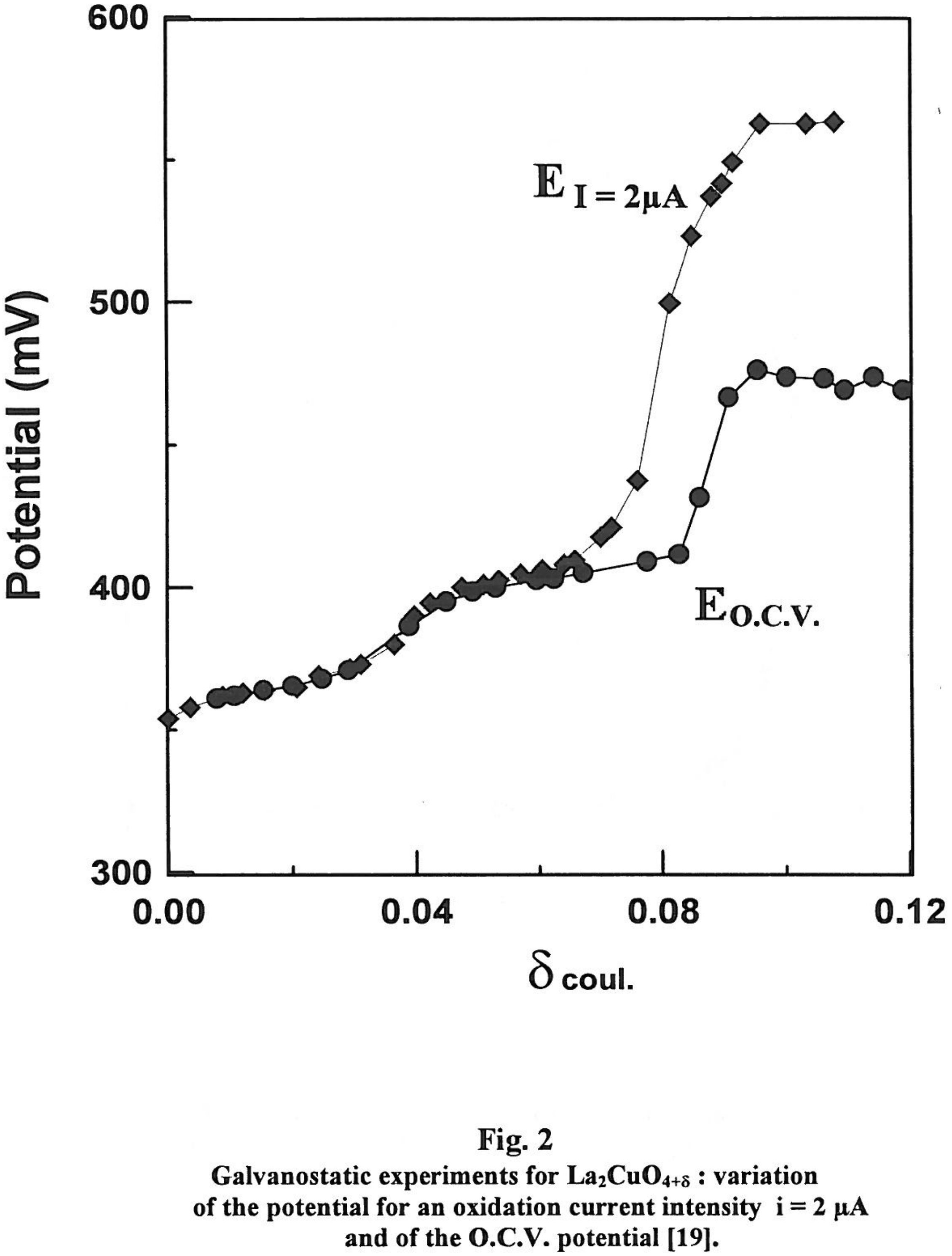

Fig. 2
Galvanostatic experiments for $La_2CuO_{4+\delta}$: variation of the potential for an oxidation current intensity i = 2 µA and of the O.C.V. potential [19].

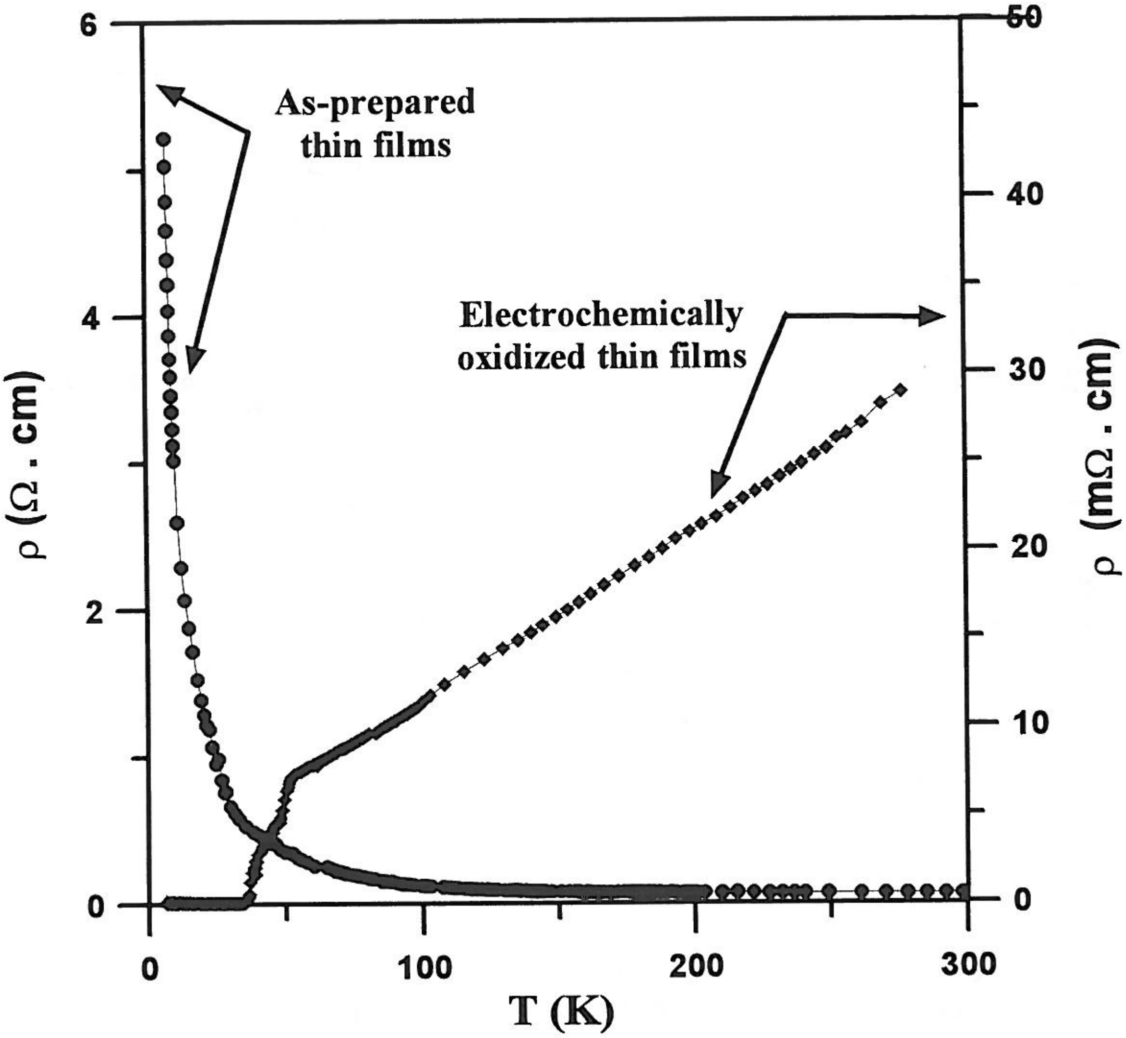

Fig. 3
Thermal variation of the electrical resistivity of La_2CuO_4 thin films before and after electrochemical oxidation [36].

Various $La_{2-x}A_xCuO_4$ (A = Sr, Ba, Nd, Bi, Pb) solid solutions have been studied in order to compare the superconducting properties of the materials prepared in air or under oxygen pressure and of those electrochemically oxidized. A common feature was that electrochemical oxidation is able to increase the oxygen content δ of all materials and to induce superconductivity [18, 37-39], even for the materials which were not initially superconductors.

The electrochemical oxidation has been proved to be also an efficient tool for extending the oxygen overstoichiometry of $La_2NiO_{4+\delta}$ from $\delta = 0.14$ (samples prepared in air) up to 0.25 [40]. Electron microscopy as well as neutron diffraction data showed for the first time that oxygen intercalation performed at room temperature leads to an ordered stage [41,42]. That was confirmed by A.J. Jacobson et al. : using galvanostatic and potential step experiments, they studied the phase diagrams of the $La_2NiO_{4+\delta}$ and $Nd_2NiO_{4+\delta}$ systems and observed the formation of staged compositions (similar to those observed in graphite and dichalcogenides) [21, 43 - 44].

III-1-4. Conclusion

Recently discovered electrochemical oxidation has rapidly appeared as a powerful technique of 'Chimie Douce' for bulky oxidizing oxides. Even though it still remains amazing, intercalation of oxygen has been clearly demonstrated. All the previous examples did show that it is an efficient process to dope AMO_{3-y} or Ln_2MO_4 compounds and that a potential of a few hundred mV applied at room temperature on an electrode can have in some cases a stronger oxidation power than high oxygen pressures at high temperature. The most outstanding example is the superconducting cuprate $La_2CuO_{4.09}$ that can be prepared only by means of this technique.

That was the reason why we used this method for oxidizing some perovskite-related ferrites.

III-2. Electrochemical Behaviors of the Oxygen-Deficient Ferrites Under Oxidation Conditions.

III-2-1. Introduction

A common structural feature of the brownmillerite phases $Sr_2Fe_2O_5$, $Ca_2Fe_2O_5$ and of the G-type phases $Sr_2LaFe_3O_8$, $Ca_2LaFe_3O_8$ is the presence of oxygen vacancy rows in their structures (*cf.* IV-1). Provided that all the oxygen vacancies are occupied, a related perovskite structure will result. That can be achieved under certain conditions. For example, the $SrFeO_{2.97}$ and $CaFeO_3$ phases were obtained under high oxygen pressures of 50 MPa [45] and $\sim 10^3$ MPa [46-48], respectively; and the perovskite phase $Sr_2LaFe_3O_{8+\delta}$ with $\delta \approx 1$ can be prepared by annealing in air at 200°C [49] or in flowing oxygen at 1000°C [50].

On the other hand, experimental results showed that the perovskite phase $SrFeO_3$ can also be obtained starting from $SrFeO_{2.50}$ phase through quite a different process, the electrochemical oxygen intercalation, which involves only room temperature and air atmosphere [14, 51].

In this work, the oxidation capabilities under electrochemical conditions of all the above-mentioned brownmillerite-type and the G-type ferrites are systematically examined. It will be seen that the electrochemical method is quite effective in oxidizing the Sr-containing phases, but not for the Ca-containing phases, the cause for which will be analyzed in IV-3.

III-2-2. Apparatus and Methods

III-2-2-1. The Electrochemical System

Studies in our research group on the electrochemical behavior of ceramic oxide samples in alkaline solution began with the work of A. Wattiaux *et al.* [10, 52]. The electrochemical system used for these experiments consists of a power supply and an electrochemical cell of three-electrode type, using alkaline solution, 1M NaOH or KOH, as electrolyte. The electrolyte concentration of 1M (pH = 14) is considered as an optimal one [15, 53]. Some important respects of experimental techniques in this work will be sketched in the following.

Fig. 4 shows the electrochemical cell, the major components of which are the three electrodes: the working electrode, the auxiliary (counter) electrode and the reference electrode.

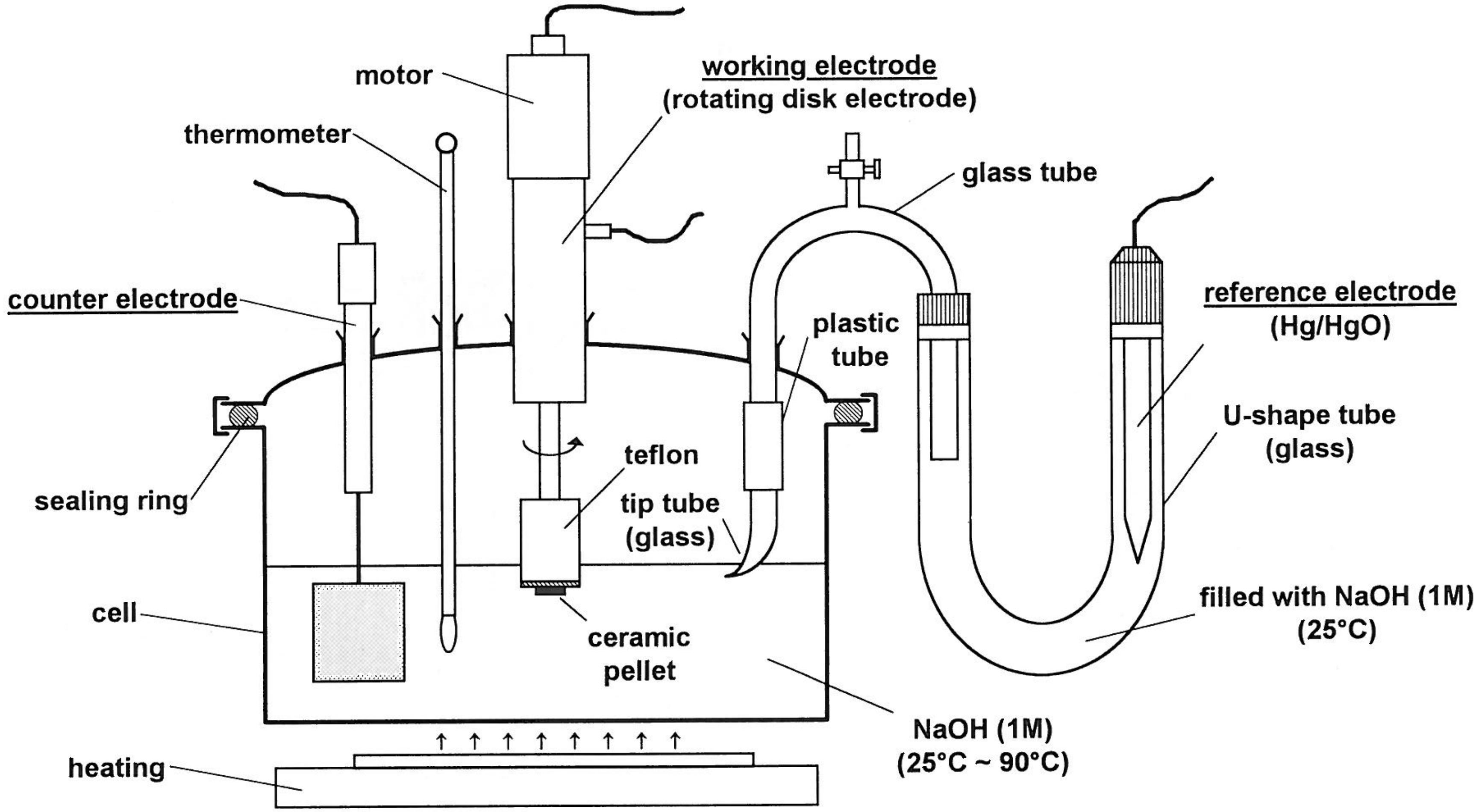

Figure 4

The electrochemical cell with three electrodes for experiments at 25°C ~ 90°C.
For T = 25°C, the reference electrode is used directly (*i.e.* without using the U-type bridge).

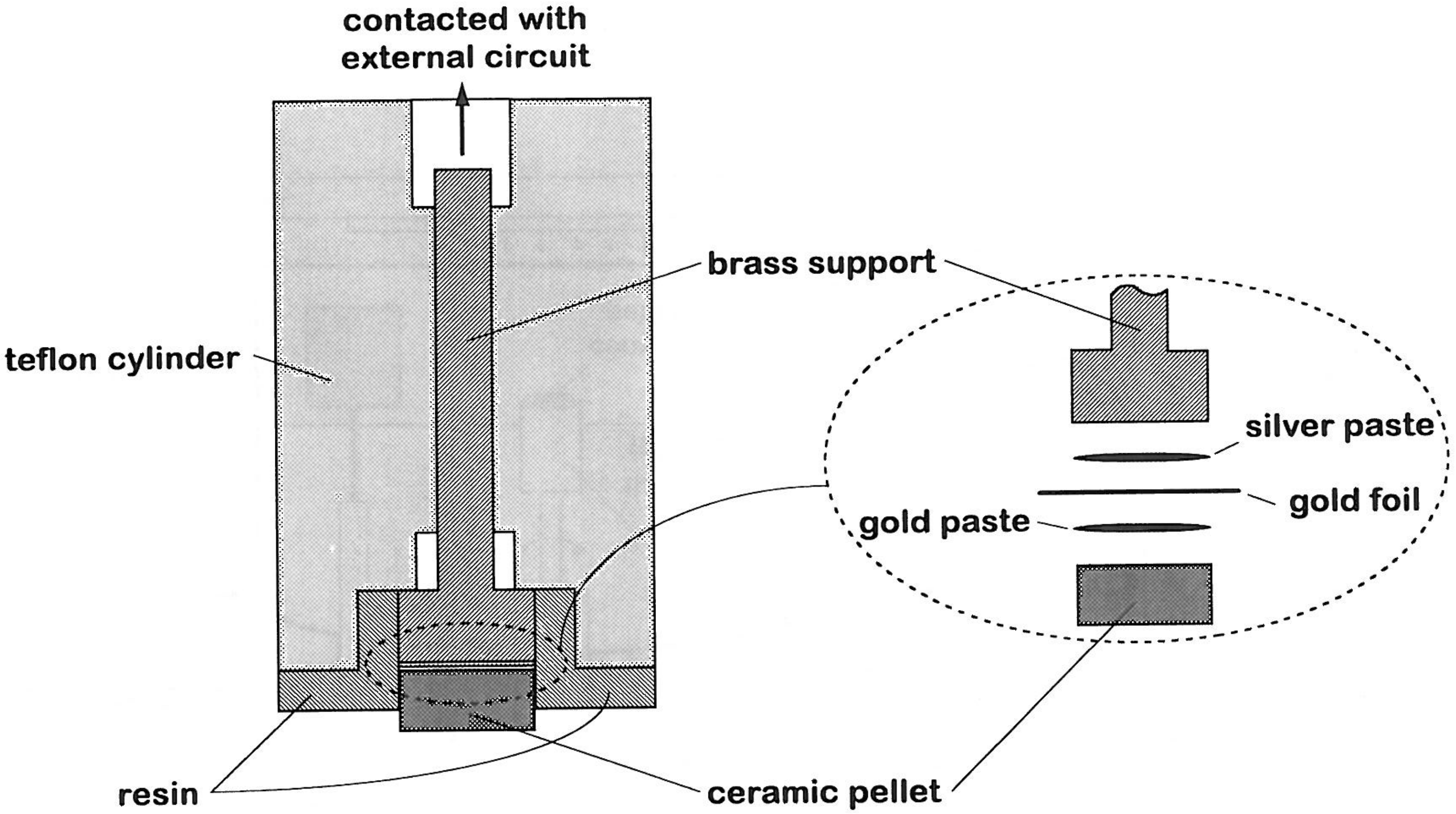

Figure 5

The section of assembly drawing (schematic) of the rotating disk electrode

- The Working Electrode

The working electrodes are ceramic pellets of the materials to be oxidized. The preparation of the ceramic pellets used for electrochemical experiments was described in Chap II. The relative densities of the pellets are around 80%, which seems to be the optimal density for the electrochemical oxidation [10, 54, 55]. That may be due to that too high density would reduce the permeation of electrolyte into ceramic pellet and, on the other hand, a pellet with too low density would have bad contact between its grains.

The working electrode of rotating disk type is preferred in this work. Its advantages are that it may produce better convection between the electrolyte in the ceramic electrode and in the bulk solution and that it usually prevents evolved gas bubbles (O_2), if any, from accumulating on the electrode surface.

A stable and ohmic contact between the ceramic pellet and metallic support (made of brass) which is connected with external circuit is important for the electrochemical process and meaningful data measurements. As the brass support is not stable during electrolysis, a gold foil is used for its protection. The assembly of the working electrode is illustrated in Fig. 5 : the ceramic pellet and the metallic support are separated by a gold foil which contacts the former by gold paste and the latter by silver paste (the silver paste has a better contact effect than the gold one). In this way, electrolyte cannot reach the silver paste and the support — an otherwise possible oxidation of them is prevented.

Moreover, in order to improve the permeation of electrolyte into the ceramic pellet, the electrode is so designed that the pellet is projected by about one third of its thickness from the resin. During experiments, the electrolyte contacts not only with the ceramic pellet but also with the metallic part (the gold foil) due to the permeation.

- The Reference Electrode

The reference electrode provides a constant reference point of potential measurements. Mercury-mercury oxide electrode (Hg / HgO) is used for this purpose in this work, which has an excellent stability in alkaline solutions. Its standard potential (at $a_{OH^-} = 1$ and T = 298K) is 0.098 V relative to SHE. ***All the potentials quoted in this work are referred to this electrode.***

In this work, some electrochemical behaviors at temperatures higher than the room temperature (25°C ≤ T ≤ 90°C) were examined. A reasonable comparison of the potential measurements at high temperatures with the room temperature ones requires a common reference point of potentials. The standard potential of an electrode usually changes with temperature, that is, $E^\circ = -\Delta G^\circ(T, P)/(n\cdot\mathfrak{I})$ and $\partial E^\circ/\partial T \neq 0$. Unfortunately, the thermal dependence of the standard potential of Hg/HgO electrode is not known, therefore it cannot be directly used as a reference electrode at temperatures higher than 25 °C.

To solve this problem, a U-type bridge of glass filled also with 1M NaOH was used. As is illustrated in Fig. 4, the Hg/HgO electrode is mounted in one end of the U-bridge. The glass tip connected with another end of the U-bridge is immersed in the electrolyte in the cell which is heated to a given temperature. The aperture of the tip is very narrow so that the electrolyte in the bridge can only drop very slowly into the cell. By this arrangement, the Hg/HgO electrode can be kept at room temperature. Measurements show that the total potential of such Hg/HgO electrode assembly is increased only by 2 ~ 3 mV at room temperature and by even a smaller value at higher temperatures. Such an increase in the electrode potential may be due to a small potential difference at the glass tip.

In such a way, potentials measured at higher temperatures using this assembly are comparable with those measured at room temperature since they are referred to the same reference potential.

- The Counter Electrode

The counter electrode is designed to have a large surface area. The materials usually used are good electronic conductors, such as foil of gold or platinum, or piece of glassy carbon.

- Usual Experimental Conditions

Table 1 summarizes the usual conditions and parameters for the electrochemical experiments in this work. Conditions for specific experiments will be described individually.

III-2-2-2. Methods of Electrochemical Oxygen Intercalation

- The Electrode Reactions

In order to oxidize an electrode material, the necessary conditions are that a non-zero current I flows from the counter electrode to the working electrode in external circuit (which is defined as $I > 0$) and the potential applied to the working electrode, E_W,

Table 1

Usual Conditions and Some Typical Parameters of Electrochemical Experiments

Ceramic Pallet	Phase: G-type or brownmillerite-type Size: ϕ 8mm × 2 ~ 2.5mm Weight: 380 ~ 440 mg Relative Density: ~ 80 %
Type of Working Electrode	Rotating Disk Electrode; Rotating Speed: 600 rpm
Reference Electrode	Hg/HgO, 1M NaOH, E°= 0.098 V/SHE
Electrolyte	1M NaOH or KOH (pH = 14)
Atmosphere	Air, 1atm
Temperature	25 °C ~ 90 °C *
Relaxation time for measuring the rest potential E_{OCV}	20 min.
Potentiostatic Mode	E_W = 400 mV ~ 700 mV
Galvanostatic Mode	I = 100 μA ~ 600 μA

* *The electrolyte begins to boil when T > 90 °C.*

should be *at least* higher than its rest potential. That is, in the electrochemical system the working electrode functions as an anode.

According to pervious works (*cf.* III-1), the oxidation of anodic material (taking G-type phase $Sr_2LaFe_3^{3+}O_8$ as an example) can be expressed as :

$$Sr_2LaFe_3^{3+}O_8 + 2\delta\,OH^- \xrightarrow{E_W\,,I_{OX}} Sr_2LaFe_{3-2\delta}^{3+}Fe_{2\delta}^{4+}O_{8+\delta} + \delta H_2O + 2\delta e^- \quad . \quad [3]$$

Here I_{OX} is the current contribution of this reaction to the total current I, and E_W is the potential applied at the working electrode, which provides the driving force for the oxygen intercalation taking place at electrolyte-electrode interface. The usual values of E_W range from 400 mV to 700 mV in this work (for the reason see below). In the present example, the δ value can vary within the range of $0 < \delta \le 1$; only in ideal case, it can reach 1.

The anodic oxidation is usually accompanied by electrolysis of the electrolyte according to the reaction :

$$4\,OH^- \xrightarrow{I_{O_2}} O_2(g) + 2H_2O + 4e^- \;, \qquad [4]$$

where I_{O_2} is its current contribution.

The total current of the anodic reactions is therefore : $I = I_{OX} + I_{O_2}$.

The standard potential (at $a_{OH^-} = 1$, $P_{O_2} = 1atm$) of reaction (*[4]*) is $\varphi°(OH^-/O_2, Pt) = 303$ mV (at T = 298K) and its derivative with respect to temperature $d\varphi°/dT = -1.68$ mV/°C. At given oxygen pressure P_{O_2}, temperature T and activity $a_{OH^-} = 1$, its potential φ, according to *Nernst formula*, is : $\varphi = \varphi° + \frac{RT}{4\mathfrak{F}}\ln P_{O_2}$ (*[5]*).

Two usual operation modes used for the anodic oxidation are the potentiostatic mode and the galvanostatic mode.

- The Potentiostatic Mode

The constant potential, E_W, between the working electrode and the reference electrode is provided by a potentiostat (Fig. 6). The directly recorded data in such experiments are current-time response $I = f(t)$.

Suppose δ_t to be the total quantity of intercalated oxygen species O^{2-} per formula unit (*e.g.* $Sr_2LaFe_3O_{8+\delta_t}$) at the end of the oxidation, then, according to the

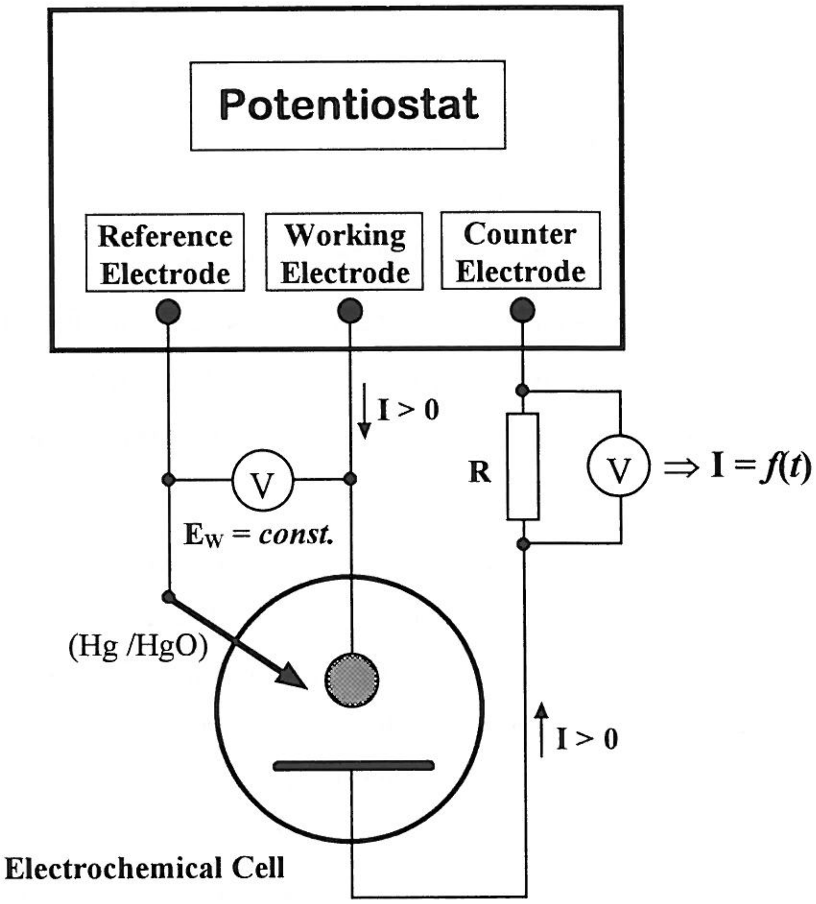

Figure 6

Schematic Representation of the Electrochemical System for *Potentiostatic Mode*.

Faraday law, the corresponding quantity of transferred charge associated with the starting phase $Sr_2LaFe_3O_8$ having a mass m is $Q_0 = 2\cdot\delta_t\cdot\frac{m}{M}\cdot\Im$

where M is the formula weight of $Sr_2LaFe_3O_8$ and $\Im$ is the *Faraday constant.*

The electric charge Q(t) which has been transferred in the external circuit at a given time t in the intercalation process can be obtained by integrating the $I = f(t)$ curve,

$$Q(t) = \int_0^t I\cdot dt\,, \quad (0 < t < T;\;\; I = I_{OX} + I_{O_2})$$

with T being the total time of the experiment.

We now define **q = Q(t)/Q₀**, which increases with time t to its final value q^F = **Q(T)/Q₀**. If the current efficiency was 100 % (*i.e.* $I = I_{OX}$, $I_{O_2} = 0$), q should vary between 0 and 1 (corresponding to the starting phase and the final oxidized phase, respectively) and it could be directly related to the δ value in *[3]* which represents the oxidation rate. But in practice the efficiency is less than 100% due to the existence of I_{O_2} ($I = I_{OX} + I_{O_2}$) so that q can exceed 1.

It is estimated (see below) that the maximum oxidation of the samples in this work could usually be attained at q > 1.2 ~ 1.3, but it is also dependent on specific experiments. Anyway, the value of q provides an estimation of the intercalated oxygen content as it will be seen later. Therefore, an alternative curve, $I = f(q)$, may approximately show the current variation with the oxidation rate.

- The Galvanostatic Mode

In this case, the current is kept at a constant value and the potential applied to the working electrode, $E_W = f(t)$, can be recorded. It is observed that E_W usually rises with time t to a finite value in the end of the oxidation. Fig. 7 shows the external circuit where a potentiostat is used. The advantage of this mode is that the electric charge, Q(t), which has been transferred at any given time t can be easily calculated:

$$Q(t) = \int_0^t I\cdot dt = I\cdot t\,, \quad (I = const.)$$

Similarly, the curve of $E_W = f(q)$ can be obtained in which $E_W \rightarrow const.$ when $q > 1$.

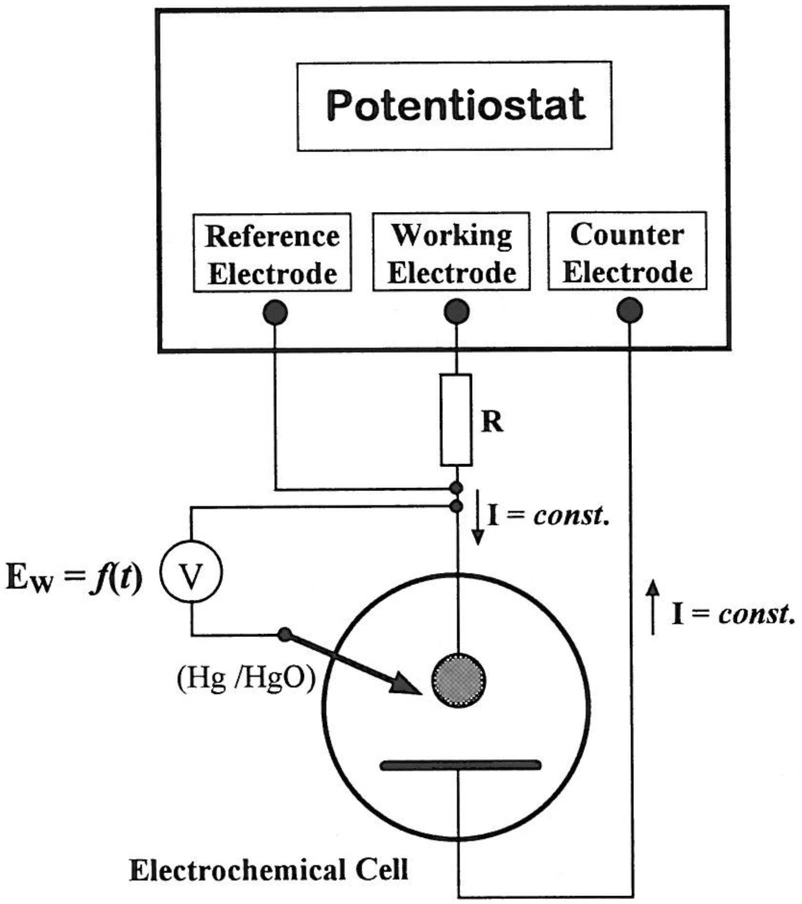

Figure 7

A Schematic Representation of the Electrochemical System for *Galvanostatic Mode* (here a potentiostat is used).

III-2-3. Preparation of the Perovskite Phase $Sr_2LaFe_3O_{8.90}$ by Electrochemical Oxygen Intercalation and Electrochemical Behaviors of $Sr_2LaFe_3O_{8+\delta}$ ($0 < \delta < 0.90$).

III-2-3-1. Voltammetric Experiments: $I = f(E_W)$

Voltammetric curves measured at 25°C for starting and final phases are shown in Fig. 8. The current response to the potential E_W shown by curve (a) (for starting phase, $\delta \approx 0$) is much weaker than that of curve (b1) and (b2) (both are for the final phase with $\delta = 0.86$), which is likely due to the high electrical resistance of the starting phase.

The curve (b2) was recorded immediately after (b1). For the final phase, oxygen evolution is the only significant reaction ($I \approx I_{O_2}$), hence the smaller current intensity of curve (b2) compared with that of (b1) at the same E_W should be due to a higher overpotential represented by *[5]* when curve (b2) was measured and may be also to the slower scanning speed for recording (b2).

A change in the slope can be seen for curve (b2), which may be related to electrochemical process on the electrode : at $E_W < 600$ mV, some surface oxidation may exist. For potentiostatic experiments, E_W was set around 500 mV, and for galvanostatic experiments the current intensity I was chosen to be 600 μA. Higher potentials E_W or current intensities I were observed to lead mainly to a larger contribution of I_{O_2} as I_{OX} is limited by diffusion process.

Another series of voltammetric experiments were carried out at 50°C (Fig. 9). Again, the slope change is observed in curve (c) with $q = 2.04$ where almost maximum oxidation is attained. It can also be seen that the curves (a) for $q = 0.22$ and (b) for $q = 0.62$ have similar current-potential responses and, as it will be see later, the main reaction at this q range is the oxygen intercalation. If the slope change in curve (c) at $E_W < 600 \sim 700$ mV is due to the saturation effect of surface oxidation of the sample, its absence in curve (a) and (b) is due to the fact that such a saturation is not expected for q values lower than 1. According to these curves, appropriate electrode potential (E_W) for potentiostatic mode at 50°C may also be around 500 mV.

III-2-3-2. The Preparation of the Perovskite Phase $Sr_2LaFe_3O_{8.90}$.

Electrochemical experiments using different modes and various conditions were performed on the starting orthorhombic G-type phase $Sr_2LaFe_3O_{8+\varepsilon}$ in order to obtain its

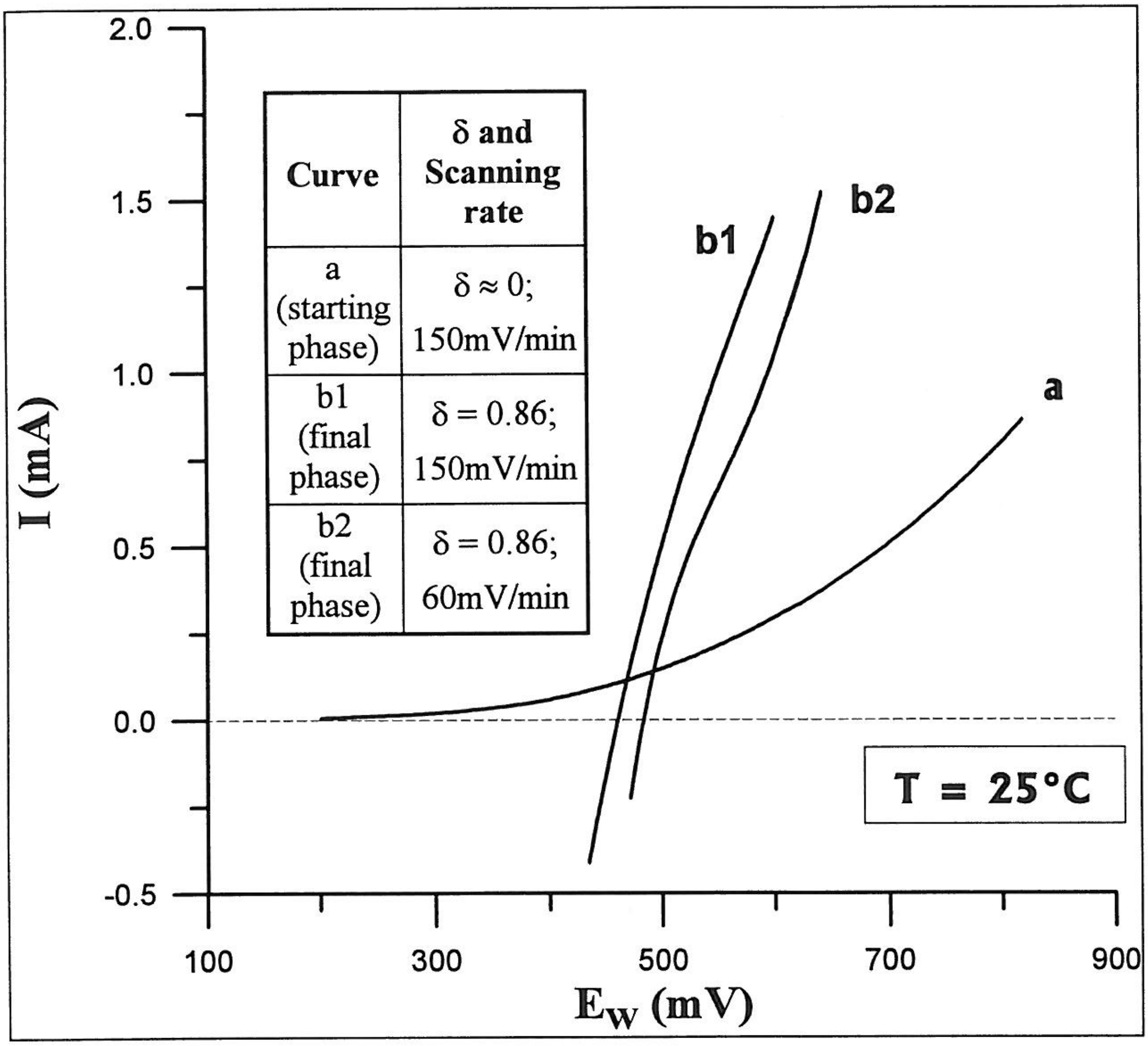

Curve	δ and Scanning rate
a (starting phase)	δ ≈ 0; 150mV/min
b1 (final phase)	δ = 0.86; 150mV/min
b2 (final phase)	δ = 0.86; 60mV/min

Figure 8

I = *f*(E_W) curves of $Sr_2LaFe_3O_{8+\delta}$ measured at room temperature
(The final phase : # SLF5)

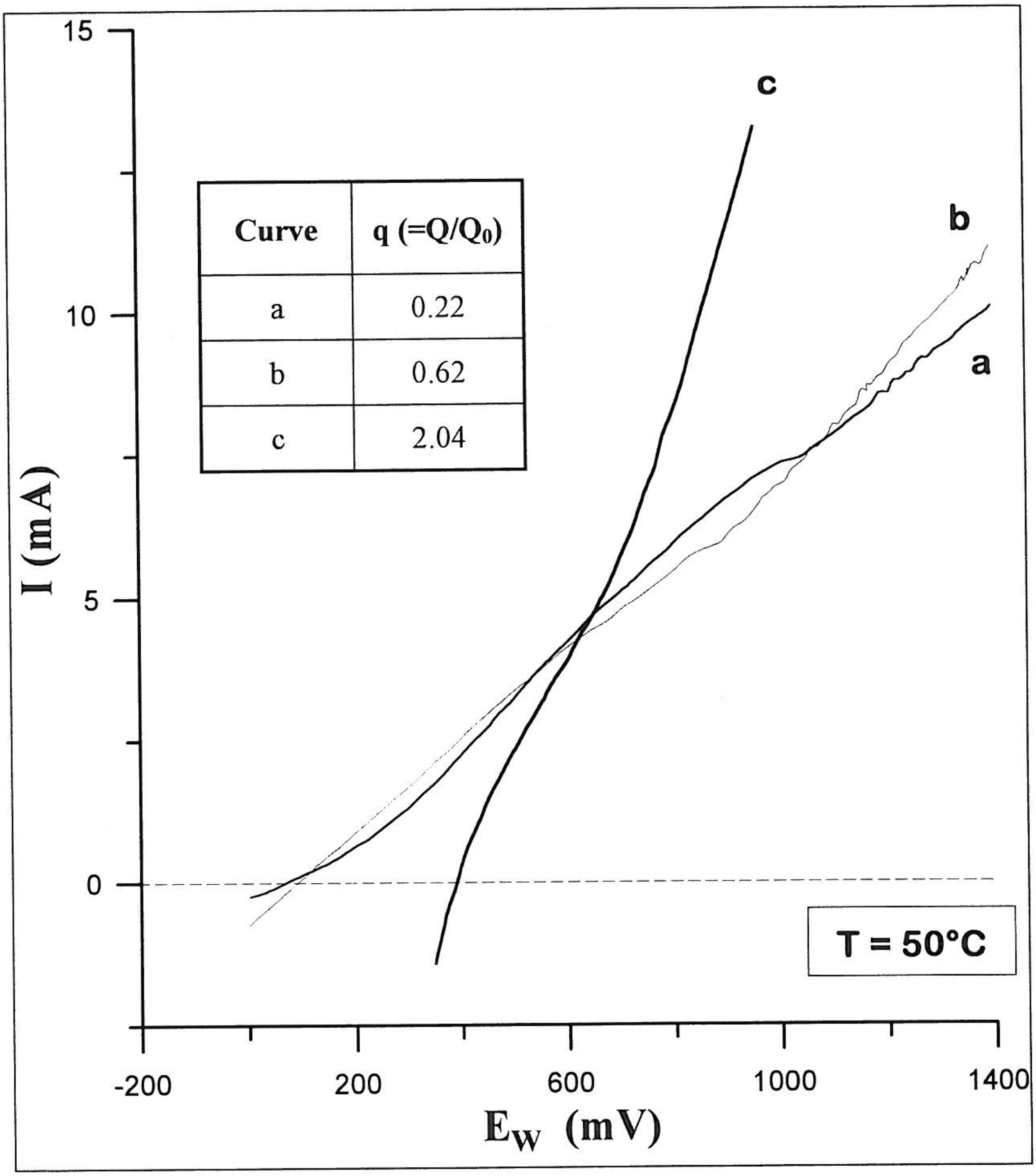

Figure 9

I = *f*(E) curves of $Sr_2LaFe_3O_{8+\delta}$ at different q values and measured at 50°C

(The scanning rate for the I-E curves was 150 mV/min.. The oxygen intercalation was done using potentiostatic mode with E_W varying from 550 mV to 700 mV.)

Table 2

Typical Experiments for Preparing the Perovskite Phase $Sr_2LaFe_3O_{8+\delta}$ ($\delta \approx 0.90$) Starting from the G-type Phase $Sr_2LaFe_3O_{8+\varepsilon}$ ($\varepsilon \approx 0$)

	Starting G-type Phase	**Final Perovskite Phase**	
Mode **and** **Conditions**	**ε Value** **E_{OCV}** **Relative Density D_r**	**δ Value** **E_{OCV}** **Sample Number**	**Intercalated Oxygen per Formula Unit** **δ - ε**
Potentiostatic mode E_W = 500 mV, I_{max}= 1.87 mA T = 25 °C Final q^F = 1.44, Q_0 = 121.0 C	ε = -0.03 E_{OCV} = 45 mV D_r = ~80%	δ = 0.90 E_{OCV} = 485 mV #. SLF9	0.93
Potentiostatic mode E_W = 500 mV, I_{max} = 3.47 mA T = 50 °C; Final q^F = 1.34, Q_0 = 105.9 C	ε = 0.10 E_{OCV} = -73 mV D_r = ~70%	δ = 0.86 E_{OCV} = 220mV # SLF15	0.76
Potentiostatic mode E_W = 500 mV, I_{max} = 16.5 mA T = 90 °C Final q^F = 3.09, Q_0 = 118.1 C	ε = 0.00 E_{OCV} = -153 mV D_r = ~80%	δ = 0.85 E_{OCV} = 360mV # SLF16	0.85
Galvanostatic mode I = 600 μA for q < 1.15 I = 100 μA for q >1.15 T = 25 °C Final q^F = 1.75, Q_0 = 117.5 C	ε = -0.07 E_{OCV} = 139 mV D_r = ~80%	δ = 0.86 E_{OCV} = 499 mV (E_W = 533 mV) # SLF5	0.93

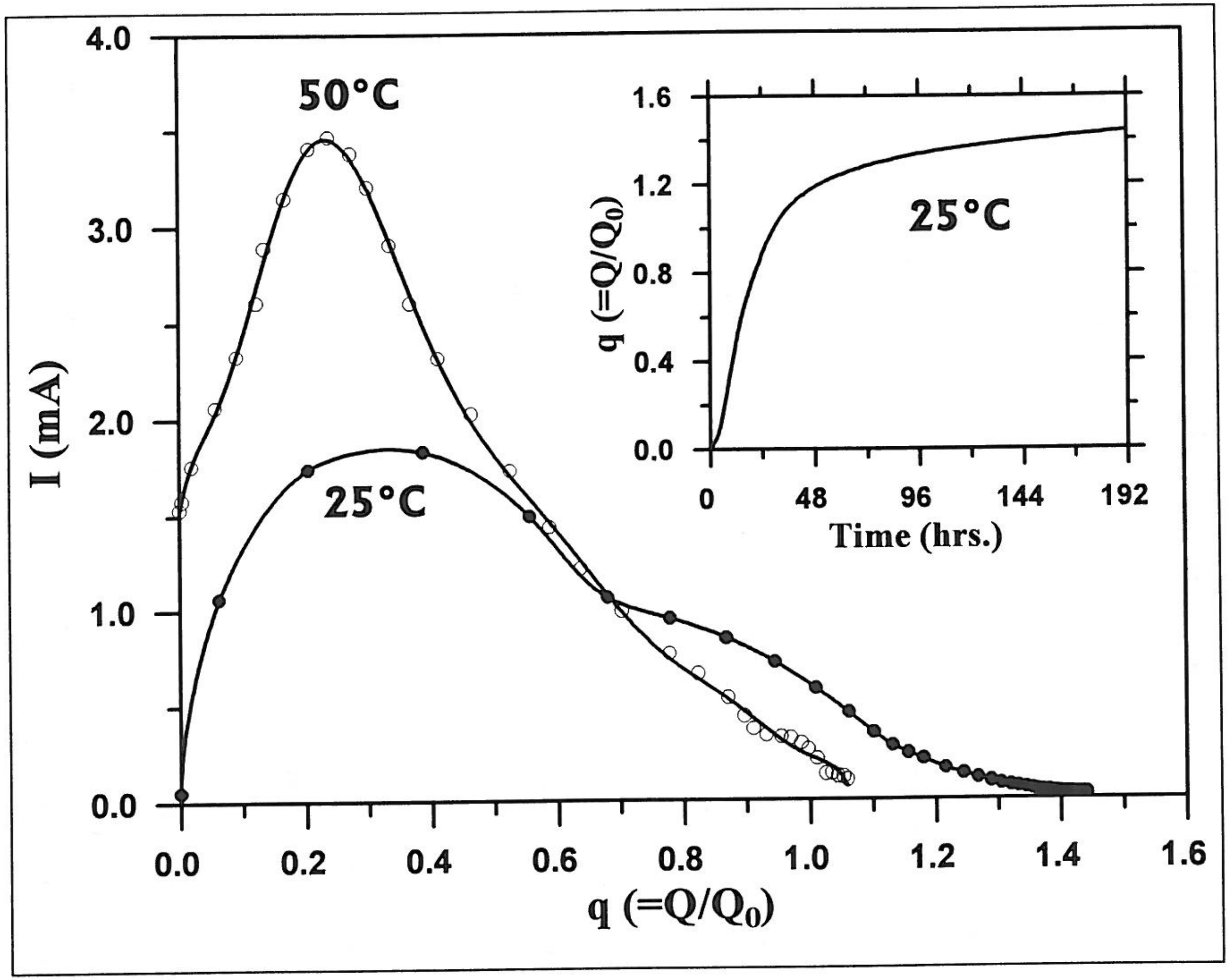

Figure 10
Variation of the current intensity with q under a constant potential of 500 mV at 25°C and 50°C for $Sr_2LaFe_3O_{8+\delta}$.
The inset shows the q = *f*(t) curve of the experiment at 25°C.
(The final phases: # SLF9 (at 25°C) and # SLF15 (at 50°C))

parent perovskite phase. Results show that *the method of electrochemical oxygen intercalation is quite efficient for this purpose, in spite of the involved "chimie douce" conditions (room temperature and atmospheric pressure).*

Some typical experiments and results are listed in Table 2. The structure and composition of the final perovskite phases given in Table 2 were determined by XRD (*cf.* IV-1 for the discussion about the symmetry) and chemical analysis (*cf.* Appendix III), respectively.

Although no remnant $Sr_2LaFe_3O_8$ phase is detected in the final oxidized samples by XRD (*cf.* V-I), Mössbauer spectroscopy data (*cf.* V-2) suggest that there still remains a small quantity of non-oxidized microdomains. In this sense the composition given by chemical analysis is only an overall one.

According to the chemical compositions, 98~99% of the oxygen sites in the final oxidized phases are occupied compared with ideal perovskite. Different experimental conditions, such as potentials (E_W), operation modes and temperature, do not significantly change the oxidation degree although the temperature influence on the current is very strong (see later).

Anyway a fully oxidized perovskite phase is not obtained in this work by electrochemical method. It may be due to some intrinsic properties of the samples. For example, some possible oxygen vacancies disorderly distributed in the octahedral layers (*cf.* IV-1), or some oxygen vacancies in the vacancy rows (*cf.* IV-1) but located in the center of some large grains, would be difficult to be occupied by intercalated oxygen atoms under the electrochemical conditions. One should not rule out that at the end of the electrochemical oxidation, the material has become electrocatalyticly speaking so active that essentially the oxygen is evolved on the surface [52, 54].

III-2-3-3. The Current Variation with Oxygen Intercalation ($I = f(q)$) and the Influence of Temperature in Potentiostatic Experiments

Two $I = f(q)$ curves obtained during two potentiostatic experiments (with $E_W = 500$ mV) at 25°C and 50°C are shown in Fig. 10.

- Experiment at 25°C

The starting phase ($q = 0$) is $Sr_2LaFe_3O_{7.97}$ and the final phase (at $q = 1.44$) is $Sr_2LaFe_3O_{8.90}$, according to chemical analysis. The wide current peak mainly extends between $q = 0$ and $q = 1.2$, while the current intensity at about $q > 1.2$ is quite small. It indicates that the most part of the total charge transfer during the oxidation process takes place in this region. That is, the oxygen intercalation should be mainly conducted within the range q = 0 ~1.2, where the current I is largely due to I_{OX} and the corresponding q values should reflect the oxidation rate. Hence the increase in q value at about q > 1.2 does not mean a significant oxidation but is rather due to oxygen evolution.

As can be seen from the figure, at low q values, the current increases with q up to its maximum (I_{max} = 1.87 mA) at about q ≈ 0.3~0.4, then it decreases. This may be explained by the fact that the starting phase, which is very close to ideal G-type phase containing only Fe^{3+} ions, has a high electrical resistivity ($\rho_{298K} > 10^8\ \Omega\cdot cm$), thus an important ohmic drop may exist even for low current intensity. After oxygen is intercalated into the structure, Fe^{4+} ions begin to appear (*cf.* reaction [*[3]*]), so that the resistivity would decrease due to the occurrence of holes resulting in an easier electron hopping. On the other hand, the diffusion channels in the structure are quite vacant at low q values which is favorable for oxygen diffusion. This may account for the rapid current increase (mainly I_{OX}) at this stage. When q continues to increase, the channels are crowded with more and more oxygen atoms, which would reduce their diffusion rate due to increasing interactions between these diffusing species. Moreover the current I_{O_2} of oxygen evolution is expected to be small and the overpotential (*[5]*) will prevent large variation in I_{O_2}. Therefore, the current decrease at q > 0.3~0.4 should be due to the slowing-down of oxygen intercalation process.

- *Experiments at 50°C and 90°C*

In the experiment at a higher temperature of 50°C, the current intensity increases considerably at lower q values compared to that at 25°C. The maximum current is I_{max} = 3.47 mA and the whole peak becomes narrower.

Another experiment at 90°C was also carried out (Table 2), the maximum current (at q ≈ 0.3) is now remarkably increased to I_{max} = 16.5 mA (not shown). During this experiment, when the current reached this maximum value, only very little and *stable* bubbles were observed on the surface of working electrode.

In spite of the considerable increases in the current intensity, no significant shift of the peak positions occurs. These observations indicate again that the oxygen concentration in the diffusion channels has an important influence on the relative rate of the intercalation process, which is independent of temperature : at a given temperature, when the concentration is higher than a certain value (q ≈ 0.3), the diffusion is slowed down hence the current decreases.

The increase of current with temperature in these experiments may be attributed to the fact that higher temperatures favor both the electronic conduction (semiconducting type) and the temperature activated ionic mobility of oxygen. The latter can be seen from the *Arrhenius* expression of the mobility μ of ions [56] : $\mu = \mu_0 \exp(\frac{-E_a}{k_B T})$, where E_a is the activation energy for ion hopping from one site to the next, k_B the Boltzmann's constant and μ_0 is proportional to 1/T.

However, such an increase of current disappears at higher q values (about $q > 0.5\sim0.6$). And, as has been mentioned (*cf.* Table 2), the oxidation degree of the samples was not raised by increasing the temperature.

III-2-3-4. Variation of Applied and Rest Potentials with Oxygen Intercalation ($E_W=f(q)$ and $E_{OCV}=f(q)$) in Galvanostatic Experiments.

In Fig. 11 is shown the q dependence of the applied potential E_W and of the rest potential E_{OCV} in a galvanostatic experiment performed at room temperature. The total current I ($=I_{OX}+I_{O_2}$) is fixed at 600 μA for $q < 1.15$ and at a smaller current, I = 100 μA, for $q > 1.15$ (since at higher q-values the oxidation is approaching the end). In the figure, three stages can be distinguished.

Stage ➊ ($0 < q \leq 0.7\sim0.8$) : The rest potential E_{OCV} is constant; the applied potential E_W is about 290 mV at $q \approx 0$ then lowers a little down to a constant value of about 200 mV. The latter may be related to the decrease in the resistance of the starting phase and/or to the double-layer charging.

The low values of the applied potential E_W (< 300 mV) and of the rest potential E_{OCV} suggest that the major contribution to the total current (I = 600 μA) is from oxygen intercalation ($I \approx I_{OX}$, $I_{O_2} \approx 0$). The increase of oxygen content in the sample appears not to influence E_{OCV} in this stage.

Stage ➋ ($0.7\sim0.8 < q \leq \sim1.2$) : Both E_W and E_{OCV} rise with q. In this stage, the concentration of oxygen in the diffusion channels is high and is approaching its maximum. Therefore the current I_{OX} , determined by the diffusing process, would decrease with q, hence I_{O_2} would increase as $I_{O_2} = I - I_{OX}$ (I being constant). That is, the reaction of oxygen evolution *[4]* is enhanced and the oxygen pressure P_{O_2} on the surface of grains in the ceramic sample would increase when dispersion of the gas into the solution is slow. As a consequence, the potential $\varphi(P_{O_2})$ on the working electrode may become significant as it rises with P_{O_2} according to relation (*[5]*) so that the overpotential at the working electrode, η_W (see below), will be shifted to higher values. Correspondingly the potential E_W at current I would also increase since it is generally expressed as :

$$E_W = E_W(eq., I = 0) + \eta_W + I \cdot R_W \ , \qquad [6]$$

where $\eta_W = \eta'_W + \varphi(P_{O_2})$, with η'_W being the other contributions (may be small or negligible) to the overpotential except $\varphi(P_{O_2})$, E_W (eq., I = 0) is the rest potential in thermodynamical equilibrium and $I \cdot R_W$ the ohmic drop at the working electrode. Note that in equilibrium $I = 0$ and $\eta_W = I \cdot R_W = 0$.

The increase in E_{OCV} may be partly attributed to the above-discussed mechanism on the supposition that oxygen (gas phase) is absorbed on the surface of the grains. That is, a finite potential $\varphi(P'_{O_2}) \neq 0$ may still exist after a short relaxation time t_R when I = 0. In this sense, the rest potential at t_R, $E_W(t_R, I = 0)$, is not the equilibrium one, E_W (eq., I = 0), as presented in *[6]* but is : $E_W(t_R, I{=}0) = E_W(eq., I{=}0) + \varphi(P'_{O_2})$, *[7]*

which rises with increasing P_{O_2} .

It is also possible that the variation of E_{OCV} may be related, to some extent, to the increase of oxygen concentration in host lattice as in the series of $Sr_2Co_2O_{5\pm x}$ ($-0.4 \leq x \leq 1.0$) prepared by thermal treatments [15, 53], where a logarithmic behavior, $E_{OCV} \propto \log[x/(1-x)]$, was observed. This is directly related to the oxidation state of the metal cation or in other words to the position of the Fermi level in the material.

In this work, the E_{OCV} values used are the rest potentials at 20 minutes after the cut of power supply, that is : $E_{OCV} = E_W(t_R = 20\text{ min.}, I = 0)$. *[8]*

As shown in Fig. 12, the rest potentials decrease slowly with time suggesting that the E_{OCV} potentials are not thermodynamical equilibrium ones.

As listed in Table 2, the E_{OCV} values of perovskites having close compositions are quite dependent on specific experimental conditions, and seem to lower with increasing temperatures. Another potentiostatic experiment performed with E_W = 400 mV at 25°C (not shown in Table 2) gave a $E_{OCV} \sim 360$ mV for a final phase with δ =

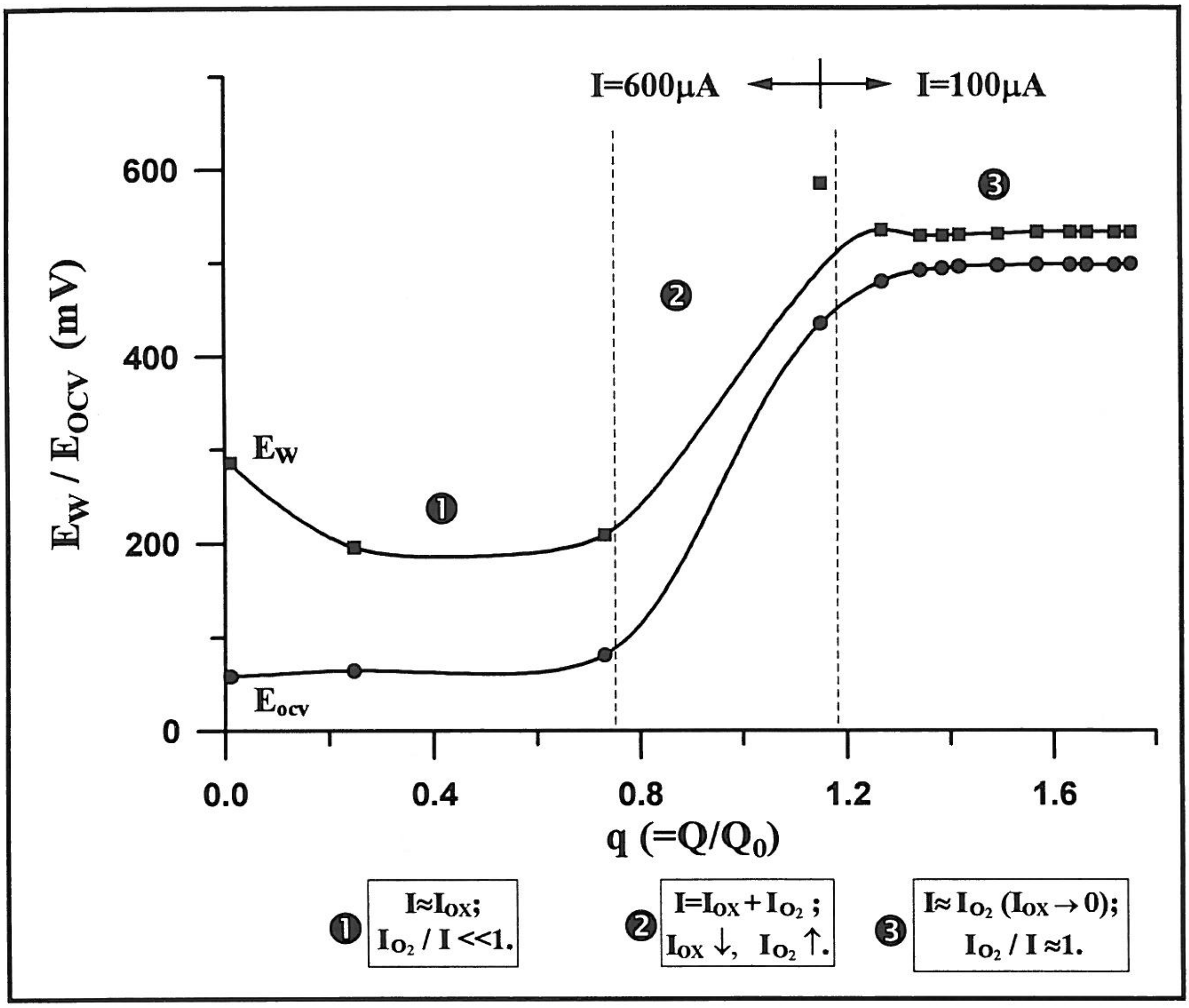

Figure 11

Dependence on q of the applied potential, E_W and of the rest potential, E_{OCV}, for $Sr_2LaFe_3O_{8+\delta}$. The experiment was carried out at room temperature using the potentiostatic mode with a current intensity $I = 600\mu A$ for $q < 1.15$ and $I = 100\mu A$ for $q > 1.15$. (The final phase: # SLF5)

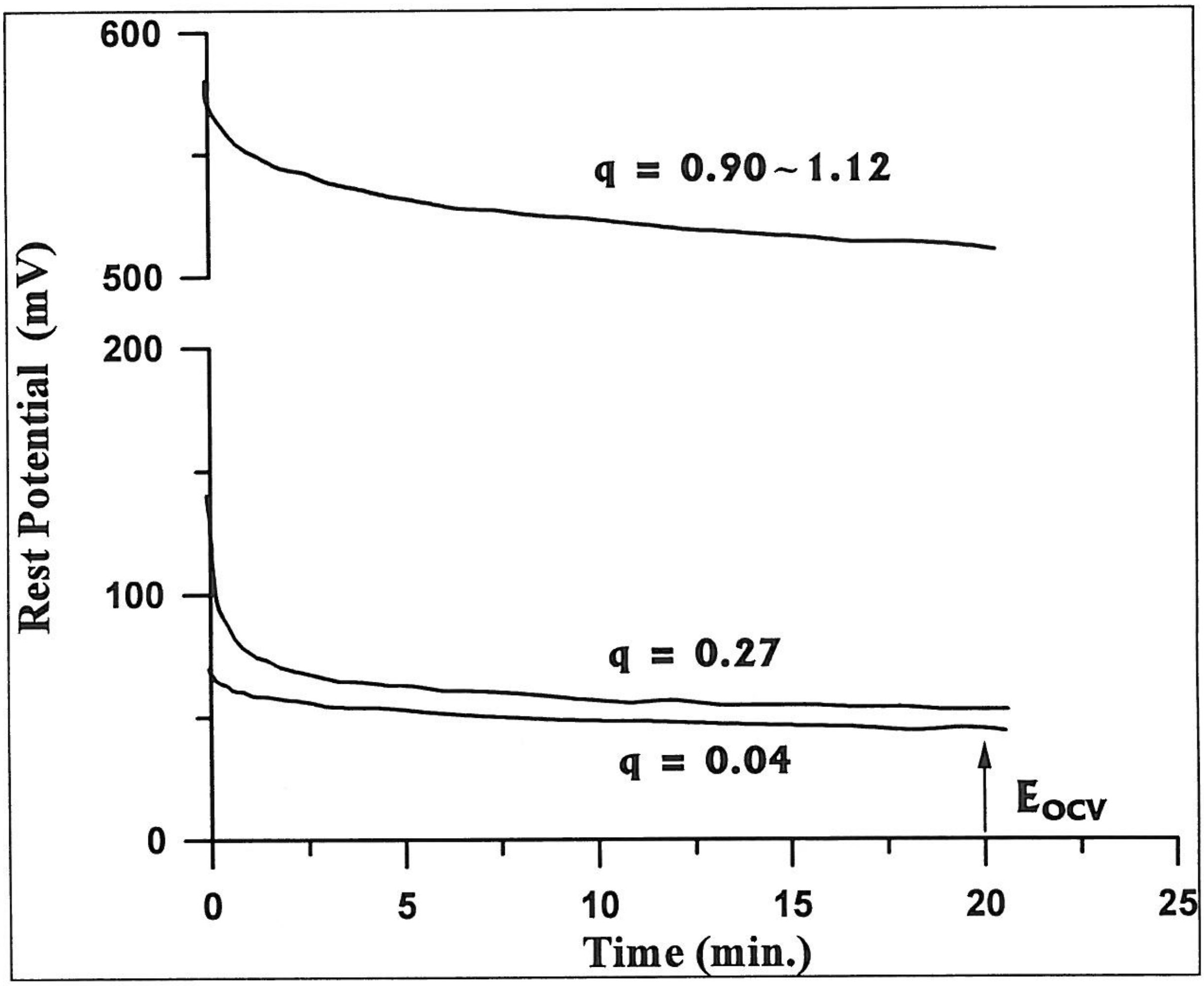

Figure 12

Time dependence of the rest potential at different q values. The electrochemical oxidation was carried out at room temperature using galvanostatic mode with I = 100 μA.

0.86. These observations suggest that surface effects (for example, due to P_{O_2}) should play an important role in E_{OCV} measurements, since the compositions of the above samples are very close.

<u>Stage ❸ (q ≥ ~1.2)</u>: Both E_W and E_{OCV} become constant. It is because that the end of the intercalation is reached : $I_{OX} \approx 0$ and almost the whole current is due to the contribution of oxygen evolution (*[4]*) so that $I_{O_2} \approx I = const.$. As a result, P_{O_2} also becomes constant, so does $\varphi(P_{O_2})$, hence E_W and E_{OCV} should be constant according to *[6]*, *[7]* and *[8]*. Therefore, constant potentials of E_W and E_{OCV} in galvanostatic experiments provide an indication of the end of oxygen intercalation.

III-2-3-5. Conclusions

The perovskite phase $Sr_2LaFe_3O_{8.90}$ can be prepared by intercalating oxygen into its G-type precursor $Sr_2LaFe_3O_8$ by electrochemical method using both potentiostatic and galvanostatic modes. Increasing temperature can make a more rapid intercalation at lower oxygen concentrations but not at higher ones, and it does not increase the oxidation degree. The end of the intercalation can be known from constant applied and rest potentials, E_W and E_{OCV}, in galvanostatic experiments, or from a weak and constant current in potentiostatic experiments performed at room temperature.

At a given temperature, the highest intercalation rate (indicated by the highest oxidation current) is observed at intermediate oxygen concentrations. It seems that, at lower oxygen concentrations, the intercalation rate is limited by the high electrical resistivity of the precursor which decreases with oxygen intercalation, so that the intercalation rate increases with the concentration; while at higher oxygen concentrations it is diffusion-determined, so that the intercalation rate decreases with increasing oxygen concentration.

The electrochemical method is also efficient for intercalating oxygen into some precursors having high resistivity (~ 10^8 Ω·cm), provided that their resistivity would decrease considerably with oxygen intercalation.

III-2-4. Electrochemical Experiments on Other Starting Phases : $SrFeO_{2.5}$, $CaFeO_{2.5}$ and $Ca_2LaFe_3O_8$

- *Experimental Results*

The electrochemical polarizations of brownmillerite phases $SrFeO_{2.5}$, $CaFeO_{2.5}$ and G-type phase $Ca_2LaFe_3O_8$ were also carried out, using the similar method as described previously.

Both the galvanostatic mode (with I ~ 100 μA) and potentiostatic mode (with E_W ~ 400 mV) were used in the case of $SrFeO_{2.5}$. According to chemical analysis and XRD examination, this phase can be easily oxidized into $SrFeO_{2.5+\delta}$ with $\delta = 0.34 \sim 0.40$, and correspondingly the structure is transformed from the brownmillerite-type to the cubic perovskite-type (Fig. 13) with a cell dimension $a_C = 3.848$Å (for $SrFeO_{2.90}$). In addition, a small quantity of $SrCO_3$ phase, formed during the electrochemical process, was detected in XRD patterns for the oxidized phase. These results are in general consistent with previous works performed in our group [14, 15, 40, 51].

A metallic behavior was observed for the fully oxidized phase $SrFeO_3$ [51], but the final phase $SrFeO_{2.90}$ obtained in the present work shows still a semiconducting behavior according to the conductivity measurement, although its conductivity is much increased compared with that of the starting phase $SrFeO_{2.5}$ and the activation energy is quite small (Fig. 14).

Electrochemical experiments for phases of $CaFeO_{2.5}$ and $Ca_2LaFe_3O_8$ were conducted using galvanostatic mode with I = 50 ~ 100 μA as their electrical resistivities are high, but no significant changes in their compositions and structures were observed after the polarizations.

- *Conclusion*

As summarized in Table 3, the orthorhombic brownmillerite phase $SrFeO_{2.5}$ can be oxidized by electrochemical method into its related cubic perovskite phase. However, our attempts were not successful to oxidize the Ca-containing ferrites, *i.e.* the brownmillerite $CaFeO_{2.5}$ and the G-type $Ca_2LaFe_3O_8$ phases, although their structures are similar to those of the Sr-containing ferrites (*cf.* IV-1). Causes of this phenomenon will be analyzed in Chap. IV-3.

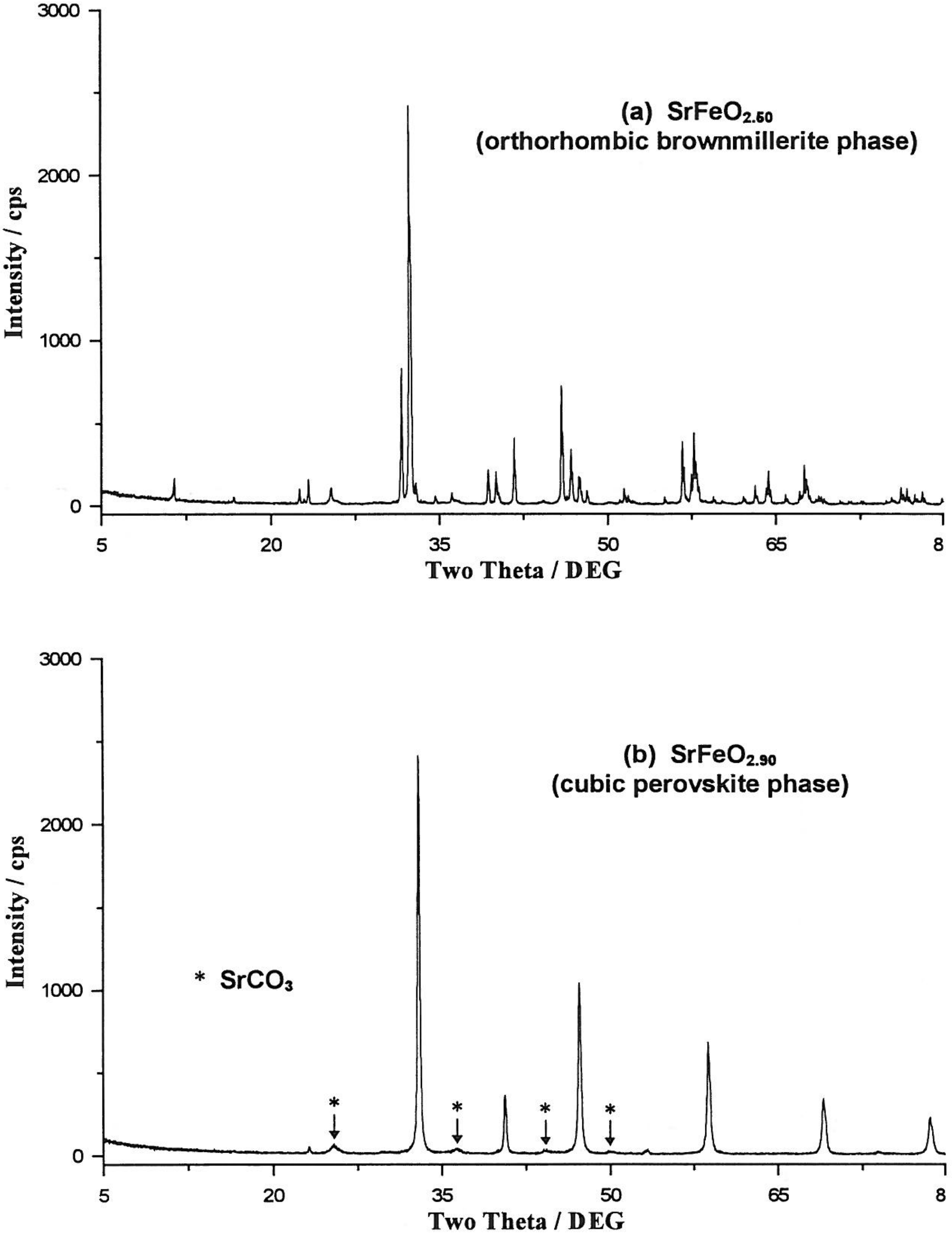

Figure 13

XRD patterns for : (a) the starting phase $SrFeO_{2.50}$
(b) the electrochemically oxidized phase $SrFeO_{2.90}$

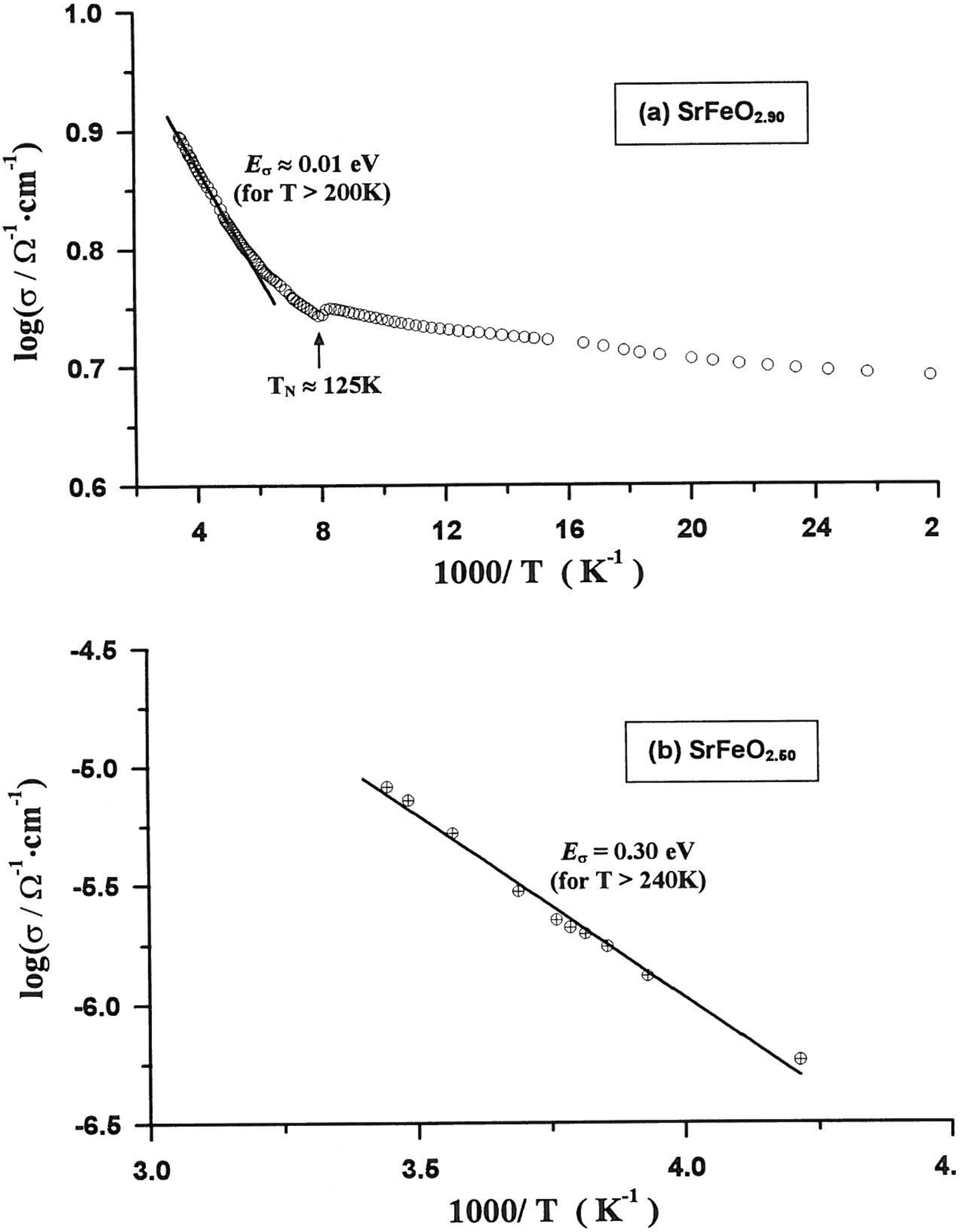

Figure 14

The logarithm of conductivity as a function of $10^3/T$ for (a) $SrFeO_{2.90}$ and (b) $SrFeO_{2.50}$. The activation energies (E_σ) are calculated from the slopes of the linear fits.

Table 3

Capabilities of Electrochemical Oxidation Intercalation of Some Brownmillerite-type and G-type Phases

Before Polarization		**After Polarization**	
Starting Phase	**E_{OCV} (mV) ***	**Final Phase**	**E_{OCV} (mV) ***
$SrFeO_{2.5}$ **(brownmillerite-type)**	-20 ~ 100	**Oxidized:** **$SrFeO_{2.90}$** **(cubic perovskite)**	~ 500
$CaFeO_{2.5}$ **(brownmillerite-type)**	~ 100	**Non Oxidized :** **composition and structure not changed**	400 ~ 500
$Ca_2LaFe_3O_8$ **(G-type)**	-15 ~ 150	**Non Oxidized :** **composition and structure not changed**	400 ~ 500

* *The rest potential E_{OCV} depends on specific experimental conditions (especially the values after polarization) ; listed here are the usual values.*

References

[1]. E. Takayama-Muromachi, T. Sasaki and Y. Matsui,
Physica C, **207**, 97-101 (1993)

[2]. M. Trari, J. Töpfer, J-P. Doumerc, M. Pouchard, A. Ammar and P. Hagenmuller.
J. Sol. State Chem., **111**, 104-110 (1994)

[3]. B. Chevalier, A. Tressaud, B. Lepine, K. Amine, J.M. Dance, L. Lozano,
E. Hickey and J. Etourneau.
Physica C, **167**, 97-101 (1990)

[4]. E. E. Fadeeva, E.I. Ardashnikova, B.A. Popovkin and M. P. Borzenkova,
Russian J. Inorg. Chem., **38**, 363-372 (1993)

[5]. A. Tressaud, C. Robin, B. Chevalier, L. Lozano and J. Etourneau,
Physica C, **177**, 330-336 (1991)

[6]. S. Petit, J-P. Doumerc, J.C. Grenier, T. Seguelong. and M. Pouchard
C.R. Acad. Sci; **321(II)**, 37-41 (1995)

[7]. M.S. Witthingham, "Intercalation Chemistry" (M.S. Witthingham and
A.J.Jacobson, Eds.), Mat. Sci. Series, p. 1, Academic Press, New York (1982)

[8]. A. Wattiaux, J-C. Park, J-C. Grenier and M. Pouchard
C. R. Acad. Sci. Paris, **310 (II)**, p. 1047-1052 (1990)

[9]. J-C. Grenier, A. Wattiaux, N. Lagueyte, J.C. Park, E. Marquestaut,
J. Etourneau and M. Pouchard
Physica C, **173**, 139-144 (1991).

[10]. A. Wattiaux, J-C. Grenier, M. Pouchard and P. Hagenmuller
Nouv. J. Chimie, **10**, 247-252 (1986)

[11]. J.C. Park, P.V. Huong, M. Rey-Lafon, J-C. Grenier, A. Wattiaux
and M. Pouchard
Physica C, **177**, 487-493 (1991)

[12]. P. Rudolf, W. Paulus and R. Schollhorn
Advanced Materials, **3**, 438-440 (1991).

[13]. N.D. Shinn, J.W. Rogers Jr.and J.E. Schirber
Phys. Rev., **41**, 7241 (1990) and refs. Therein.

[14]. A. Wattiaux, L. Fournes, A. Demourgues, N. Bernaben, J-C. Grenier
and M. Pouchard.
Sol. State Commun.., **77**, p. 489-493 (1991)

[15]. P. Bezdicka, A. Wattiaux, J-C. Grenier, M. Pouchard and P. Hagenmuller
Z. anorg. allg. Chem., **619(1)**, 7-12 (1993)

[16]. P. Bezdicka, L. Fournes, A. Wattiaux, J.C. Grenier and M. Pouchard.
Sol. State Commun., **91(7)**, 501-507 (1994)

[17]. R. Mahesh, K. R. Kannan and C. N.R. Rao
J. Solid State Chem., **114**, 294-296 (1995).

[18]. F.C. Chou, J.H. Cho and D.C. Johnston
Physica C, **197**, 303-314 (1992)

[19]. C. Monroux, A. Wattiaux and J.C. Grenier
(to be published)

[20]. J-C. Grenier, N. Lagueyte, A. Wattiaux J.P. Doumerc, P. Dordor,
J. Etourneau, J.B. Goodenough, J.S. Zhou and M. Pouchard
Physica C, **202**, 209-218 (1992).

[21]. J.D. Di Carlo, I. Yazdi, S. Bhavaraju, and A.J. Jacobson
Chem. Mater., **5**, 1692 (1993).

[22]. J-C. Grenier, A. Wattiaux and M. Pouchard, "Phase separation in cuprates"
(Ed. by K.A. Müller and G. Benedeck, World Scientific, Singapore),
p. 187-207 (1992)

[23]. N. Casan-Pastor, P. Gomez-Romero, A. Fuertes, J. M. Navarro, M. J. Sanchis and S. Ondono,
Physica C, **216**, 478-490 (1993).

[24]. N. Casan-Pastor, P. Gomez-Romero, A. Fuertes and J. M. Navarro
Solid State Ionics, **63-65**, 938-944 (1993).

[25]. J.S. Zhou, H. Chen and J.B. Goodenough,
Phys. Rev. B, **50(6)**, 4168-4180 (1994).

[26]. J. Beillle, R. Cabanel, C. Chaillout, B. Chevalier, G. Demazeau, F. Deslandes,
J. Etourneau, P. Lejay, C. Michel, J. Provost, B. Raveau, A. Sulpice,
J.L. Tholence and R. Tournier,
C. R. Acad. Sc. Paris, **304(II)** (1987), 1097.

[27]. M. K. Crawford, R. L. Harlow, E. M. Mc Carron, N. Herron, W. E. Farneth,
W. J. Donahue, B. A. Parkinson and J. Schirber.
J. Phys. Chem. Solids, **56(10)**, 1459-1469 (1995).

[28]. P. G. Raedelli, J.D. Jorgensen, R. Kleb, B. A. Hunter, F. C. Chou
and D. C. Johnston.
Phys. Rev., **49**, 6239 (1994)

[29]. W. Paulus, G. Heger, P. Rudolf and R. Schollhorn,
Physica C, **235-240**, 861-862 (1994).

[30]. "Phase separation in cuprates" (Ed. by K.A. Müller et G. Benedeck, World
Scientific, Singapore), J.C. Grenier, F. Arrouy, J-P. Locquet, C. Monroux,
M. Pouchard, A. Villesuzanne et Wattiaux, p. 237-256 (1994)

[31]. H. H. Feng, Z.G. Li, P. H. Hor, S. Bhavaraju, J. F. Di Carlo and A.J. Jacobson,
Phys. Rev., **51**, 16499 (1995)

[32]. C. Monroux, A. Wattiaux and J.C. Grenier
(to be published) and C. Monroux, Ph.D., Univ. of Bordeaux, # 1465 (1996).

[33]. F.C. Chou, D.C. Johnston, S.W. Cheong and P.C. Canfield,
Physica C, **216**, 66 (1993)

[34]. R.D. Sanchez, R.M. Torresi, C. Rettori, S. Oseroff and Z. Fisk,
Electrochemica Acta, **40**, 209 (1995)

[35]. J-P. Locquet, C. Gerber, A. Cretton, Y. Jaccard, E .J. Williams, and E. Mächler,
Appl. Physics, **A57**, 211 (1993).

[36]. F. Arrouy, J-P. Locquet, E.J. Williams, E. Mächler, R. Berger, C. Gerber,
C. Monroux, J-C. Grenier and A. Wattiaux.
Phys. Rev., (submitted)

[37]. M. Itoh, Y.J. Shan, S. Sakamoto, Y. Inaguma and T. Nakamura,
Physica C, **223**, 75-82 (1994).

[38]. Y. Takeda, H. Tomita, Y. Mukai, A. Sato, N. Imanishi, O. Yamamoto,
M. Azuma, Z. Hiroi and M. Takano.
Mat. Res. Bull., **28**, 775-783 (1993)

[39]. F. Arrouy, A. Wattiaux, E. Marquestaut, C. Cros, G. Demazeau, J-C. Grenier
and M. Pouchard
J. Sol. State Chem., **115**, p. 540-548 (1995)

[40]. A. Demourgues, A. Wattiaux, J-C. Grenier, M. Pouchard, J-M. Dance and P. Hagenmuller
J. Sol. State Chem.,**105**, 458-468 (1993)
[41]. A. Demourgues, F. Weill, J-C. Grenier, A. Wattiaux, and M. Pouchard
Physica C, **192**, 425-434 (1992)
[42]. A. Demourgues, F. Weill, B. Darriet, A. Wattiaux, J-C. Grenier, P. Gravereau and M. Pouchard
J. Sol. State Chem.,**105**, 317-329 (1993)
J. Sol. State Chem.,**105**, 330-338 (1993)
[43]. I. Yazdi, S. Bhavajaru, J. D. Di Carlo, D. P. Scarfe and A. J. Jacobson
Chem. Mater., **6**, 2078 (1994).
[44]. S. Bhavajaru, J. D. Di Carlo, D. P. Scarfe, I. Yazdi and A. J. Jacobson
Chem. Mater., **6**, 2172 (1994).
[45]. Y. Takeda, K. Kanno, T. Takada, O. Yamamoto, M. Takano, N. Nakayama, and Y. Bando,
J. Solid State Chem. **63**, 237 (1986)
[46]. F. Kanamaru, H. Miyamoto, Y. Mimura, and M. Koizumi,
Mat. Res. Bull. **5**, 257 (1970)
[47]. Y. Takeda, S. Naka, M. Takano, T. Shinjo, T. Takada, and M. Shimada,
Mat. Res. Bull. **13**, 61 (1978)
[48]. S. Darracq, G. Demazeau, P. Fabritchnti, L. Fournes, I.A. Presniakov, K.V. Pokholok, and V.P. Gorkov,
Solid State Commun. **91**, 681-685 (1994)
[49]. P.D. Battle, T.C. Gibb, and S. Nixon,
J. Solid State Chem. **77**, 124 (1988)
[50]. J.T. Wang, C.L. Lin, and T. Mihalisin,
J. Appl. Phys. **79**, 6608 (1996)
[51]. A. Demourgues, Ph.D. Thesis, University Bordeaux I (1992)
[52]. A. Wattiaux, Ph.D. Thesis, University Bordeaux I (1985)
[53]. P. Bezdicka, Ph.D. Thesis, University Bordeaux I (1993)
[54]. A. Wattiaux, J.C. Grenier, M. Pouchard, and P. Hagenmuller,
J. Electrochem. Soc. **137**, 1714 (1987) and **137**, 1718 (1987)
[55]. N. Lagueyte, A. Wattiaux, J.C. Park, J.C. Grenier, L. Fournes, and M. Pouchard, J. Phys. **III**, **1**, 1755 (1991)
[56]. A.R. West, Solid State Chemistry and its Applications, John Wiley & Sons, Ltd (1990)

Chapter IV

Structures of the Oxygen-Deficient Brownmillerite and G-type Ferrites and Their Influence on the Oxygen Intercalation

IV-1. Structural Aspects

IV-1-1. General Remarks

The brownmillerite-type or G-type structures have characteristic orthorhombic unit cells which are related to their parent cubic perovskite cells (see below). However, the space group for various brownmillerite phases may be different, indicating subtle crystallographic differences between them.

-About the Brownmillerite-Type Phases

Brownmillerite, as a major constituent of Portland cement, was first described by Törnebohm in 1897 and named 'celite'. In 1928, Hanson, Brownmiller and Bogue reported that celite is $4CaO{\cdot}Al_2O_3{\cdot}Fe_2O_3$ and that a solid-solution extends to $2CaO{\cdot}Fe_2O_3$ [1].

The crystal structure of brownmillerite, Ca_2FeAlO_5 (the $x = 1$ member of the solid-solution $Ca_2Fe_{2-x}Al_xO_5$), was suggested by Büssem in 1937 and Imma was thought to be the most probable space group with the basic structure consisting of layers of AlO_6 octahedra alternating with layers of FeO_4 tetrahedra ; but, later, several authors proposed a random distribution of Al^{3+} and Fe^{3+} ions in octahedral and tetrahedral sites and their site occupancies were studied [1]. Structural models in space group Imma and space group Pcmn were also suggested by Smith [2] and Bertaut *et al.* [3], respectively.

A generally accepted, detailed structure of Ca_2FeAlO_5 was reported by Colville *et al.* [1] and their refinements from single-crystal data showed that the most probable space group is Ibm2 (Ima2 for standard setting) but not Icmm (Imma for standard setting). This structure, involving a random cationic distribution as $Ca_2[Fe_{0.76}Al_{0.24}](Al_{0.76}Fe_{0.24})O_5$, has sheets of corner-sharing [Fe, Al]-O octahedra (normal to *b*-axis) connected to single chains of (Al, Fe)-O tetrahedra which are parallel to the *a*-axis (here, the *a*-axis is referred to the setting with $b > c > a$; [ ] and ( ) indicate octahedral and tetrahedral sites, respectively).

Dicalcium ferrite, $Ca_2Fe_2O_5$, is an end member ($x = 0$) of the solid-solution series $Ca_2Fe_{2-x}Al_xO_5$ related to the brownmillerite ($x = 1$). The most probable space group, Pcmn (Pnma for standard setting), and the general atomic arrangement for $Ca_2Fe_2O_5$ structure were first determined by Bertaut *et al.*[3], and later refined by Colville [4] and Berggren [5] from single-crystal data. The result of Colville's refinement is adopted in this work for its structural description.

It was established that $Ca_2Fe_2O_5$ is an antiferromagnet ($T_N \approx 730K$) [8] with a *G*-type magnetic structure in which nearest-neighboring Fe^{3+} ions have oppositely directed spins and shows weak ferromagnetism below T_N, which is consistent with this magnetic structure and the primitive space group.

$Sr_2Fe_2O_5$ is another one of a number of compounds related to brownmillerite and was first assumed to be isostructural with $Ca_2Fe_2O_5$ due to the similarity between their XRD patterns and lattice parameters [6, 7]. $Sr_2Fe_2O_5$ also has a *G*-type magnetic structure [9] with $T_N = 700$ K, but no parasitic ferromagnetism as in $Ca_2Fe_2O_5$ was detected. It was suggested that this last observation cast doubt on the assumption that the space group is Pcmn and that $Sr_2Fe_2O_5$ is isostructural with $Ca_2Fe_2O_5$. By profile refinement of neutron powder diffraction data collected at 4.2K, Greaves *et al.* [10] re-examined the crystal and magnetic structure of $Sr_2Fe_2O_5$ and determined the space group to be Icmm for the crystal structure, in which disorder of iron and oxygen atoms in the tetrahedral positions was allowed with half occupation of 8(*i*) position. Later on, the crystal structure of $Sr_2Fe_2O_5$ was refined for the first time by X-ray single-crystal method using space group Ibm2 (Ima2 for standard setting), without assuming such a disorder of atomic positions [11]. It is this result that will be used for its structural description in the following section.

-About the G-type Phases

Since the work of Wadsley [12] who predicted the existence of oxygen-deficient ordered structures deriving from the perovskite AMO_3 , a lot of such phases have been evidenced, especially the $A_3M_3O_8$ term (*i.e.* $AMO_{2.67}$, the n = 3 member of the series $A_nM_nO_{3n-1}$). This kind of phase, having the so-called G-type structure, was first synthesized by Grenier *et al.* [13], who also proposed a structural model (*cf.* Chap. I) (*Note*: Do not confuse this "G-type *crystal* structure" with the "G-type *magnetic* structure" which refers to a kind of spin ordering).

G-type compounds can be obtained either with two differently charged cations occupying the A sites of the perovskite structure, as in $Ca_2LaFe_3O_8$ [14], or with two cations in the M sites, as in $Ca_3Fe_2TiO_8$ [15]. In the following, only the first kind is concerned.

This term was also famous when high T_C superconductivity was discovered in metallic oxides by Bednorz and Müller [16], more especially in $YBa_2Cu_3O_7$ that contains a cationic ordering and a higher content of oxygen vacancies showing a different ordering.

Although no structural refinement from single-crystal data has been reported for G-type compounds due to the difficulty of preparing single crystals, the occurrence of ordered oxygen vacancies and OOT stacking sequence (*cf.* I-4) as proposed by Grenier *et al.*, have been verified by many researchers using methods such as X-ray and neutron powder diffraction, electron diffraction, transmission electron microscopy, and Mössbauer spectroscopy (*cf.* IV-1-3).

The oxygen-deficient compound $Sr_2LaFe_3O_8$ is one of the G-type phases. Its detailed crystal and magnetic structure characterization was carried out by Battle *et al.* [17] using synchrotron X-ray powder diffraction and neutron powder diffraction techniques. Their refinements showed that the most probable space group for the crystal structure is Pmma (standard setting).

$Ca_2LaFe_3O_8$ is also known as a G-type compound. Although its full crystal structure has not yet been obtained, the major structural features are beyond doubt (*cf.* IV-1-3).

-About the Setting of the Unit Cell Axes

For a given orthorhombic space group, *six* different settings are possible (corresponding to six permutations of the basis vectors ***a***, ***b***, ***c***) and therefore the space group symbols may be different [18].

In early works, different space group symbols have been used for describing the structures of brownmillerite phases. In this thesis, in order to facilitate the comparison of the structures, only the setting with $b > c > a$ has been adopted for both the B-type and the G-type structures, and appropriate transformations [18] of reported crystallographic data have been made if they are in other settings. In Table 1 are listed the space group symbols corresponding to such a setting for the different phases, together with those used by previous authors.

For the structure of $Ca_2Fe_2O_5$, the lattice vectors ***a***, ***b***, ***c*** corresponding to space group symbol Pnma and the vectors ***a'***, ***b'***, ***c'*** corresponding to Pcmn are transformed as

$$\mathbf{a} = \mathbf{c}' \ ; \quad \mathbf{b} = \mathbf{b}' \ ; \quad \mathbf{c} = -\mathbf{a}'$$

and the transformation between atomic positions x, y, z referring to ***a***, ***b***, ***c*** and x', y', z' referring to ***a'***, ***b'***, ***c'*** is :

$$x = z' \ ; \ y = y' \ ; \ z = -x'.$$

For the structure of $Sr_2Fe_2O_5$, the unit cell vectors and atmic coordinates corresponding to the space group symbol I2mb, which are not primed, and those corresponding to Ibm2, which are primed, are transformed as

$$a = -c' \; ; \quad b = b' \; ; \quad c = a'$$

and

$$x = -z' \; ; \; y = y' \; ; \; z = x' \; .$$

Table 1
Space Group Symbols and Corresponding Settings for the Brownmillerite and G-type Phases.

Compounds	**Space Group Symbols Corresponding to** $\underline{b > c > a}$ *	**Space Group Symbols Used in Literature**
$Ca_2Fe_2O_5$	Pnma (standard setting)	Pcmn (Colville [4]) (corresponding to $b' > a' > c'$)
$Sr_2Fe_2O_5$	I2mb	Ibm2 (Harder *et al.* [11]) (corresponding to $b' > a' > c'$)
$Sr_2LaFe_3O_8$	Pmma (standard setting)	Pmma (Battle *et al.* [17]) (corresponding to $b>c>a$)
Note	* *This is the setting used in present work.*	

IV-1-2. The Brownmillerite-type Structures

- *The Structure of $Sr_2Fe_2O_5$*

The polyhedral representation of the structure is shown in Fig. 1, which is based on crystallographic data (Table 2) obtained using single-crystal technique [11]. The space group is I2mb (with $b > c > a$), and each unit cell contains four formula units ($Z = 4$). The structure projected on yz-plane is illustrated in Fig. 2a.

It can be seen from Fig. 1 that the FeO_6 octahedral (**O**) and FeO_4 tetrahedral (**T** and **T′**) layers are perpendicular to b-direction, with **O**-layers repeated at $y = 0$, 1/2 and **T**, **T′**-layers repeated at $y = 3/4$, 1/4, respectively. The **T** and **T′**-layers are crystallographically equivalent and can be transformed to each other by twofold rotation axes parallel to a-axis and located at the sites of octahedral Fe1 atoms ; therefore the tetrahedra in the two layers are differently oriented as far as *b*-translation is concerned, giving rise to the **OTOT′** stacking sequence along *b*-axis. The tetrahedral Fe2 atoms are in mirror planes of symmetry perpendicular to *b*-direction. The Sr^{2+} ions occupy large irregular cavities between the corner-sharing octahedral and tetrahedral layers and are surrounded by eight oxygen atoms.

In the tetrahedral layers, two corners (O2) of each tetrahedron are shared with adjacent octahedra while the other two (O3) are shared with adjacent tetrahedra, thus forming single chains of tetrahedra zigzagging along the *a*-axis and separated to each other by oxygen vacancy rows which are along the $[101]_C$ direction.

In Table 2 are listed the atomic positions [11], bond lengths and bond angles for the $Sr_2Fe_2O_5$ structure. It can be immediately noticed that the octahedral sites (Fe1) and tetrahedral sites (Fe2) are irregular, their symmetry being comparatively lower than O_h (m3m) and T_d ($\bar{4}$3m), respectively.

The octahedra are distorted primarily by elongation along the *b*-axis, the Fe1–O2 distance in this direction being 2.180Å compared with 1.870 and 2.091 Å for the two bond distances at approximately right angles to ***b***. Here the O2 oxygen atoms are those who link the octahedral and tetrahedral layers.

The distortion from the T_d symmetry of the tetrahedra can be shown by a comparison of the oxygen–oxygen distances: the O2–O2 distance is 3.494Å (along *b* direction) while the O3–O3 distance is 3.001Å (these are not shown in Table 2). One tetrahedral angle is 131.6°, to be contrasted with the others which average about 104°.

The $Sr_2Fe_2O_5$ compound has a *G*-type magnetic structure (T_N = 700 K). Using neutron powder diffraction data collected at 4.2 K, Greaves *et al.* [10] refined iron spin contribution to the profile simultaneously with nuclear one, which gave the effective spins (parallel to the ***a***-direction), $S(Fe^{3+}$, oct.)=1.99(6) and $S(Fe^{3+}$, tet.)=2.05(7), for the octahedral and tetrahedral Fe^{3+} ions, respectively. The corresponding spin-only magnetic moments are $\mu(Fe^{3+}$, oct.) = $4.88\mu_B$ and $\mu(Fe^{3+}$, tet.) = $5.00\mu_B$. The fact that the magnetic moments are reduced from the Fe^{3+} free ion value was attributed to covalence effects [19].

- *The Structure of $Ca_2Fe_2O_5$*

The polyhedral representation of the structure is shown in Fig. 3, based on crystallographic data refined from single-crystal diffraction data [4]. The space group is

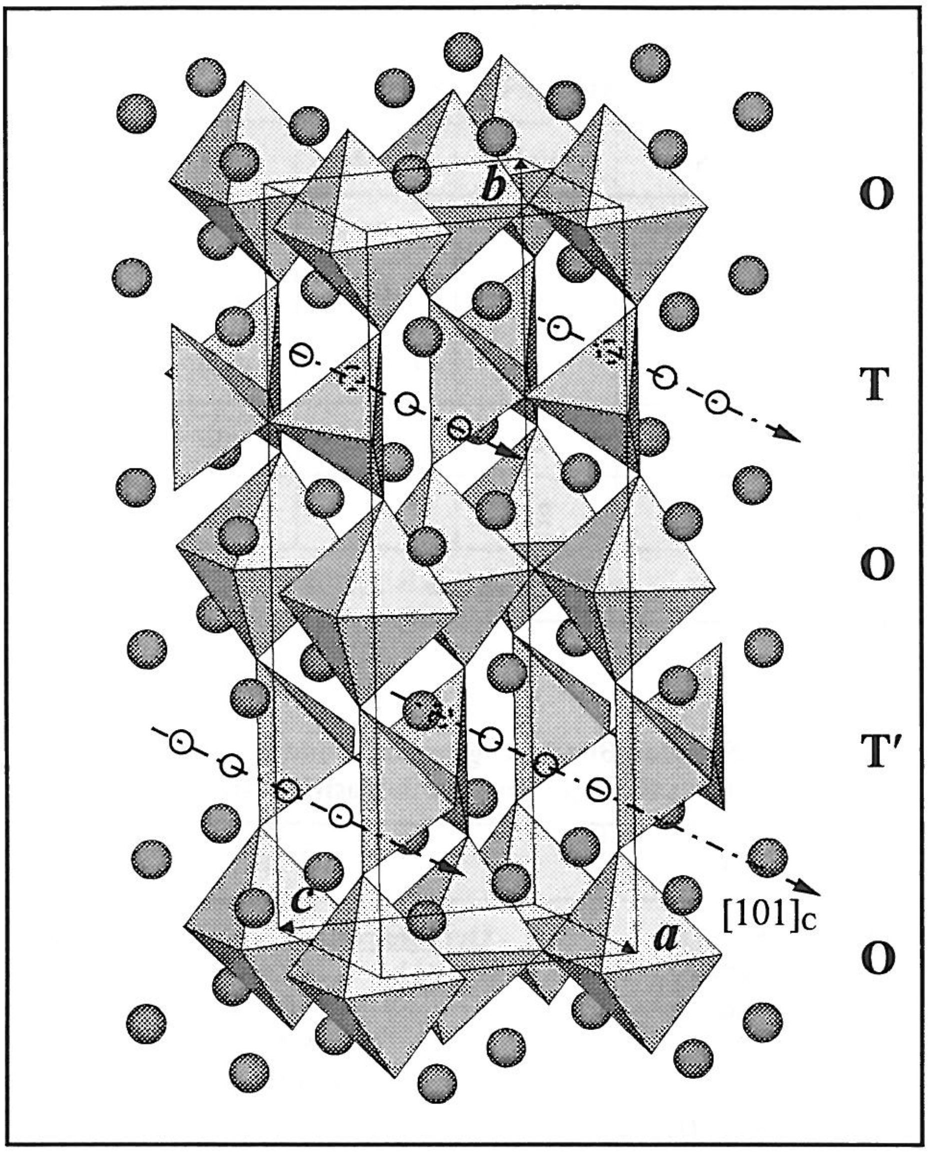

Figure 1

The orthorhombic brownmillerite-type structure of $Sr_2Fe_2O_5$

The structure of $Sr_2Fe_2O_5$ is based on crystallographic data reported by Harder *et al.* (11). The space group symbol has been changed into I2mb (see text), to which the basis vectors shown in the figure refer. The FeO_6 octahedral (**O**) and FeO_4 tetrahedral (**T** and **T′**) layers perpendicular to the ***b*** direction are stacked in the sequence of **OTOT′**, resulting in the cell parameter of $b \approx 4 \cdot a_C$ (a_C is the cell parameter of parent cubic perovskite structure). The Sr^{2+} ions, indicated by shaded balls, are located in the cavities between the polyhedral layers. The oxygen vacancies in the two tetrahedral layers, which are represented by small open circles in the figure, are so ordered that vacancy chains are formed along $[101]_C$ direction of the cubic perovskite cell, which is parallel to $[100]_B$ direction of the Brownmillerite lattice. The fact that $c > a$ (with $a \approx \sqrt{2} \cdot a_C$) is a manifestation of such vacancy ordering.

Table 2
Crystallographic Data for $Sr_2Fe_2O_5$

(a) Atomic Positions (S.G.: I2mb) [11]

Atoms	Sr	Fe1	Fe2	O1	O2	O3
x	-0.5047	0	-0.9606	-0.266	-0.025	-0.612
y	0.1097	0	1/4	0.995	0.138	1/4
z	0.0156	0	0.9323	0.262	0.056	0.853
Site	8*c*	4*a*	4*b*	8*c*	8*c*	4*b*
Site Symmetry	1	2..	.*m*.	1	1	.*m*.
Unit Cell	$a = 5.531$ Å, $b = 15.598$ Å, $c = 5.661$ Å; Z = 4.					

(b) Selected Bond Lengths and Bond Angles (calculated from the reported atomic positions listed in (a))

Bond Lengths (Å)		Bond Angles (°)			
Octahedron Fe1–O:		**Octahedron:**		**Fe–O–Fe:**	
Fe1–O1	1.870×2	O1–Fe1–O1	92.4	Fe1–O1–Fe1	175.4
	2.091×2		90.5	Fe1–O2–Fe2	146.7
Fe1–O2	2.180×2		88.5×2	Fe2–O3–Fe2	130.5
			179.1×2		
Tetrahedron Fe2–O:		O1–Fe1–O2	96.2×2		
Fe2–O2	1.916×2		91.2×2		
Fe2–O3	1.819		88.9×2		
	1.980		83.6×2		
		O2–Fe1–O2	172.7		
Sr–O:					
Sr–O1	2.611	**Tetrahedron:**			
	2.622	O2–Fe2–O2	131.6		
	2.623	O2–Fe2–O3	105.3×2		
	2.625		103.8×2		
Sr–O2	2.468	O3–Fe2–O3	104.3		
	2.699				
	2.920				
Sr–O3	2.447				
Mean	2.627				

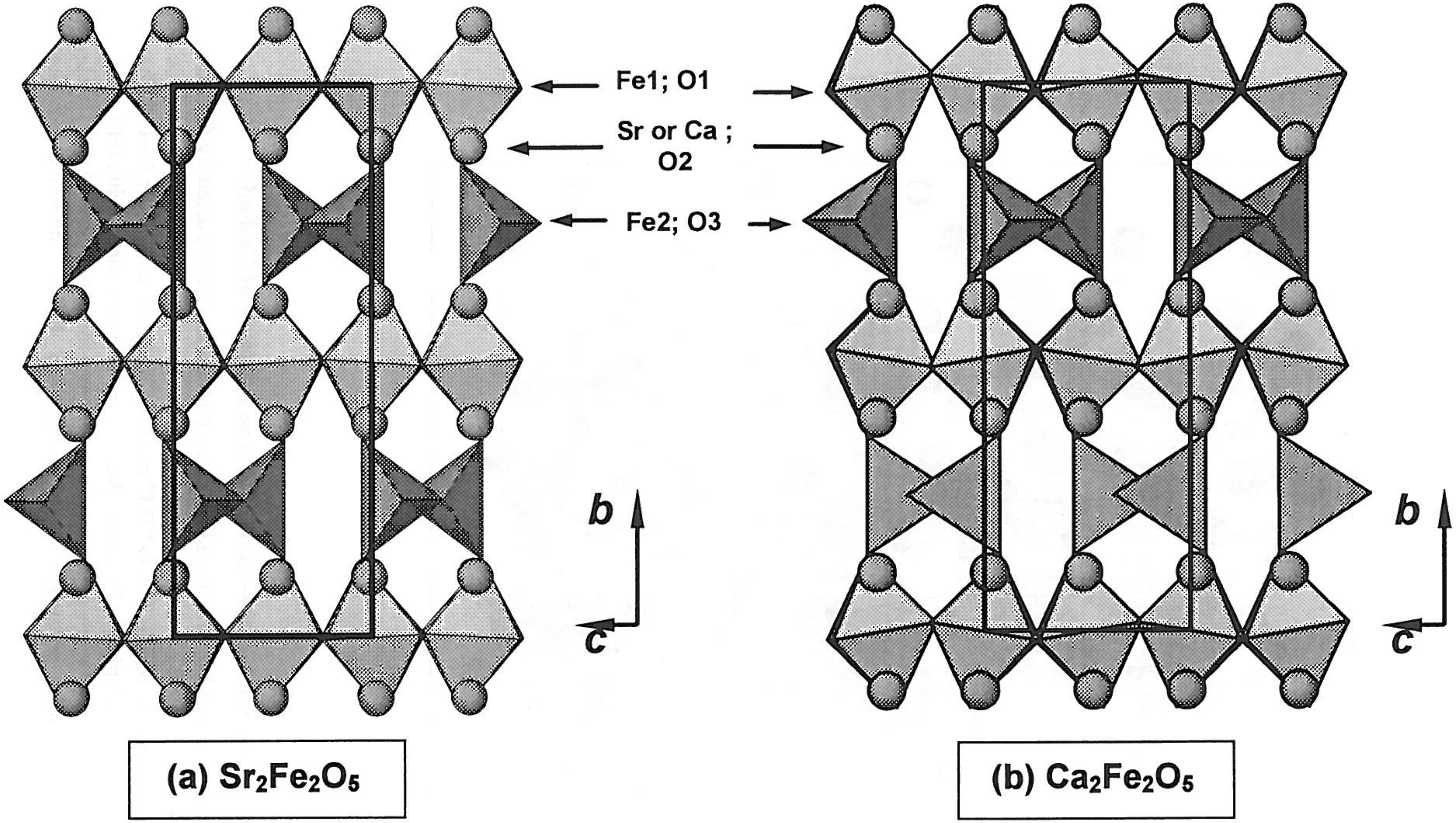

(a) $Sr_2Fe_2O_5$

(b) $Ca_2Fe_2O_5$

Figure 2
Structures of $Sr_2Fe_2O_5$ and $Ca_2Fe_2O_5$ (projection along the *a*-axis)
(*cf.* Tables 2 and 3 for atom labels).

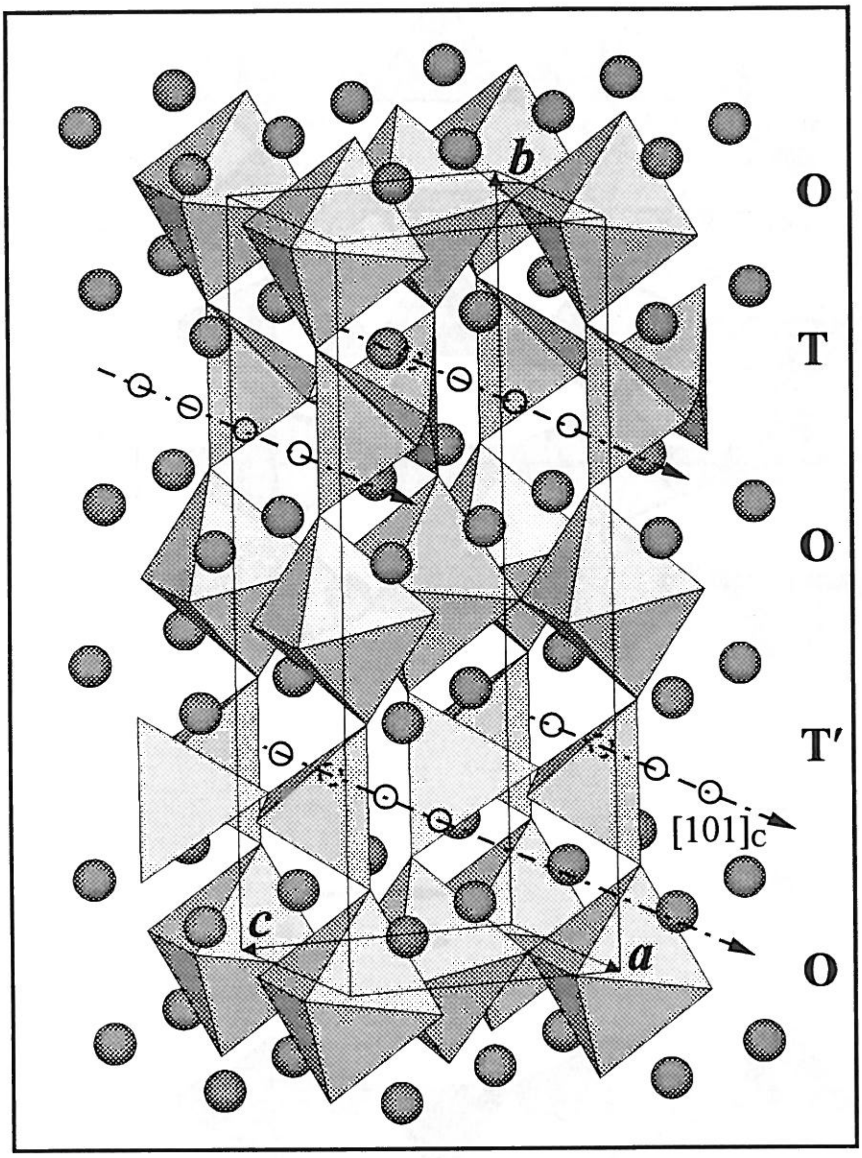

Figure 3

The orthorhombic brownmillerite-type structure of $Ca_2Fe_2O_5$

This structure of $Ca_2Fe_2O_5$ is based on crystallographic data reported by Colville (4). The basis vectors have been transformed according to the standard setting (space group symbol Pnma (see text)). The **OTOT'** stacking is the same as in $Sr_2Fe_2O_5$. The Ca^{2+} ions, indicated by shaded balls, are in the cavities between the polyhedral layers. The oxygen vacancies are again in the tetrahedral layers forming chains along $[101]_C$ direction of the cubic perovskite cell, parallel to $[100]_B$ direction of the brownmillerite.

Pnma (with $b > c > a$), and each unit cell contains four formula units ($Z = 4$). The structure projected on *yz*-plane is illustrated in Fig. 2b.

The structure is similar to that of $Sr_2Fe_2O_5$, the FeO_4 tetrahedral chains are oriented in such a way that we have again the **OTOT′** stacking sequence along the *b*-axis. The Ca^{2+} ions are coordinated to eight oxygen atoms according to Colville [4], or to nine oxygen atoms according to Berggren [5].

In Table 3 are listed the atomic positions, bond lengths and bond angles for the structure of $Ca_2Fe_2O_5$ [4]. These data indicate again that both the octahedra and the tetrahedra are considerably distorted from O_h (m3m) and T_d ($\bar{4}3m$) symmetries into the site symmetry $\bar{1}$ for Fe1 ions at octahedral sites and *.m.* for Fe2 ions at tetrahedral sites.

The magnetic structure of $Ca_2Fe_2O_5$ is also of *G*-type ($T_N = 730$ K), with the antiferromagnetically coupled moments, $4.5\mu_B$ per Fe^{3+} ion [9], lying along the *a*-axis according to Mössbauer spectra recorded using linearly polarized γ-rays [20]. The same structure was confirmed by three neutron diffraction studies carried out by Corliss *et al.* [21], Friedman *et al.* [22] and Takeda *et al.* [9].

IV-1-3. The G-type Structures

- *The Structure of $Sr_2LaFe_3O_8$*

The structure is represented in Fig. 4 on the basis of crystallographic data obtained by neutron powder diffraction at room temperature [17]. The space group is Pmma (with $b > c > a$), and each unit cell contains two formula units ($Z = 2$). The structure projected on *yz*-plane is illustrated in Fig. 5.

As shown in Fig. 4, the FeO_6 octahedral (**O**) and FeO_4 tetrahedral (**T**) layers are perpendicular to the *b*-direction, with **O**-layers repeated at about $y = 0.339$, 0.661 and **T**-layers repeated at $y = 0$. The two **O**-layers in unit cell are related to each other by mirror plane normal to ***b*** and located at $y = ½$ (*cf.* Table 4a). The **T**-layers are crystallographically equivalent and can be repeated by ***b***-translation ; hence the tetrahedra in different T-layers have same orientation as far as ***b***-translation is concerned, giving rise to the **OOT** stacking sequence along *b*-axis. The octahedral and tetrahedral Fe^{3+} ions in $Sr_2LaFe_3O_8$ structure are located in mirror planes which are perpendicular to the *a*-axis for the former and perpendicular to the *b*-axis for the latter. The 2:1 Sr^{2+} and La^{3+} ions occupy two kinds of cavities between the corner-sharing polyhedral layers :

- one is between tetrahedral and octahedral layers (4*k* site) with a 8-fold coordination.

- the other one is between two octahedral layers (2*f* site), with a 12-fold coordination, having a bigger size than the previous one (*cf.* distances in Table 4b).

Although the ratio of the former cavity to the latter one is also 2:1, no ordered distribution of these cations over the two sites was observed [17]. Hereafter, the disordered 2:1 mixture of Sr^{2+} and La^{3+} will be denoted by (2Sr, La) ions.

In the tetrahedral layers, exists a similar picture as in the brownmillerite structures, *i.e.* single chains of tetrahedra which are zigzag along the *a*-axis and are separated by rows of oxygen vacancies along the same direction.

In Table 4 are listed the atomic positions, bond lengths and bond angles for the structure of $Sr_2LaFe_3O_8$ [17]. Again in this structure, the octahedra (with central cation Fe1) and the tetrahedra (with central cation Fe2) are both distorted.

The octahedra are elongated along the *b*-axis resulting in long Fe1–O4 distance (2.365 Å) compared with the mean (1.975 Å) of the four Fe1–O bond distances. Here the O4 oxygen atoms, like O2 in the brownmillerite structures, play the similar role of linking the octahedral layers and tetrahedral layers. In contrast, the Fe1–O3 bond which joins pairs of octahedral layers is exceptionally short at 1.929 Å.

The distortion from the T_d symmetry of the tetrahedra can be shown by a comparison of the oxygen–oxygen distances: the distance O4–O4 is 3.380Å (along *b* direction) while the distance O5–O5 is 3.090Å (these are not shown in Table 4). One tetrahedral angle is 133.5°, to be contrasted with the others which average about 104.8°.

Note that the occupancy for Fe2, O4 and O5 positions is 1/2 (with the occupancy for O6 being taken as zero), which involves positional disorder around the tetrahedral sites.

The magnetic structure $Sr_2LaFe_3O_8$ was refined simultaneously with its crystal structure from the neutron diffraction data collected at room temperature [17]. The $Sr_2LaFe_3O_8$ phase is a *G*-type antiferromagnet in which spin on each Fe^{3+} ion is coupled antiparallelly to spins on its six nearest-neighboring Fe^{3+} ions, irrespective of whether they occupy octahedral or tetrahedral sites. The Néel temperature obtained from Mössbauer data is $T_N = 715 \pm 5$ K [23]. The ordered magnetic moments are along the *a*-axis, with the values of $3.77(5)\mu_B$ and $3.15(11)\mu_B$ for octahedral and tetrahedral sites, respectively, which are lower than free ion value. That may be explained by assuming

Table 3

Crystallographic Data for $Ca_2Fe_2O_5$ [4]

(a) Atomic Positions (S.G.: Pnma)

Atoms	**Ca**	**Fe1**	**Fe2**	**O1**	**O2**	**O3**
x	0.4806(2)	0	0.9459(2)	0.2632(8)	0.0234(8)	0.6005(9)
y	0.1079(1)	0	1/4	0.9839(2)	0.1403(2)	1/4
z	-0.0233(2)	0	-0.9338(2)	-0.2366(7)	-0.0716(7)	-0.8746(8)
Site	8*d*	4*a*	4*c*	8*d*	8*d*	4*c*
Site Symmetry	1	$\bar{1}$	*.m.*	1	1	*.m.*
Unit Cell	*a*=5.429(1) Å, *b*=14.771(2) Å, *c*=5.599(1) Å; Z=4.					

(b) Selected Bond Lengths and Bond Angles

Bond Lengths (Å)		**Bond Angles (°)**			
Octahedron Fe1–O:		**Octahedron:**		**Fe–O–Fe:**	
Fe1–O1	1.963×2	O1–Fe1–O1	92.6×2	Fe1–O1–Fe1	164.8
	1.970×2		87.4×2	Fe1–O2–Fe2	140.2
Fe1–O2	2.115×2		180.0×2	Fe2–O3–Fe2	125.9
		O1–Fe1–O2	93.0×2		
Tetrahedron Fe2–O:			90.9×2		
Fe2–O2	1.844×2		89.1×2		
Fe2–O3	1.904		87.0×2		
	1.920	O2–Fe1–O2	180.0		
Ca–O:		**Tetrahedron:**			
Ca–O1	2.427	O2–Fe2–O2	123.1		
	2.483	O2–Fe2–O3	107.3×2		
	2.484		106.1×2		
	2.741	O3–Fe2–O3	105.9		
Ca–O2	2.330				
	2.542				
	3.000				
Ca–O3	2.350				
Mean	2.545				

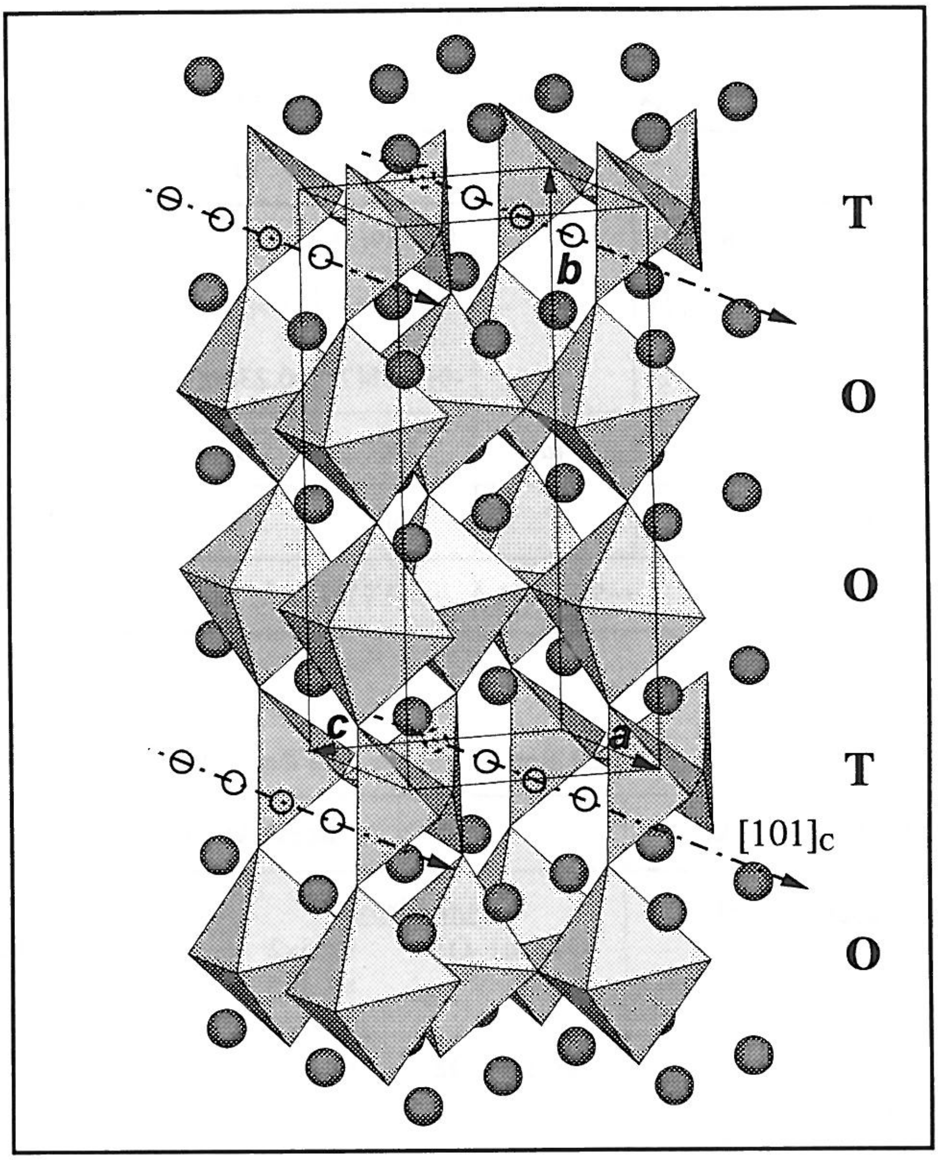

Figure 4

The orthorhombic G-type structure of $Sr_2LaFe_3O_8$

This G-type structure of $Sr_2LaFe_3O_8$, having the Pmma space group, is based on previously reported crystallographic data [17]. The FeO_6 octahedral **(O)** and FeO_4 tetrahedral **(T)** layers perpendicular to the ***b*** direction are stacked in the sequence of **OOT**, giving rise to the cell parameter $b \approx 3 \cdot a_C$ (a_C being the parameter of parent cubic perovskite cell). In the cavities between the polyhedral layers are disorderly located the 2:1 Sr^{2+} and La^{3+} ions as shown in the figure by shaded balls. The oxygen vacancies in the tetrahedral layers, indicated by smaller open circles, are considered to be ordered along $[101]_C$ direction of the related cubic perovskite lattice, which is parallel to $[100]_G$ direction of the G-type structure. Such a vacancy ordering produces a difference between the cell parameters c and a of the G-type structure with $c > a \approx \sqrt{2} \cdot a_C$.

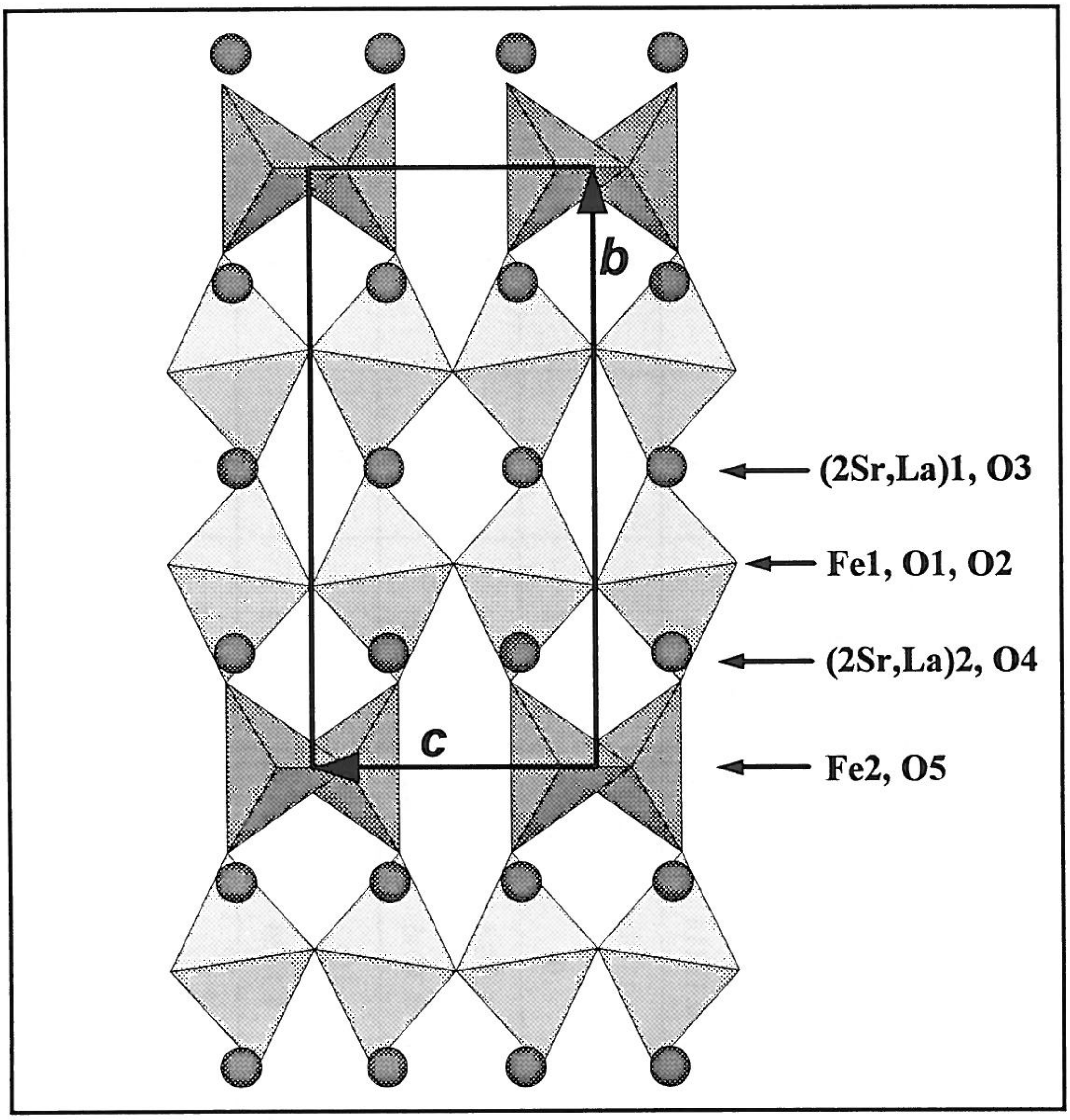

Figure 5

The G-type structure of $Sr_2LaFe_3O_8$ projected on the yz-plane.

(*cf.* Table 4a for atom labels).

Table 4 Crystallographic Data for $Sr_2LaFe_3O_8$ [17]

(a) Atomic Positions (S.G.: Pmma)

Atoms	*x*	*y*	*z*	**Occupancy**	**Site**	**Site Symmetry**
(2Sr, La)1	1/4	1/2	0.7443	1	*2f*	*mm2*
(2Sr, La)2	1/4	0.19114	0.7307	1	*4k*	*m..*
Fe1	1/4	0.33884	0.2415	1	*4k*	*m..*
Fe2	0.2078	0	0.1786	1/2	*4i*	*.m.*
O1	0	0.3025	0	1	*4g*	.2.
O2	0	0.3406	1/2	1	*4h*	.2.
O3	1/4	1/2	0.2001	1	*2f*	*mm2*
O4	0.268	0.1420	0.3013	1/2	*8l*	1
O5	0.134	0	0.875	0.46	*4i*	*.m.*
O6	0.074	0	0.688	0.04	*4i*	*.m.*
Unit Cell	$a = 5.5095(1)$ Å, $b = 11.8845(5)$ Å, $c = 5.6028(1)$ Å; Z = 2.					

Table 4 Crystallographic Data for $Sr_2LaFe_3O_8$ [17]

(b) Selected Bond Lengths and Bond Angles (Fe–O–Fe bond angles are calculated and added based on the reported atomic positions listed in Table (a))

Bond Lengths (Å)				Bond Angles (°)			
Octahedron Fe1–O:		**(2Sr, La)1–O:**		**Octahedron:**		**Tetrahedron:**	
Fe1–O1	1.952×2	(2Sr, La)1–O1	2.968×4	O1–Fe1–O1	89.8	O4–Fe2–O4	133.5
Fe1–O2	1.999×2	(2Sr, La)1–O2	2.713×4	O1–Fe1–O2	91.0×2	O4–Fe2–O5	104.3×2
Fe1–O3	1.929	(2Sr, La)1–O3	3.049		171.8×2		103.7×2
Fe1–O4	2.365		2.554	O1–Fe1–O3	93.6×2	O5–Fe2–O5	108.1
			2.772×2	O1–Fe1–O4	89.0		
Tetrahedron Fe2–O:		mean	2.823		85.5	**Fe–O–Fe:**	
Fe2–O4	1.85×2			O2–Fe1–O2	87.1	Fe1–O1–Fe1	154.8
Fe2–O5	1.91	**(2Sr, La)2–O:**		O2–Fe1–O3	94.4×2	Fe1–O2–Fe1	178.8
	1.91	(2Sr, La)2–O1	2.515×2	O2–Fe1–O4	86.3	Fe1–O3–Fe1	166.2
		(2Sr, La)2–O2	2.593×2		83.0	Fe1–O4–Fe2	148.5*
		(2Sr, La)2–O4	2.47	O3–Fe1–O4	177.3	Fe2–O5–Fe2	126.2
			2.72				
			2.92				
		(2Sr, La)2–O5	2.49				
		mean	2.60				

* This value is an averaged one due to the positional disorder of Fe2.

that the magnetization is not completely saturated at room temperature [23]. The small value of the observed magnetic moment at tetrahedral site was also assigned to the influence of structural disorder on the superexchange interactions, as well as to another possibility that the moment may disorderedly deviate from the *a*-direction [24].

- *The Structure of $Ca_2LaFe_3O_8$*

Although no full structural data have been reported for $Ca_2LaFe_3O_8$, its major G-type structural features were confirmed in many investigations carried out by several authors using X-ray powder diffraction, electron diffraction (ED), transmission electron microscopy (TEM) and Mössbauer spectroscopy. For example, ED and TEM analysis by Alario-Franco *et al.* [25] clearly showed the characteristic G-type lattice which is derived from the parent cubic perovskite one in the way presented in Fig. 3 of Chap. I.

As $Ca_2LaFe_3O_8$ is also an antiferromagnet with the magnetic ordering temperature being circa 770 K [26], its Mössbauer spectrum recorded at 295 K [26, 27], comprising two well-resolved six-line magnetic hyperfine splittings, confirms the presence of tetrahedral and octahedral iron sites in the expected ratio of [T]/[O] = 1:2.

IV-1-4. Discussions and Conclusions

- *Comparison of the Structures*

Common features in those anion-deficient structures of brownmillerite-type and G-type are that all polyhedra, both the FeO_6 octahedra and FeO_4 tetrahedra, are linked to one another by sharing corners as in the perovskite structure, and that the oxygen vacancies in their tetrahedral layers are ordered along $[101]_C$ direction of the related perovskite cubic subcell, resulting in similar single chains of tetrahedra along that direction as well as similar orientation of their unit cells. On the other hand, the difference between brownmillerite and G-type structures is evident due to their different polyhedral stacking sequences. Even the two brownmillerite-type structures of $Sr_2Fe_2O_5$ and $Ca_2Fe_2O_5$ are not ideally isostructural due to their different symmetries. From the polyhedral representation shown in Fig. 2, it is clearly seen that the tetrahedral chains are differently oriented in the two brownmillerite structures.

- *The Disorder of Sr and La Ions in $Sr_2LaFe_3O_8$.*

It has been mentioned in IV-1-3 that, although the 2:1 Sr^{2+} and La^{3+} ions occupy two kinds of cavities (the 4*k*, 8-coordinated, and 2*f* , 12-coordinated, positions) with their relative quantity being also 2:1, their distribution over these two sites is *not* ordered. Here we will show that the observed disorder is consistent with the bond length data.

The size of the *2f* cavity may be represented by the mean of A1–O distances $\bar{\mathbf{d}}_{A1\text{-}O}$, and that of the *4k* cavity by the mean of A2–O distances $\bar{\mathbf{d}}_{A2\text{-}O}$. Here A1 = (2Sr, La)1 and A2 = (2Sr, La)2.

From Table 5, it can be seen that, the Δ values of Sr^{2+} and La^{3+} cations for the two cavities have the same sign but with small differences; on the other hand, the weighed average $\overline{(\mathbf{r}_M + \mathbf{r}_O)}_W$ for the two cavities are close to $\bar{\mathbf{d}}_{A1\text{-}O}$ or $\bar{\mathbf{d}}_{A2\text{-}O}$, although the average values with some different weighing do not make large difference.

These data indicate that the observed mean distances of A1-O and A2-O do not correspond to ordered occupation such as the two Sr^{2+} ions in the two *4k* sites and the La^{3+} ion in the *2f* site . It is a way to confirm the cationic disorder over these two sites.

It will be known later that this disordered distribution of 2:1 Sr^{2+} and La^{3+} ions is also observed in perovskite phase of $Sr_2LaFe_3O_{8.95}$. Since this perovskite is obtained starting from $Sr_2LaFe_3O_8$ phase by a "*chimie douce"* method, such a disorder is a natural consequence.

- The Influence of Bonding on the Cell Parameters

As it has been previously mentioned, the cell parameters of brownmillerite (n = 2) and G-type (n = 3) structures can be approximately related to the cubic cell as: $a_n \approx \sqrt{2}\cdot a_c$, $b_n \approx (6\text{-n})\cdot a_c$, and $c_n \approx \sqrt{2}\cdot a_c$. Observed cell parameters have the relative magnitude of $c_n > a_n \geq \sqrt{2}\cdot a_c$ (with c_n being greater than a_n by 0.1~0.2 Å) and $b_n \geq (6\text{-n})\cdot a_c$.

The observation of $c_n > a_n$ can be attributed to the ordered oxygen vacancies in the tetrahedral layers, where O3 (in the brownmillerite structures) or O5 (in the G-type structure) are only bonded to the tetrahedral Fe2 ions in forming zigzag chains along the ***a***-direction while the crosswise bonding between the parallel tetrahedral chains are absent due to the oxygen vacancy rows (Fig. 6).

The fact that $b_n \geq (6\text{-n})\cdot a_c$ is due to long octahedral Fe1–O distances along ***b***-direction (*cf.* IV-1-2 and IV-1-3), which was also observed in brownmillerite structure of Sr_2CoFeO_5 [24].

Therefore, the transition from the orthorhombic structures to the cubic ones after oxygen intercalation will shrink the structures due to additional bonding effect provided by intercalated oxygen atoms as well as smaller ionic radius of Fe^{4+} ions which are present after the oxidation process.

It can be seen from the following table that the decrease in unit cell volume after oxygen intercalation is an usual phenomenon in the $A_nB_nO_{3n-1}$ series.

Variations in Unit Cell Volumes after Oxygen Intercalation into Brownmillerite and G-type Phases Belonging to the Series of $A_nB_nO_{3n-1}$

Phase	**$\Delta V/V_0$ (%)**	**a_C (Å)**	**Reference**
G-type Perovskite $Sr_2LaFe_3O_8 \Rightarrow Sr_2LaFe_3O_{8.90}$	- 5.2	3.8769(2)	This work
Brownmillerite Perovskite			
$Sr_2Fe_2O_{2.5} \Rightarrow SrFeO_3$	- 5.8	3.835(2)	Wattiaux *et al.* [28]
$Sr_2Co_2O_{2.5} \Rightarrow SrCoO_3$	- 6.3	3.845(2)	Bezdicka *et al.* [29]
$Sr_2CoFeO_5 \Rightarrow Sr_2CoFeO_6$	- 6.7	3.837(2)	Bezdicka *et al.* [30]

- The Degree of Distortion from the Cubic Perovskite Structure

For brownmillerite (n = 2) or G-type (n = 3) phases in $A_nM_nO_{3n-1}$ series, intercalation of oxygen atoms into their tetrahedral layers may transform the structures into the perovskite one ($n = \infty$). Various starting phases may have structures distorted to different extent from their "parent" perovskite structure, therefore, the influence of their structure on the oxygen intercalation would be different, as energies involved in the structural changes would be different.

To simplify the comparison of the distortions of the oxygen-deficient ferrites concerned here, their parent structures are assumed to be ideal cubic perovskite, with all the Fe–O–Fe bond angles (between octahedra) being 180° and the O–Fe–O bond angles (within octahedra) being 180° or 90°. The corresponding bond angles in brownmillerite and G-type structures are distorted from these ideal values, and various kinds of bond angles should be distinguished, *e.g.* Fe–O–Fe bond angles can be between octahedra

Table 5

The Comparison of Cavity Size with Metal-Oxygen Radius Sum for Sr^{2+} and La^{3+} Cations in the Structure of $Sr_2LaFe_3O_8$

In 2*f* cavity (12-Coordination) (mean A1–O distance $\bar{d}_{A1\text{-}O}$ =2.82 Å) [a]			In 4*k* cavity (8-Coordination) (mean A2–O distance $\bar{d}_{A2\text{-}O}$ =2.60 Å) [a]		
cations	Sr^{2+}	La^{3+}	**cations**	Sr^{2+}	La^{3+}
ionic radius [b] r_M (Å)	1.58	1.50	**ionic radius** [b] r_M (Å)	1.40	1.30
radius sum [b] $r_M + r_O$ (Å)	2.84	2.76	**radius sum** [b] $r_M + r_O$ (Å)	2.66	2.56
Δ (Å) $[=(r_M + r_O) - \bar{d}_{A1\text{-}O}]$	0.02	-0.06	Δ (Å) $[=(r_M + r_O) - \bar{d}_{A2\text{-}O}]$	0.06	-0.04
Weighed Average [c] $\overline{(r_M + r_O)_W}$ (Å)	2.81		**Weighed Average** [c] $\overline{(r_M + r_O)_W}$ (Å)	2.63	
Note	a. A1=(2Sr, La)1 and A2=(2Sr, La)2; see also Table 4b. b. All the ionic radii used here including that for oxygen anion O^{2-}, $r_{O^{2-}}$ = 1.26 (Å), are those of Shannon *et al.* [31]. c. $\overline{(r_M + r_O)_W} = (2/3)\cdot(r_M + r_O)_{Sr} + (1/3)\cdot(r_M + r_O)_{La}$.				

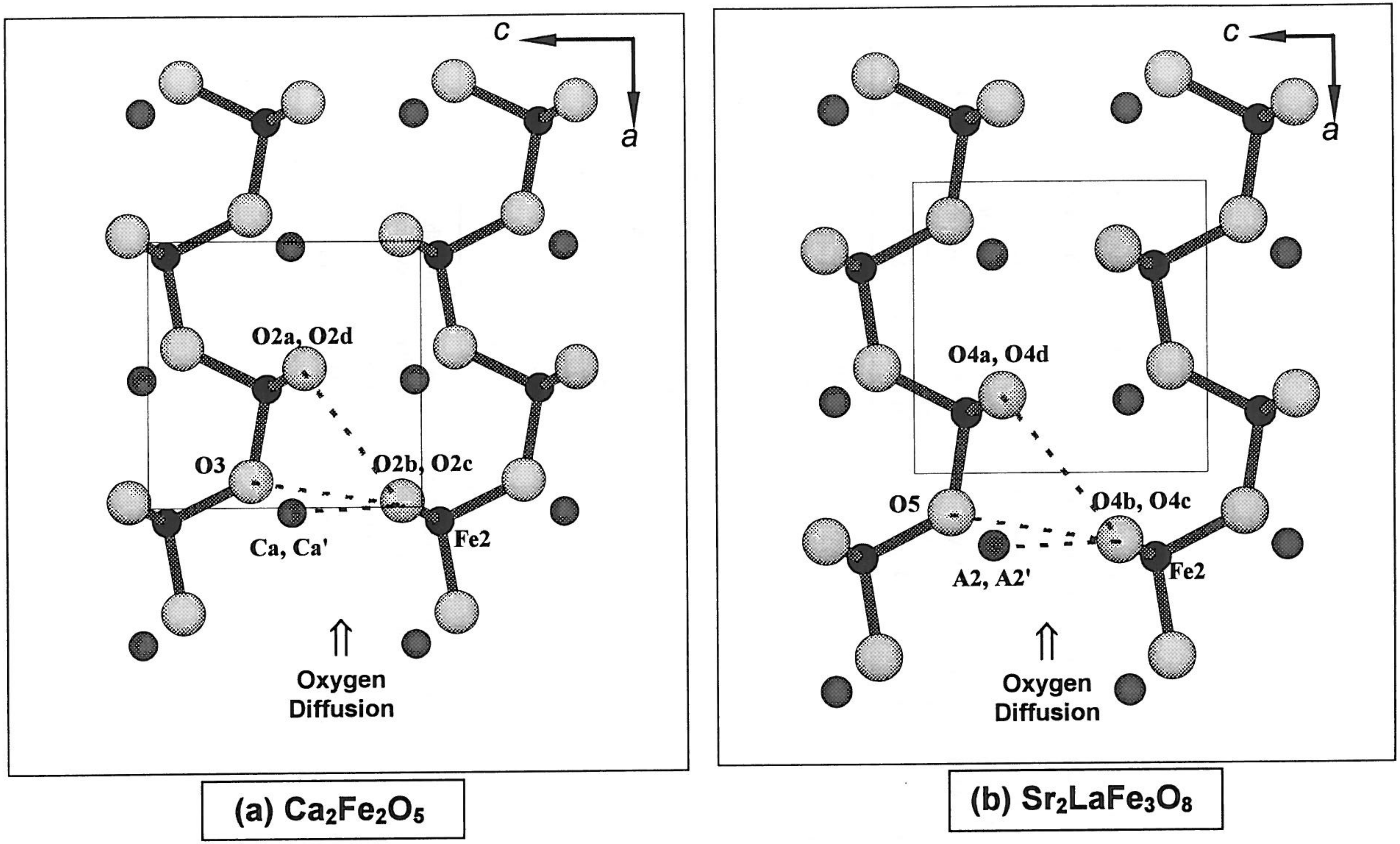

(a) $Ca_2Fe_2O_5$

(b) $Sr_2LaFe_3O_8$

Figure 6

A section of tetrahedral layers : **(a)** in the structure of $\mathbf{Ca_2Fe_2O_5}$ ($0.64 \leq y \leq 0.86$) **(b)** in the structure of $\mathbf{Sr_2LaFe_3O_8}$ ($-0.14 \leq y \leq 0.14$). The dashed lines indicate the three polygonal windows along the channel, which are shown in Fig. 7. The representation of (a) also applies for the tetrahedral layer in $Sr_2Fe_2O_5$ at $0.14 \leq y \leq 0.36$.

and/or tetrahedra and the bond angles of O–Fe2–O and O–Fe1–O are within tetrahedra and octahedra, respectively.

Therefore, the degree of structural distortion of these oxygen-deficient ferrites may be examined by averaged difference between the corresponding bond angles in the derived orthorhombic structures and the perovskite structure.

In the following, the calculations are performed on the phases of $Ca_2Fe_2O_5$, $Sr_2Fe_2O_5$ and $Sr_2LaFe_3O_8$, their bond angle values are given in Table 2b, 3b and 4b. The average distortion involving all Fe–O–Fe bond angles will be denoted by $\overline{D}_{Fe-O-Fe}$, the distortions within tetrahedra and octahedra by $\overline{D}_{tetr}$ and $\overline{D}_{octa}$, respectively.

As an example, in the $Ca_2Fe_2O_5$ structure (brownmillerite-type), we obtain the following results :

(a) Average distortion of Fe–O–Fe bond angles **:**

The corresponding bond angles in the parent cubic structures are 180°. As can be known from Table 3b, each unit cell has 20 oxygen atoms (*i.e.* O1×8 + O2×8 + O3×4), therefore,

$$\begin{aligned}\overline{D}_{Fe-O-Fe} &= [(180-164.8)\times8 + (180-140.2)\times8 + (180-125.9)\times4]/20 \\ &= 32.8\ (^\circ/\text{ per bond angle}).\end{aligned}$$

(b) Average distortion of O–Fe1–O bond angles within octahedra **:**

The corresponding bond angles in the parent cubic structures are 90° (12 bond angles) or 180°(3 bond angles).

$$\begin{aligned}\overline{D}_{octa} &= [(92.6-90)\times2 + (90-87.4)\times2 + (180-180)\times2 + (93.0-90)\times2 \\ &\quad + (90.9-90)\times2 + (90-89.1)\times2 + (90-87.0)\times2 + (180-180)]/15 \\ &= 1.7\ (^\circ/\text{ per bond angle}).\end{aligned}$$

(c) Average distortion of O–Fe2–O bond angles within tetrahedra **:**

The corresponding bond angles in the parent cubic structures are 90° (5 bond angles) or 180° (1 bond angle). Therefore,

$$\begin{aligned}\overline{D}_{tetr} &= [(180-123.1) + (107.3-90)\times2 + (106.1-90)\times2 + (105.9-90)]/6 \\ &= 23.3\ (^\circ/\text{ per bond angle}).\end{aligned}$$

In the same way, calculations were carried out for $Sr_2Fe_2O_5$ and $Sr_2LaFe_3O_8$ structures. For clarity, all the results are listed in Table 6. It can be seen that large distortions are found between polyhedra ($\overline{D}_{Fe-O-Fe}$) and within tetrahedra ($\overline{D}_{tetr}$) ; for $Sr_2Fe_2O_5$ and $Sr_2LaFe_3O_8$ phases, these two distortions are close and smaller than those of $Ca_2Fe_2O_5$. By contrast, the distortions within octahedra are much smaller. In other words, the structural changes during the transformation ,

$$\left.\begin{array}{r}\text{brownmillerite - type structure}\\ \text{G} - \text{type structure}\end{array}\right\} \Rightarrow \text{perovskite structure},$$

will arise mainly from the changes of Fe–O–Fe and O–Fe2–O bond angles (changes in bond lengths are not considered here). One may expect that smaller energies would be required for the transformations involved in $Sr_2Fe_2O_5$ and $Sr_2LaFe_3O_8$ phases.

Table 6
The Averaged Distortions (°/ per bond angle) in the Structures of $Ca_2Fe_2O_5$, $Sr_2Fe_2O_5$ and $Sr_2LaFe_3O_8$

Phases	**$Ca_2Fe_2O_5$**	**$Sr_2Fe_2O_5$**	**$Sr_2LaFe_3O_8$**
Distortion between Polyhedra, $\overline{D}_{Fe-O-Fe}$	32.8	25.1	22.9
Distortion Within Tetrahedra, $\overline{D}_{tetr}$	23.3	20.2	20.1
Distortion Within Octahedra, $\overline{D}_{octa}$	1.7	3.0	3.8

IV-2. The Oxygen Vacancy Rows : the Channels for Oxygen Diffusion and the Channel Widths

A section of the tetrahedral layers in $Ca_2Fe_2O_5$ and $Sr_2LaFe_3O_8$ structures are shown in Fig. 6. Due to close structural similarity, the same representation of Fig. 6a can be applied to the case of $Sr_2Fe_2O_5$ after the atom label Ca is changed to Sr. It can be clearly seen from this figure that the space between the single tetrahedral chains (due to oxygen vacancy rows) produce continuous channels. It is via these channels that oxygen atoms may be intercalated into the structures, involving simultaneous increase in the oxidation state of iron cations and possible structural changes.

Therefore the channel width, with respect to the size of the diffusing oxygen anion, appears to be an important parameter for the diffusion process.

IV-2-1. The Calculation of the Channel Widths.

As shown in Figs. 6 ~ 8, along the diffusing channels, there exist three kinds of periodic polygonal "windows" through which the intercalated oxygen has to squeeze; they are so-called trapezoid window, triangular window and rectangular window . Fig 7 gives a view of the channels showing clearly the three kinds of windows. Calculation results of interatomic distances suggest that such a route (through the windows) should be *the most possible* for the diffusion process, because along any other path the diffusing oxygen atoms would have to squeeze through narrower space.

The widths of the diffusing channels are therefore determined by the distances between the ions which form the polygonal windows as well as the sizes of the ions themselves.

In the calculations of the channel widths, all the ions are assumed to be spheres. The shapes of the three polygonal windows are shown in Fig. 7 and separately in Fig. 8. The window sizes are represented by corresponding radii, $\mathbf{r}_\mathbf{W}$, of the inscribed circles to the circles of the atoms which form the polygonal windows (*cf.* the figure given in Appendix II).

The ionic radii used in the calculations are taken from those of Shannon *et al.* [31] and are listed as follows (with the roman numbers in the brackets indicating the coordination numbers):

O^{2-}(VI): $\mathbf{r}_{O^{2-}} = 1.26$Å; Ca^{2+}(VIII): $\mathbf{r}_{Ca^{2+}} = 1.26$Å;
Sr^{2+}(VIII): $\mathbf{r}_{Sr^{2+}} = 1.40$Å; La^{3+}(VIII): $\mathbf{r}_{La^{3+}} = 1.30$Å.

Note that, for $Sr_2LaFe_3O_8$ structure, the radius of the 2:1 disordered A2 cations (A2 = (2Sr, La)2, with 8-fold coordination) is taken as the average of

$$\mathbf{r}_{A2} = \frac{2}{3}\,\mathbf{r}_{Sr^{2+}} + \frac{1}{3}\,\mathbf{r}_{La^{3+}} = 1.37\ \text{Å}.$$

The formulas for calculating the radii, $\mathbf{r}_\mathbf{W}$, of the polygonal windows in the structures of $Ca_2Fe_2O_5$, $Sr_2Fe_2O_5$ and $Sr_2LaFe_3O_8$ are those in the following. The parameters in the formulas are defined in Fig. 8 and the values of the interatomic distances, $\mathbf{d}_1$, $\mathbf{d}_2$ and $\mathbf{d}_3$, are listed in Table 7 (they are calculated from the atomic positions previously given in Tables 2a, 3a and 4a).

(a) For the trapezoid windows (cf. Appendix II) :

$$r_W = \frac{-M(r_A - r_{O^{2-}}) + H\sqrt{[d_2^2 - (r_A - r_{O^{2-}})^2][d_2^2 + d_1 d_3 - (r_A - r_{O^{2-}})^2]}}{2[H^2 - (r_A - r_{O^{2-}})^2]} - r_{O^{2-}},$$

with $H^2 = d_2^2 - (\frac{d_3 - d_1}{2})^2$ and $M = \frac{2d_2^2 - d_1^2 + d_1 d_3}{2} - (r_A - r_{O^{2-}})^2$.

Here, r_A can be $r_{Ca^{2+}}$ (for $Ca_2Fe_2O_5$), $r_{Sr^{2+}}$ (for $Sr_2Fe_2O_5$) and r_{A2} (for $Sr_2LaFe_3O_8$).

(b) For the triangular windows :

Note that (r_W+$r_{O^{2-}}$) is the radius of the circumscribing circle to the triangle O2b(O4b)–O2c(O4c)–O3(O5), so that :

$$r_W = \frac{d_1}{2\sqrt{1-\cos^2\theta}} - r_{O^{2-}}, \quad \text{with} \quad \cos\theta = \frac{2d_2^2 - d_1^2}{2d_2^2}.$$

(c) For the rectangular windows :

$$r_W = \frac{\sqrt{d_1^2 + d_2^2} - 2r_{O^{2-}}}{2}.$$

IV-2-2. Results and Conclusions

The window radii r_w calculated for the three phases are shown in Table 8 . Although the radius of diffusing oxygen anions is not known, it is assumed to be $r_{O^{2-}}$ = 1.26Å. The magnitude of negative r_W-$r_{O^{2-}}$ (Table 8) values provides a measure of the narrowness of the windows.

From Table 8 , the following points can be concluded :

(i) The radii of the three windows in the Ca-containing phase $Ca_2Fe_2O_5$ are the smallest compared to those in the Sr-containing phases, $Sr_2Fe_2O_5$ and $Sr_2LaFe_3O_8$. That is, the diffusion space in $Ca_2Fe_2O_5$ is the narrowest.

(ii) Among the three windows of each phase, the narrowness of the windows increases in the following order:

rectangular r_W > trapezoid r_W > triangular r_W ,

indicating that the triangular window, maybe also the trapezoid window, should be the determining ones for the oxygen diffusion process in each phase.

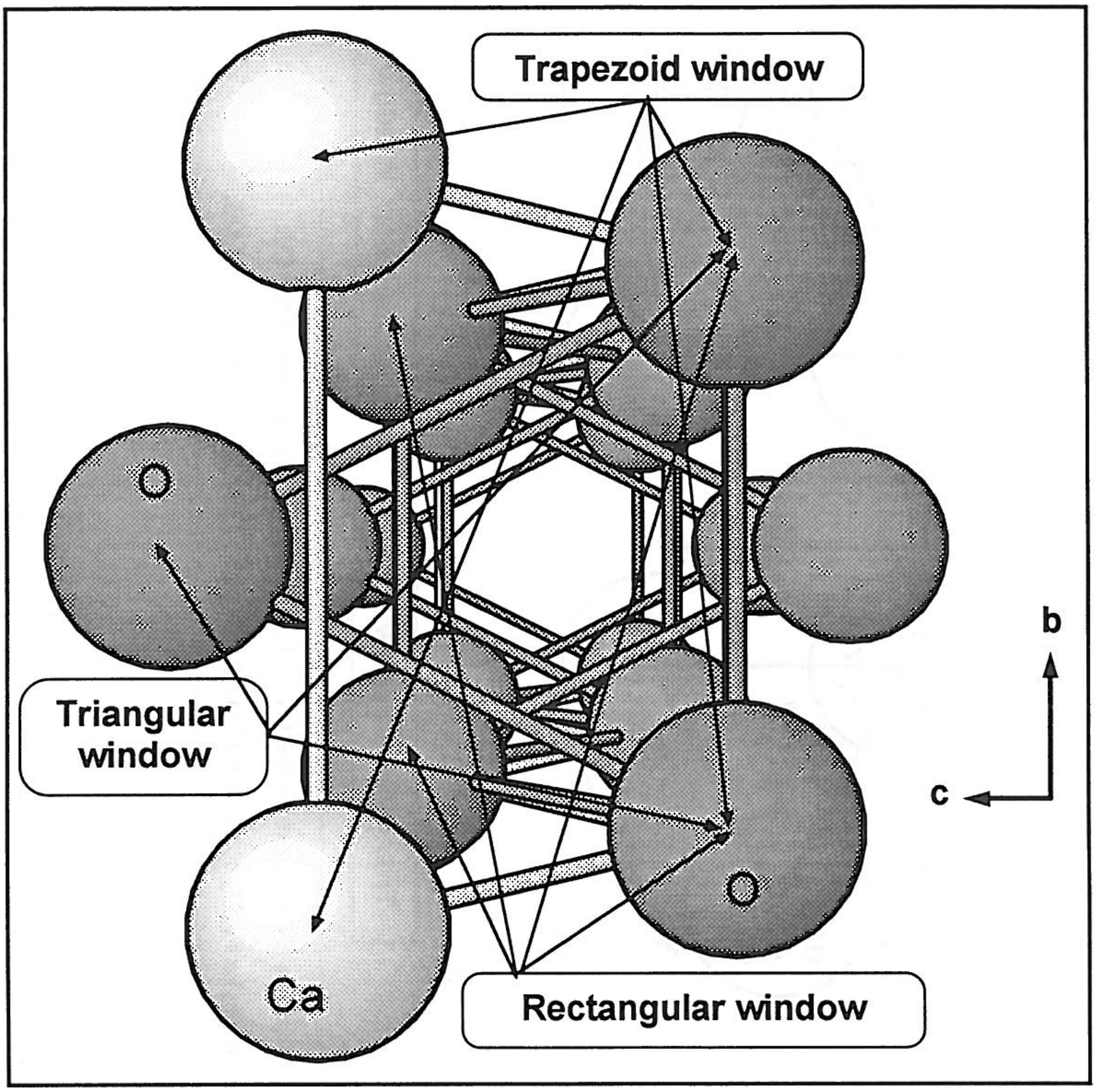

Figure 7
View of the diffusion channel in a tetrahedral layer of the oxygen deficient ferrites (here is the case of $Ca_2Fe_2O_5$).

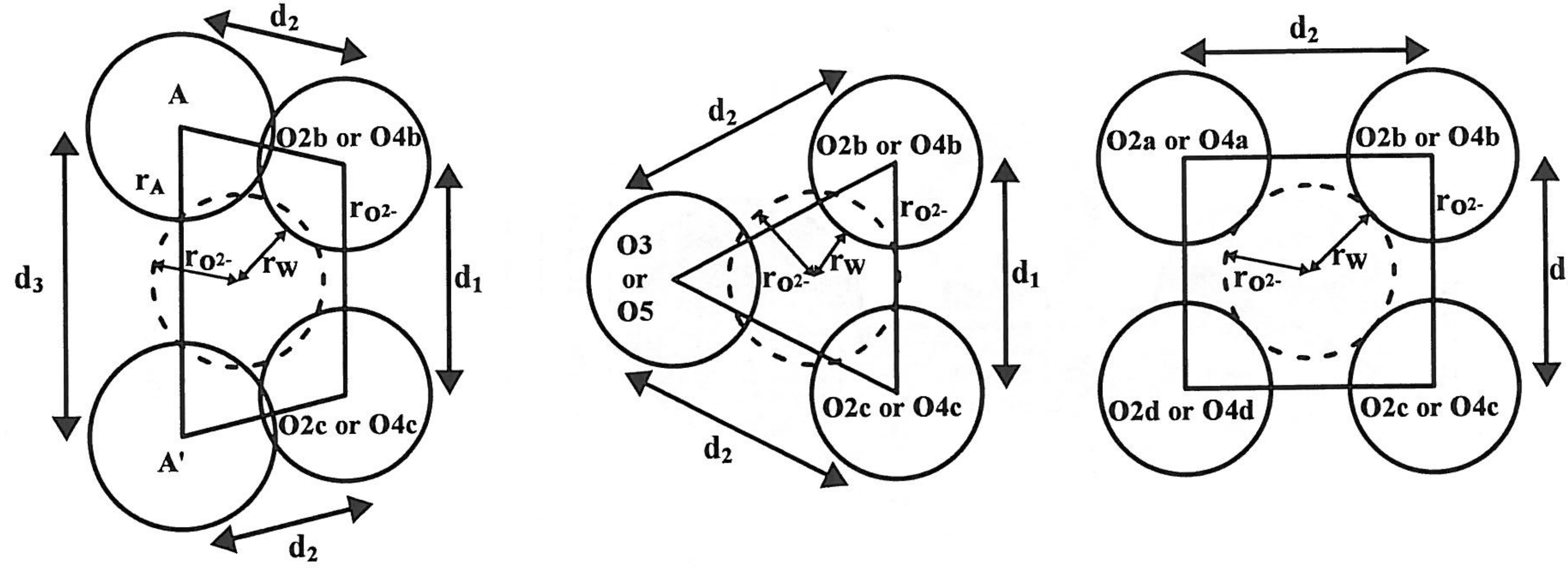

Trapezoid Window **Triangular Window** **Rectangular Window**

Atoms Involved in $Ca_2Fe_2O_5$ and $Sr_2Fe_2O_5$: A, A'=Ca, Ca' or Sr, Sr'; O2; O3.

Atoms Involved in $Sr_2LaFe_3O_8$: A, A'= (2Sr, La)2 (A2), (2Sr, La)2' (A2'); O4; O5.

Figure 8

The three polygonal windows which control the width of diffusion channels in the structures of $Ca_2Fe_2O_5$, $Sr_2Fe_2O_5$ and $Sr_2LaFe_3O_8$. These drawings are proportional to the real sizes in $Sr_2LaFe_3O_8$ (the distances of upper limits in Table 7c are used). The values of the distances d_1, d_2, d_3 are given in Table 7 and the calculated window radii, r_W, are listed in Table 8. The dashed circles in the figure represent imaginary diffusing oxygen anion O^2, with its radius taken as $r_{O^{2-}}$=1.26Å.

Table 7

Distances (in Å) between atoms which form the polygonal windows in the concerned phases. For the definitions of the windows and the distances see text and Fig. 7and 8.

(a) $Ca_2Fe_2O_5$

Trapezoid Window (Ca-O2b-O2c-Ca')	d_1 (=$d_{O2b\text{-}O2c}$)	d_2 (=$d_{Ca\text{-}O2b}$)	d_3 (=$d_{Ca\text{-}Ca}$)'
	3.241	2.330	4.198
Triangular Window (O2b-O2c-O3)	d_1 (=$d_{O2b\text{-}O2c}$)	d_2 (=$d_{O2b\text{-}O3}$)	–
	3.241	3.524	–
Rectangular Window (O2a-O2b-O2c-O2d)	d_1 (=$d_{O2b\text{-}O2c}$)	d_2 (=$d_{O2a\text{-}O2b}$)	–
	3.241	3.370	–

(b) $Sr_2Fe_2O_5$

Trapezoid Window (Sr-O2b-O2c-Sr')	d_1 (=$d_{O2b\text{-}O2c}$)	d_2 (=$d_{Sr\text{-}O2b}$)	d_3 (=$d_{Sr\text{-}Sr}$)'
	3.494	2.468	4.377
Triangular Window (O2b-O2c-O3)	d_1 (=$d_{O2b\text{-}O2c}$)	d_2 (=$d_{O2b\text{-}O3}$)	–
	3.494	3.805	–
Rectangular Window (O2a-O2b-O2c-O2d)	d_1 (=$d_{O2b\text{-}O2c}$)	d_2 (=$d_{O2a\text{-}O2b}$)	–
	3.494	3.532	–

(c) $Sr_2LaFe_3O_8$

Trapezoid Window (A2-O4b-O4c-A2')	d_1 (=$d_{O4b\text{-}O4c}$)	d_2 (=$d_{A2\text{-}O4b}$)	d_3 (=$d_{A2\text{-}A2}$)'
	3.375~3.381	2.478	4.543
Triangular Window (O4b-O4c-O5)	d_1 (=$d_{O4b\text{-}O4c}$)	d_2 (=$d_{O4b\text{-}O5}$)	–
	3.375~3.381	3.670~3.705	–
Rectangular Window (O4a-O4b-O4c-O4d)	d_1 (=$d_{O4b\text{-}O4c}$)	d_2 (=$d_{O4a\text{-}O4b}$)	–
	3.375~3.381	3.390~3.698	–

Note: (1). A2=(2Sr, La)2.

(2). In some cases, ranges of distance are given due to the positional disorder of the atoms concerned (see V-2-3).

Table 8

The Radii, r_W (in Å), of the Polygonal Windows Along the Diffusion Channels in the Three Structures Concerned and Their Differences with the Radius of Oxygen Anion, r_W-$r_{O^{2-}}$ (in Å).

		$Ca_2Fe_2O_6$	$Sr_2Fe_2O_6$	$Sr_2LaFe_3O_8$
Trapezoid Window	r_W	0.97	1.00	1.05
	r_W-$r_{O^{2-}}$	-0.29	-0.26	-0.21
Triangular Window	r_W	0.72	0.88	0.81 ~ 0.82
	r_W-$r_{O^{2-}}$	-0.54	-0.38	-0.45 ~ -0.44
Rectangular Window	r_W	1.08	1.22	1.13 ~ 1.24
	r_W-$r_{O^{2-}}$	-0.18	-0.04	-0.13 ~ -0.02

Note: For the definitions and the calculations of r_W see Fig. 8 and text.

(iii) The differences in the window radii, r_W, between the Ca-phase and the Sr-phases may be related to their different capabilities of oxygen intercalation (see next section for details).

IV-3. What Influences the Oxygen Intercalation ?

IV-3-1. Introduction

Experiments have revealed that oxygen can be intercalated into the brownmillerite $Sr_2Fe_2O_5$ and G-type $Sr_2LaFe_3O_8$ phases by electrochemical method. Structurally, the existence of the continuous oxygen vacancy rows (the channels) in their tetrahedral layers should be an important precondition for this phenomenon. However, it does not provide a complete explanation, because under similar conditions it is not possible to intercalate oxygen into $Ca_2Fe_2O_5$ and $Ca_2LaFe_3O_8$ structures although they are also of the brownmillerite-type and the G-type, respectively.

Suppose one intercalated oxygen, its diffusion along a channel in the structures will be influenced, of course, by the channel width. On the other hand, since the diffusing oxygen species is negatively charged, its coulombic interaction with the ions in the host lattices may also have an important influence on the diffusion process.

Based on available crystallographic data and the ionic model, two energy terms, resulting from short-range and long-range interionic interactions, will be examined and compared for the three phases of $Ca_2Fe_2O_5$, $Sr_2Fe_2O_5$ and $Sr_2LaFe_3O_8$ (unfortunately a full crystal structure of $Ca_2LaFe_3O_8$ has not yet been reported), in order to explain their different capabilities of oxygen intercalation. The influence of other effects will also be discussed.

IV-3-2. The Width of the Diffusion Channels and the Short-Range Pauli Interaction

As has just been described, along the diffusion channels (the oxygen vacancy rows) in both the brownmillerite and G-type structures, there exist three periodic polygonal windows (Figs. 7 and 8) through which a diffusing oxygen has to squeeze.

Generally, for two given atoms or ions, if they get so close together that their electron clouds begin to overlap, a short-range repulsive force becomes important due to *Pauli repulsion* [32]. The corresponding repulsive energy, E_{rep}, can be represented by an exponential function :

$$E_{rep} = B\exp(\frac{-r}{\rho}),$$

where r is the separation between the two atoms or ions, B is a constant and ρ another constant, typically 0.35 [33]. A smaller r means a stronger overlap of the electron clouds hence a higher repulsive energy E_{rep}.

As can be seen from Fig. 7, 8 and Tables 7 and 8, when a diffusing oxygen anion comes near the window centers, an overlap of its electron cloud with those of the lattice ions forming the windows may occur. The narrower the windows, the stronger the overlap and hence the higher the repulsive energy.

From the previously obtained results (the radii r_W), it is clear that, for each phase, such an overlap at the triangular window center is the strongest, next to it is the trapezoid window center.

The most important thing is that, among the three concerned phases, the corresponding window radii of $Ca_2Fe_2O_5$ are the narrowest (the averaged differences in their triangular and trapezoid window radii being about 0.09Å). Therefore,

(a) the repulsive energies experienced by a supposed oxygen atom diffusing in the channels of $Ca_2Fe_2O_5$ could be significantly higher than the corresponding energies in the other two structures ;

(b) for each phase, the repulsive energy at the three window centers increases in the following order :

$4\times E_{rep}$ (rectangular center) < $4\times E_{rep}$ (trapezoid center) < $3\times E_{rep}$ (triangular center),

here the coefficients are the numbers of the interaction pairs;

(c) the effect of the "channel width" is nothing than the effect of the repulsive energy.

IV-3-3. Electrostatic Potentials Along the Diffusion Paths and the Long-Range Coulomb Interaction.

As all the three phases concerned here, $Ca_2Fe_2O_5$, $Sr_2Fe_2O_5$ and $Sr_2LaFe_3O_8$, are magnetic insulators or semiconductors (*G*-type, T_N= 700~730K) with localized electrons, the ionic model may apply.

In ionic crystals, the ions may be regarded as *point charges* with a regular three-dimensional arrangement and each of them experiences an electrostatic *Madelung potential* of appropriate sign, which depends on summation of long-range Coulomb potentials from other ions in the lattice. In an ionic oxide, the Madelung potential is positive at sites occupied by oxygen anions and is negative at cation sites, thus stabilizing the ionic charge distribution. That is, filled oxygen levels have lower energy than that of empty metal levels.

Energy levels may be influenced by the effect of *polarization*. For example, the energy of empty metal levels may be lowered and that of filled oxygen levels be raised to some extent [34]. In what follows, however, the effect of polarization is not considered. It will not qualitatively influence our conclusions because it is not unreasonable to suppose that the polarization effects in the three phases under consideration would be similar.

- The Calculation of Electrostatic Potential and Electrostatic Energy

In an ionic lattice, the electrostatic potential, V_i, at an arbitrary site i (*i.e.* not necessary the lattice site) equals the sum of all the electrostatic potentials due to individual lattice ions:

$$V_i = A \cdot \sum_{\substack{j \\ (j \neq i)}} \frac{q_j}{r_{ij}},$$

where q_j is the charge of the ion at lattice site j, r_{ij} the distance between site i and j, and A is a conversion factor depending on the units. (*Note*: In the present calculation, the unit of electric charge is the absolute value of one electron charge e, the distances r_{ij} are in Å, and the conversion factor is chosen to be A=14.40 which converts potentials in e/Å into potentials in V (Volt) and energies in e^2/Å into those in eV.)

If there is a charge q_i at site i, its electrostatic potential energy (or coulombic potential energy), $E_{coul,i}$, due to its interactions with the charges of lattice ions will be :

$$E_{coul,i} = q_i \cdot V_i = A \cdot q_i \cdot \sum_{\substack{j \\ (j \neq i)}} \frac{q_j}{r_{ij}}.$$

Suppose now i also to be a lattice site and correspondingly q_i is the charge of the lattice ion at i, the electrostatic energy of the whole lattice (the *Madelung energy*) is given by

$$E_M = \frac{A}{2} \cdot \sum_{\substack{i,j \\ (i \neq j)}} \frac{q_i \cdot q_j}{r_{ij}}.$$

Here the division by 2 is to avoid counting each interionic interaction twice.

The above summations (involving inverse of distances) converge very slowly, that is, the interionic coulombic interaction is a long-range effect.

Our calculations were done using a program (MADEL [35]) based on Ewald's rapid-convergence method [36].

- Calculation Results and Discussions

Fig. 9 shows the variations of electrostatic potentials with x-coordinate along the diffusion paths in the tetrahedral layers of $Ca_2Fe_2O_5$, $Sr_2Fe_2O_5$ and $Sr_2LaFe_3O_8$ (*cf.* IV-1-2 and IV-1-3), which are calculated using the method described above for numerous positions along the paths. For simplicity, the diffusion paths have been approximated to straight lines connecting the centers of the neighboring polygonal windows as shown in Fig. 10 (the window centers are the origins of $\mathbf{r}_W$, *cf.* Fig. 8). The y-coordinates of these straight lines are $y = 0.75$ for $Ca_2Fe_2O_5$, $y = 0.25$ for $Sr_2Fe_2O_5$ and $y = 0$ for $Sr_2LaFe_3O_8$.

The coulombic potential energies of a charge (-2e) at the window centers, which are indicated by corresponding polygonal symbols in Fig. 9, are listed in Table 9.

According to the obtained results, following discussions can be made.

(i) As can be seen from Fig. 9, the electrostatic potentials along the diffusion paths are almost all negative for $Ca_2Fe_2O_5$ and positive for $Sr_2Fe_2O_5$ and $Sr_2LaFe_3O_8$. Therefore, for a negatively charged oxygen species, its diffusion along the channels in $Sr_2Fe_2O_5$ and $Sr_2LaFe_3O_8$ phases may be favored by the Coulomb energy, but it is not the case for $Ca_2Fe_2O_5$ phase. Or in other words, the Coulomb energy of the diffusing oxygen in the channels of $Ca_2Fe_2O_5$ structure is again significantly higher than the corresponding energies in the structures of $Sr_2Fe_2O_5$ and $Sr_2LaFe_3O_8$.

(ii) Even if an oxygen anion has somehow entered into the channels in $Ca_2Fe_2O_5$, it still has to overcome a higher coulomb energy barrier than in the other two structures for continuing its diffusion. In Table 9 are shown such energy barriers, ($E_{coul}^{max} - E_{coul}^{min}$), along the channels in the three phases (with the charge being taken as *-2e*).

(iii) For each phase, the Coulomb energy of a negative charge at the three window centers increases according to

$$E_{coul}\text{ (rectangular center)} < E_{coul}\text{ (triangular center)} < E_{coul}\text{ (trapezoid center)}.$$

Note that the Coulomb energy at the trapezoid center is also the highest one along the channel.

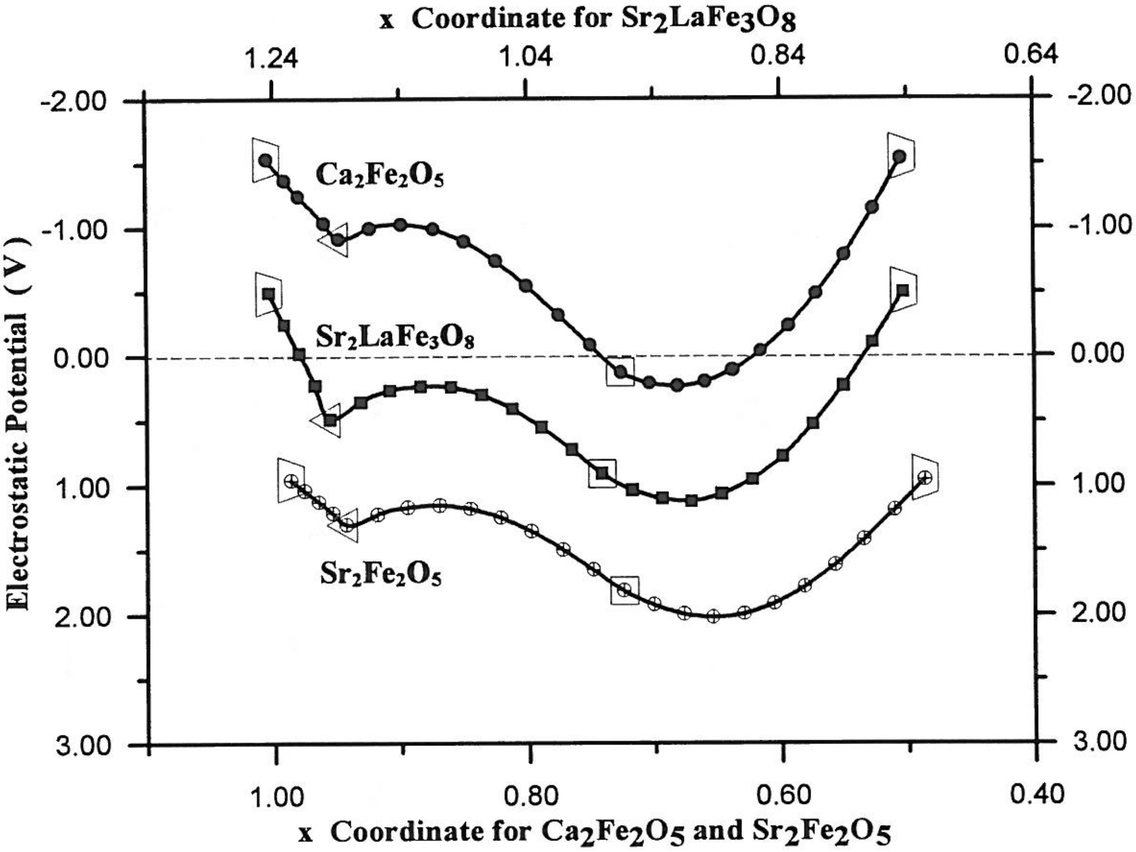

Figure 9

Variations of electrostatic potentials with x coordinates along the lines connecting the polygonal window centers in $Ca_2Fe_2O_5$ (y coordinate=0.75), $Sr_2Fe_2O_5$ (y=0.25) and $Sr_2LaFe_3O_8$ (y=0). Only the variation within one period is shown for each phase, the period being $\frac{1}{2}a$. Values at trapezoid, triangular and rectangular window centers are marked by the corresponding polygonal symbols.

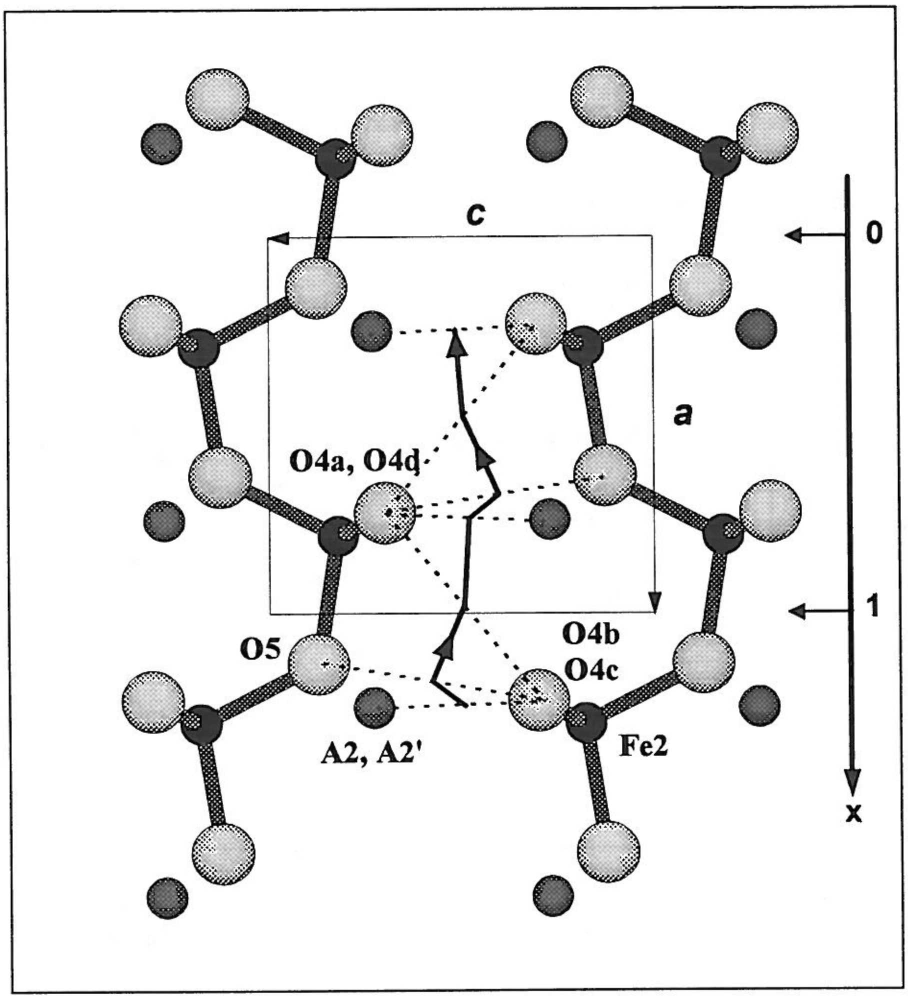

Figure 10

Representation of the diffusion path taken as zigzaging lines connecting the centers of the neighboring polygonal windows (here is the case of $Sr_2LaFe_3O_8$).

Table 9

Electrostatic Potential Energies for a Charge (-2e) at the Polygonal Window Centers and the Maximum Energy Differences Along Channels in the structures of $Ca_2Fe_2O_5$, $Sr_2Fe_2O_5$ and $Sr_2LaFe_3O_8$.

	Electrostatic Potential Energy * for a charge of (-2*e*) (*eV*)			$E_{coul}^{max} - E_{coul}^{min}$ ** (*eV*)
	Trapezoid Centre	**Triangular Centre**	**Rectangular Centre**	
$Ca_2Fe_2O_5$	3.06	1.84	-0.26	3.52
$Sr_2Fe_2O_5$	-1.90	-2.60	-3.62	2.12
$Sr_2LaFe_3O_8$	1.00	-0.96	-1.80	3.22

* The zero of the potential energy is taken as the energy of free charge.

** $E_{coul}^{max} - E_{coul}^{min}$ is the difference between the highest and lowest potential energy along a channel (*cf.* Fig. 9).

The relative Coulomb energies at the trapezoid centers of the three phases for a charge (-2*e*) are schematically shown in Fig. 11. Note that these energy values are only estimated ones since some approximation is involved (see below).

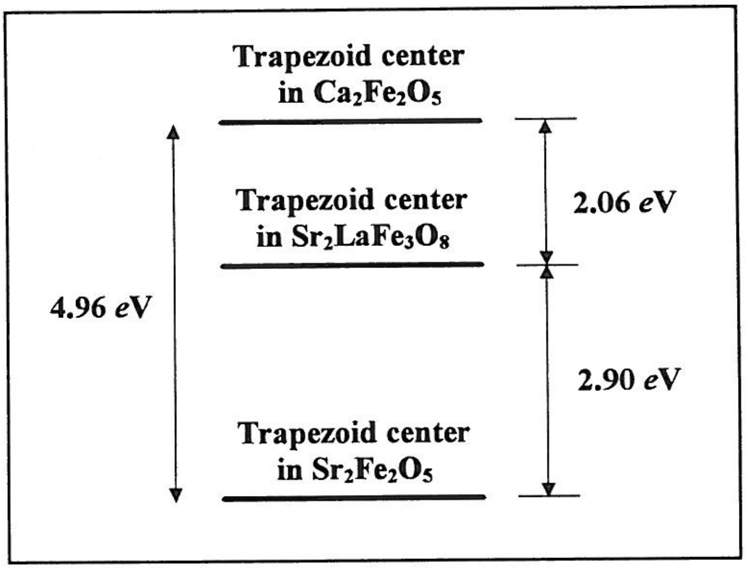

Figure 11

The differences in the coulombic potential energies of a charge (-2*e*) at the trapezoid centers of $Ca_2Fe_2O_5$, $Sr_2Fe_2O_5$ and $Sr_2LaFe_3O_8$.

IV-3-4. The Different Capabilities of Oxygen Intercalation of the Ferrites : the Influence of Energies

For one diffusing oxygen, besides the short-range repulsive and long-range coulombic interactions considered in the sections of IV-3-2 and IV-3-3, its energy may also be influenced, more or less, by some other effects such as polarization (as mentioned previously), its dispersion interaction [32] with lattice ions (which results in an attractive potential energy proportional to $1/r^6$), and local lattice relaxation [37].

However, since the dispersion interaction is quite weak [32, 33] and the effects of the polarization and the local lattice relaxation may be assume to be similar for the three phases under consideration, neglect of them will not influence our examination of *the relative energies* of the diffusing oxygen in the three structures.

Therefore, from the results obtained in IV-3-2 and IV-3-3, the energetics of the oxygen diffusion can be qualitatively discussed as follows.

(i). The oxygen intercalation capabilities of the three ferrites are mainly determined by the two interaction energies at the triangular or the trapezoid window centers, *i.e.* the short-range repulsive energy (E_{rep}) and the long range coulombic energy (E_{coul}); while the interactions at the rectangular centers are not the controlling factor for the intercalation. (Note that for each phase the repulsive energies and the coulombic energies at the triangular and trapezoid centers have inverse order.)

The total interaction energy of a diffusing oxygen anion, $E_{tot}(x)$, may thus be approximately expressed by the sum of these two contributions :

$$E_{tot}(x) = E_{coul}(x) + n \cdot E_{rep}(x) ,$$

where x is the x-coordinate along the diffusing path (Fig. 9, 10), n the number of the repulsive interaction pairs at the window centers. Note that $E_{rep}(x)$ is only important when the oxygen comes near the window centers (the short-range nature) and that the energy zero for $E_{tot}(x)$ is taken as the energy of free ion.

Therefore the maximum total energy along a given channel can be written as

$$E_{tot}^{max} = \max\{E_{tot}(\text{Tri.}), E_{tot}(\text{Trape.})\} ,$$

where E_{tot}(Tri.) and E_{tot}(Trape.) are the total interaction energies at triangular and trapezoid window centers along the channel. In other words, for each phase the largest energy for the diffusion is found at either the triangular or the trapezoid window centers.

(ii). According to the results listed in Table 8 and Fig. 9, we have :

$$E_{tot}^{max}(Ca_2Fe_2O_5) > E_{tot}^{max}(Sr_2LaFe_3O_8) \text{ and } E_{tot}^{max}(Sr_2Fe_2O_5),$$

or more generally,

$$E_{tot}(x, Ca_2Fe_2O_5) > E_{tot}(x, Sr_2LaFe_3O_8) \text{ and } E_{tot}(x, Sr_2Fe_2O_5) ,$$

for any given x value (note however that here x represents x-coordinates corresponding to similar positions along the diffusing paths in the three structures, not necessarily having the same value). That is :

- ***the total energy experienced by an oxygen anion diffusing along a channel in $Ca_2Fe_2O_5$ structure is significantly higher than the corresponding energies in the other two structures.***

Therefore, the reason why oxygen atom cannot be intercalated into the structure of $Ca_2Fe_2O_5$ by electrochemical method may be assigned to the fact that the energy required for the intercalation is relatively high and it should exceed the effect of the "driving force" provided by the electrochemical experiments. The opposite situations for

$Sr_2Fe_2O_5$ and $Sr_2LaFe_3O_8$ are likely due to that the corresponding energies are low enough.

(iii). The diffusion process may be facilitated if the diffusing oxygen species is O^- rather than O^{2-}, because lower oxygen charge will reduce the energy barrier to the diffusion arising from both the coulombic and repulsive interactions. Anyway, the qualitative conclusions obtained above would not be changed by this consideration.

From the calculated electrostatic potentials along the diffusing paths (Fig. 9) and the Madelung potentials of lattice oxygen anions O^{2-} given in Table 10, it is known that an intercalated oxygen anion would have a much higher Coulomb energy than the lattice oxygen anions, it would therefore not be stable. That is why the host lattices are necessarily distorted after the intercalation so that the Coulomb energy may be decreased (the potentials at oxygen sites in related perovskites are also around 24 V).

(iv). The above discussions apply to the initial stage of the oxygen intercalation, at the time of which other effects, such as interactions between diffusing oxygen atoms and changes in the host lattices, are not important. That is, the comparison of the different capabilities of oxygen intercalation (*i.e.* can or can not be oxidized) involves only the brownmillerite and G-type structures of the precursors. Therefore, the arguments given above may explain why $Ca_2Fe_2O_5$ cannot be oxidized by electrochemical method (with intercalated oxygen content $\delta \approx 0$), but they are not sufficient to explain why a large quantities of oxygen ($\delta \approx 0.90$) can be intercalated into the Sr-ferrites.

(v). Structural distortions of brownmillerite $Ca_2Fe_2O_5$, $Sr_2Fe_2O_5$ and G-type $Sr_2LaFe_3O_8$ phases with respect to their parent perovskite structure were examined in IV-1-4 (Table 6). The results show that the distortion in $Ca_2Fe_2O_5$ is the largest while the distortions in $Sr_2Fe_2O_5$ and $Sr_2LaFe_3O_8$ are relatively small and similar. As has been discussed, $Ca_2Fe_2O_5$ may need more energy to complete its structural transformation from brownmillerite to perovskite structure during the oxygen intercalation.

Although the energies associated with the structural transformations are not related to the different capabilities of the electrochemical oxygen intercalation, it may be another factor which, together with the factors discussed above, causes different oxidation capabilities of these phases in high oxygen pressure process. For example, $Sr_2Fe_2O_5$ can be oxidized to its related perovskite phase under an oxygen pressure of 50 MPa, while the same process for $Ca_2Fe_2O_5$ needs a much higher oxygen pressure ($\sim 10^3$ MPa) (*cf.* III-2-1).

Table 10

Madelung Potentials (in V) at Lattice Sites and Madelung Energies for $Ca_2Fe_2O_5$, $Sr_2Fe_2O_5$ and $Sr_2LaFe_3O_8$

	$Ca_2Fe_2O_5$	$Sr_2Fe_2O_5$	$Sr_2LaFe_3O_8$
Ca, Sr, (2Sr,La)2	-20.90	-20.11	-23.15
(2Sr,La)1	-	-	-21.78
Fe1	-36.35	-37.02	-36.51
Fe2	-33.61	-32.50	-33.37
O1	22.41	21.22	21.94
O2	23.07	22.13	21.73
O3	25.52	26.14	22.77
O4	-	-	22.12
O5	-	-	25.62
Madelung Energy (kJ/Mol)	25410	24842	40445 *

* The Madelung energy for the formula unit of $Sr_{4/3}La_{2/3}Fe_2O_{5.33}$ is 26963 (kJ/Mol).

IV-3-5. Summary and Conclusions

From a viewpoint of ionic structure, the energy experienced by an oxygen anion diffusing along the channels in the structures of the involved precursors depends mainly on its two kinds of interactions with the ions in the host lattices : one is the short-range Pauli interaction (repulsive) which involves only the lattice ions forming the channel windows and occurs when the diffusing oxygen squeezes between them ; another is the long-range Coulomb interaction between the electric charges of the diffusing oxygen anion and of the lattice ions. The total interaction energy can be approximately represented by the sum of these two contributions.

This picture applies to the initial stage of the oxygen intercalation, at the time of which other effects, such as interactions between diffusing oxygen atoms and changes in the host lattices of the precursors, are not important. It provides an estimation about the relative energies of the diffusing oxygen anion in the three structures, on the supposition that the effects of polarization and local lattice relaxation would be similar for the ferrites concerned (the contribution of dispersion energy is negligible).

Based on available crystallographic data and the ionic model, the repulsive energies and electrostatic potentials along the diffusing paths have been examined and calculated for brownmillerite $Ca_2Fe_2O_5$, $Sr_2Fe_2O_5$ and G-type $Sr_2LaFe_3O_8$ phases.

Experiments show that oxygen can be intercalated into the structures of $Sr_2Fe_2O_5$ and $Sr_2LaFe_3O_8$ by electrochemical method, but the electrochemical intercalation is not possible in the cases of $Ca_2Fe_2O_5$ and $Ca_2LaFe_3O_8$, although the continuous oxygen vacancy rows also exist in the two latter structures. This phenomenon is due to that the involved energies for the intercalation are different for these phases.

Following conclusions can be drawn :

(i) The reason why the oxygen cannot be intercalated into the structure of $Ca_2Fe_2O_5$ by electrochemical method may be assigned to the fact that the energy required for the intercalation is relatively high and it should exceed the effect of the "driving force" provided by the electrochemical experiments.

The energy analysis for $Ca_2LaFe_3O_8$ phase is not possible due to the lack of full crystallographic data, but it is expected that the cause for its similar electrochemical behavior like that of $Ca_2Fe_2O_5$ may be the same.

(ii) It is shown that, in each of the three structures, a diffusing oxygen will experience the highest energy at either the triangular or the trapezoid window centers, therefore the capabilities of oxygen intercalation of these phases are determined by the interionic interactions at these two positions.

(iii) It is suggested that the oxygen species involved in the diffusion process may be O^- but not O^{2-}, in the sense that a lower energy barrier (of both the Coulomb and the Pauli interaction origin) is expected for O^-.

(iv) Calculations also indicate that the structural distortion from parent perovskite is larger for $Ca_2Fe_2O_5$ than for the other two phases, which, in addition to the effects mentioned above, may also be responsible, to some extent, for their different oxygen intercalation capabilities under electrochemical conditions as well as under high oxygen pressures.

References

[1] Colville, A.A. and Geller, S. *Acta Crystallogr.*, **B27**, 2311 (1971). References cited herein: Törnebohm, A.E. *Tonindustrie Z.* p.1148 (1897); Hanson, W.C., Brownmiller, L.T., and Bogue, R.H. *J. Amer. Chem. Soc.* **50**, 396 (1928); Büssem, W. *Fortschr. Min.* **22**, 31 (1937).

[2] Smith, D.K *Acta Crystallogr.*, **15**, 1146 (1962).

[3] Bertaut, E.F., Blum, P., and Sagnières, A. *Acta Crystallogr.*, **12**, 149 (1959).

[4] Colville, A.A. *Acta Crystallogr.*, **B26**, 1469 (1970).

[5] Berggren, J. *Acta Chem. Scand.*, **25**, 3616 (1971).

[6] Gallagher, P.K., MacChesney, J.B., and Buchanan, D.N.E. *J. Chem. Phys.*, **41**, 2429 (1964).

[7] Gallagher, P.K., MacChesney, J.B., and Buchanan, D.N.E., *J. Chem. Phys.*, **43**, 516 (1965).

[8] Geller, S., Grant, R.W., and Gonser, U., in *Progress in solid State Chem.*, (ed. H. Reiss), **5**, p.1, Pergamon Press, Ltd.. (1971).

[9] Takeda, T., Yamaguchi, Y., Tomiyoshi, S., Fukase, M., Sugimoto, M., and Watanabe, H., *J. Phys. Soc. Japan*, **24**, 446 (1968).

[10] Greaves, C., Jacobson, A.J., Tofield, B.C. and Fender, B.E. *Acta Crystallogr.*, **B31**, 641 (1975).

[11] Harder, Von M. and H. Müller-Buschbaum *Z. Anorg. Allg. Chem.*, 464, 169 (1980).

[12] Wadsley, D.A. in *Nonstoichiometric Compounds* (ed. L. Mandelcom), *Chapter 3*, p. 135, Academic Press, New York (1964).

[13] Grenier, J.C., Darriet, J., Pouchard, M., and Hagenmuller, P. *Mat. Res. Bull.*, **11**, 1219 (1976).

[14] Grenier, J.C., Ménil, F., Pouchard, M., and Hagenmuller, P. *Mat. Res. Bull.*, **12**, 79 (1977).

[15] Grenier, J.C., Schiffmacher, G., Caro, P., Pouchard, M., and Hagenmuller, P. *J. Solid State Chem.* **20**, 365 (1977).

[16] Bednorz, J.G. and Müller, K.A.. *Z. Phys.* **B64**, 189 (1986)

[17] Battle, P.D., Gibb, T.C., and Lightfoot, P. *J. Solid State Chem.* **84**, 237 (1990).

[18] Hahn, T. (ed.) *Internat. Tables Crystallogr.*, Vol. A, *Space-Group symmetry*, 2nd rev. edn., Internat. Union of Crystallogr./Kluwer Academic Pub. (1989).

[19] Hubbard, J. and Marshall, W. *Proc. Phys. Soc.* **86**, 561 (1965).

[20] Gonser, U., Grant, R.W, Wiedersich, H., and Geller, S. *Appl. Phys. Lett.*, **9**, 18 (1966).

[21] Corliss, L.M., Hastings, J.M., Kunnmann, W., and Banks, E. *Acta Crystallogr.*, *Sect. A*, *Suppl.*, **21**, 95 (1966).

[22] Friedman, Z., Shakad, H., and Shtrikman, S. *Phys. Lett.*, **A25**, 9 (1967).

[23] Battle, P.D., Gibb, T.C., and Nixon, S. *J. Solid State Chem.* **79**, 75 (1989).

[24] Battle, P.D., Gibb, T.C., and Lightfoot, P., *J. Solid State Chem.* **76**, 334, (1988)

[25] Alario-Franco, M.A., Henche, M.J.R., Vallet, M., Calbet, J.M.G., Grenier, J.C., Wattiaux, A., and Hagenmuller, P. *J. Solid State Chem.* **46**, 23 (1983).

[26] Gibb, T.C. *J. Solid State Chem.* **74**, 176 (1988).

[27] Grenier, J.C., Fournès, L., Pouchard, M., Hagenmuller, P. And Komornicki, S. *Mat. Res. Bull.*, **17**, 55 (1982).

[28] Wattiaux, A., Fournès, L., Demourgues, A., Bernaben, N., Grenier, J.C., and Pouchard, M. *Solid State Commun.* **77**, 489 (1991).

[29] Bezdicka, P., Wattiaux, A., Grenier, J.C., Pouchard, M., and Hagenmuller, P. *Z. Anorg. Allg. Chem.* **619**, 7 (1993).

[30] Bezdicka, P., Fournès, L., Wattiaux, A., Grenier, J.C., and Pouchard, M., *Solid State Commun.* **91**, 501 (1994).

[31] Shannon, R.D. and Prewitt, C.T. *Acta Crystallogr.* **B25**, 925 (1969).
Shannon, R.D. and Prewitt, C.T. *Acta Crystallogr.* **B26**, 1046 (1970).
Shannon, R.D. *Acta Crystallogr.* **A32**, 751 (1976).

[32] Levine, I.N. *Physical Chemistry*, McGraw-Hill Book Co. (1988).

[33] West, A.R. *Solid State Chemistry and its Applications*, John Wiley & Sons, Ltd (1990).

[34] Cox, P.A. *Transition Metal Oxides: An Introduction to their Electronic Structure and Properties*, Oxford (1992).

[35] Demourgues, A. Ph.D. Thesis, University Bordeaux I (1992).

[36] Ewald, P.P. *Ann. Phys.* **64**, 253 (1921).

[37] Cherry, M., Islam, M.S., and Catlow, C.R.A. *J. Solid State Chem.* **118**, 125 (1995).

Chapter V

Studies on Some Physical Properties of Perovskite Phase $Sr_2LaFe_3O_{8.95}$ Prepared by Electrochemical Oxidation

V-1. The Crystal Structure of the Perovskite Phase $Sr_2LaFe_3O_{8.90\pm0.05}$

V-1-1. Results of X-ray Powder Diffraction.

Powder XRD experiments were carried out for $Sr_2LaFe_3O_{8.90\pm0.05}$ in the temperature range from 300K down to 80K ; the patterns can indexed in both cubic perovskite cells and related rhombohedral cells.

However, neutron diffraction experiments performed at room temperature and 50K by Battle *et al.* [1] both showed the $R\bar{3}c$ symmetry for the crystal structure of a very close composition of $Sr_2LaFe_3O_{8.94}$. The rhombohedral structure can be viewed as distorted from the related cubic perovskite one, having the $Pm\bar{3}m$ space group, by a small compression along one of the body-diagonals of the cubic cell.

Such a difference between the trigonal and the cubic symmetry can not be distinguished by X-ray diffraction according to our results as well as to those of Battle *et al.* [2], the cause of which will be discussed later.

The room temperature cell parameters, both the rhombohedral ones and the cubic ones of $Sr_2LaFe_3O_{8.90}$ are listed in Table 1.

Table 1

Cell Parameters for Perovskite Phase $Sr_2LaFe_3O_{8.90\pm0.05}$

Obtained by XRD at Room Temperature

Rhombohedral Cell	a_R=5.4853 Å; α_R=59.96°; V_R=116.61 Å^3; Z= 2/3.
In Hexagonal Setting:	a_H= 5.4822(5)Å; c_H= 13.440(8)Å; V_H= 349.83 Å^3 S.G.: $R\bar{3}c$; Z=2; D_x=5.925 g /cm^3;
Cubic Cell	a_C= 3.8769(2) Å; V_C= 58.27 Å^3; S.G.: $Pm\bar{3}m$; Z=1/3; D_x=5.928 g /cm^3;

The powder XRD pattern and its indexing in the two unit cells are shown in Fig. 1 and Table 2, respectively. The rhombohedral lattice is indicated by the reflection condition $-h + k + l = 3n$ in the hexagonal indexing. The relations between the cell

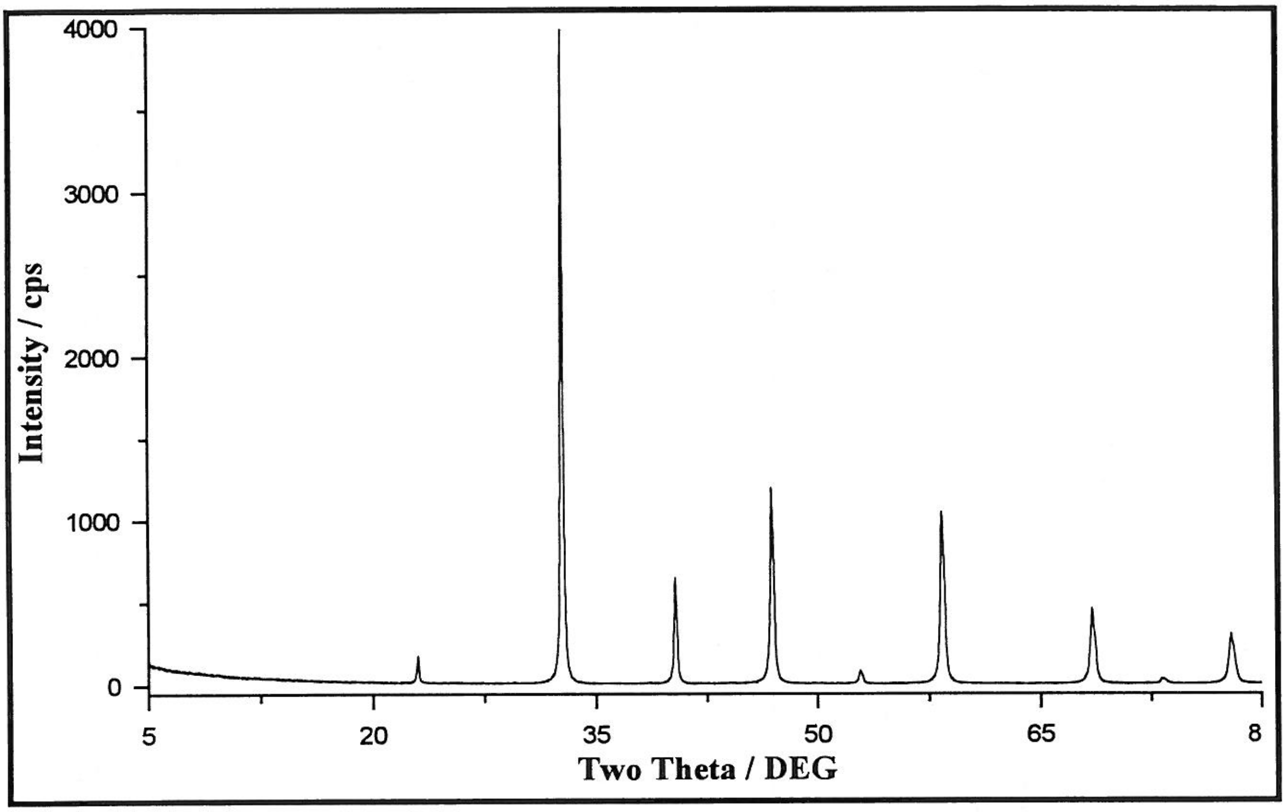

Figure 1

Powder XRD Pattern (at Room Temperature) for $Sr_2LaFe_3O_{8.90\pm0.05}$.

Table 2

Room Temperature Powder XRD Pattern for $Sr_2LaFe_3O_{8.90}$
Indexed with both the Rhombohedral and Cubic Cells.

Indexing in the Rhombohedral Cell (in hexagonal setting). a_H = 5.4822(5)Å; c_H = 13.440(8)Å				**Indexing in Cubic Cell** a_C = 3.8769(2) Å	
h k l	**d_{calc}**	**d_{obs}**	**I/I_0**	**h k l**	**d_{calc}**
1 0 2	3.878	3.878	3	1 0 0	3.877
1 0 4	2.743	2.742	100	1 1 0	2.741
1 1 0	2.741				
0 0 6	2.240				
2 0 2	2.238	2.239	18	1 1 1	2.238
2 0 4	1.9388	1.9391	43	2 0 0	1.938
1 1 6	1.7345	1.7344	3	2 1 0	1.7338
2 1 2	1.7337				
2 1 4	1.5829	1.5828	44	2 1 1	1.5827
3 0 0	1.5826				
2 2 0	1.3705	1.3706	22	2 2 0	1.3707
3 0 6	1.2925				
3 1 2	1.2922	1.2921	2	3 0 0	1.2923
3 1 4	1.2260	1.2259	18	3 1 0	1.2260
Smith-Snyder figure of merit [59]: F_9 = 27 (0.0109, 31)				Smith-Snyder figure of merit [59]: F_9 = 92 (0.0109, 9).	

Note: Si (99.999%) was used as internal standard; the results were obtained by least-squares refinements.

parameters a_H, c_H of the hexagonal cell and the cell parameters a_R, α_R of the rhombohedral cell are as follows:

$$a_H = 2 \cdot a_R \cdot \sin\frac{\alpha_R}{2}, \qquad c_H = \sqrt{3} \cdot a_R \cdot \sqrt{1+2\cdot\cos\alpha_R} \; ;$$

$$a_R = \frac{1}{3} \cdot \sqrt{3 \cdot a_H^2 + c_H^2}, \qquad \sin\frac{\alpha_R}{2} = \frac{3}{2 \cdot \sqrt{3+(c_H^2 / a_H^2)}} .$$

V-1-2. Discussions

- *Some Crystallographic Relations*

For a given cubic perovskite structure having $Pm\bar{3}m$ symmetry, its derived rhombohedral cell with an ideal angle $\alpha_R = 60°$ and the corresponding hexagonal cell are schematically shown in Fig. 2. In the figure and hereafter in the text, all the parameters referring to the three cells are indicated by corresponding subscripts C (*cubic* cell), R (derived *rhombohedral* cell) and H (derived *hexagonal* cell).

As can be seen from Fig. 2, the transformation between the lattice vectors of the hexagonal and cubic cells can be expressed by

$$\begin{pmatrix} \boldsymbol{a}_H & \boldsymbol{b}_H & \boldsymbol{c}_H \end{pmatrix} = \begin{pmatrix} -\boldsymbol{b}_C + \boldsymbol{c}_C & \boldsymbol{a}_C - \boldsymbol{c}_C & 2\boldsymbol{a}_C + 2\boldsymbol{b}_C + 2\boldsymbol{c}_C \end{pmatrix}$$

$$= \begin{pmatrix} \boldsymbol{a}_C & \boldsymbol{b}_C & \boldsymbol{c}_C \end{pmatrix} \cdot \underbrace{\begin{pmatrix} 0 & 1 & 2 \\ -1 & 0 & 2 \\ 1 & -1 & 2 \end{pmatrix}}_{\boldsymbol{P}}, \qquad (1)$$

and the cell dimensions are related as : $a_H = b_H = \sqrt{2} \cdot a_C$, $c_H = 2 \cdot \sqrt{3} \cdot a_C$.

Hence, the coordinate triplets and the Miller indices referring to the two unit cells are transformed, respectively, by

$$\begin{pmatrix} x_H \\ y_H \\ z_H \end{pmatrix} = \underbrace{\begin{pmatrix} \frac{1}{3} & -\frac{2}{3} & \frac{1}{3} \\ \frac{2}{3} & -\frac{1}{3} & -\frac{1}{3} \\ \frac{1}{6} & \frac{1}{6} & \frac{1}{6} \end{pmatrix}}_{\boldsymbol{Q}=\boldsymbol{P}^{-1}} \cdot \begin{pmatrix} x_C \\ y_C \\ z_C \end{pmatrix} = \begin{pmatrix} \frac{x_C}{3} - \frac{2y_C}{3} + \frac{z_C}{3} \\ \frac{2x_C}{3} - \frac{y_C}{3} - \frac{z_C}{3} \\ \frac{x_C}{6} + \frac{y_C}{6} + \frac{z_C}{6} \end{pmatrix} \qquad (2)$$

and

$$\begin{pmatrix} h_H & k_H & l_H \end{pmatrix} = \begin{pmatrix} h_C & k_C & l_C \end{pmatrix} \cdot \underset{\boldsymbol{P}}{\begin{pmatrix} 0 & 1 & 2 \\ -1 & 0 & 2 \\ 1 & -1 & 2 \end{pmatrix}} \qquad (3)$$

$$= \begin{pmatrix} -k_C + l_C & h_C - l_C & 2(h_C + k_C + l_C) \end{pmatrix} .$$

The reflection conditions for the derived hexagonal lattice can be deduced from relation *(3)* . That is : $-h_H + k_H + l_H = 3n$ and $l_H = 2n$, for reflections $h_H\, k_H\, l_H$, since there is no restriction on $h_C\, k_C\, l_C$ reflections [3].

Similarly, the rhombohedral lattice vectors can be derived from the cubic ones according to

$$\begin{pmatrix} \boldsymbol{a}_R & \boldsymbol{b}_R & \boldsymbol{c}_R \end{pmatrix} = \begin{pmatrix} \boldsymbol{a}_C + \boldsymbol{c}_C & \boldsymbol{a}_C + \boldsymbol{b}_C & \boldsymbol{b}_C + \boldsymbol{c}_C \end{pmatrix}$$

$$= \begin{pmatrix} \boldsymbol{a}_C & \boldsymbol{b}_C & \boldsymbol{c}_C \end{pmatrix} \cdot \begin{pmatrix} 1 & 1 & 0 \\ 0 & 1 & 1 \\ 1 & 0 & 1 \end{pmatrix} ,$$

with the cell dimensions having a relation of $a_R = \sqrt{2} \cdot a_C$ (with $\alpha_R = 60°$).

Consequently, the volumes of the hexagonal, rhombohedral and cubic unit cells (denoted by V_H, V_R and V_C, respectively) have the relative sizes of

$$V_H : V_R : V_C = 6 : 2 : 1 .$$

- About the Structural Distortion and the Symmetry

Using *(2)*, the atomic coordinates referring to hexagonal axes for AMO_3 with $Pm\bar{3}m$ symmetry can be obtained from those referring to the cubic ones. They are listed in Table 3 where the crystallographic parameters and reflection conditions [3] of the two related symmetries, $Pm\bar{3}m$ ($\alpha_R = 60$ °) and $R\bar{3}c$ ($\alpha_R \neq$ or $= 60$ °), are compared.

One should point out that a structural distortion from $Pm\bar{3}m$ to $R\bar{3}c$ symmetry occurs when the x-coordinate of oxygen deviates from the representative value of 1/2 required by $Pm\bar{3}m$ symmetry (*cf.* Table 3), but the α_R angle may or may not deviate from 60° (*).

(*) Note: In the case where the x-coordinate of oxygen remains to be $x = 1/2$ while the cubic perovskite lattice is elongated or compressed along $[111]_C$ direction, the distorted structure will have $R\bar{3}$ symmetry which necessarily involves an angle $\alpha_R \neq 60$ ° (for the hexagonal setting used here).

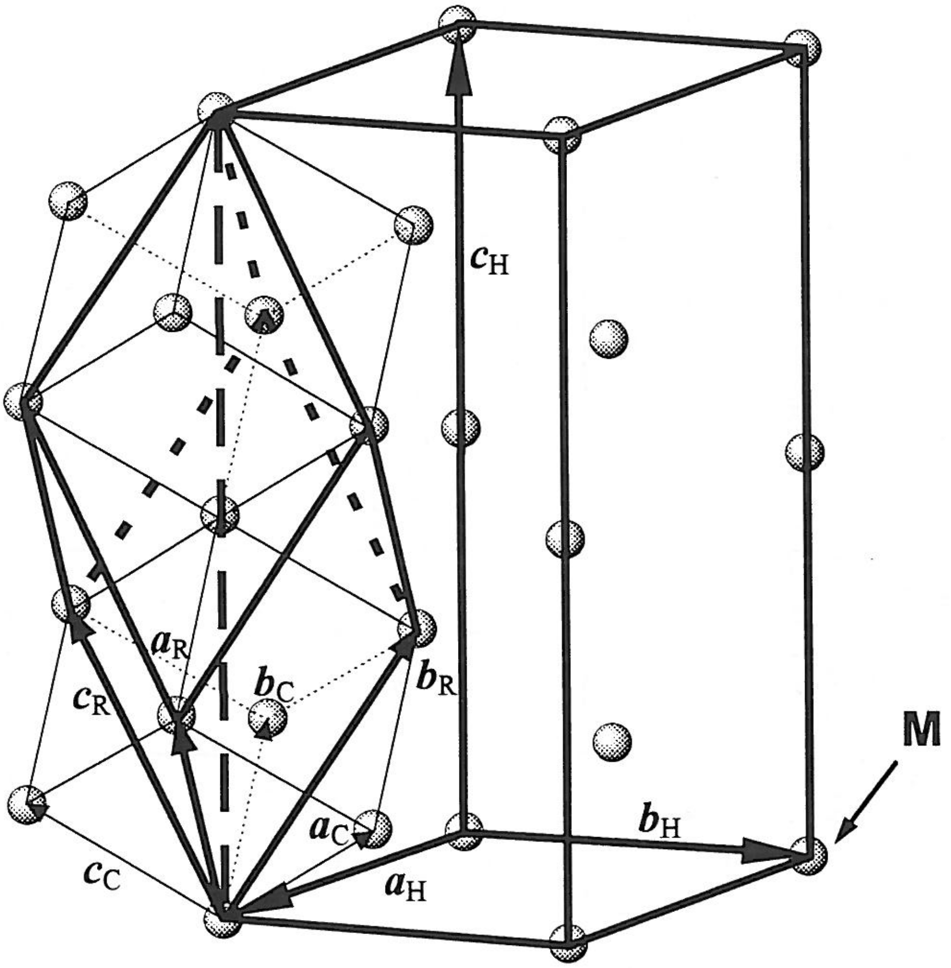

Figure 2

Representation of the Primitive Cubic (C) cell
and its derived Rhombohedral (R) and Hexagonal (H) cells.
For clarity, the origins of the cubic and rhombohedral cells have been translated by a_H.

Table 3

Comparison of Crystallographic Parameters and Reflection Conditions
Between Cubic Perovskite Structure of AMO_3 and a Related Trigonal Structure .
All the atom positions are given in the hexagonal setting (a_H, c_H) shown in Fig. 2 ,
and positions for the $Pm\bar{3}m$ symmetry are obtained from the positions in the cubic cell (*cf.* *(2)*):
A: (1b), (1/2,1/2,1/2) ; M: (1a), (0,0,0) ; O: (3d), (1/2, 0 0)

	Cubic Perovskite Structure : **S.G.: $Pm\bar{3}m$; $a_R=\sqrt{2}\cdot a_C$, $\alpha_R = 60°$.**					**A related Trigonal Structure:** **S.G.: $R\bar{3}c$; a'_R, α'_R (= or ≠ 60°).**				
	Atom positions in Hexagonal Setting				**Reflection [a] Conditions**	**Atom positions in Hexagonal Setting**				**Reflection [a] Conditions** *General*:
Atom	Multiplicity	x_H	y_H	z_H	*General*:	Multiplicity; Wyckoff letter	x'_H	y'_H	z'_H	$h\bar{h}l$: $h+l=3n$, $l=2n$; $00l$: $l=6n$.
A	6	0	0	1/4	*hkl*: $l=2n$	6 a	0	0	1/4	*Special*: *hkl*: $l=2n$
M	6	0	0	0	*hkl*: $l=2n$	6 b	0	0	0	*hkl*: $l=2n$
O	18	1/2	0	1/4	*hkl*: $l=2n$	18 e	x^b	0	1/4	no

a. Only independent conditions are listed; plus the common general condition $-h+k+l=3n$.
b. $x \neq 1/2$ for the structural distortion discussed here.

It can be seen from Table 2 that the XRD pattern is satisfactorily indexed with both the rhombohedral and the cubic cells, leading to an ambiguity about the assignation of the symmetry. That should be related to the two facts:

(i) The possible distortion of the unit cell is very small (with α_R being very close to 60°), so that, within the experimental resolution for the XRD peak positions, the choice between the rhombohedral cell and the cubic one cannot be decided.

(ii) Observed reflections agree with both $Pm\bar{3}m$ and $R\bar{3}c$ symmetries (*cf.* Table 2 and 3), *i.e.* no extra reflections corresponding to $R\bar{3}c$ symmetry are present in the XRD patterns.

However, diffraction peaks characterizing the rhombohedral cell were detected in neutron diffraction experiments for $Sr_2LaFe_3O_{8.94}$ [1] at both room temperature and 50K and the $R\bar{3}c$ symmetry was assigned although the distortion of the unit cell appears to be very small. The crystallographic data are listed in Table 4 and the structural representation will be given later in V-3-2 (Fig. 12).

According to the reflection conditions listed in Table 3, only oxygen atoms can possibly contribute to the observed extra reflections, that is, any occurrence of extra reflections involved in such a structural distortion is due to coordinate shifts of oxygen atoms as will be argued in the following.

Indeed, the intensity of a diffracted beam from given *hkl* planes is : $I_{hk} \propto |F_{hkl}|^2$ ***(4)*** , with F_{hkl} being the structure factor given by the summation over all the atoms j in the unit cell :

$$F_{hkl} = \sum_j f_j \cdot \exp[i \cdot 2\pi(hx_j + ky_j + lz_j)] \qquad \textbf{\textit{(5)}},$$

where $2\pi(hx_j+ky_j+lz_j)$ is the phase difference of atom j, at the position of (x_j, y_j, z_j), between atom at origin; $f_j = f(\sin\theta_{hkl}/\lambda)$ is its scattering factor which can be considered as constant in present case.

Since the coordinates of the cations (Fe, 2:1 Sr and La) are the same for the two structures (*cf.* Table 3 and 4), it can be concluded from ***(4)*** and ***(5)*** that the relative contributions to the intensity I_{hkl} from these cations do not depend on the structures. On the contrary, oxygen coordinates in the rhombohedral and the cubic cells are different as is reported in Table 3 and Table 4 (with observed $x > 1/2$), so that the intensity contributions from the oxygen atoms to a given *hkl* reflection are different for the two structures, accounting for the observed extra reflections in the neutron experiments which are not allowed by the cubic structure where $x = 1/2$.

The above analysis explains the experimental observations of Battle *et al.* [1]. Although the authors did not report the indexing of their neutron diffraction data, we have verified by calculations that those extra *hkl* reflections characterizing the rhombohedral cell are of the form of $l \neq 2n$ (Table 5) ; therefore they undoubtedly arise from the contribution of oxygen atoms. Moreover, the intensities of those reflections are weak although they become relatively a little stronger at 50K where the shifts of oxygen positions are larger than those at room temperature.

In conclusion, the presence of the extra reflections is due to a small distortion of oxygen octahedra (having O_h ($m\bar{3}m$) symmetry in the cubic structure and $\bar{3}$ symmetry in the trigonal structure), which involves coordinate shifts of oxygen atoms. Indeed a distortion only in the unit cell will shift the peak positions but will not give extra peaks in the diffraction patterns.

The above arguments explain also why those reflections unique to the rhombohedral structure are absent in the XRD patterns, since oxygen has a weak scattering power for X-ray photons but it is not the case for neutrons (on the other hand, iron in the composition has a strong absorption of Cu Kα X-ray, which makes weak reflections more difficult to be detected). For this reason, we will adopt the rhombohedral symmetry for the present phase in agreement with the neutron diffraction results mentioned above.

When the $R\bar{3}c$ symmetry is used, the rhombohedral angle α_R obtained by XRD is very close to 60° (Table 1 and Fig. 3b). Then it appears difficult to decide whether a elongation or compression of the unit cell along $[111]_C$ direction of pseudo cubic lattice really exists or not.

- The Disorder of Sr and La Ions.

Sr and La ions in $Sr_2LaFe_3O_{8.90}$ phase can be considered to be disorderly distributed at the pseudo cubic centers. This is deduced from the fact that the XRD data can be satisfactorily indexed with a cubic perovskite cell, since any long-range ordering of Sr and La ions, being the two heaviest ions in the structure and having different scattering factors for X-ray, should have produced peaks associated with superlattice in the XRD patterns. This conclusion is in accordance with the neutron diffraction results [1].

Moreover, since the phase $Sr_2LaFe_3O_{8.90}$ was prepared, under "Chimie Douce" conditions (*cf.* III-2-3-2), from the G-type phase $Sr_2LaFe_3O_8$ where exists the same

Table 4

Crystal Structure Data for $Sr_2LaFe_3O_{8.94}$ [1]

(a) Atomic Positions (S.G.: R$\bar{3}$c, Hexagonal Setting)

at 50K					at Room Temperature				
Atom	Site	x	y	z	Atom	Site	x	y	z
La/Sr	6a	0	0	1/4	La/Sr	6a	0	0	1/4
Fe	6b	0	0	0	Fe	6b	0	0	0
O	18e	0.5266(2)	0	1/4	O	18e	0.5190(2)	0	1/4
a_H=5.4733(2) Å, c_H=13.3504(2) Å. (a_R =5.4580 Å, α_R =60.19°)					a_H=5.4784(3) Å, c_H=13.3928(4) Å. (a_R =5.4712 Å, α_R =60.09°)				

(b) Bond Lengths and Bond Angles

at 50K				at Room Temperature			
Bond Lengths (Å)		Bond Angles (°)		Bond Lengths (Å)		Bond Angles (°)	
Fe –O	1.936(1)×6	Fe–O–Fe′	171.4	Fe –O	1.938(1)×6	Fe–O–Fe′	173.8
La/Sr–O	2.591(1)×3	O–F –O′	90.32	La/Sr–O	2.635(1)×3	O–Fe–O′	90.16
	2.883(1)×3		89.68		2.843(1)×3		89.84
	2.733(1)×6				2.738(1)×6		
O–O′	2.748(2)×4			O–O′	2.745(2)×4		
	2.733(2)×4				2.738(2)×4		

Table 5

Extra reflections characterizing the rhombohedral cell of $Sr_2LaFe_3O_{8.94}$ observed only in the neutron diffraction experiments *

Possible Indices h k l	d_{obs} (Å)	$2\theta_{obs}$ (°) (λ_N =1.909 Å)	I/I_0
2 0 1 1 1 3 1 0 5	~ 2.347	~ 48.0	W
2 1 1 2 0 5 1 0 7	~ 1.789	~ 64.5	VW
3 0 3 2 1 5 2 0 7	~ 1.497	~ 79.2	VW
3 1 1 2 2 3 2 1 7 1 1 9	~ 1.316	~ 93.0	W
4 0 1 3 1 5 1 0 11	~ 1.186	~ 107.2	W
3 2 1 4 0 5 3 1 7 3 0 9 2 0 11	~ 1.089	~ 122.4	W
4 1 3 3 2 5 4 0 7 2 2 9 2 1 11 1 0 13	~ 1.010	~ 141.7	W

*All the *hkl* indices close to the extra peaks are listed, which are calculated from the room temperature neutron diffraction data reported by Battle *et al.* [1]. Among them, only some may be really assigned.

disorder (*cf.* IV-1-2 and IV-1-4), this disordered distribution of Sr and La ions should remain in $Sr_2LaFe_3O_{8.90}$ structure.

- Thermal Variation of the Cell Parameters.

XRD experiments for $Sr_2LaFe_3O_{8.90}$ phase were carried out at various temperatures from 300K down to 80K. All the XRD patterns are of the same feature and can be indexed in both the cubic perovskite cell and the rhombohedral cell, and no discontinuities are present in the thermal dependencies of the unit cell parameters, as shown in Fig 3a, 3b and 3c. Therefore, in the above temperature range, the structure only undergoes a normal contraction with lowering temperature. The previously mentioned neutron diffraction results for $Sr_2LaFe_3O_{8.94}$ also revealed that the $R\bar{3}c$ symmetry remains unchanged at 50K.

V-1-3. Conclusions

From a general viewpoint, for a given perovskite phase AMO_3, a structural distortion from $Pm\bar{3}m$ to $R\bar{3}c$ symmetry necessarily involves coordinate variations of oxygen atoms (*i.e.* $x \neq 1/2$), while the unit cell may or may not be elongated or compressed along the $[111]_C$ direction of pseudo cubic lattice (corresponding to $\alpha_R \neq$ or $= 60°$). If such a structural distortion is not associated with a significant deviation in the angle (*i.e.* $\alpha_R =$ or $\approx 60°$), it would not be detected by the XRD analysis. By contrast, a structural distortion from $Pm\bar{3}m$ to $R\bar{3}$, which involves a lattice distortion but no variations in atomic coordinates, may be easily determined using XRD method.

Despite the fact that the characteristic rhombohedral reflections are absent in our XRD patterns for $Sr_2LaFe_3O_{8.90}$ and that no significant unit cell distortion is observed, for reasons given above, we still adopt the $R\bar{3}c$ symmetry which was previously reported for a close composition of $Sr_2LaFe_3O_{8.94}$ based on neutron diffraction data.

The room-temperature unit cell parameters of the perovskite phase $Sr_2LaFe_3O_{8.90}$ are determined by XRD to be (in hexagonal setting): $a_H = 5.4822(5)$Å, $c_H = 13.440(8)$Å. The Smith-Snyder figure of merit is $F_9 = 27$ (0.0109, 31)

It is confirmed that the A-site Sr^{2+} and La^{3+} ions are disorderly distributed in $Sr_2LaFe_3O_{8.90}$ structure and that no structural transition and discontinuity in the cell dimensions occur at low temperatures.

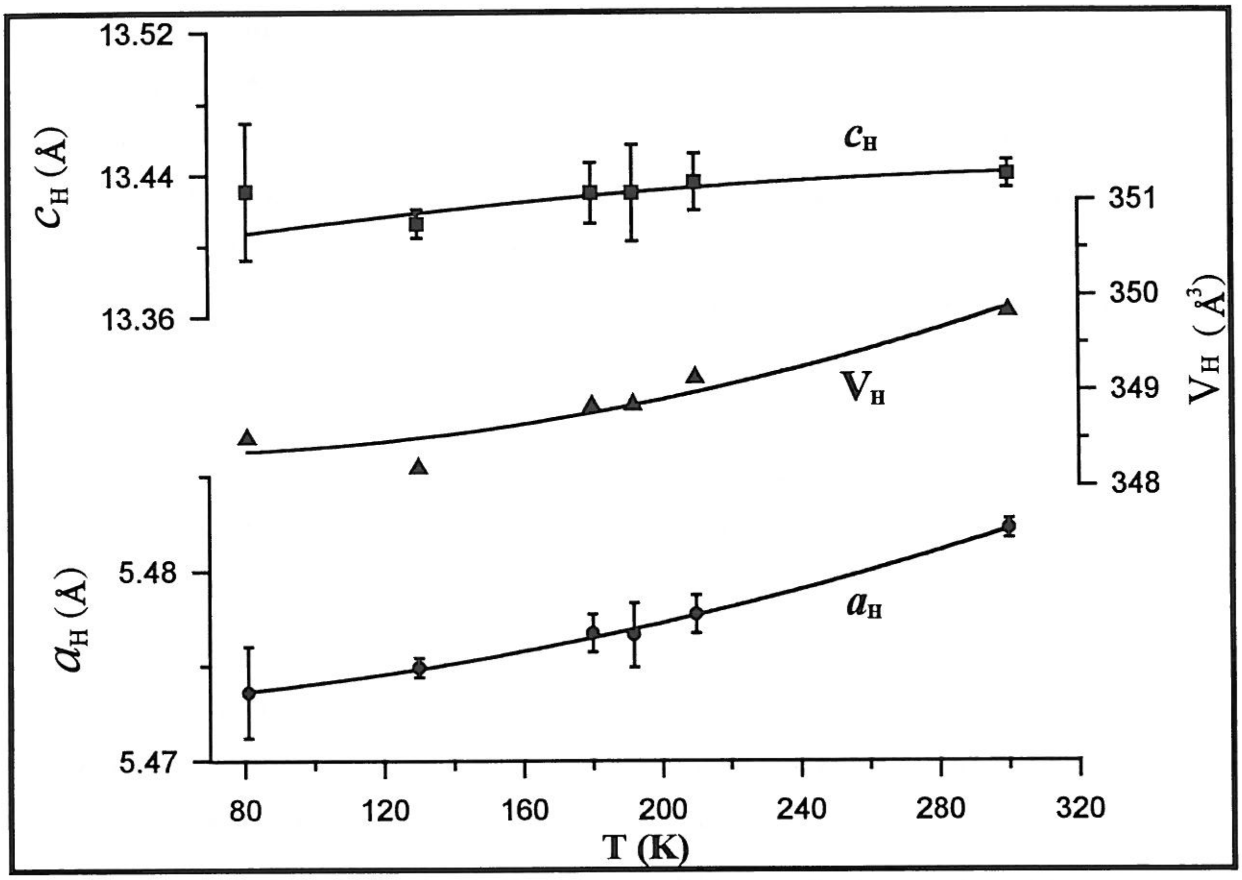

Polynomial Coefficients for $V_H = f(T)$ Fit:

Degree 0:	**348.368**
Degree 1:	**-2.0219E-3**
Degree 2:	**2.3552E-5**

Figure 3a

Temperature dependence of the hexagonal cell dimensions of $Sr_2LaFe_3O_{8.90}$ (rhombohedral structure in hexagonal setting)

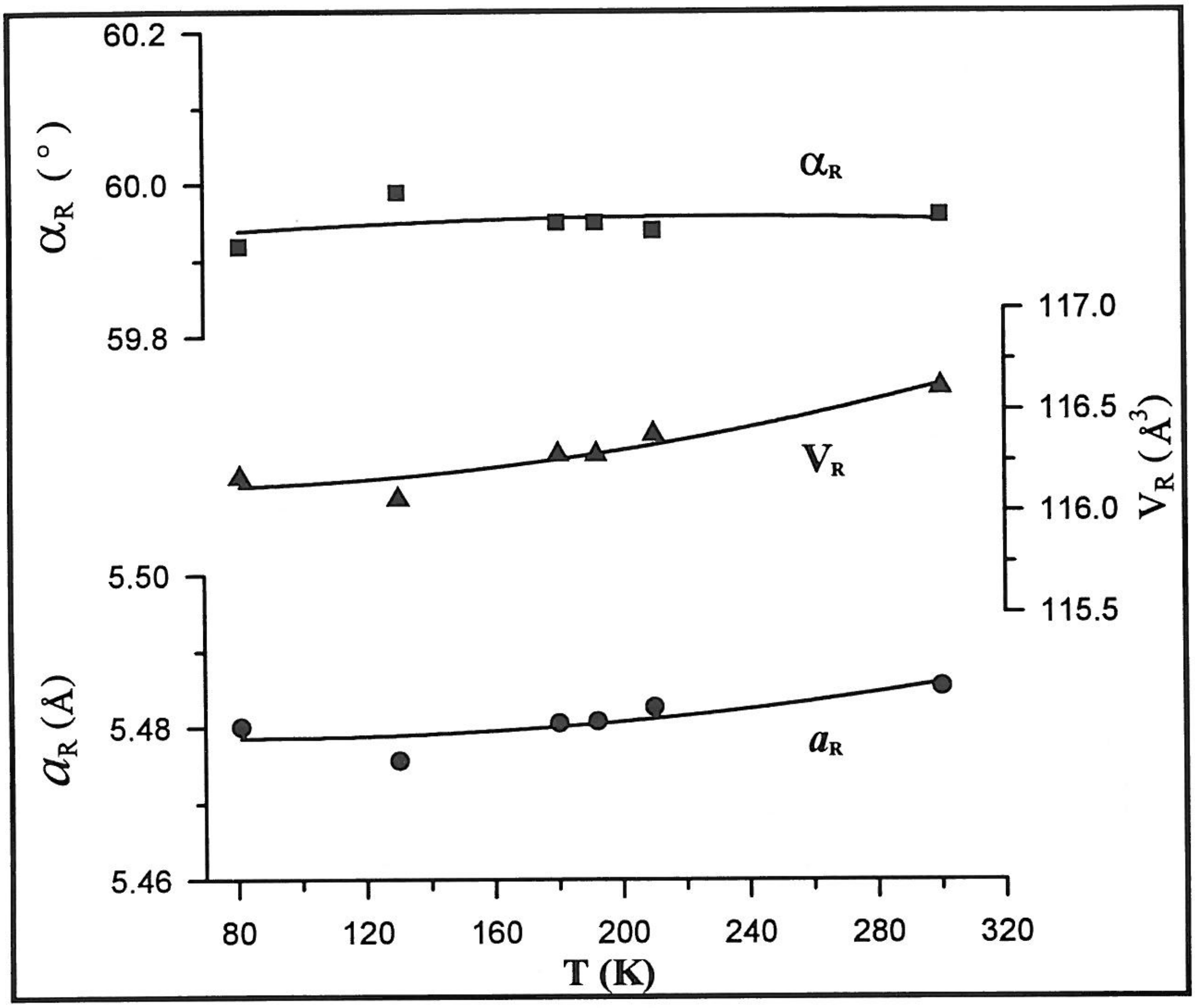

Figure 3b

Temperature dependence of the rhombohedral cell dimensions of $Sr_2LaFe_3O_{8.90}$

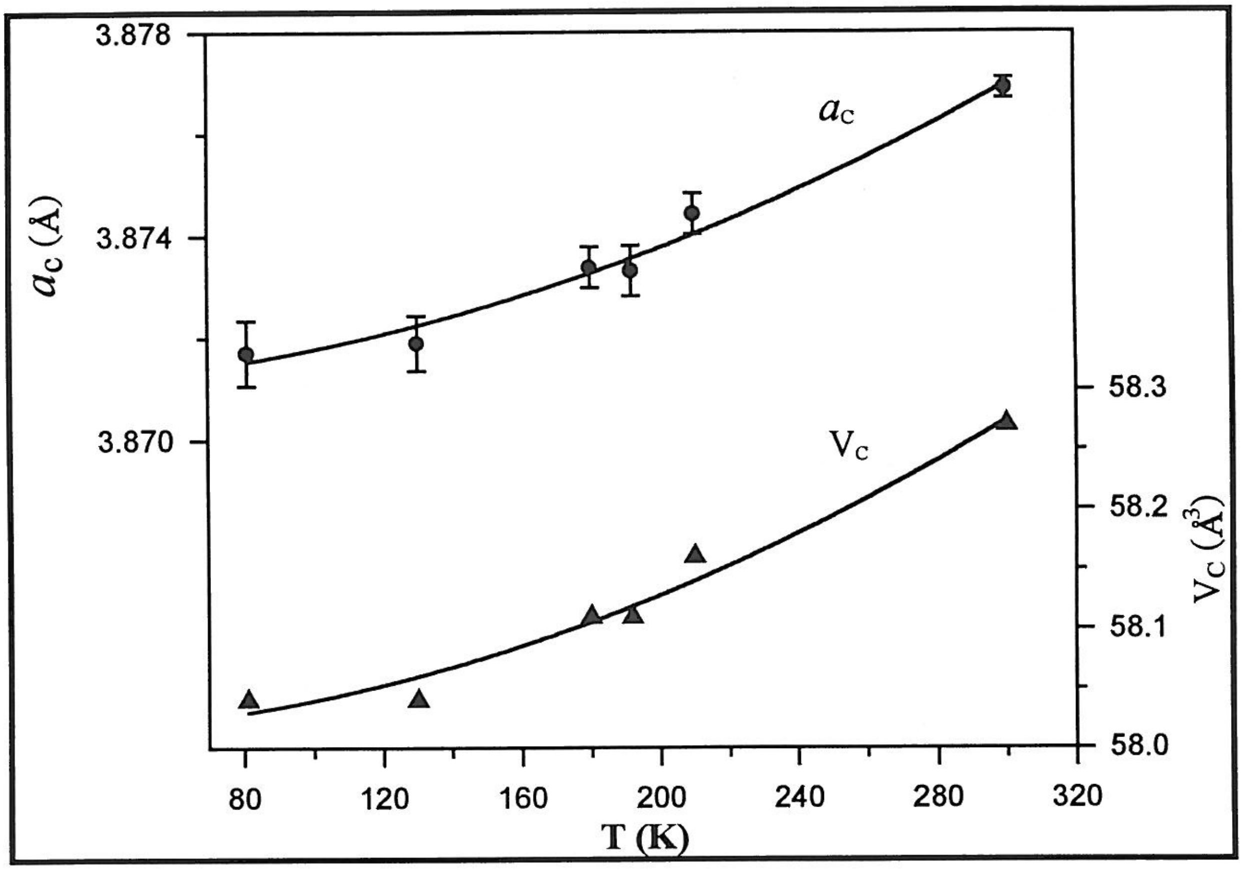

Polynomial Coefficients for $V_C = f(T)$ Fit:
Degree 0: 58.010
Degree 1: 7.005E-6
Degree 2: 2.9098E-6

Figure 3c

Temperature dependence of the cubic cell dimensions of $Sr_2LaFe_3O_{8.90}$

V-2. Mössbauer Spectroscopy Study

V-2-1. Experimental Results

The ^{57}Fe Mössbauer spectra for $Sr_2LaFe_3O_{8.90}$ were recorded at various temperatures from 4.2 K up to room temperature.

- High Temperature Range ($T \geq 200$ K)

In the temperature range 200 K $\leq T \leq$ 293 K, the spectra exhibit a single broad symmetrical peak : typical spectra are given in Fig. 4. Good fits are obtained using a doublet, *i.e.* pairs of lines with equal intensities, which is assumed to be due to quadrupole interactions (the quadrupole splitting Δ varies from 0.155 mm·s^{-1} at 293 K to 0.182 mm·s^{-1} at 200 K). The width at half-height at 293 K is Γ = 0.35 mm·s^{-1}. The isomer shifts (δ = 0.141 mm·s^{-1} (293K) ~ 0.193 mm·s^{-1} (200 K)) of iron are intermediate between the values expected for Fe^{3+} ($\delta \approx$ 0.39 mm·s^{-1} as in $LaFeO_3$ [4]) and Fe^{4+} ($\delta \approx$ 0.06 mm·s^{-1} as in $SrFeO_{2.97}$ [5]).

These results indicate a paramagnetic "averaged" valence state of iron [2, 6], which is in agreement with magnetic measurements (cf. V-3) and the electron hopping model proposed in V-4-2. Assuming a linear variation of δ between Fe^{3+} and Fe^{4+}, the resulting valence is close to Fe $^{+3.63}$ as predicted by the chemical composition (*i.e.* $\approx$ $1/3Fe^{3+} + 2/3\ Fe^{4+}$).

- Low Temperature Range ($T < 200$ K)

Given in Fig. 5 is the spectrum at 4.2 K showing the analysis in terms of two magnetic hyperfine splittings and a central single but rather wide line having an isomer shift of δ = 0.37 mm·s^{-1} and a relative area of 5.3%.

The two sets of six-line magnetic hyperfine splitting characterizes a magnetic ordering and hyperfine fields of 46.6 and 26.4 Tesla, isomer shifts of 0.366 and -0.025 mm·s^{-1}, and relative areas of 64.6% and 30.1% (*i.e.* a ratio of 2.05:0.95), respectively. Moreover, no detectable quadrupole perturbations exist for the two hyperfine sextets (ε = or $\approx$ 0). These observations can be readily explained by the existence of mixed valence states of $Fe^{3+}$and Fe^{5+} with oriented (high) spins (Fig. 5).

The relative areas (including that of the single line, for discussions see below) correspond to a concentration ratio of $[Fe^{3+}]:[Fe^{5+}]=2.1:0.9$, which is in excellent agreement with the overall chemical formula of $Sr_2LaFe_3O_{8.90}$ as obtained by chemical analysis.

It can be seen from Figs. 4 ~ 8 that the hyperfine fields exist up to T ≈ 198 K.

V-2-2. Discussions

- The Charge Disproportionation and Nonintegral Charge States

It will be known later in V-3 that there exists a drastic magnetic transition (para-antiferromagnetic transition) in $Sr_2LaFe_3O_{8.90}$ in the temperature range 180 K ~ 200 K, which accounts for the hyperfine splitting in the Mössbauer spectra. Moreover, the Mössbauer data also clearly show a charge disproportionation of the averaged valence state into mixed valence state, as was first suggested by Takano *et al.* for $CaFeO_3$ and $Sr_{2.1}La_{0.9}Fe_3O_9$ [6, 7].

Here, referring to the composition of $Sr_2LaFe_3O_9$ for simplicity, the charge disproportionation can be expressed as :

$$3\,Fe^{3.67+}\,(PM) \Rightarrow Fe^{(5-2\lambda)+} + 2\,Fe^{(3+\lambda)+}\,(AFM) \quad (0 < \lambda < 0.67),$$

when the temperature is lowered from the paramagnetic (PM) region to the antiferromagnetic (AFM) region. The introduction of the parameter λ is due to that the charge states are believed to be nonintegral.

Mössbauer data can provide strong support for the nonintegral charge states, according to the arguments by Battle *et al.* [1], in that the magnetic flux density (B = 46.6 T) observed for nominal "Fe^{3+}" state in $Sr_2LaFe_3O_{8.90}$ is intermediate between the flux densities (B ≈ 55 T) of localized Fe^{3+} states in various compounds having similar oxygenated sites and that of nominal Fe^{4+} state (B = 33.1 T) in perovskite $SrFeO_3$ as shown in Table 6, where some parameters for phases whose structures are related to the perovskite are also listed for comparison. Moreover, nonintegral charge states assumed for a similar composition of $Sr_2LaFe_3O_{8.94}$ ([1] and *cf.* V-3) are consistent with the unusual iron spin densities observed in neutron diffraction experiment.

- The Temperature Range and Features of the Transition

According to the Mössbauer spectra recorded at various temperatures shown in Figs. 4-8 , the hyperfine field exists up to T ≈ 198K within the experimental resolution. Moreover, it can be seen that the paramagnetic averaged-valence state and the antiferromagnetic mixed-valence state coexist over a range of temperatures (170 K up to 200 K), which coincides with the region where takes place the abrupt magnetic transition (*cf.* V-3). Also the temperature dependence of the hyperfine fields of the remnant antiferromagnetic phase shows a discontinuity near the Néel temperature.

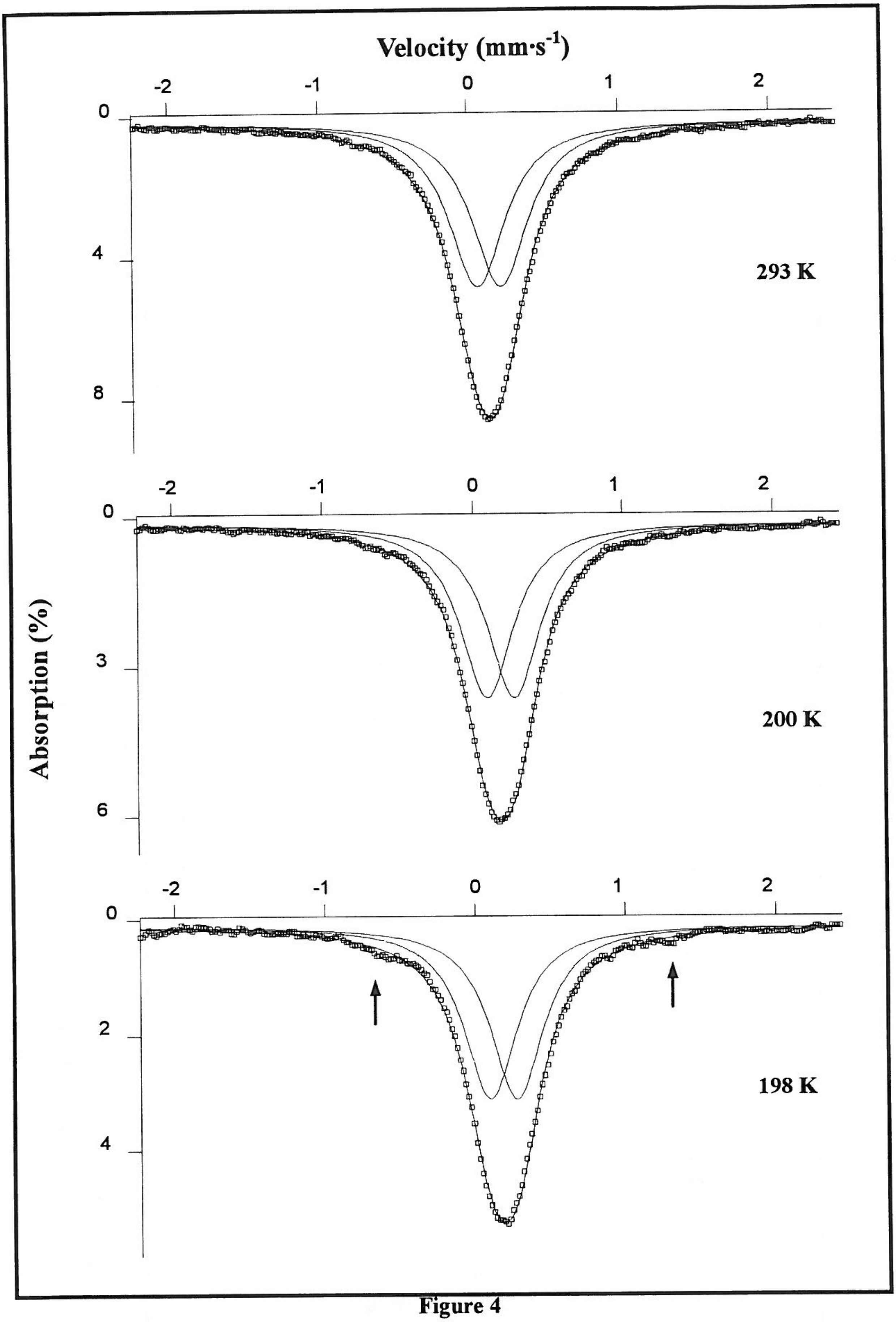

Figure 4

^{57}Fe Mössbauer spectra recorded at 293K, 200K and 198K for "$Sr_2LaFe_3O_{8.90}$". It can be seen that the hyperfine field (indicated by the arrows in the figure) exists up to about 198K within the experimental resolution. For 200K ≤ T ≤ 293K, each spectrum (only two are shown) comprises a single broad symmetrical peak which can be well fitted using a doublet and corresponds to the paramagnetic averaged-valence state.

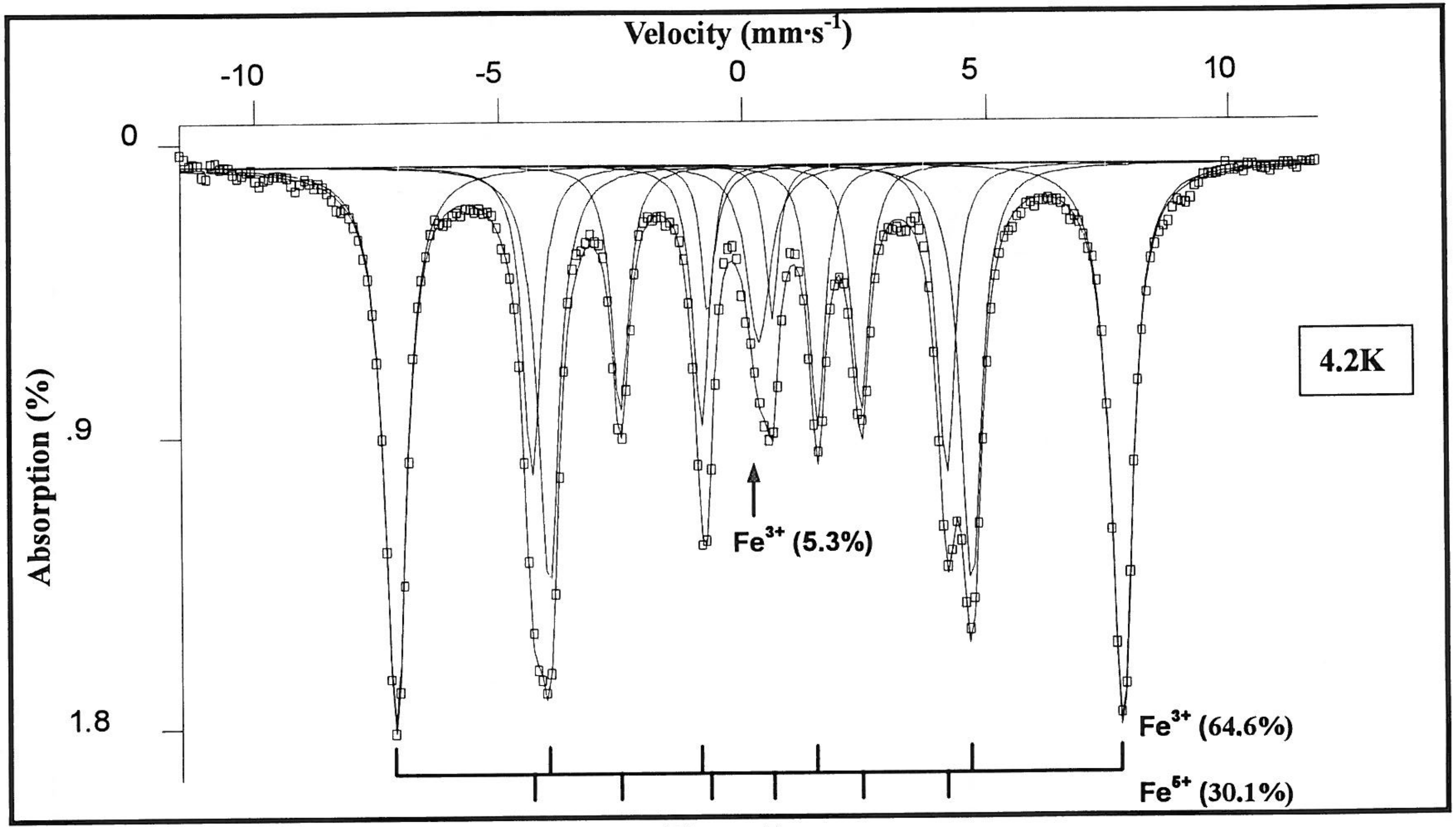

Figure 5

The ^{57}Fe Mössbauer spectrum recorded at 4.2K for "$Sr_2LaFe_3O_{8.90}$". It is analyzed in terms of two sets of hyperfine splitting, which characterize the oriented spin and mixed-valence states of Fe^{3+} and Fe^{5+} ions in perovskite **$Sr_2LaFe_3O_{8.95}$**, as well as one single line (indicated by the arrow), which is explained by superparamagnetism of some non-oxidized domains containing only Fe^{3+} (for discussions see text).

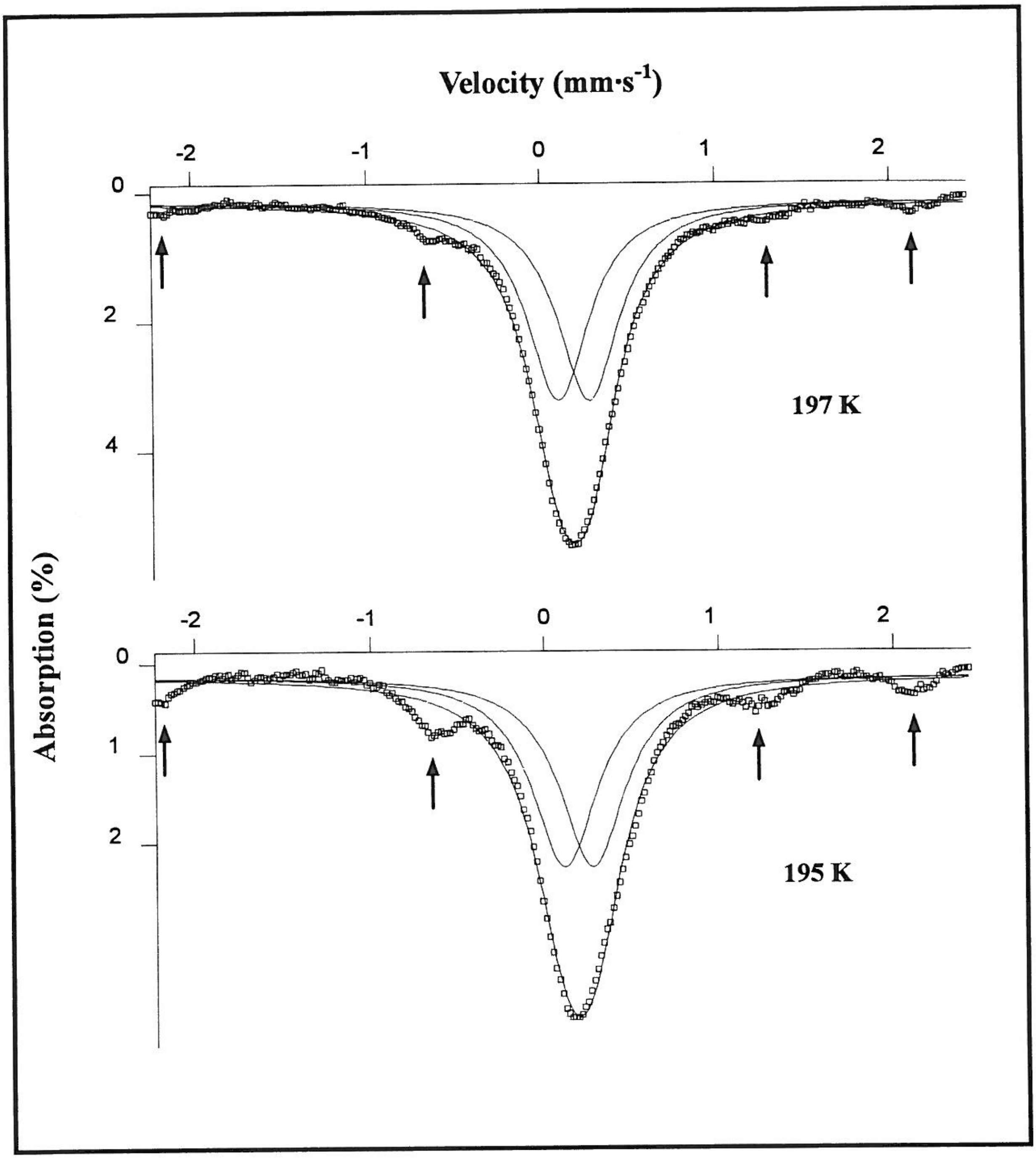

Figure 6
Mössbauer spectra recorded at 197 K and 195 K for "$Sr_2LaFe_3O_{8.90}$", showing coexistence of the major phase of paramagnetic averaged-valence state (represented by the central peak) with the minor phase of antiferromagnetic mixed-valence state (represented by the hyperfine field indicated by the arrows).

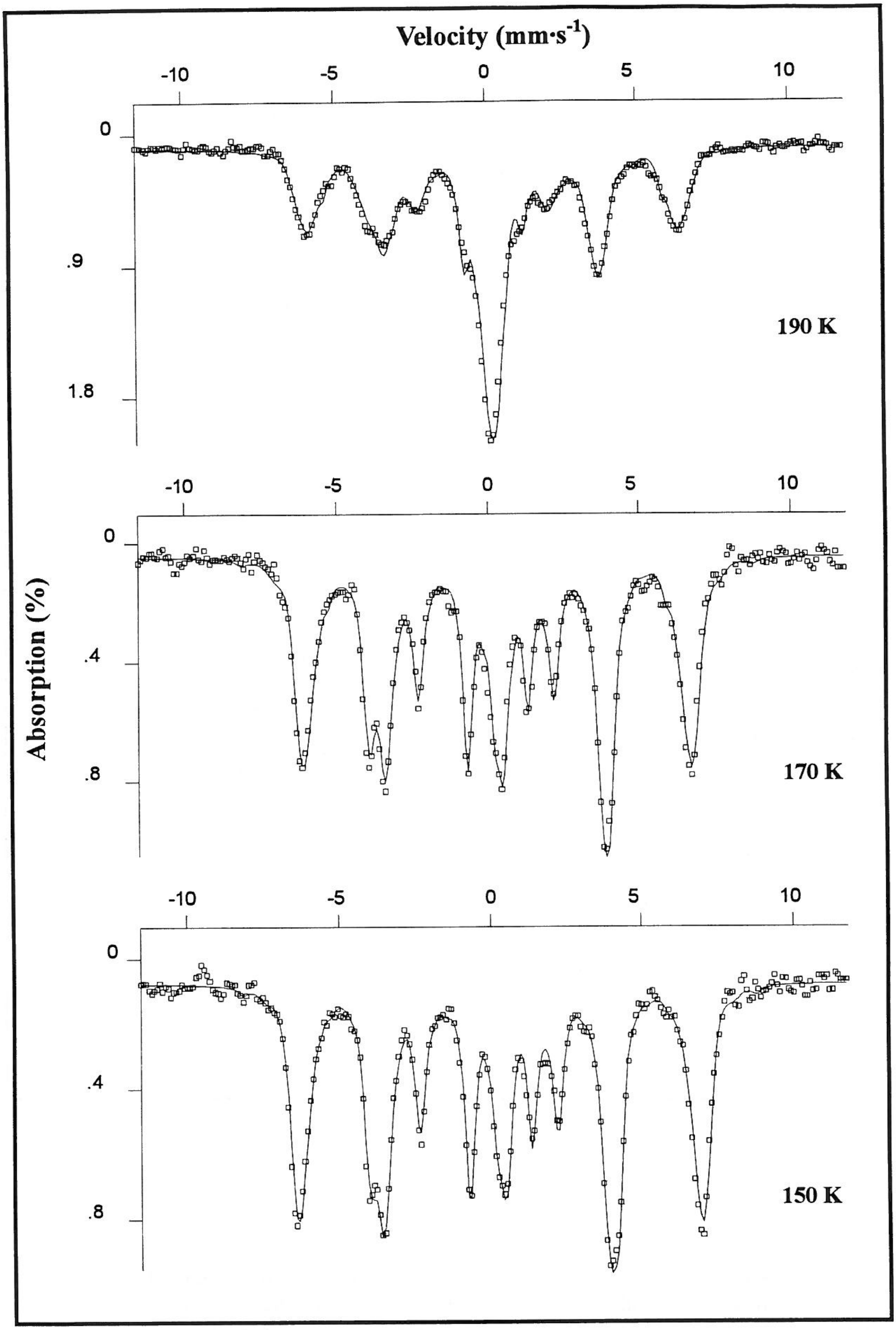

Figure 7

Mössbauer spectra at 190 K, 170 K and 150 K for "$Sr_2LaFe_3O_{8.90}$". Now the phase of antiferromagnetic mixed-valence state can be well defined, while the phase of paramagnetic averaged-valence state becomes the minor phase and it almost disappears for T < 170 K.

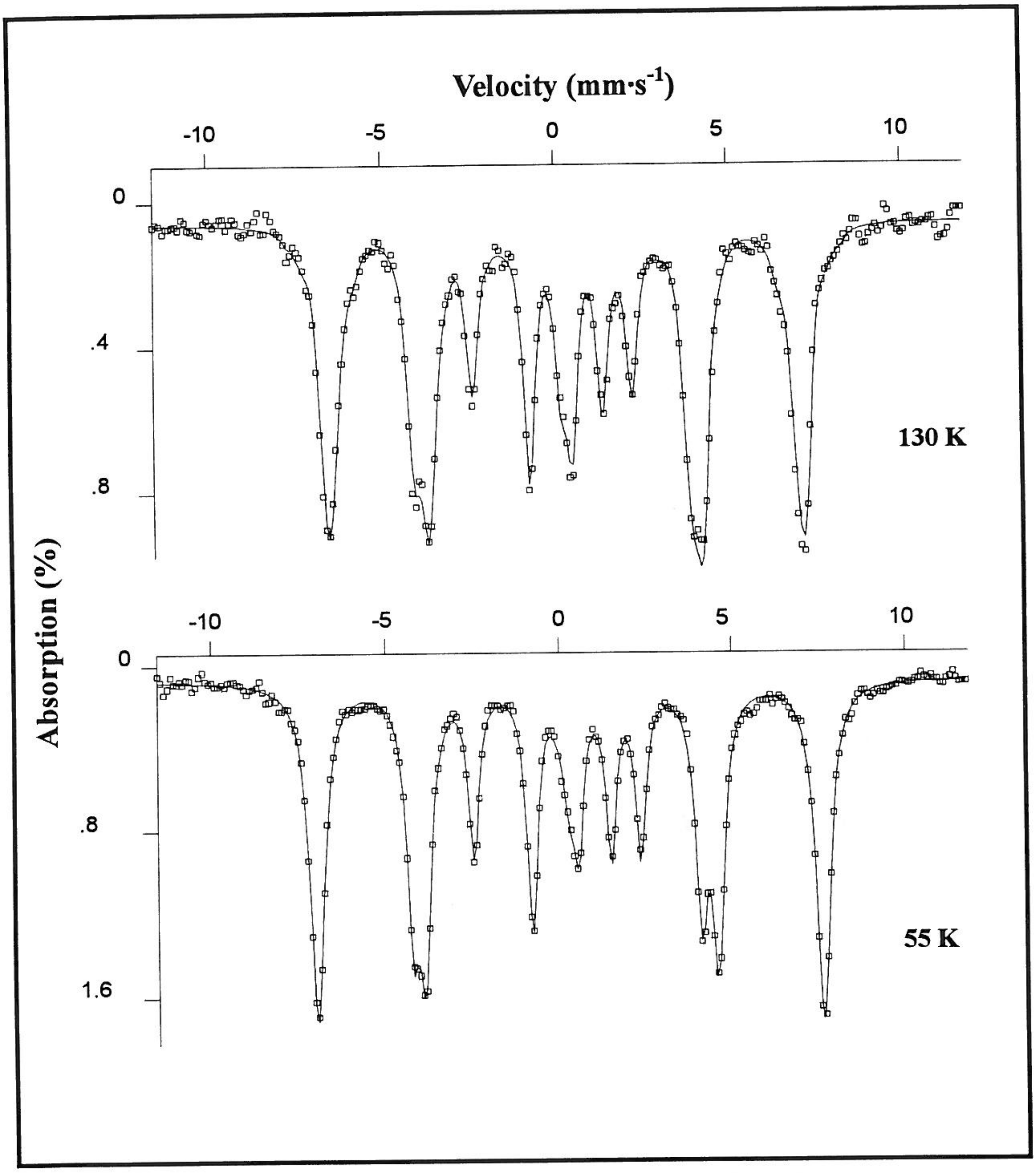

Figure 8
Mössbauer spectra for "$Sr_2LaFe_3O_{8.90}$" at 130 K and 55 K.

Table 6

Mössbauer Parameters at 4.2 K for Iron Ions in Octahedral Oxygenated Sites

Compounds	**Valence States**	**B (Tesla)**	**δ (mm·s^{-1})**	**References**
$Sr_2Fe_2O_5$	Fe^{3+}	53.9	0.50	[60]
$Ca_2Fe_2O_5$	Fe^{3+}	54.7	0.46	[8, 60]
$Sr_2LaFe_3O_8$	Fe^{3+}	55.5	0.46	[60]
$LaFeO_3$	Fe^{3+}	56.4	0.46	[4]
$SrFeO_3$	Fe^{4+}	33.1	0.15	[9]
$Sr_{2.1}La_{0.9}Fe_3O_9$	Fe^{3+} Fe^{5+}	46.0 26.9	0.36 -0.05	[6]
$Sr_2LaFe_3O_{8.94}$ (at 78K)	Fe^{3+} Fe^{5+}	45.1 25.9	0.352 -0.027	[2]
$Sr_2LaFe_3O_{8.95}$	Fe^{3+} Fe^{5+}	46.6 26.4	0.366 -0.025	This work

These facts suggest that the two phases make a *locally* first-order transition to each other (*i.e.* the transition takes place first in some domains before the whole system is transformed), as was first observed and discussed by Takano *et al.* [6] and Battle *et al.* [1, 2] for two close phases of $Sr_{2.1}La_{0.9}Fe_3O_9$ and $Sr_2LaFe_3O_{8.94}$. Some further discussions concerning the phase transition will be given later in V-5 and V-6.

- The Overall Composition and the Composition of the Main Perovskite Phase: Evidence from the Mössbauer Data at 4.2K

Although our Mössbauer data for $Sr_2LaFe_3O_{8.90}$ phase are generally in agreement with the previously reported ones, the above-mentioned weak single line resolved in the low-temperature spectra was not observed in the previous experiments for phases of $Sr_{1-y}La_yFeO_3$ ($0.1 \leq y \leq 0.6$, [6]), $Sr_2LaFe_3O_{8.94}$ [2] and $Sr_2LaFe_3O_9$ [10]. Since its isomer shift at 4.2K is δ=0.37 mm·s^{-1}, this line may be assigned to nominal Fe^{3+} state. The single-line feature leads us to assume that it may be of superparamagnetic (SPM) origin.

As the present sample (with the overall composition of $Sr_2LaFe_3O_{8.90}$ according to chemical analysis) was obtained by electrochemical oxidation (cf. III-2) from G-type phase $Sr_2LaFe_3O_8$ containing only Fe^{3+}, it is possible that there may exist domains deep in some larger grains which remain non-oxidized after the electrochemical process, or some very small grains located in cavities formed by larger grains may not experience the electrochemical oxidation. If the size of these non-oxidized domains or grains are small enough and the anisotropy effect is weak, a superparamagnetism phenomenon will occur [11].

Therefore, according to the Mössbauer data recorded at 4.2K, the composition of $Sr_2LaFe_3O_{8.90}$ obtained from chemical analysis is only an overall one, with about 5% of "non-oxidized phase" intergrown with the major (95%) "oxidized" perovskite phase having following nominal composition at 4.2K :

$$Sr_2LaFe^{3+}_{2.05}Fe^{5+}_{0.95}O_{8.95} .$$

The physical properties for T < 300 K concerned and studied in the following sections can be attributed to the main perovskite phase of $Sr_2LaFe_3O_{8.95}$ (the sample concerned in this and the following sections is the same).

V-2-3. Conclusions

Although the overall composition of $Sr_2LaFe_3O_{8.90}$ was given by chemical analysis, the Mössbauer results reveal that the real composition of the main perovskite phase is $Sr_2LaFe_3O_{8.95}$. It is this phase which accounts for the physical properties studied in the following sections and will be referred to from now on.

At high temperatures, the iron ions in $Sr_2LaFe_3O_{8.95}$ phase are in paramagnetic averaged-valence state, while at lower temperatures they are in antiferromagnetic mixed-valence state ; the two states make a *locally* first-order transition to each other over a temperature range of $170 < T < 200$ K, involving a disproportionation of iron charge.

Although it is convenient to denote the low-temperature mixed-valence states by Fe^{3+} and Fe^{5+}, it is understood that they only have a nominal meaning as the charge states are non-integral in nature.

V-3. Magnetic Properties.

V-3-1. Dependencies of the Magnetic Susceptibility on Temperature and Field.

- Thermal Dependence of the Magnetic Susceptibility ($\chi_m(T)$).

The temperature dependence of the molar susceptibility of $Sr_2LaFe_3O_{8.95}$ (corrected for diamagnetic susceptibilities of all the ions in the phase) is shown in Fig.9, which is measured in an applied field $H = 1.7\times10^4$ Oe ; in the inset of Fig. 9 is also shown the reciprocal susceptibility as a function of the temperature in the range of 170K < T < 350K.

The susceptibility displays an abrupt decrease when the temperature is lowered below about 200K, characterizing the antiferromagnetic ordering of the iron spins. It is consistent with the Mössbauer spectroscopy data and the anomalies in the specific heat (*cf.* V-5) as well as in the conductivity and thermoelectric power measurements (*cf.* V-4). The peak position of the specific heat is considered as determining the Néel temperature, that is, $T_N = 196$K.

(a) In the paramagnetic region, it can be seen from the inset of Fig. 9 that the susceptibility at about T > 280 K can be well described by the Curie-Weiss law: $\chi_m = \dfrac{C_m}{T-\theta_P}$, where C_m is the Curie constant and θ_P the Weiss constant.

From the linear fit of χ_m^{-1} vs. T plot (for T ≈ 280 ~ 350 K), the following quantities for $Sr_2LaFe_3O_{8.95}$ phase can be obtained :

$C_m = 11.17$ (emu·K/Oe·mol) , $\theta_P = -177$ (K).

Thus the averaged effective moment per iron atom is $\mu_{Fe} = 5.46\ \mu_B$. This value agrees with the magnetic moment of 5.55 μ_B previously reported by Battle *et al.* [2] for $Sr_2LaFe_3O_{8.94}$.

On the other hand, it is known that the site symmetry of the iron ions is very close to O_h (*cf.* IV-1-1), so that the ground states due to the crystal field splitting can be either high-spin $t_{2g}^3e_g^2$ (Fe^{3+}) and $t_{2g}^3e_g^1$ (Fe^{4+}) configurations having, respectively, ${}^6A_{1g}$ and ${}^5E_g$ symmetries (note that for the former the orbital quantum number $L = 0$ and for the latter the orbital moment is predicted to be quenched [12]), or possibly low-spin t_{2g}^4 (Fe^{4+}) configuration having ${}^3T_{1g}$ symmetry. With the spin-only moment for a spin S given by $\mu^{spin} = 2[S(S+1)]^{1/2}$ (μ_B), the averaged spin-only moment of high-spin iron ions in the nominal composition of $Sr_2LaFe^{3+}_{1.10}Fe^{4+}_{1.90}O_{8.95}$ may be obtained from

$$(\mu^{spin}_{Fe})^2 = \frac{1.10}{3}\times(\mu^{spin}_{Fe^{3+}})^2 + \frac{1.90}{3}\times(\mu^{spin}_{Fe^{4+}})^2 = \frac{1.10}{3}\times5.92^2 + \frac{1.90}{3}\times4.90^2,$$

with the value being $\mu^{spin}_{Fe} = 5.30\ \mu_B$. It is close to the observed value.

Those results indicate that the iron *d*-electrons are in localized high-spin states.

However, a small difference between the observed and the spin-only moment exists, with the observed one being a little larger. It cannot be explained by possible incomplete quenching of the iron orbital moment due to the presence of spin-orbit coupling, because if it is so the magnetic moment of the ^5E_g state (with the spin-orbit coupling parameter $\lambda > 0$) will be a little smaller, but not larger, than the spin-only one. Nor can it be explained by the contribution due to Van Vleck temperature-independent paramagnetism since it is only of the order of 10^{-5} emu/Oe·mol. In fact, as the *d*-electron orbitals of the central iron ions are to mix, to a certain extent, with those of the oxygen ligands, the above deviations from the spin-only moment are reduced since the orbital mixing corresponds to an additional quenching of the orbital angular momentum [12].

Therefore other causes have to be considered : this a little higher effective moment than the spin-only one may be related to the influences of the non-oxidized superparamagnetic domains (*cf.* V-2-2) and of some spin-polarization effect (which will be presented later), and/or to that the extrapolation is made on a too small temperature range.

At temperatures near T_N (about 200 ~ 280 K), the Curie-Weiss law is somewhat deviated, suggesting some short-range spin ordering.

(b) In the antiferromagnetic region, the susceptibility χ_m is almost temperature independent until the magnetic transition sets in. Such a behavior could be due to spin polarization effect (which will be discussed later in V-6-3), or to the peculiar magnetic interactions in this material (*cf.* recent theoretical results reported in Appendix I).

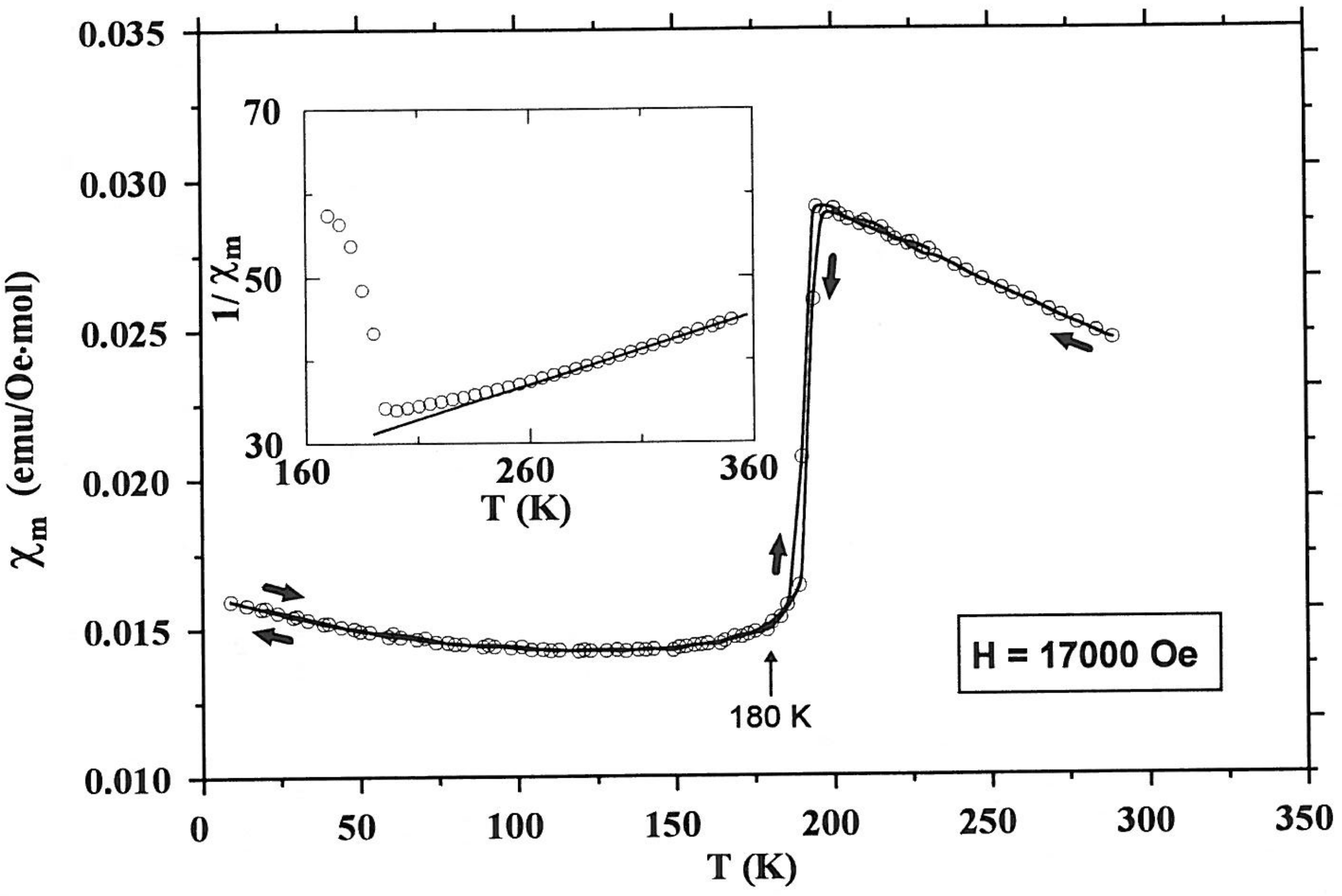

Figure 9

Molar susceptibility and its reciprocal (shown in the inset) for $Sr_2LaFe_3O_{8.95}$ as a function of temperature under a field of $H = 1.7\times10^4$ Oe. The susceptibility is measured at both decreasing and increasing temperature, but no hysteresis exists at the transition (being consistent with the fact that no structural distortion is observed).

- Field Dependence of the Magnetic Susceptibility ($\chi_m(H)$).

The variation of the susceptibility as a function of applied field is shown in Fig. 10 for various temperatures : it is obtained according to $\chi_m = \frac{\Delta M_m}{\Delta H}$ (corrected for atomic diamagnetic susceptibility). Slight deviations from linearity are present in the $M_g = f(H)$ curves (three of these curves are shown in Fig. 11), and these can be clearly seen from the χ_m *vs.* H plots given in Fig. 10.

The common feature is that, in both the paramagnetic and antiferromagnetic region, the susceptibility decreases with the field H for $H < 2500$ Oe ~ 3000 Oe. However, the explanation of these observations is complicated by experimental errors which may be important at low fields.

The fact that at various temperatures below T_N the susceptibilities increase with the field for $H >\sim 7000$ Oe could be explained by the effect of anisotropy.

For an antiferromagnet with sublattice magnetizations $\boldsymbol{M_A}$ and $\boldsymbol{M_B}$ (they make an angle to each other when a field $\boldsymbol{H}$ is applied), its susceptibility (for polycrystalline sample) is given by [11]:

$$\chi = \frac{1}{3}\chi_{\parallel} + \frac{2}{3}\chi_{\perp} + \frac{2}{15K}(\chi_{\parallel} - \chi_{\perp})^2 H^2 ,$$

where $\chi_{\parallel}$ and $\chi_{\perp}$ are the susceptibilities parallel and perpendicular to ($\boldsymbol{M_A} - \boldsymbol{M_B}$), and K is the constant.

Therefore, with the presence of anisotropy, the susceptibility is field-dependent (*), although the application of the above equation to $Sr_2LaFe_3O_{8.95}$ phase can only be an approximation due to multiple sublattices. The susceptibility is observed to rise with the field more rapidly at lower temperatures (especially at 5K), suggesting that the term $(\chi_{\parallel} - \chi_{\perp})^2/K$ may be larger for low temperature.

(*) Note that if the anisotropy field is small compared with the molecular field and if the applied field is not too large, then in the mean field approximation the susceptibility is field independent and is given by $\chi = \frac{1}{3}\chi_{\parallel} + \frac{2}{3}\chi_{\perp}$ for polycrystalline samples. Here $\chi_{\parallel}$ and $\chi_{\perp}$ are defined as parallel and perpendicular to the easy direction.

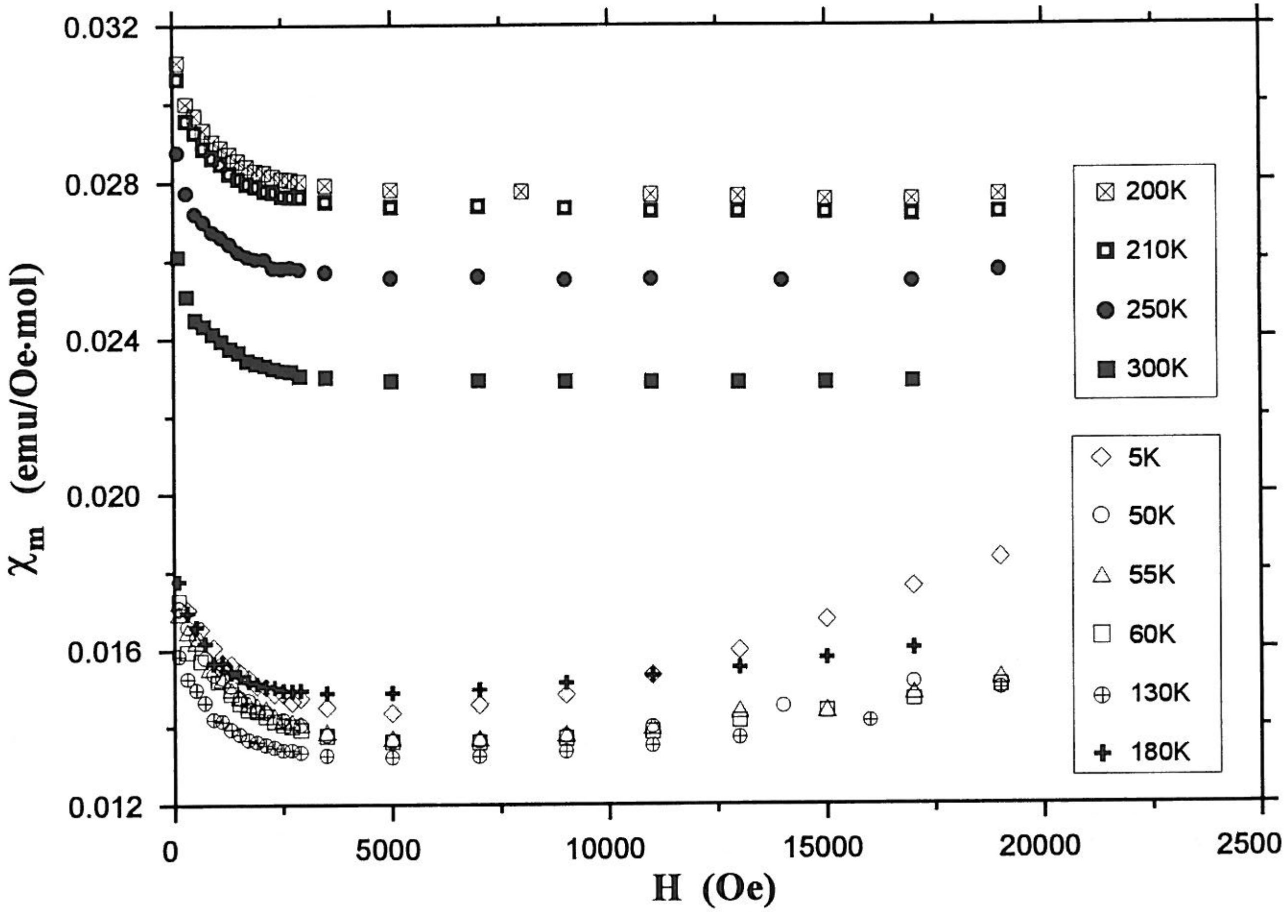

Figure 10
Field dependence of the molar susceptibility of $Sr_2LaFe_3O_{8.95}$ at various temperatures.

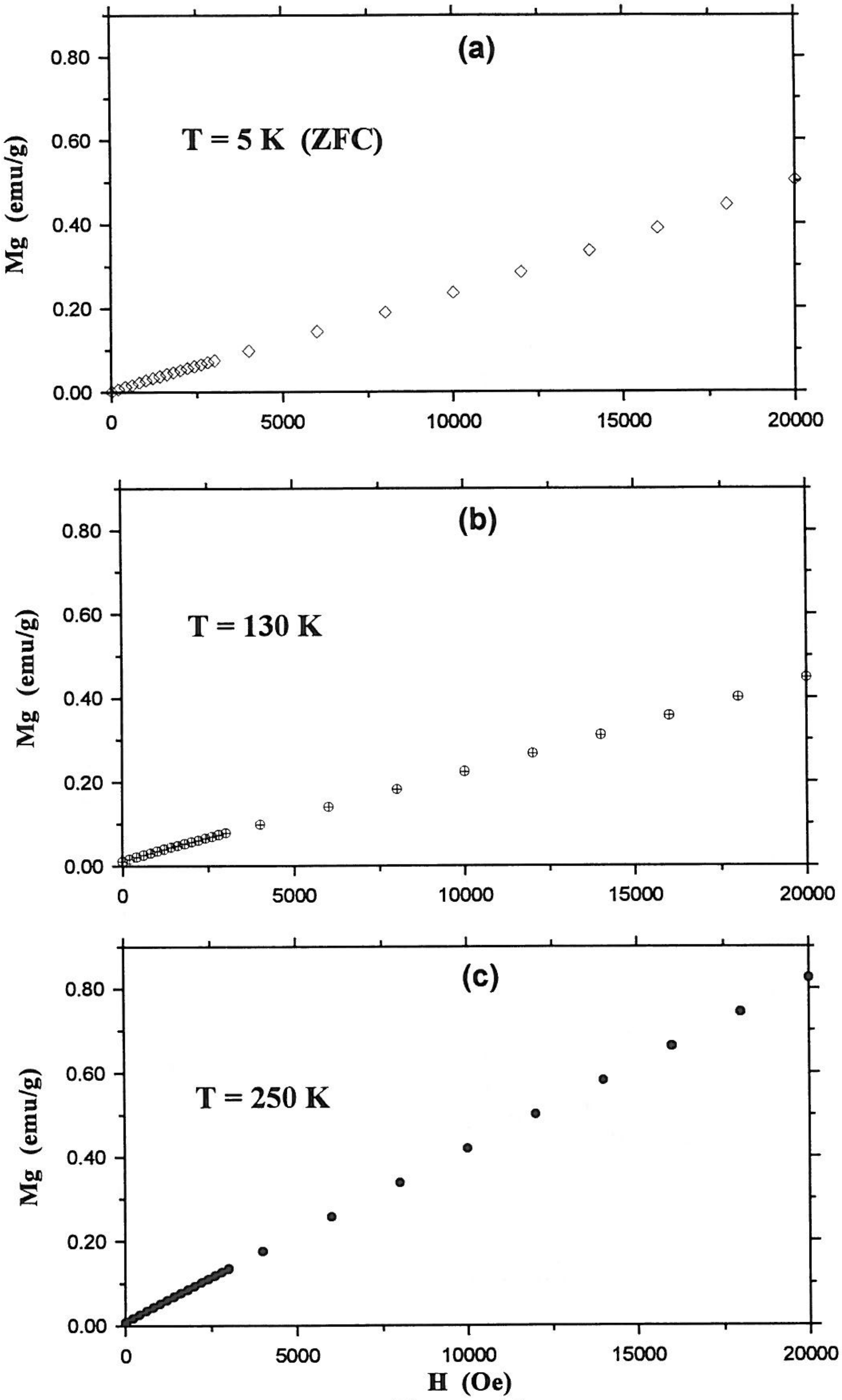

Figure 11

Field dependence of the magnetizations measured with increasing field at :

(a) 5K (after zero field cooled (ZFC) from 300K to 5K)

(b) 130K (measured after exposed to a field of 2×10^4 Oe.

(c) 250K (in PM region, measured as in **(b)**).

V-3-2. The Magnetic Structure of "$Sr_2LaFe_3O_9$".

We can reasonably assume that the magnetic structure, as well as the crystal structure, of our compound $Sr_2LaFe_3O_{8.95}$ are similar to those previously reported [1] for a very close composition ; it is shown in Fig 12.

In this magnetic structure, the rhombohedral lattice translations and *c*-glide plane of the crystal structure (space group $R\bar{3}c$) are absent, which results, for the spin structure, in the space group $P\bar{3}m1$ and a primitive trigonal unit cell (in hexagonal axes) commensurate with the triple unit cell (in hexagonal axes) of the crystal structure. The ordered iron spins lie in the *xy*-plane, with magnetic moments (at 50K) of $3.61(3)\mu_B$ for nominal Fe^{3+} ions and $2.72(6)\mu_B$ for nominal Fe^{5+} ions, respectively.

For simplicity, the ideal composition $Sr_2LaFe_3O_9$ is assumed in the following.

The spin interactions between the localized *d*-electrons on iron sites are dominated by superexchange interaction, which couples two nearest neighboring magnetic iron cations via the non-magnetic oxygen anion. Because of the structural arrangement of corner-sharing FeO_6 octahedra of the perovskite-type, there exist superexchange interactions along 180° Fe — O — Fe pathway of both σ-type and π-type. The σ-type interaction is much stronger than the π-type one, hence decides the sign of effective exchange coupling constant J_{eff} [15].

Generally, three kinds of superexchange interactions are possible among high spin d^5 and d^3 configurations. But in $Sr_2LaFe_3O_9$, only the antiferromagnetic ($J_{eff} < 0$) coupling,

$$(S_{5/2})\uparrow — \downarrow(S_{5/2}) \ , \quad Fe^{3+}(d^5) — O(2p) — Fe^{3+}(d^5) \ , \quad (6)$$

and the ferromagnetic ($J_{eff} > 0$) one,

$$(S_{5/2})\uparrow — \uparrow(S_{3/2}) \ , \quad Fe^{3+}(d^5) — O(2p) — Fe^{5+}(d^3) \ , \quad (7)$$

really exist.

Another antiferromagnetic coupling,

$$(S_{3/2})\uparrow — \downarrow(S_{3/2}) \ , \quad Fe^{5+}(d^3) — O(2p) — Fe^{5+}(d^3) \ , \quad (8)$$

is absent in the system, as its superexchange energy is smaller than the two previous ones [15], resulting in the observed magnetic structure.

This magnetic structure of the ideal "$Sr_2LaFe_3O_9$" phase can be described as that each Fe^{5+} ion with spin S=3/2 is ferromagnetically coupled with six Fe^{3+} ions with spin S=5/2, while each Fe^{3+} ion is antiferromagnetically coupled with three other Fe^{3+} ions as well as ferromagnetically coupled with three Fe^{5+} ions. As a result, the ordered spin and charge densities of iron ions vary periodically along pseudo cubic directions of $[100]_C$, $[010]_C$ and $[001]_C$ (note that they are the directions of superexchange pathway) in the sequence of :

$$\text{Charge state :} \qquad 3+\ 5+\ 3+\ 3+\ 5+\ 3+\ \cdots, \qquad \textit{(9)}$$

$$\text{Spin state :} \qquad \uparrow\ \uparrow\ \uparrow\ \downarrow\ \downarrow\ \downarrow\ \cdots, \qquad \textit{(10)}$$

$$\text{Sublattices :} \qquad A_\alpha\ B_\alpha\ C_\alpha\ D_\beta\ E_\beta\ F_\beta\ \cdots. \qquad \textit{(11)}$$

Here 3+ and 5+ are the charge states of irons with high spin d^5 ($S_{5/2}$) and d^3 ($S_{3/2}$) configurations, respectively; the arrows show the relative orientation and size of the iron spins; and A_α , B_α , C_α , D_β , E_β and F_β represent six sublattices of the magnetic structure shown in Fig 12, with subscripts α and β indicating the two antiparallel spin directions. Due to the lattice translations of a_H and b_H , layers with constant iron spin and charge densities are formed which, perpendicular to c_H , have the same sequences of spin and charge orderings as *(9)* and *(10)* along c_H direction.

It is noted that this magnetic structure leads to a site ratio $[Fe^{3+}]:[Fe^{5+}] = 2:1$, which is in complete agreement with the charge disproportionation model presented in V-2-2.

In the notation of the sublattices, the magnetic structure can also be described as that each set of sublattice is coupled, ferromagnetically or antiferromagnetically as shown in *(11)*, with two nearest-neighboring sets of sublattices along pseudo cubic edges with an interaction distance of $a_C \approx 3.877$ Å (short-range nature of superexchange interactions). Since each sublattice with α-spin (say, B_α) can find a sublattice with antiparallel β-spin of the same size (E_β, in this case), the $Sr_2LaFe_3O_9$ compound is macroscopically an antiferromagnet. All possible magnetic couplings between the six sublattices are tabulated in Table 7.

V-3-3. Conclusions.

The $Sr_2LaFe_3O_{8.95}$ phase is an antiferromagnet with $T_N = 196$ K. It shows an abrupt magnetic transition which is associated with a charge disproportionation.

In the paramagnetic region, the Curie-Weiss behavior is observed for T > 280 K, with an observed iron moment of $\mu_{Fe} = 5.46\ \mu_B$ which is a little higher than the spin-only value of $\mu_{Fe}^{spin} = 5.30\ \mu_B$; but this behavior is deviated at T = 200 ~ 280 K due

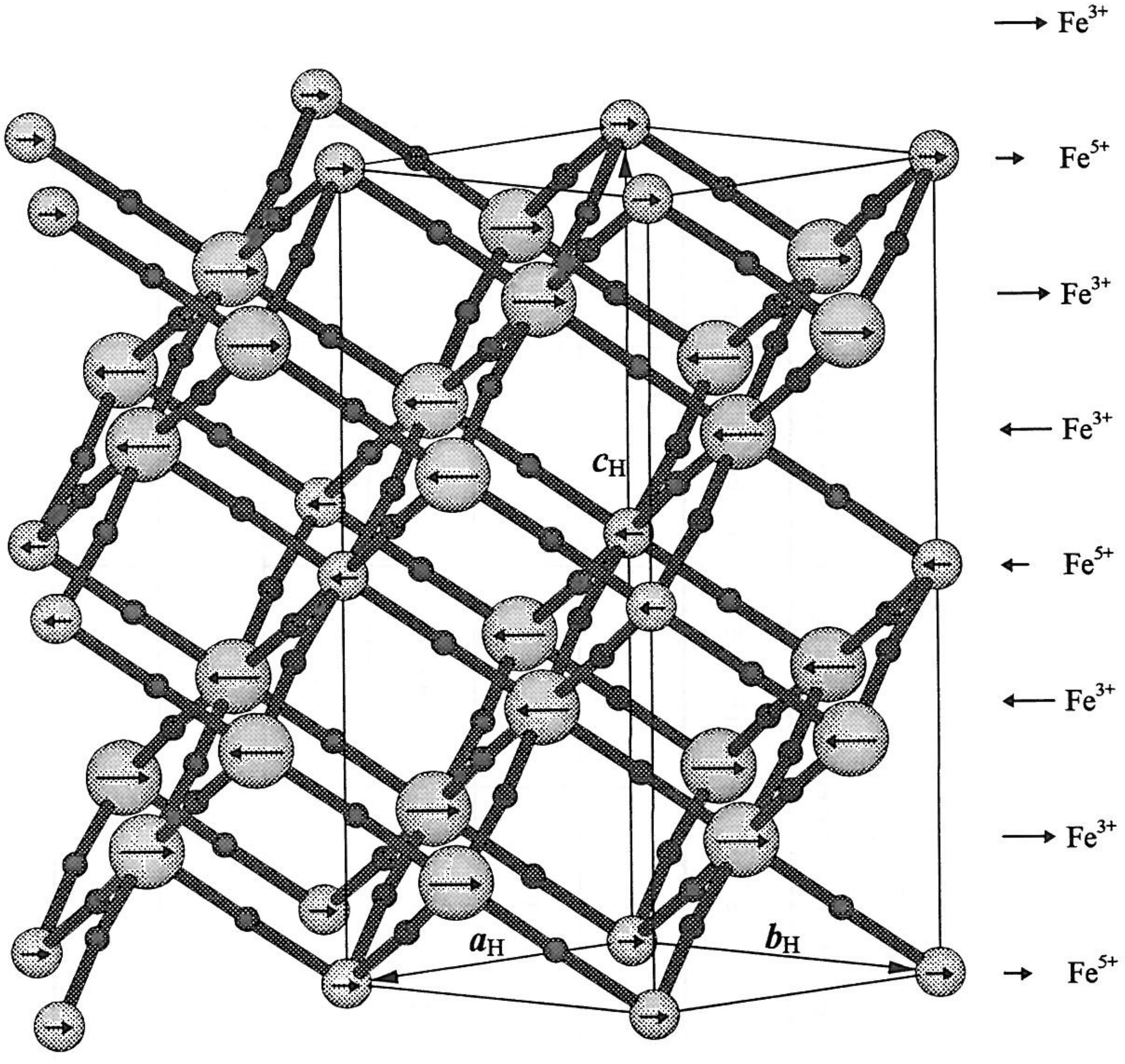

Figure 12 The Crystal and Magnetic Structure of "$Sr_2LaFe_3O_9$" [1].

The largest balls in the figure represent Fe^{3+} ions and the medium ones the Fe^{5+} ions, with the arrows indicating the size and orientation of their spins lying in xy-plane; the smallest balls are the oxygen atoms. The $2Sr^{2+}$:La^{3+} cations which are disorderly located in the cubic centers are not shown in the figure for clarity. The space group for the crystal structure is $R\bar{3}c$, and that for the spin structure is $P\bar{3}m1$. The unit cells (in hexagonal axes) of the two structures are commensurate, as shown in the figure, but the unit cell of the crystal structure is a triple one, while that of the magnetic structure is a primitive trigonal one, for the rhombohedral translations are absent in the magnetic structure. Each unit cell contains two formula units of $Sr_2LaFe_3O_9$ (Z=2), hence six iron ions, which form six magnetic sublattices below the ordering temperature. The spin and charge densities of the iron ions located within the same layers perpendicular to c_H are constant due to $\boldsymbol{a}_H$ and $\boldsymbol{b}_H$ translations, but they vary periodically from layer to layer along c_H direction in the same sequence as that of the rows along $\boldsymbol{a}_C$ directions of the pseudo cubic cell, with a period c_H shorter than that along $\boldsymbol{a}_C$ directions which is $6a_C \approx \sqrt{3}\cdot c_H$.

Table 7

The Magnetic Couplings Between the Six Sublattices in the Structure of "$Sr_2LaFe_3O_9$"

Sublattices	A_α (Fe^{3+}, d^5)	B_α (Fe^{5+}, d^3)	C_α (Fe^{3+}, d^5)	D_β (Fe^{3+}, d^5)	E_β (Fe^{5+}, d^3)	F_β (Fe^{3+}, d^5)
A_α (Fe^{3+}, d^5)	/	F	/	/	/	AF
B_α (Fe^{5+}, d^3)	F	/	F	/	/	/
C_α (Fe^{3+}, d^5)	/	F	/	AF	/	/
D_β (Fe^{3+}, d^5)	/	/	AF	/	F	/
E_β (Fe^{5+}, d^3)	/	/	/	F	/	F
F_β (Fe^{3+}, d^5)	AF	/	/	/	F	/
Note	F: Ferromagnetic Coupling; AF: Antiferromagnetic Coupling.					

to short-range spin ordering. The experimental observations lead to following conclusions:

(a) The iron *d*-electrons are in localized high-spin states . The closeness between the observed and spin-only moments reflects the quenching of the orbital moment of the ^5E_g (Fe^{4+}) state by the chemical environment as theoretically predicted.

(b) The susceptibility vs. field dependence for $H < \sim3000$ Oe reveals some contribution from spin-polarization effect of conduction electrons.

(c) The fact that the observed iron moment is a little higher than the spin-only value could be attributed to the spin polarization effect, the influence of non-oxidized domains and/or to the limitation of the fitting temperature range.

In the antiferromagnetic region, the increase of the susceptibility with magnetic field (for $H > \sim7000$ Oe) is explained by the effect of anisotropy.

The low temperature magnetic structure of $Sr_2LaFe_3O_{8.95}$ phase is described based on the structural model previously reported for a phase of very close composition.

Theoretical thermal dependencies of the magnetization, the susceptibility and specific heat are reported in Appendix I.

V-4. Electron Transport Properties.

V-4-1. Theoretical Models.

- Electronic Conduction in Localized States

The electronic conductivity of any solid is given by

$$\sigma = \sigma_e + \sigma_h = n_e \cdot e \cdot \mu_e + n_h \cdot e \cdot \mu_h\,, \qquad (1)$$

where e is the absolute value of the electron charge; n_e, n_h are the concentrations of the charge carriers (electrons and holes, respectively); μ_e, μ_h the corresponding carrier mobilities defined as their average drift velocity in an electric field of unit strength. Hence σ_e and σ_h are the conductivity contributions due to each kind of carriers. Often the conduction may be predominated by electrons or by holes.

An *Arrhenius* behavior, $\sigma = \sigma_0 \exp(-E_\sigma/k_B\mathrm{T})$, *(2)*

is frequently observed for the temperature dependence of the electrical conductivity (here E_σ is the activation energy). For example, it applies to conventional band conduction when carrier concentration is thermally activated while the mobility decreases slightly with temperature. This behavior can also arise from *small polaron hopping* involving thermally activated mobility when the carrier concentration is temperature-independent. In the latter case, electronic conduction originates in diffusion of carriers in localized states.

A small polaron is formed when a charge carrier is trapped at a site by a local lattice distortion that it causes. The carrier and the distortion can move as a whole, and at temperatures of $\mathrm{T} > \frac{\Theta_D}{2}$ (here Θ_D is the Debye temperature) the activated hopping mobility is given by [16]

$$\mu = \frac{1}{6}(ea^2\omega/k_B\mathrm{T})\exp(-E_\mu/k_B\mathrm{T})\,, \qquad (3)$$

where E_μ is the activation energy for the self-trapped carrier to hop to a neighboring site ; a is the distance between atoms and ω the attempt-to-escape frequency. It describes the adiabatic case in which the carrier goes backwards and forwards several times during the period of excitation, *i.e.* when the two neighboring sites are of the same energy level. At temperatures of $\mathrm{T} < \frac{\Theta_D}{2}$, however, the zero-point energy $\frac{\hbar\omega}{2}$ takes the place of the thermal energy $k_B\mathrm{T}$ in *(3)* and the process is no longer activated.

When electron states are localized at the Fermi level with a finite density of states and there exists some dispersion of energy in the vicinity of the Fermi level, variable range hopping conduction may occur at low temperatures, giving rise to the conductivity of the form

$$\sigma = A\exp[-(T_0/T)^{1/\nu}] , \qquad (4)$$

where ν may be 2 or 4 (for three-dimensional process), depending whether Coulomb interaction is important or not [17 - 20].

- The Thermoelectric Power (Seebeck Coefficient)

The Seebeck coefficient, α, is defined as the open-circuit potential difference (ΔV) per unit temperature difference (ΔT) across a sample in the limit of $\Delta T \to 0$:

$$\alpha = -(\frac{\Delta V}{\Delta T})_{\Delta T \to 0} . \qquad (5)$$

Generally, the sign of α corresponds to the sign of carrier charges [21].

By *Onsager* and *Kelvin* relations [22], the Seebeck coefficient *(5)* can be expressed as

$$\alpha = -\frac{1}{e}(\overline{S} + \frac{Q^*}{T}) , \qquad (6)$$

where $\overline{S}$ is the particle entropy and Q^* is the heat transferred by the particle [23].

For a hopping conduction (*e.g.* small polaron hopping) involving fixed concentrations of localized electron carriers and of available hopping sites (denoted by n and N, respectively), when the entropy is mainly determined by the configurational one and the transferred heat (Q^*) is negligible with respect to the thermal energy k_BT [23, 24], or k_BT exceeds the spread of carrier energy levels [25, 26], or, in other words, in high temperature limit (T → ∞) [27], the Seebeck coefficient is temperature-independent and takes the form of Heikes formula [28] :

$$\alpha \approx -\frac{S^*_{config}}{e} = -\frac{k_B}{e}\ln(\frac{1-c}{c}) , \qquad (7)$$

where $c = n/N$. Note that the configurational entropy per carrier, $S^*_{config} = \frac{\partial S_{config}}{\partial n} = k_B \ln(\frac{1-c}{c})$, corresponds to the case where only one hopping electron is permitted on a given site. The sign of the Seebeck coefficient represented by *(7)* determines the type of conduction: if $n < N/2$ then $\alpha < 0$, the conduction is due to electrons; while for $n > N/2$, $\alpha > 0$, it is caused by holes. Further, if c varies, the magnitude of the Seebeck coefficient increases with decreasing c, so that the maximum $|\alpha|$ occurs where c is minimized.

For amorphous non-degenerate semiconductors, the Seebeck coefficient is given by [29, 30]

$$\alpha \; = \; \pm\frac{k_B}{e}(\frac{|E_C - E_F|}{k_B T} + A) \; = \; \pm\frac{k_B}{e}(\frac{E_\alpha}{k_B T} + A) \, , \qquad \textit{(8)}$$

where E_C is the mobility edge energy, $E_\alpha = |E_C - E_F|$, and A is a dimensionless constant which depends on the details of the scattering mechanism [31] and is not easy to estimate. In the n-type conduction $\alpha < 0$; if p-type conduction dominates $\alpha > 0$.

If two kinds of charge carriers (electrons and holes) are simultaneously present, the net Seebeck coefficient [32] is : $\alpha = \dfrac{\alpha_e\sigma_e + \alpha_h\sigma_h}{\sigma_e + \sigma_h}$.

V-4-2. The Small Polaron Hopping at High Temperatures (T > 195 K)

In Fig. 13, the logarithm of conductivity, logσ, and the reduced Seebeck coefficient, $\alpha' = \dfrac{\alpha}{(k_B/e)\ln 10}$, of $Sr_2LaFe_3O_{8.95}$ are plotted versus $10^3/T$ (in the inset logσ is given *vs.* $T^{-1/4}$).

The following general features can be noticed :

- In the measured temperature range of 58 to 290 K, the conductivity is low (*e.g.* $\sigma_{290K} = 1.41\times10^{-5}\ \Omega^{-1}cm^{-1}$) and increases with rising temperature, characterizing a semiconducting behavior.
- The Seebeck coefficient is negative, indicating that the dominant carriers are electrons.
- The Seebeck coefficient and the conductivity have remarkable changes in their behaviors at about 180 K and 195 K, the latter temperature coinciding with the critical temperature of the magnetic transition (*cf.* V-3).

In the following part of this section, the temperature range of T > 195K is concerned, where the iron ions are in paramagnetic state.

- Evidence for the Small Polaron Formation

For T > 195K, the conductivity is thermally activated while the Seebeck coefficient is temperature-independent : it is typical of a small polaron conduction involving a temperature-independent carrier concentration (*cf.* formula ***(7)***), and can be assigned to localized e_g-electron hopping between high-spin iron sites :

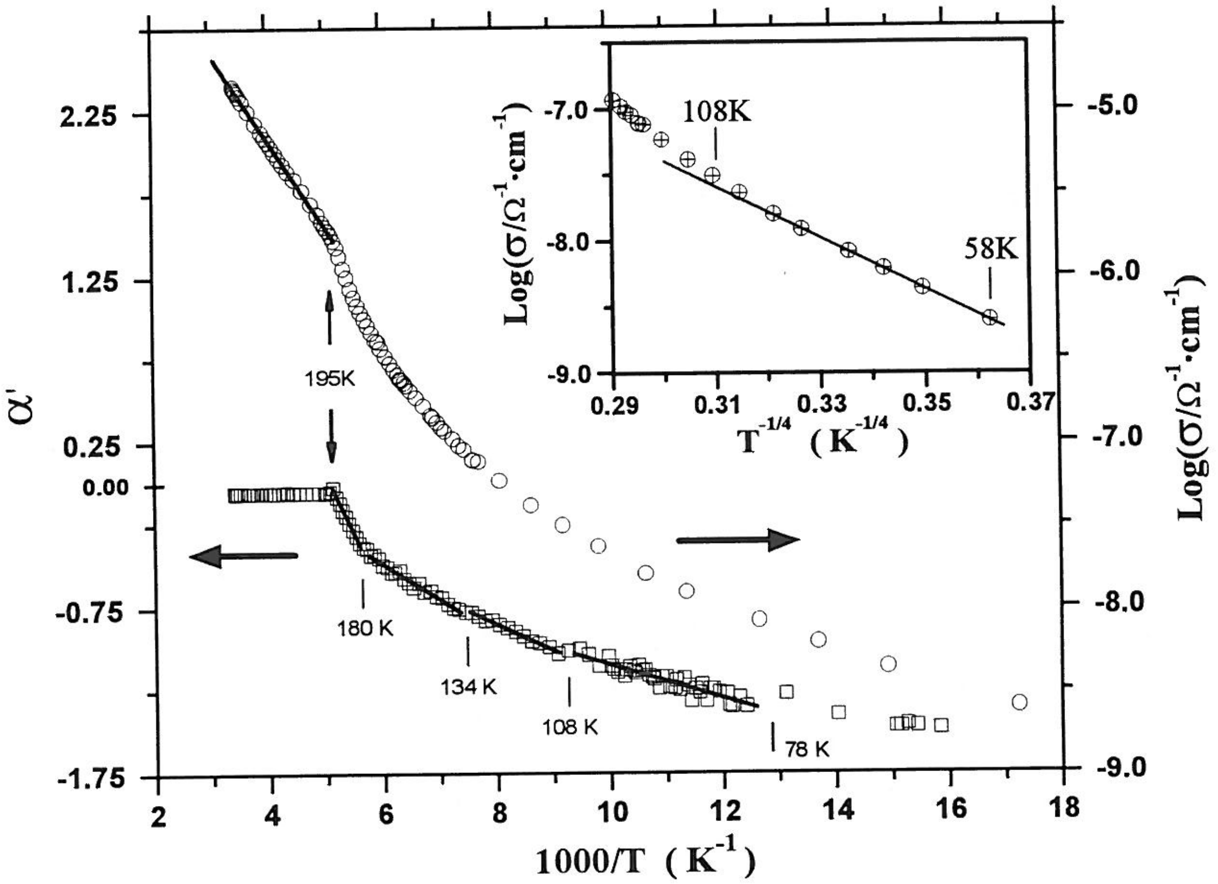

Figure 13

Temperature dependencies of logarithm of the conductivity and of the reduced Seebeck coefficient, $\alpha' = \frac{\alpha}{(k_B/e)\ln 10}$, for $Sr_2LaFe_3O_{8.95}$. Note that the spacings of $\log(\sigma)$ and α' axes are the same, so that the temperature dependencies can be directly compared in the figure. The inset shows that the conductivity obeys the Mott $T^{-1/4}$ law for temperatures of 58 to about 100 K.

$$\underset{\mathrm{Fe}^{3+}}{(\mathrm{Fe}^{4+}+e^-)} + \mathrm{Fe}^{4+} \longleftrightarrow \mathrm{Fe}^{4+} + \underset{\mathrm{Fe}^{3+}}{(\mathrm{Fe}^{4+}+e^-)} \quad . \qquad (9)$$

According to the discussion given in V-2, for T > 195 K, the nominal composition of the perovskite is $\mathrm{Sr_2LaFe^{3+}_{1.10}Fe^{4+}_{1.90}O_{8.95}}$, with $[\mathrm{Fe^{3+}}]/[\mathrm{Fe^{4+}}] = 1.10/1.90$. Since all the iron sites are equivalent for the hopping process, the constant site ratio $c = \frac{1.10}{3} = 0.367$.

Therefore, the activated temperature dependence of the conductivity arises from the dependence of the hopping mobility as described by equation *(3)*, that is,

$$\sigma = n_e \cdot e \cdot \mu_e \propto \frac{1}{\mathrm{T}} \exp(-E_\mu / k_B \mathrm{T}\ ).$$

The activation energy calculated from the slope of log(σT) vs. $10^3/\mathrm{T}$ plot is $E_\mu = 0.13$ eV.

The applicability of equation *(3)* in the case of $\mathrm{Sr_2LaFe_3O_{8.95}}$ for at least T > 200 K suggests that the Debye temperature $\Theta_D < 400$ K.

As can be seen from Fig. 14, a good linear behavior in log(σT) against $10^3/\mathrm{T}$ plot occurs for T > 240 K, and, at temperatures between 240 and 195 K, the conductivity is slightly higher compared with the extension of the linear fit. It may be a manifestation of the short-range ferromagnetic ordering of iron spins in the temperatures near $\mathrm{T_N}$, since parallelly oriented spins surrounding a site of $\mathrm{Fe^{3+}}$ (= $\mathrm{Fe^{4+}} + e^-$) will make the localized electron hop easierly.

- *Contributions to the Seebeck Coefficient*

With the ratio $c = \frac{n}{N} = 0.367$, the Seebeck coefficient calculated using formula *(7)* is α = - 47 μV/K, being considerably lower than the observed average value $\overline{\alpha} = -11$ μV/K (for T > 195 K). On the other hand, the ratio obtained from $\overline{\alpha}$ using *(7)* is $c' \approx 0.47$, which corresponds to an oxygen content significantly lower than 8.95/*f.u.*. These facts cannot be explained by experimental errors, suggesting that some other effects must exist.

In fact, terms due to contributions of spin and orbital degeneracy, spin polarization as well as lattice entropy may be added into equation *(7)*, so that

$$\alpha = -\frac{k_B}{e}\{\ln[\beta_{spin} \cdot \beta_{orbit} \cdot (\frac{1-c}{c})] + \frac{S_{polar}}{k_B} + \frac{S_{lat}}{k_B}\} \ . \qquad (10)$$

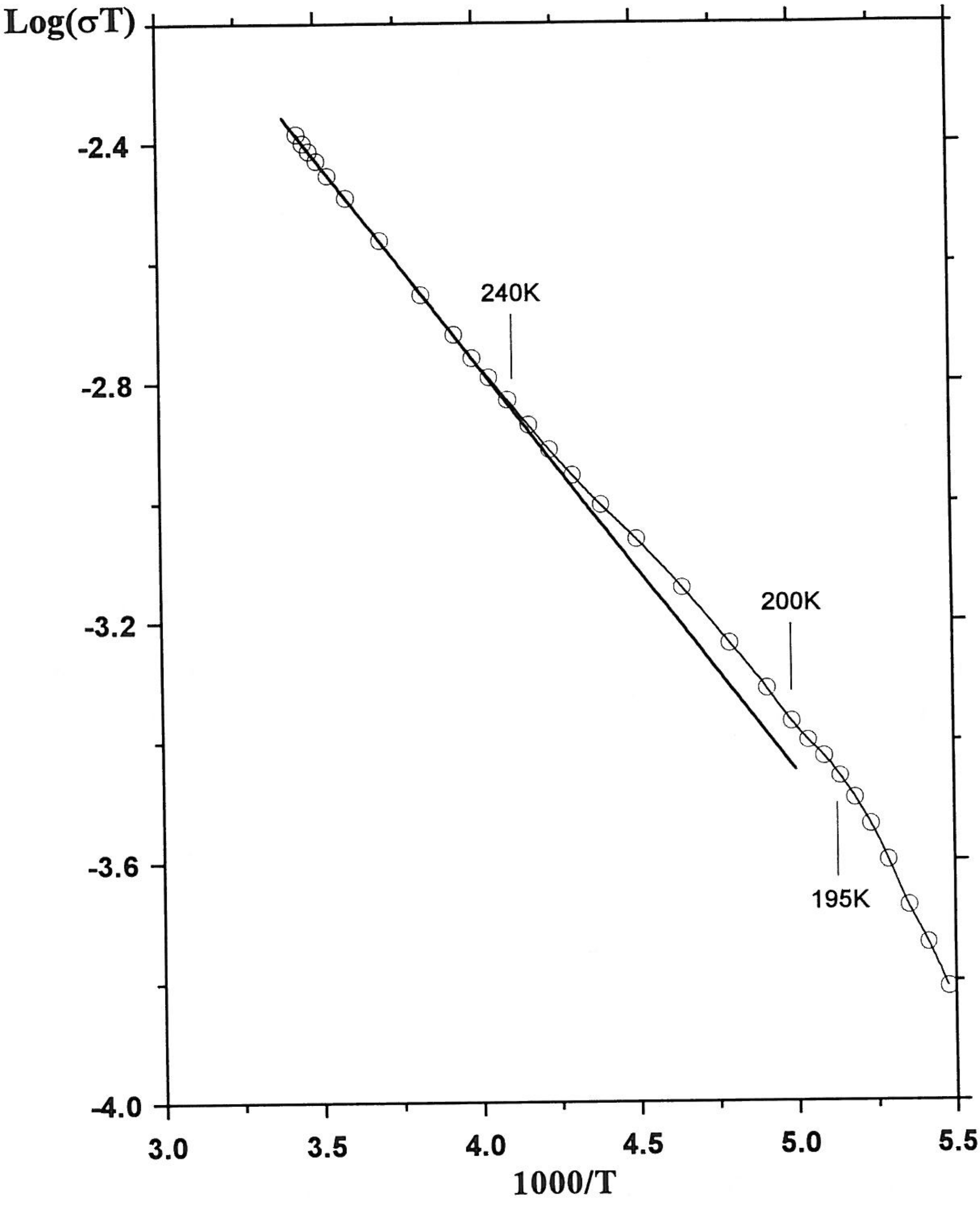

Figure 14

A close view of log(σT) versus $10^3/T$ plot of $Sr_2LaFe_3O_{8.95}$ in the temperature range from 180 to 300 K. A good linear relation exists only for T > 240 K.

The parameters present in *(10)* are described as follows:

(i) In the present case, the spin degeneracy factor $\beta_{spin} = \frac{2S+1}{2S_0+1} = \frac{6}{5}$, where S and S_0 denote the net spin of a iron site with and without the presence of the carrier spin, respectively [33 - 35]; and $\beta_{orbit} = \frac{1}{2}$ is the orbital degeneracy factor [31], which is obtained by analogy with the consideration of Marsh *et al.* [36] and by assuming that the energy difference (if any) between two e_g-orbitals is negligible since the site symmetry is (or quite close to) O_h . Note that two configurations of e_g^2 (with the carrier) and e_g^1 (without the carrier) are involved.

(ii) The term arising from lattice vibrational entropy change S_{lat} (associated with the ions surrounding a carrier on a given site) was previously estimated to be $\frac{S_{lat}}{e} \approx$ 10 (μV/K) [24, 31, 37].

(iii) Moreover, for small polarons in magnetic semiconductors, over a large temperature range above the magnetic transition temperature, there exists a term $\frac{S_{polar}}{k_B}$ due to spin-polarization effect according to Liu and Emin [38]. This term originates from magnetic exchange interaction of the hopping electron with adjacent sites, and contributes positively to the Seebeck coefficient since the corresponding entropy change $S_{polar} < 0$.

(*Note*: For a simple-cubic lattice with a spin $s = 1/2$, it was estimated by Liu and Emin that $S_{polar} = -5J^2/k_B T^2$, with J being the exchange integral.)

Including all the above effects, the Seebeck coefficient for the present system is then :

$$\alpha = \alpha_0 + \alpha_{polar} \approx -13 + \frac{|S_{polar}|}{e} \ (\mu V/K), \tag{11}$$

where $\alpha_0 \approx -13$ (μV/K) accounts for the contributions of spin and orbital degeneracies as well as for the configurational and vibrational entropy contributions; $\alpha_{polar} = \frac{|S_{polar}|}{e}$ is due to the spin-polarization effect. According to the theoretical treatment of Liu and Emin, the value of α_{polar} is expected to be small (see also below), therefore the observed Seebeck coefficient, $\bar{\alpha} = -11$ μV/K (averaged value for T > 195K), can be well accounted for by the combined contributions presented above.

In the above discussion, we have taken the Seebeck coefficient for T > 195 K as being temperature-independent. However, a closer examination (Fig. 15) reveals that it decreases slightly with rising temperature.

If we assume that, following Liu and Emin, the Seebeck coefficient due to the spin-polarization takes the form of

$$\alpha_{polar} = \frac{P}{\mathrm{T}^2} \tag{12}$$

and that the term $\frac{S_{lat}}{e}$ (*cf.* equation *(10)*) involved in α_0 is independent of the temperature, such a decrease in the observed Seebeck coefficient could be attributed to the spin-polarization effect.

In fact, according to *(11)* and *(12)*, a linear fit of α vs. $10^4/\mathrm{T}^2$ plot (Fig. 15) in the temperature range of about 200 to 293 K gives two constants of α_0^{fit} = - 12 (μV/K) and $P = 4.95 \times 10^4$ (μV·K). The former is in good agreement with the theoretical value of $\alpha_0 \approx$ -13 (μV/K); from the latter, the spin-polarization contribution to the Seebeck coefficient in this temperature range is found to be $\alpha_{polar} \approx 1$ (μV/K), which is small and decreases with rising temperature.

Further, we would like to point out that:

(a) The agreement between the calculated and observed Seebeck coefficient values in turn suggests that the estimate of the lattice vibration contribution, *i.e.* $\frac{S_{lat}}{e} \approx 10$ (μV/K), is acceptable.

(b) It is possible to estimate, from the observed constant P, the exchange integral J involved in the spin-polarization interaction in present case after an appropriate modification of the theoretical treatment of Liu and Emin (for the case considered by Liu and Emin, $P = \frac{\gamma \cdot J^2}{e \cdot k_B}$ with $\gamma = 5$).

(c) A cusp in α is observed in the vicinity of the critical temperature (Fig. 15). We think it may be related, to some extent, to the critical behavior of $-\frac{k_B}{e}\ln(\beta_{spin})$ term in formula *(10)*, because the spin degeneracy factor β_{spin} would change with rising temperature from 1 to $\frac{6}{5}$ around the critical temperature. In this sense, the critical temperature indicated by the Seebeck coefficient is between 195 K and 199 K. The terms of $-\frac{k_B}{e}\ln(\beta_{orbit})$ and $-\frac{S_{lat}}{e}$ may also vary during the transition, but their behaviors are not known.

V-4-3. Electronic Conduction at Low Temperatures (T ≤ 195 K)

Now the temperature range of T ≤ 195K is concerned, where both the spin and charge states of the irons in $Sr_2LaFe_3O_{8.95}$ are ordered so that the sample is an antiferromagnet with mixed valence states of Fe^{3+} and Fe^{5+} (*cf.* V-2 and V-3).

- *Observations of the Seebeck Coefficient and the Conductivity*

For T ≤ 195 K, the reduced Seebeck coefficient ($\alpha' = \frac{\alpha}{(k_B/e)\ln 10}$) generally shows linear dependencies on 1/T (Fig. 13) like the activated form of ***(8)***, but several kinks are present in the curve (as marked in the figure) involving changes in the slope, with the most remarkable ones being at T ≈ 180 K and 195 K.

The low-temperature conductivity of $Sr_2LaFe_3O_{8.95}$ deviates from the Arrhenius behavior of ***(2)***. At about 60 to 100 K, it can be appropriately described by equation ***(4)*** with ν chosen to be 4 (inset of Fig. 13).

At temperatures between 100 and 195 K, however, no single mechanism can account for the conductivity behavior to our knowledge.

- *Discussions*

(a) About the $T^{-1/4}$ behavior of the conductivity

The $\exp[-(T_0/T)^{1/4}]$ behavior of the conductivity at about 60 ~100 K may be related to variable-range hopping (VRH) (*cf.* equation ***(4)***). The VRH conduction involves, at low temperatures, hopping over larger distances than between nearest neighbors.

Below the ordering temperature, the charge disproportionation (*cf.* V-2 and below) occurs in the present system. It indicates that the energy level of the nominally empty e_g-orbitals of Fe^{5+} states is higher than the e_g-levels of the Fe^{3+} states as schematically represented in Fig.16.

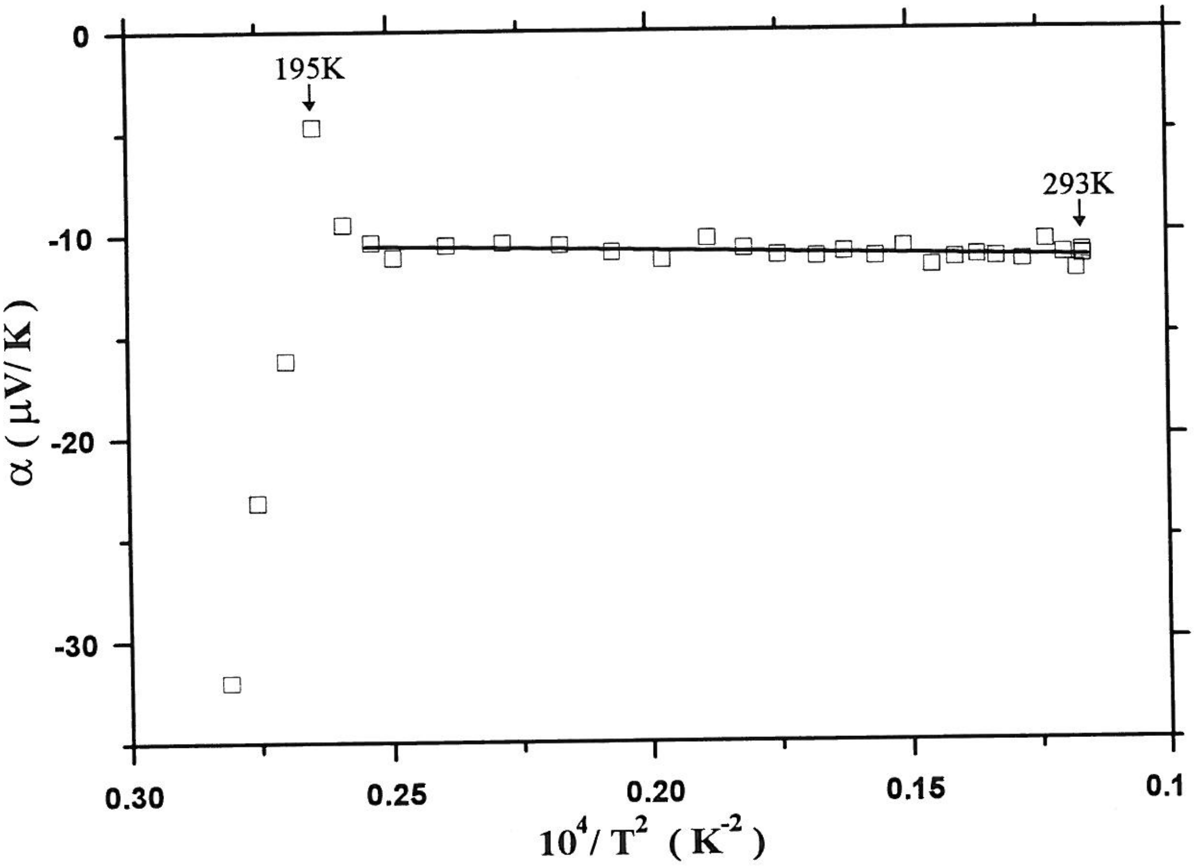

Figure 15

The Seebeck coefficient α plotted as a function of $10^4/T^2$ for $Sr_2LaFe_3O_{8.95}$.
Its slight decrease with rising temperature is attributed to spin polarization effect.

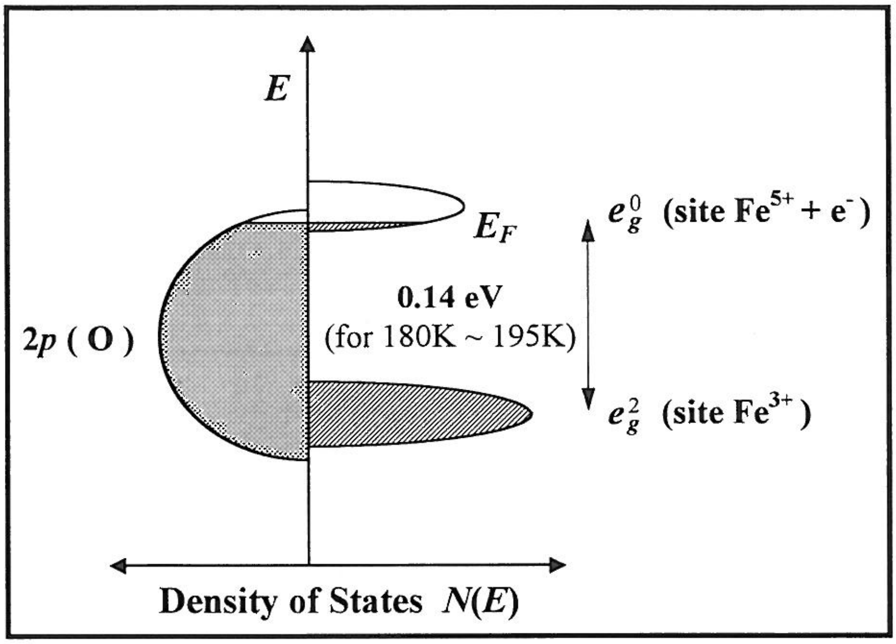

Figure 16

Schematic representation of some energy levels involved in $Sr_2LaFe_3O_{8.95}$ for about T < 195K. The activation energy for temperatures between 180 and 195 K is indicated.

According to V-2-2, the iron charges are nonintegral, and the *d*-electron number of Fe^{5+} is somewhat greater than 3, *i.e.* its e_g-level is not quite empty. Such an e_g-electron density of Fe^{5+} states could arise from a small charge transfer (for instance, from oxygen 2p-orbitals to iron Fe^{5+} e_g-orbitals) due to some covalence (which is responsible for the superexchange interactions). As a consequence, the Fermi level is pinned at the bottom of the e_g-band as shown in the figure, giving rise to the $T^{-1/4}$ dependence of the conductivity between 60 ~ 100 K.

The Seebeck coefficient for VRH conduction was predicted to have a temperature dependence as $\alpha \propto T^{1/2}$, ***(13)***

when the density of states (DOS) is a slowly varying function of energy [21, 39].

However, as pointed out by Zvyagin [22], for many semiconductors in the VRH regime the energy layer for the conduction is quite large and the slow variation of the DOS in the conduction layer seems to be rather an exception. One might expect large variations of the DOS and a weaker temperature dependence of the Seebeck coefficient than that given by ***(13)***.

In the present case, the Seebeck coefficient is observed to be proportional to 1/T in the region where the conductivity obeys the Mott law, and this behavior exists up to T = 195 K (Fig. 13). The energies of E_α' calculated from the slopes of α against 1/T plot for various temperature ranges are given in Table 8.

When VRH conduction is the appropriate model, the mean hopping distance $\overline{R}_{hop}(T)$, the mean hopping energy $\bar{\varepsilon}_{hop}(T)$ and the Mott characteristic temperature T_0 (which can be obtained by fitting the experimental data) are given as follows [40, 41]:

$$\overline{R}_{hop}(T) \approx \frac{3}{8} \cdot a \cdot (T_0/T)^{1/4}, \qquad \textit{(14a)}$$

$$\bar{\varepsilon}_{hop}(T) \approx \frac{1}{4} \cdot k_B \cdot T^{3/4} \cdot T_0^{\ 1/4}, \qquad \textit{(14b)}$$

$$T_0 \approx 18/[k_B \cdot N(E_F) \cdot a^3]. \qquad \textit{(14c)}$$

Here, $N(E_F)$ is the density of states in the vicinity of the Fermi level, a is the localization length which is chosen in the calculation to be 5 Å (approximately the distance between nearest-neighboring Fe^{5+} sites). Listed in Table 8 are quantities calculated using above equations as well as activation energies calculated from the Seebeck coefficient.

The small hopping energy of $\bar{\varepsilon}_{hop}$ (~ 10^{-2} eV) suggests that the electrons hop between Fe^{5+} sites with parallel spins. As a consequence, the spin ordering (*cf.* Fig. 12) may be reinforced by such a hopping process due to spin polarization effect (*cf.* V-6-3 for further discussions about this effect).

Based on the magnetic structure given in V-3-3 (Fig. 12), the Fe^{5+} sites form alternative planes with parallel and antiparallel spins, and the distance between planes of parallel spins is $c_H \approx 13.4$Å (one of the cell dimensions). Since the mean hopping distance $\overline{R}_{hop}(T)$ at low temperatures is larger than c_H (*cf.* Table 8), the electron hopping *between* the planes with parallel spin orientation can be present, but the probability for hopping *within* such planes is expected to be greater. That is, although the hopping process is not homogeneous for all directions, it is all the same a three-dimensional one. Correspondingly, the best linear dependence of the conductivity on $T^{-1/\nu}$ is observed when ν is chosen to be 4, since $\nu = d + 1$ with d representing the dimensionality [41] and the value of $\nu = 4$ corresponds to a three-dimensional process (d = 3).

(b) The charge disproportionation : evidence from the Seebeck coefficient.

As previously mentioned, the Seebeck coefficient exhibits sharp changes at about 180 and 195 K (Fig. 13): when temperature increases up to about 180 K, the activation energy changes from 0.04 eV to 0.14 eV (*cf.* Table 8) as reflected by the changes in the slope; while at about T>195 K, the activated behavior changes to the non-activated one. It is worth mentioning that, at about 180 K, the magnetic susceptibility (*cf.* Fig. 9 of V-3) and the specific heat (*cf.* V-5) begin to increase anomalously, and a small quantity of the paramagnetic phase coexists with the major antiferromagnetic phase according to Mössbauer data (*cf.* V-2). These observations indicate that the electronic phase transition (from antiferromagnetic mixed-valence state into paramagnetic averaged-valence) sets in at about T = 180 K as temperature rises.

Thus, the activation energy $E_\alpha' = 0.14\ eV$, obtained from the Seebeck coefficient for T = 180 ~ 195 K, can be attributed to the activation of the e_g-electrons of the Fe^{3+} states to the e_g-levels of the Fe^{5+} states, as shown schematically in Fig. 16. This process results in Fe^{4+} states which do not involve strong spin interaction so that tend to disordered spin states. On the other hand, such an electron activation is also consistent with the observations that the conductivity σ (not shown) and the carrier concentration (see below) begin to increase more rapidly with the temperature for T > 180 K than at lower temperatures (but for T > 195 K, the carrier concentration becomes constant). These facts can be readily explained by thermodynamics : an energy-increased process necessarily involves an increase in the entropy.

Note that the above-mentioned electron activation is just the reverse process of the charge disproportionation associated with decreasing temperature (*cf.* V-2-2). Therefore, T ≈ 180 K is the lower temperature limit of the charge disproportionation process (*i.e.* it is the temperature below which the charge disproportionation is almost complete).

On the other hand, it is clear that the temperature T ≈ 195 K is the border between the small polaron hopping with constant carrier number (for T > 195 K) and the conduction with activated carrier concentration (for T < 195 K). In other words, T ≈ 195 K is the upper temperature limit of the disproportionation process, since the charge disproportionation involves a carrier concentration which decreases with lowering temperature (as it is revealed by the temperature dependence of the Seebeck coefficient, see below).

In conclusion, as temperature lowers, the charge disproportionation occurs simultaneously with the magnetic transition at about $T_N = 196$ K (*cf.* V-3 and V-5), and it is almost complete at about 180 K. These results are in agreement with the Mössbauer data and magnetic measurements, as well as with the nature of the electronic phase transition (*cf.* V-6).

Table 8

Some Parameters Obtained From the Seebeck Coefficient and the Conductivity

Temperature (K)	60~100	100~180	180~195	195~300
Energies (E_α') Calculated From the Thermopower [a] **(eV)**	0.015~0.02	0.03~0.04	0.14	/
Energies Calculated From the Conductivity (eV)	0.02~0.03 $(\bar{\varepsilon}_{hop})$ [b]	/	/	0.13 (E_μ) [c]
T_0 (K) (for VRH)	3.97×10^6	/	/	/
$\overline{R}_{hop}(T)$ (Å) (for VRH) (taking a=5Å)	26 ~ 30	/	/	/
$N(E_F)$ ($eV^{-1}\cdot cm^{-3}$) (for VRH) (taking a=5Å)	4.2×10^{20}	/	/	/

a. Calculated from the slopes of α vs. $10^3/T$ plot ; ***b.*** Calculated using ***(14b)***;
c. Calculated according to *(3)*.

(c) The temperature dependence of the carrier concentration and its relation with the Seebeck coefficient.

Below the transition temperature, the temperature dependence of the Seebeck coefficient $\alpha(T)$ may be assumed to be mainly due to the dependence of the ratio $c(T)$, so that equation *(10)* can be rewritten as :

$$\alpha(T) = -\frac{k_B}{e}\ln[\frac{1-c(T)}{c(T)}] + D\,, \qquad (15)$$

with D approximated to a constant. From *(15)*, we deduce :

$$c(T) = \frac{1}{1+M\cdot e^{\frac{-\alpha(T)}{(k_B/e)}}}\,, \qquad (16)$$

which relates the ratio $c(T)$ to the Seebeck coefficient $\alpha(T)$ (here $M = e^{\frac{D}{(k_B/e)}}$).

On the other hand, the site ratio may be expressed as $c(T) = \frac{n(T)}{N(T)} = \frac{n_i+\Delta n(T)}{N_i+\Delta n(T)}$, with n_i and N_i being the carrier and site concentrations at a certain temperature T_i, respectively, and $\Delta n(T)$ the concentration increment from T_i to T (let $|\Delta n(T)| < n_i$). Thus, the carrier concentration takes the form of :

$$n(T) = (N_i - n_i)\,\frac{c(T)}{1 - c(T)}\,, \qquad (17a)$$

or

$$\log[n(T)] = \log[\frac{c(T)}{1 - c(T)}] + \log(N_i - n_i)\,. \qquad (17b)$$

Comparing *(15)* and *(17b)*, we see that the same temperature-dependent term, $\log[\frac{c(T)}{1-c(T)}]$, is present in both the expressions for the reduced Seebeck coefficient ($\alpha' = \frac{\alpha}{(k_B/e)\ln 10}$) and the logarithm of the carrier concentration.

Thus, assuming that the term D in formula *(15)* is (or almost) temperature-independent, ***the reduced Seebeck coefficient α' should show the same temperature dependence as the logarithm of carrier concentration (log[n(T)]), except for a difference in the constant terms. Therefore the temperature dependence of carrier mobility can be evaluated from the difference (if any) between the dependencies of α' and of the logarithm of conductivity (logσ).***

For the present case, it can be seen from Fig. 13 that the logarithm of the conductivity increases with temperature quikerly than the reduced Seebeck coefficient α'

(referring to $10^3/T$ axis). It is just a reflection of the contribution of the mobility in the conductivity in addition to the contribution of the carrier concentration.

In Fig. 17, $c(T)$ and $\frac{c(T)}{1-c(T)}$ (proportional to $n(T)$) are plotted against temperature according to *(16)* for $M = 1$ (corresponding to $D = 0$, the Heikes formula). For T < 195K, it is apparent that $\frac{dc(T)}{dT} > 0$ and $\frac{dn(T)}{dT} > 0$. Moreover, for reasonable D values (values of $D < 100$ μV/K are examined), we have found that $\frac{d^2c(T)}{dT^2}$ and $\frac{d^2n(T)}{dT^2}$ are still > 0. These conditions characterize upward-curved $c(T)$ and $n(T)$ *vs.* T curves, like the behaviors shown in Fig. 17 for $D = 0$. That is, the carrier concentration $n(T)$ increases more and more rapidly with temperature (for T < 195 K).

The deviation of the conductivity from the $T^{-1/4}$ behavior for T>100 K suggests that some other effects may have set in. For example, for reasons given above, the contribution of carrier concentration $n(T)$ to the temperature dependence of the conductivity may become important at these temperatures, which makes the conductivity to rise quickerly with the temperature.

In addition, we have noted that a slight kink occurs at about 108 K in the plot of α' against $10^3/T$, and the involved slope change corresponds to an energy increase of about 0.01eV. It may be an indication that some electrons trapped in lower-lying states begin to be activated and participate in the conduction, being consistent with the above discussions.

In conclusion, between 100 ~ 195 K, both the carrier concentration and the mobility have significant contributions to the temperature dependence of the conductivity, so that the conductivity behavior cannot be described only by the dependence of the mobility or of the carrier concentration.

V-4-4. Why the Electrons Are Localized ?

The structure of $Sr_2LaFe_3O_{8.95}$ is similar to that of metallic perovskite $SrFeO_3$, and, at about T>200K, the presence of the charge carriers in $Sr_2LaFe_3O_{8.95}$ (with a carrier concentration of $n_e = n_{Fe^{3+}} = 6.29\times10^{21}$ cm^{-3}) is determined by the chemical composition (*cf.* V-4-1) and does not involve charge transfer energies [57, 58].

However, the $Sr_2LaFe_3O_{8.95}$ phase does not show any metallic behavior even above the ordering temperature.

As it has been previously discussed, the electronic conduction in $Sr_2LaFe_3O_{8.95}$ in the considered temperature range can be appropriately described by localized electron models. The observed electron localization may originate from various mechanisms as will be discussed in the following.

- Anderson Localization

Anderson [42] pointed out that, in a random field, the electron wave function can become localized if V_0/B is larger than a critical value $(V_0/B)_{\text{crit}}$, here V_0 is the variation range of the random potential and B is the band width. Several authors gave for $(V_0/B)_{\text{crit}}$ a value of 1.5 for a coordination number $z = 6$ [43].

The electron localization in $Sr_2LaFe_3O_{8.95}$ may be mainly attributed to the random distribution of Sr^{2+} an La^{3+} ions (*cf.* V-1) as well as possible influence of the oxygen vacancies. These effects may result in a random field with a V_0 large enough with respect to the narrow e_g-band.

- Self-Trapping Due to Small Polaron Formation

A localized charge carrier will necessarily cause a local lattice distortion (especially in ionic lattices), and the so-formed energy well will in turn trap the carrier. On the other hand, due to strong electron-phonon interaction, the carrier can move by phonon-assisted hopping from one localized state to another. Such a hopping process is observed in $Sr_2LaFe_3O_{8.95}$ for T > 195 K, indicating the self-trapping effect in addition to the Anderson localization.

- Localization Associated with the Spin and Charge Orderings

When the temperature is lowered below 195 K, occur simultaneously the magnetic transition and the charge disproportionation, and more and more hopping electrons become immobile as evidenced by the temperature dependence of the Seebeck coefficient (the carrier concentration decreases with lowering temperature for T < 195K, while it is constant for T > 195K).

It can be understood as that, below the critical temperature, such electron localization and the involved superexchange interactions lead to a lowering in the internal energy of the electronic system which, according to thermodynamic laws, should be large enough for compensating for the effect associated with the decrease in the electronic entropy (*cf.* V-5 and V-6). Above the ordering temperature, however, the paramagnetic

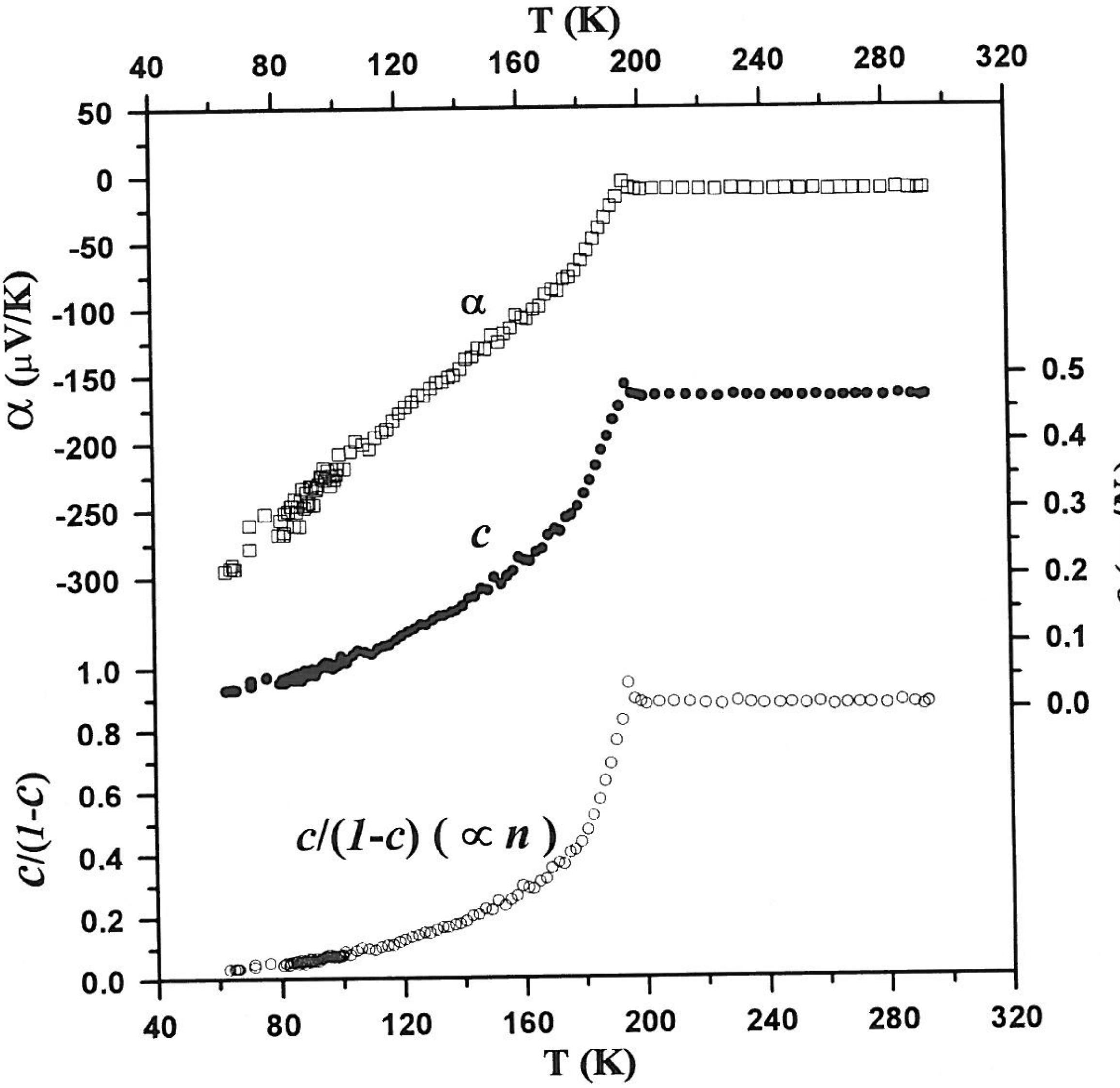

Figure 17

The Seebeck coefficient α, the site ratio $c = \frac{n}{N}$ and the value $c/(1-c)$ (proportional to $n(T)$) as a function of temperature for $Sr_2LaFe_3O_{8.95}$. The temperature dependence of the c value is obtained from $\alpha(T) = \frac{k_B}{e}\ln[\frac{c(T)}{1 - c(T)}]$ (see text).

averaged-valence state involves higher internal energy hence larger electronic entropy which corresponds to higher degree of freedom of the *d*-electrons.

V-4-5. Summary and Conclusions

Based on conductivity and Seebeck coefficient measurements, the electron transport in perovskite $Sr_2LaFe_3O_{8.95}$ are described and discussed. In the whole measured temperature range from about 60 to 300K, the conduction is caused by electrons in localized states.

Both the Seebeck coefficient and the conductivity of $Sr_2LaFe_3O_{8.95}$ show sharp changes at about 195 K, which are associated with the charge disproportionation phenomenon and coincide with the paramagnetic-antiferromagnetic transition. That is, the magnetic transition and the charge disproportionation take place simultaneously, but these processes occur over a range of temperatures from about 180 to 195 K. In other words, with rising temperature, the electrons at the lower-lying e_g-levels of the Fe^{3+} states with oriented spins begin to be activated, at about 180 K, to the partially occupied e_g-levels of the Fe^{5+} states, resulting in Fe^{4+} states tending to disordered spin states; and this process is complete at about 195 K. It is just the reverse process of the charge disproportionation with lowering temperature.

Three temperature ranges, involving different conduction mechanisms, can be distinguished:

(i) At 195 ~ 300 K (or higher), the electronic conduction is via small polaron hopping with a constant carrier concentration. The activation energy associated with the hopping mobility is determined to be 0.13 eV. A slight deviation from the Arrhenius behavior is detected between 240 and 195 K, which may be related to short-range parallel spin alignment.

The corresponding Seebeck coefficient, which decreases slightly with rising temperature, can be well accounted for by combined contributions of configurational and vibrational entropies, spin and orbital degeneracies, as well as spin polarization effect.

(ii) At T = 60 ~ 100 K, the conductivity obeys Mott $T^{-1/4}$ law, which is expalined by the variable-range hopping at e_g-levels of the Fe^{5+} states where the Fermi level is pinned, while the Seebeck coefficient is proportional to 1/T.

(iii) Between 100 and 195 K, the conductivity behavior cannot be described by a single mechanism – both the carrier concentration and carrier mobility contribute significantly to the temperature dependence of the conductivity.

It is shown that, if the temperature dependence of the Seebeck coefficient $\alpha(T)$ is determined by the dependence of the site ratio $c(T)$, the reduced Seebeck coefficient α' ($= \frac{\alpha}{(k_B/e)\ln 10}$) will exhibit the same temperature dependence as the logarithm of carrier concentration ($\log[n(T)]$), except for a difference in constant terms.

At low temperatures, the small hopping energies (of the order of 10^{-2} eV) calculated from the conductivity data indicate that the electron hopping is between nominal iron Fe^{5+} sites with parallel spins. This process will reinforce the spin ordering by spin polarization effect (*cf.* V-6-3).

The electron localization observed in $Sr_2LaFe_3O_{8.95}$ can be attributed to the combined effects such as Anderson localization caused by a random field arising from the disorder of Sr^{2+} and La^{3+} ions, the self-trapping due to small polaron formation (for $T > T_N$) and the spin and charge orderings (for $T < T_N$).

V-5. Thermodynamic Properties

V-5-1. Some Thermodynamic Relations

For a homogeneous closed system which can do only p-V work (here p is the pressure and V the volume of the system), its specific heat at constant pressure is given by [44] :

$$C_p = \frac{\delta Q_p}{dT} = \left(\frac{\partial H}{\partial T}\right)_p , \qquad (1)$$

where Q_p and H denote the absorbed heat and the enthalpy of the system, respectively, and the subscripts p indicate the condition of constant pressure.

Moreover, according to the first and the second law of thermodynamics, we have : $dH = TdS + Vdp$ and $dU = TdS - pdV$,

with S being the entropy, U the internal energy and T the temperature of the system. Thus, the following relations

$$\left(\frac{\partial H}{\partial T}\right)_p = T\left(\frac{\partial S}{\partial T}\right)_p \text{ and } \left(\frac{\partial U}{\partial T}\right)_p = T\left(\frac{\partial S}{\partial T}\right)_p - p\left(\frac{\partial V}{\partial T}\right)_p$$

can be deduced, by which the specific heat defined by *(1)* can also be expressed as

$$C_p = T\left(\frac{\partial S}{\partial T}\right)_p \qquad (2)$$

$$= \left(\frac{\partial U}{\partial T}\right)_p + p\left(\frac{\partial V}{\partial T}\right)_p . \qquad (3)$$

Therefore, an anomaly in the specific heat in a constant-pressure process can be related to corresponding anomalies in the rates of change with the temperature of the system's entropy S, or of the internal energy U and the volume V.

For the phase studied in this work, the unit cell volume contracts normally with lowering temperature as shown in Fig. 3a ~ 3c in V-1. The corresponding partial derivatives of mole volume with respect to temperature is $\left(\frac{\partial V}{\partial T}\right)_p \approx 10^{-3}$ (cm^3/mol·K) for temperatures of interest, as shown in Fig. 18. Thus, the term in *(3)* involving volume effect, $p\left(\frac{\partial V}{\partial T}\right)_p$, is of the order of 10^{-4} (J/mol·K) for p = 1atm, so that its contribution to C_p is quite negligible and the expression *(3)* can be well approximated by

$$C_p \approx \left(\frac{\partial U}{\partial T}\right)_p \qquad (4)$$

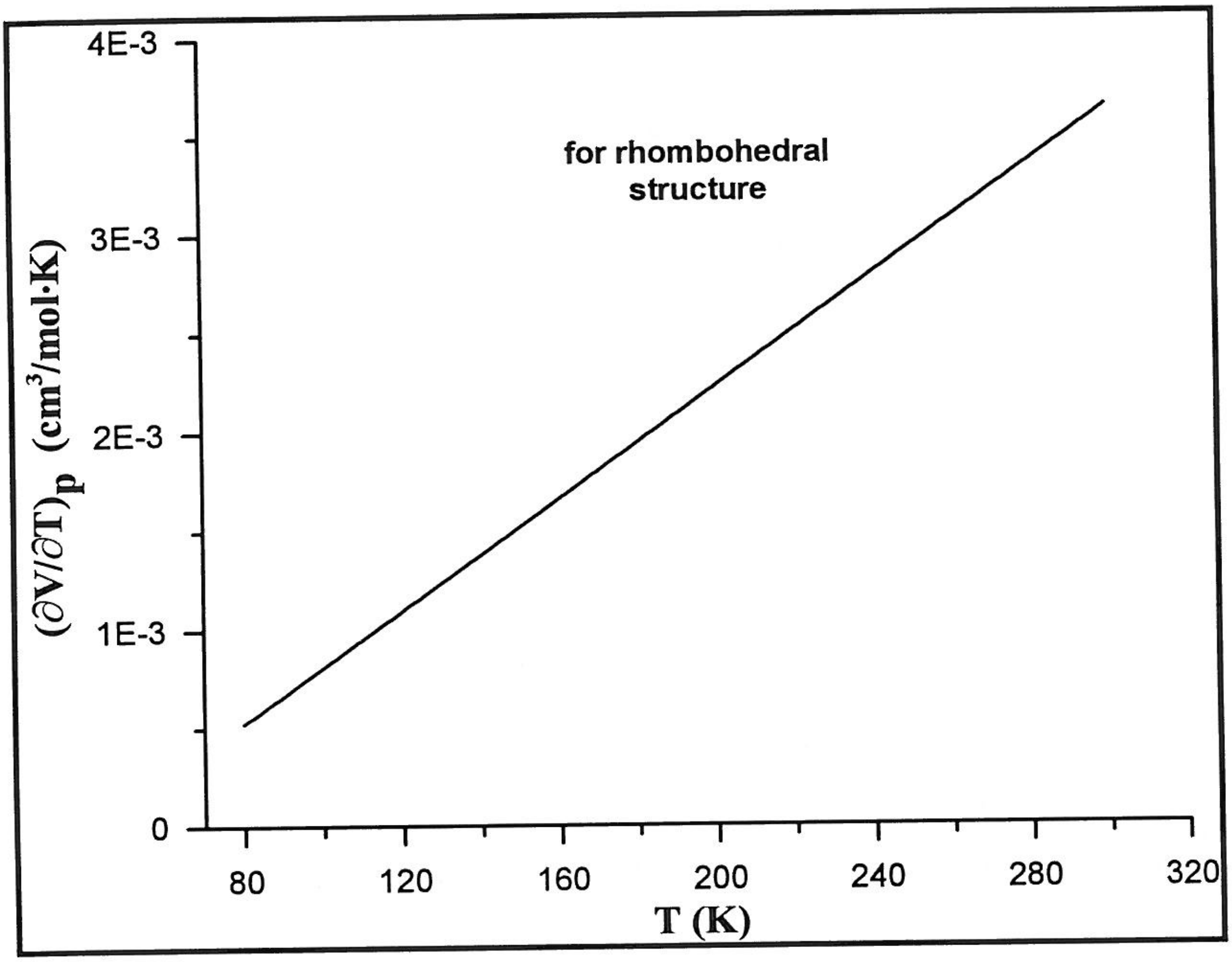

Figure 18

The partial derivatives of mole volumes with respect to temperature for the rhombohedral structure of $Sr_2LaFe_3O_{8.90}$ at P = 1 atm. The values are quite small, being of the order of $(\frac{\partial V}{\partial T})_p \approx 10^{-3}$ (cm^3/mol·K) for temperatures of interest.

V-5-2. Experimental Results: the Specific Heat C_p and the Thermodynamic Quantities Associated with the Transition (changes in entropy (ΔS), enthalpy (ΔH) and internal energy (ΔU))

Shown in Fig. 19 are the specific heat C_p at constant pressure of $Sr_2LaFe_3O_{8.95}$ and the entropy change ΔS_{exp} calculated from the C_p data (*cf.* the calculation below). One can see an anomalous region in the C_p data, which coincides with the region of the electronic phase transition (*cf.* precedent sections) as expected and shows two peaks at 189 K (the small one) and 196 K (the large one).

The dashed curve in the figure is obtained by fitting to the specific heat data showing no anomaly, and is assumed to be the contribution of lattice vibration, C_p^{lat}. The specific heat contributed by the electronic phase transition, denoted by C_p^{tran}, can be obtained by subtracting this part of contribution from the total value C_p, that is, $C_p^{tran} = C_p - C_p^{lat}$.

The entropy change ΔS_{exp} associated with the transition is then given, according to *(2)*, by the integral :

$$\Delta S_{exp}(T) = \int_{T_L}^{T} \frac{C_p^{tran}(T)}{T}\, dT ,$$

where T_L is a temperature below the transition region and $T > T_L$.

In the calculation, the above integral was approximated by a summation with small temperature steps of $\Delta T = 0.1$ K and T_L was chosen to be 140 K. The results of the calculation are shown as a function of temperature in Fig. 19 ; and the entropy change due to the transition is obtained to be $\Delta S_{exp} = 22.5$ J/mol·K.

The enthalpy H relative to that at 150 K is given in Fig. 20 for temperatures from 150 to 240 K. A corresponding anomaly is also observed in the temperature range of 180 to 200 K, while at the temperatures above 200 K and below 180 K the enthalpy varies with the temperature in a similar way.

According to formula *(1)* and the approximation *(4)*, we have

$$\Delta U \approx \Delta H = \int C_p\, dT .$$

Therefore, from the specific heat C_p^{tran}, the internal energy and enthalpy change due to the electronic phase transition are obtained to be $\Delta U \approx \Delta H = 4.33$ KJ/mol.

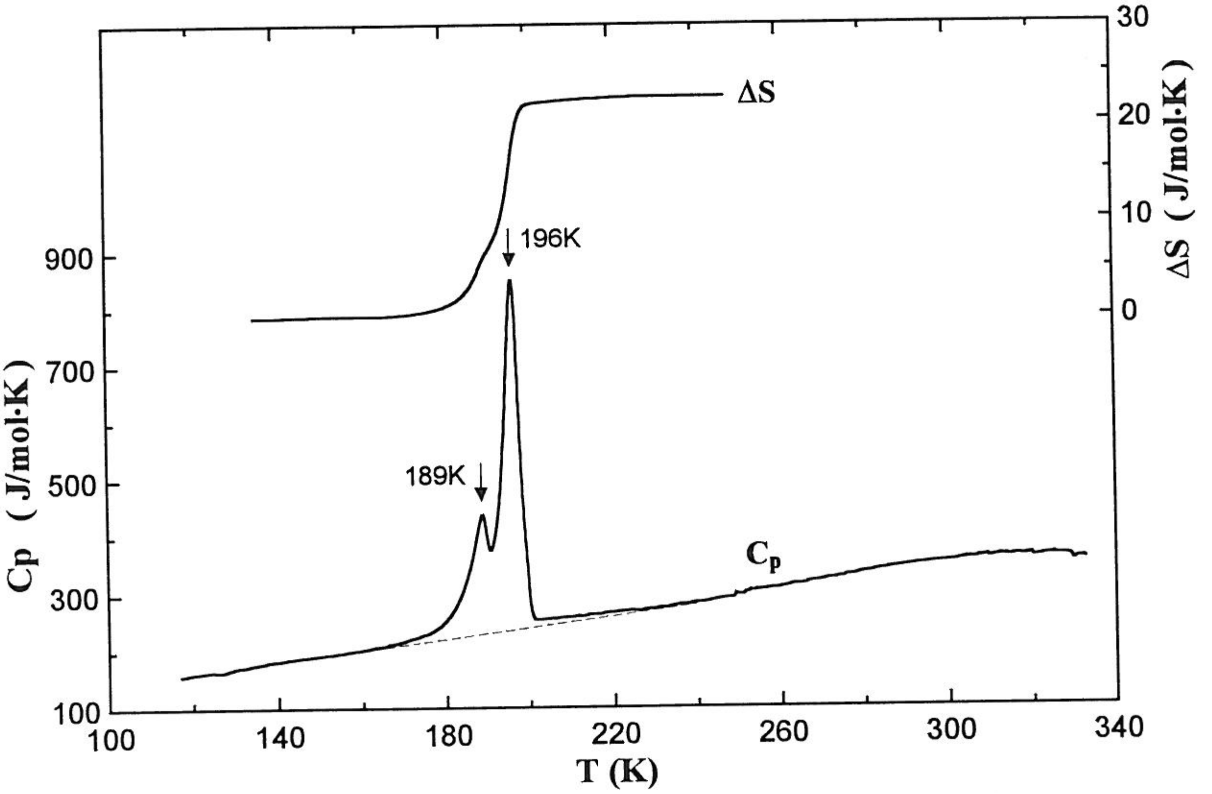

Figure 19

The specific heat C_p, which shows anomaly at the transition region of about 180K to 200K, and the entropy change ΔS due to the transition obtained from the C_p data (*cf.* text) for perovskite $Sr_2LaFe_3O_{8.95}$.

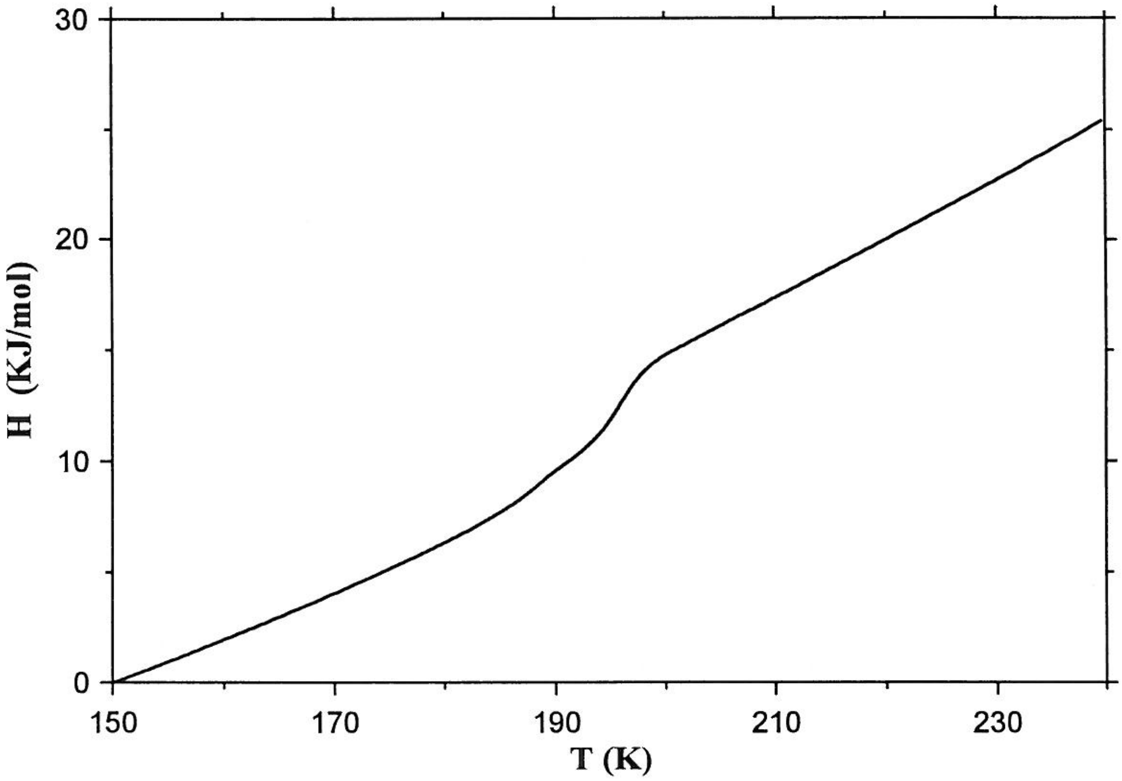

Figure 20

The enthalpy H, relative to that at 150 K, of $Sr_2LaFe_3O_{8.95}$ for T = 150 to 240 K.

V-5-3. Discussions

For T > 300 K, the specific heat reaches an average value of about 24 J/mol·K for each atom in $Sr_2LaFe_3O_{8.95}$ phase, which is close to the high temperature limit of 25 J/mol·K (law of Dulong and Petit) for the specific heat C_V at constant volume (for solid samples C_p is close to C_V). With this observation as well as the estimation from the conductivity data that the Debye temperature $\Theta_D < 400$ K (*cf.* V-4), we can safely estimate that the Debye temperature of $Sr_2LaFe_3O_{8.95}$ phase is around 300 K.

In addition, the behavior of the specific heat above and below the transition region is consistent with the fact that no cell dimension anomaly or structural transition accompanies the electronic phase transition.

Given in the following are some other discussions.

- *The Two-Peak Anomaly in the Specific Heat and the Transition Character*

(a) The large peak (at 196 K) in the specific heat data

It has been mentioned that the anomaly observed in the specific heat occurs in the same temperature range (from 180 to 200 K) as the anomalies in the magnetic susceptibility, the Mössbauer data and the electron transport properties. Since there exist no structural transition nor discontinuity in the unit cell dimension (*cf.* V-1), this anomaly can only be attributed to the electronic phase transition involving iron spin and charge order-disorder phenomena according to *(2)*.

As the spin and charge orderings (described in V-2 and V-3) occur simultaneously at decreasing temperature, the large peak in the C_p curve can be assigned to the combined effects of the magnetic transition and the charge disproportionation. That is, their critical temperatures (denoted by T_N and T_D, respectively) coincide at $T_N = T_D = 196$ K.

(b) About the small peak (at 189K) in the specific heat data

Due to incomplete electrochemical oxidation, the concentration ratio $[Fe^{3+}]:[Fe^{5+}]$ in $Sr_2LaFe_3O_{8.95}$ is a little higher than 2:1 (the ratio 2:1 is only true for stoichiometric $Sr_2LaFe_3O_9$), which also leads to some oxygen nonstoichiometry. As a consequence, the ideal magnetic structure reported in V-3 is locally mismatched around "impurity sites" involving these extra nominal iron Fe^{3+} and the oxygen vacancies. Moreover, the non-oxidized microdomains (showing superparamagnetism) deep in grains (*cf.* V-2-2) may also distort the lattice and perturb the spin interactions in nearby regions to some extent.

The e_g states of Fe^{3+} associated with those defective regions are expected to have relatively high energies. That is, they may give rise to a small peak in the upper region of the density of states of the Fe^{3+} e_g-band previously shown in Fig. 16. It is thus reasonable that the phase transition may first take place in these states. In other words, the transition temperature for the regions with and without the defects could be somewhat different, so that the two electronic phases may coexist to some extent during the transition. In fact, it was observed in the Mössbauer experiments (*cf.* V-2) that, when the temperature increases to about 190 K, a minor phase of paramagnetic averaged-valence state is already present and coexists with the major phase of antiferromagnetic mixed-valence state.

Therefore, the above mechanism could account for the small peak in the specific heat at 189 K, as well as the origin of the coexistence of the two phases over a range of temperatures during the transition. When the temperature continues to rise, the spin and the charge orderings of the major phase are broken down simultaneously as mentioned above, giving rise to the large peak at 196 K.

Moreover, the specific heat data recently reported by Wang *et al.* [10] for $Sr_2LaFe_3O_9$ was explained by one-peak anomaly (the small peak being obscured). Their observation could be attributed to the higher oxygen stoichiometry of their sample and would be consistent with the above discussion.

(c) Some points concerning transition characters

Strictly speaking, in a second-order transition (or continuous order-disorder transition), the critical temperature represents the condition under which the low-temperature to high-temperature phase transition is complete, and at no stage do two phases coexist in equilibrium. Such a transition is also characteristic of a finite λ-shape C_P curve.

On the other hand, according to the phase rule, a first-order transition in one-component system occurs at a fixed temperature when the pressure is constant. At this critical temperature, two phases coexist in equilibrium, and the C_P curve has an infinite discontinuity [14].

It is thus evident that the transition behavior observed in $Sr_2LaFe_3O_{8.95}$ agrees with neither the first-order nor the second-order type completely, but seems to be of mixed characters of the two ideal limits. For the time being, we adopt the term, *"locally first-order transition"*(*cf.* V-2), for its description.

- The Theoretical Entropy Change of the Transition and its Comparison with the Experimental One

In the following, we will calculate the theoretical entropy change ΔS_{theo} associated with the transition for one mole of $\mathrm{Sr_2LaFe^{3+}_{1.10}Fe^{4+}_{1.90}O_{8.95}}$. According to Boltzmann formula, the electronic entropy in the paramagnetic averaged-valence state, relative to that with completely ordered spin and charge states, can be obtained as follows:

(a) The entropy change due to the spin order-disorder is given by [56]

$$\Delta S_{\mathrm{theo}}^{\mathrm{spin}} = k_B \ln(\Omega_{\mathrm{spin}}) = 41.8 \ \mathrm{J/mol{\cdot}K},$$

where $\Omega_{\mathrm{spin}} = (2S_{Fe^{3+}}+1)^{1.1N_A} \cdot (2S_{Fe^{4+}}+1)^{1.9N_A}$ is the number of possible spin states of the system in paramagnetic region, with $S_{Fe^{3+}} = 5/2$ and $S_{Fe^{4+}} = 4/2$ being the spins of nominal $\mathrm{Fe^{3+}}$ and $\mathrm{Fe^{4+}}$ ions, respectively, and N_A the Avogadro constant.

(b) The change in the configurational entropy (associated with the charge disproportionation) can be calculated according to the electron hopping mechanism for $T > T_N$ previously described in V-4. The result is

$$\Delta S_{\mathrm{theo}}^{\mathrm{conf}} = k_B \ln(\Omega_{\mathrm{conf}}) = 16.4 \ \mathrm{J/mol{\cdot}K}.$$

Here the number of configurations for one mole sample is $\Omega_{\mathrm{conf}} = \dfrac{N!}{(N-n)! \cdot n!}$, with $N = 3 \cdot N_A$ being the number of available hopping sites and $n = 1.1 \cdot N_A$ the number of $\mathrm{Fe^{3+}}$ ions (with the hopping electron). The Stirling formula ($\ln Z! = Z \cdot \ln Z - Z$, for $Z >> 1$) was used in the calculation.

(c) The total theoretical entropy change is the summation of the two contributions:

$$\Delta S_{\mathrm{theo}}^{\mathrm{tot}} = k_B \ln(\Omega_{\mathrm{spin}} \cdot \Omega_{\mathrm{conf}}) = \Delta S_{\mathrm{theo}}^{\mathrm{spin}} + \Delta S_{\mathrm{theo}}^{\mathrm{conf}} = 58.2 \ \mathrm{J/mol{\cdot}K}.$$

The entropy change obtained from the specific heat C_p^{tran}, *i.e.* $\Delta S_{\mathrm{trans}}$ = 22.5 J/mol·K, is much smaller than that theoretically predicted, $\Delta S_{\mathrm{theo}}^{\mathrm{tot}} \approx 58$ J/mol·K, for the change between ideally ordered and disordered states. This fact provides another evidence for that the spin and charge states still have some degree of disorder in the measured temperature range below the transition. It is in agreement with the relatively low spin densities and nonintegral charge states of the irons (*cf.* V-3 and V-2, respectively) as well as the electron motion at low temperatures (*cf.* V-4). In this sense, the estimation of the specific heat contributed by lattice vibration is not be so straightforward as in the above.

V-5-4. Conclusions

The anomaly in the specific heat of $Sr_2LaFe_3O_{8.95}$ is due to the transition of iron spin and charge states. Since the changes of the two states occur simultaneously, the Néel temperature and the disproportionation temperature deduced from the specific heat data are $T_N = T_D = 196$ K. It is consistent with the magnetic and Mössbauer measurements and the electron transport properties presented previously.

It is suggested that, when temperature rises, the phase transition first occurs in defective regions where the magnetic and/or the crystal structure are mismatched and perturbed, before the whole system is transformed. This mechanism accounts for the small peak at 189K in the specific heat and the coexistence of the two phases over a range of temperatures during the transition.

The entropy change during the transition obtained from the specific heat data is $\Delta S_{exp} \approx 22.5$ J/mol·K, which is much smaller than that calculated using Boltzmann formula for the ideal cases. It confirms that, at least in the measured temperature range below the ordering temperature, the valence states of Fe^{3+} and Fe^{5+} and the spin densities of $S_{Fe^{3+}}=5/2$ and $S_{Fe^{5+}}=3/2$ are more nominal than real.

From the specific heat data, the internal energy and enthalpy changes due to the electronic phase transition are obtained to be $\Delta U = \Delta H = 4.33$ KJ/mol.

The Debye temperature Θ_D of $Sr_2LaFe_3O_{8.95}$ is estimated to be around 300 K.

V-6. The Electronic Phase Transition and Others

V-6-1. The Energy Terms Involved in the Transition

It has been well established in the precedent sections that, when the temperature is lowered below about 200 K, takes place in $Sr_2LaFe_3O_{8.95}$ the electronic phase transition from disordered iron spin and charge states into ordered ones. The energy changes associated with the changes in the electronic states will be analyzed in the following and the results will be used later to examine the transition behavior.

- Energy Change Due to the Spin Ordering (ΔU_{theo}^{spin})

The iron *d*-electrons in $Sr_2LaFe_3O_{8.95}$ are in localized state, and the low-temperature magnetic structure can be reasonably assumed to be the same as described in V-3. Thus, the energy decrease due to the superexchange interactions within each hexagonal unit cell is given by

$$U_{ex} \quad = \quad -[n_a \cdot |J_a^{eff}| \cdot S_{Fe^{3+}}^2 + \; n_f \cdot J_f^{eff} \cdot S_{Fe^{3+}} \cdot S_{Fe^{5+}}] \; . \qquad (1)$$

Here $J_a^{eff} = k_B T_a$ and $J_f^{eff} = k_B T_f$ are the effective exchange integrals for the antiferromagnetic and ferromagnetic superexchange interactions, respectively, with $n_a = 6$ and $n_f = 12$ being the corresponding numbers of the interaction pairs in the unit cell; $S_{Fe^{3+}}$ and $S_{Fe^{5+}}$ are the spin densities of nominal Fe^{3+} and Fe^{5+} irons, respectively. Calculation in the mean field approximation led to $T_a = 58.1K$ and $T_f = 13.5K$ for the ideally ordered case with $S_{Fe^{3+}} = 5/2$ and $S_{Fe^{5+}} = 3/2$ (*cf.* Appendix I and [45]). In this case, the energy decrease for one mole $Sr_2LaFe_3O_{8.95}$ is

$$\Delta U_{theo}^{spin} \quad = \quad \frac{1}{2} \cdot U_{ex} \cdot N_A = - \; 11.6 \text{ KJ/mol.}$$

Here the division by 2 is due to that the number of formula unit per unit cell is Z=2. Note that this energy value is the energy difference between ideally ordered and disordered spin states.

- Energy Change Due to the Charge Ordering (ΔU^{ch})

The influence of the charge ordering on the internal energy is due to two factors, as described in the following.

(a) The decrease in the Madelung energy ($\Delta E_M < 0$)

The charge disproportionation in $Sr_2LaFe_3O_{8.95}$ may be approximated by that in stoichiometric perovskite $Sr_2LaFe_3O_9$ (*cf.* V-2), with the general expression of

$$3Fe^{3.67+} \text{ (HT)} \;\Rightarrow\; Fe^{(5-2\lambda)+} + 2Fe^{(3+\lambda)+} \text{ (LT)} \qquad (0 \le \lambda < 0.67).$$

Based on the structural model (*cf.* V-1 and V-3) and the methods presented in IV-3, we have calculated the changes in the Madelung energy due to the charge disproportionation associated with different λ values, *i.e.*

$$\Delta E_M(\lambda) = E_M(\lambda) - E_M(\lambda = 0.67, \text{ with } Fe^{3.67+}) .$$

The results are shown in Fig. 21.

It can be seen that $\Delta E_M(\lambda) < 0$ for $\lambda < 0.67$, that is, the charge disproportionation lowers the Madelung energy. The largest energy decrease, $\Delta E_M(\lambda=0) \approx -780$ KJ/mol, is associated with the integral charge states of $2Fe^{3+} + Fe^{5+}$ (the Madelung energy of $Sr_2LaFe_3O_9$ is -5.105×10^4 (KJ/mol) for $\lambda = 0.67$ and is -5.183×10^4 (KJ/mol) for $\lambda = 0$).

(b) The energy increase due to Hubbard-like iron-to-iron charge transfer ($\Delta E_{CT} > 0$)

For the ideal case of $\lambda=0$, the Hubbard-like energy U_0 is associated with the following charge transfer between one pair of centers:

$$Fe^{4+} + Fe^{4+} \Rightarrow Fe^{5+} + Fe^{3+} .$$

For simplicity, we consider one mole $Sr_2LaFe_3O_9$ phase (it will be a good approximation for the case in $Sr_2LaFe_3O_{8.95}$). The energy change due to the charge transfer is

$$\Delta E_{CT} = N_A \cdot U_0. \qquad (2)$$

For gas phase, U_0 can be estimated as [46]

$$U_0 = I_5(Fe) - I_4(Fe) = 20.2 \text{ eV},$$

where $I_4(Fe)=54.8$ eV and $I_5(Fe)=75$ eV are the 4th and 5th ionization potentials of iron [47].

In ionic solids, however, the energy U_0 may be much reduced from the gas-phase value by electronic and lattice polarizations [46, 57]. Unfortunately, it is difficult to estimate the exact influence of these effects on U_0. Anyway, the energy U_0 results in a positive contribution to the internal energy, *i.e.* $\Delta E_{CT} > 0$.

(c) Therefore, the sum of the two contributions, with opposite signs, gives the energy change involved in the charge disproportionation:

$$\Delta U^{ch} = \Delta E_M + \Delta E_{CT} . \qquad (3)$$

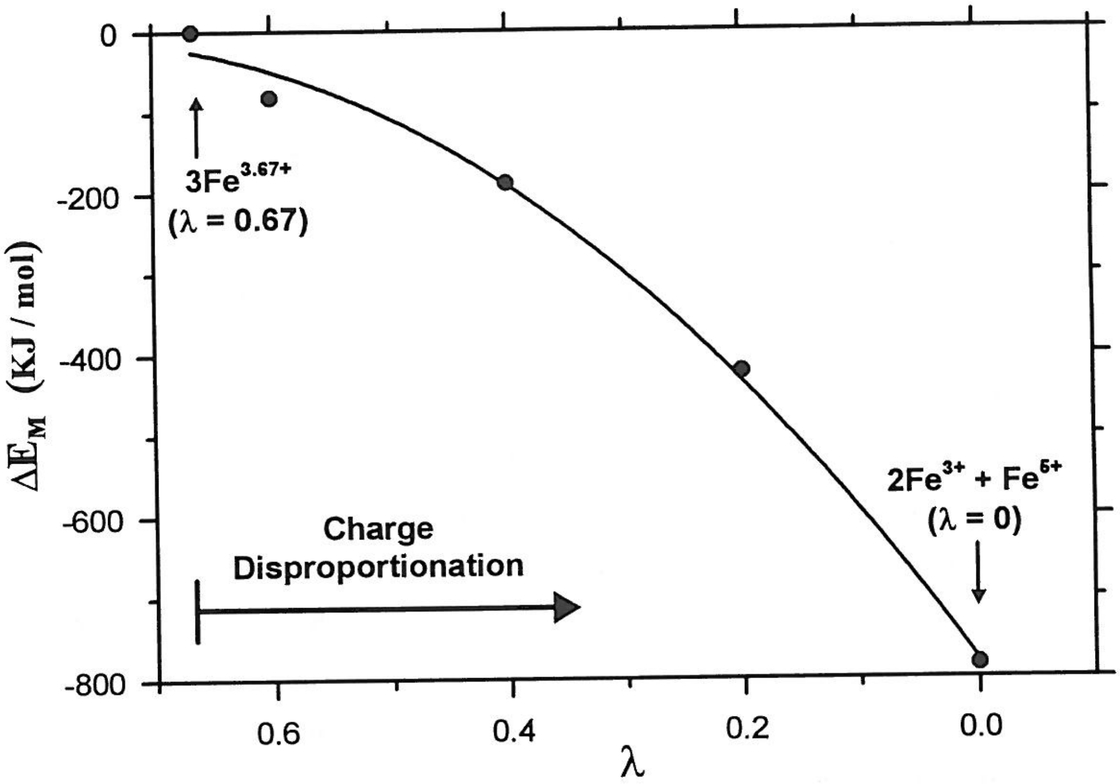

Figure 21

The changes in the Madelung energy, $\Delta E_M(\lambda) = E_M(\lambda) - E_M(\lambda = 0.67)$, for various charge distributions (related with different λ values) of perovskite $Sr_2LaFe_3O_9$.

It can be seen that the charge disproportionation (with $0.67 > \lambda \geq 0$) lowers the Madelung energy. The two ideal limits at $\lambda = 0.67$ and $\lambda = 0$ correspond to the high-temperature averaged valence state of $3Fe^{3.67+}$ and the low-temperature mixed valence state of $2Fe^{3+} + Fe^{5+}$, respectively.

- Conclusion

In perovskite $Sr_2LaFe_3O_{8.95}$, the internal energy change during its electronic phase transition can be attributed to the superexchange interactions between iron spins, the interionic coulombic interactions and the Hubbard-like iron-to-iron charge transfer. The first two effects lower the energy, the last one increases the energy. The net internal energy change is the sum of the three contributions:

$$\Delta U^{tot} = \Delta U^{spin} + \Delta U^{ch} = \Delta U^{spin} + \Delta E_M + \Delta E_{CT} .$$

V-6-2. The Investigation of the Electronic Phase Transition from a Thermodynamic Point of View

- Introduction

We have argued, based on our experimental results, that in perovskite $Sr_2LaFe_3O_{8.95}$ the spin and charge orderings occur simultaneously ($T_N = T_D = 196$ K). In other words, the *ordered* iron charge state (the mixed-valence state) is not present when the spin states are *disordered* (the paramagnetic state); nor is observed some kind of *ordered* spin state coexisting with a *not ordered* charge state. The latter is related to the nature of the low-temperature superexchange interactions and the associated magnetic structure (*cf.* V-3). That is, when the spin ordering occurs, the charge ordering is necessarily involved. However, one can still raise such a question: why the charge ordering in $Sr_2LaFe_3O_{8.95}$ does not occur independently, *i.e.* in the paramagnetic region ?

In fact, different electronic transition phenomena were observed in some other perovskites. For example, in $CaFeO_3$, a charge disproportionation (from iron averaged-valence state into its mixed-valence one) occurs in paramagnetic region before the iron spins are antiferromagnetically coupled. In $SrFeO_3$, however, only exists a magnetic transition, the iron averaged-valence state remains down to 4.2 K.

In what follows, we will examine the transition behavior observed in $Sr_2LaFe_3O_{8.95}$ from a thermodynamic point of view, based on the thermodynamic quantities obtained experimentally and theoretically. Discussions for more general cases will also be given.

- The Thermodynamic Quantities in the Phase Equilibrium

At the equilibrium temperature T_{tran} of a phase transition under a constant pressure p, the Gibbs free energy of the two involved phases are equal, *i.e.*

$$\Delta G = \Delta H - T_{tran} \cdot \Delta S = 0 , \qquad (4a)$$

where $\Delta H = \Delta U + p\cdot\Delta V$. For the case where the volume change $\Delta V = 0$ (corresponding to no structural transition), ***(4a)*** becomes the expression for the Helmholtz free energy:

$$\Delta F = \Delta U - T_{tran}\cdot\Delta S = 0\ . \qquad \textbf{\textit{(4b)}}$$

In the system of $Sr_2LaFe_3O_{8.95}$, the total internal energy change during the transition is the sum of two contributions due to the spin and charge orderings:

$$\Delta U^{tot} = \Delta U^{spin} + \Delta U^{ch}; \qquad \textbf{\textit{(5)}}$$

and the corresponding entropy change is

$$\Delta S^{tot} = \Delta S^{spin} + \Delta S^{conf}\ . \qquad \textbf{\textit{(6)}}$$

Substituting ΔU in ***(4b)*** with ***(5)***, it follows that the transition temperature below which occur simultaneously the spin and charge orderings is :

$$T_{tran}^{S+C} = \frac{\Delta U^{ch} + \Delta U^{spin}}{\Delta S^{tot}} = \frac{1}{\Delta S^{tot}}\cdot\Delta U^{ch} + \frac{\Delta U^{spin}}{\Delta S^{tot}}\ . \qquad \textit{(7a)}$$

Let us assume now the charge ordering and the spin ordering are independent of each other ; their transition temperatures would be, respectively,

$$T_{tran}^{C} = \frac{1}{\Delta S^{conf}}\cdot\Delta U^{ch} \qquad \textit{(7b)}$$

and

$$T_{tran}^{S} = \frac{\Delta U^{spin}}{\Delta S^{spin}}\ . \qquad \textit{(7c)}$$

In relations *(7a)*, *(7b)* and *(7c)*, the total entropy change has been experimentally determined, *i.e.* $\Delta S_{exp}^{tot} = -\ 22.5\ \mathrm{J/mol\cdot K}$, and theoretically calculated one is $\Delta S_{theo}^{tot} = -\ 58.2\ \mathrm{J/mol\cdot K}$ (*cf.* V-5-3).

For the other quantities, only theoretical values (*cf.* V-5-3, V-6-1) are available:

i.e. $\Delta U_{theo}^{spin} = -11600\ \mathrm{J/mol}$, $\Delta S_{theo}^{spin} = -\ 41.8\ \mathrm{J/mol\cdot K}$,

and $\Delta S_{theo}^{conf} = -16.4\ \mathrm{J/mol\cdot K}$.

However we do not have an estimate of the energy ΔU^{ch} (*cf.* V-6-1).

Those theoretical values were calculated for a transition towards an ideal ordered state, which is not the real situation. Experimental values are reduced with respect to the theoretical ones as already observed for ΔS. One can expect that the reduction factors relating these experimental and theoretical values are similar.

Therefore, for the terms in ratios in *(7a)*, *(7b)* and *(7c)*, the value of a ratio with two theoretical data would be close to the corresponding one with two experimental data.

Thus, the values used in the three formulas are the followings :

- <u>theoretical values</u> for the second term in *(7a)* and the term in *(7c)*

That is, $\dfrac{\Delta U^{\mathrm{spin}}_{\mathrm{theo}}}{\Delta S^{\mathrm{tot}}_{\mathrm{theo}}} = \dfrac{-11600 \quad (\mathrm{J/mol})}{-58.2 \quad (\mathrm{J/mol \cdot K})} = 199.3\ \mathrm{K}$ for the former

and $\dfrac{\Delta U^{\mathrm{spin}}_{\mathrm{theo}}}{\Delta S^{\mathrm{spin}}_{\mathrm{theo}}} = \dfrac{-11600 \quad (\mathrm{J/mol})}{-41.8 \quad (\mathrm{J/mol \cdot K})} = 277.5\ \mathrm{K}$ for the latter.

- <u>experimental values</u> for the first term in *(7a)* and the term in *(7b)*

We use the observed value $\Delta S^{\mathrm{tot}}_{\mathrm{exp}} = -\ 22.5$ J/mol·K (*cf.* V-5-3) for the entropy change in the first term of *(7a)* (as the transition region is quite narrow), so that the energy ΔU^{ch} in this term also corresponds to the one in the real process. Note that one of our purpose is to examine the influence of energy ΔU^{ch} on the transition (see below).

For the term in *(7b)*, since the theoretical ratio $\dfrac{\Delta S^{\mathrm{conf}}_{\mathrm{theo}}}{\Delta S^{\mathrm{tot}}_{\mathrm{theo}}} = \dfrac{-16.4}{-58.2} = 0.28$, it leads to an estimate of the configurational entropy change in the real process : $\Delta S^{\mathrm{conf}}_{\mathrm{exp}} = \Delta S^{\mathrm{tot}}_{\mathrm{exp}} \times 0.28 \approx -\ 6.3$ J/mol·K.

* Note that all those negative quantities correspond to a high-temperature to low-temperature phase transition.

- The "Phase Diagram" of the Electronic States as a Function of ΔU^{ch}

Based on the above data for $Sr_2LaFe_3O_{8.95}$, we have plotted in Fig. 22(a) the possible transition temperatures $T^{\mathrm{S+C}}_{\mathrm{tran}}$, $T^{\mathrm{C}}_{\mathrm{tran}}$ as linear functions of ΔU^{ch} according to *(7a)* and *(7b)* and $T^{\mathrm{S}}_{\mathrm{tran}}$ according to *(7c)*.

First, we note that the three straight lines intersect at a common point, *i.e.* have a equal temperature, at a critical energy $\Delta U^{\mathrm{ch}}_{\mathrm{crit}} = \dfrac{\Delta S^{\mathrm{conf}}}{\Delta S^{\mathrm{spin}}} \Delta U^{\mathrm{spin}}$. It can be seen that for $\Delta U^{\mathrm{ch}} < \Delta U^{\mathrm{ch}}_{\mathrm{crit}}$, $T^{\mathrm{C}}_{\mathrm{tran}} > T^{\mathrm{S}}_{\mathrm{tran}}$; when $\Delta U^{\mathrm{ch}} > \Delta U^{\mathrm{ch}}_{\mathrm{crit}}$, $T^{\mathrm{C}}_{\mathrm{tran}} < T^{\mathrm{S}}_{\mathrm{tran}}$. The $T^{\mathrm{S+C}}_{\mathrm{tran}}$ line is always intermediate between the $T^{\mathrm{C}}_{\mathrm{tran}}$ and $T^{\mathrm{S}}_{\mathrm{tran}}$ lines.

(a) General features of the "phase diagram"

Generally, three different situations of transition can be distinguished as follows:

(i). If $\Delta U^{ch} > \Delta U^{ch}_{crit}$, then $T^{S}_{tran} > T^{C}_{tran}$. Since a spin ordering may be associated with either an ordered or a constant charge density, there are two possibilities:

- when the spin ordering involves an ordered charge density, the T^{S}_{tran} and T^{C}_{tran} lines are not present independently, but converge to the intermediate T^{S+C}_{tran} line. The corresponding "phase diagram" has two regions with paramagnetic averaged-valence state (PM+AV) and antiferromagnetic mixed-valence state (AFM+MV), as shown in Fig. 22(b). What is more, in this case the charge ordering may coexist with the spin ordering even for some values of $\Delta U^{ch} > 0$, which, otherwise, will not occur on its own.
- when the spin ordering is associated with a constant charge density, it will occur at T^{S}_{tran}. In this case, any possible charge ordering at $T^{C}_{tran} < T^{S}_{tran}$ will disturb the already established spin ordering involving a constant charge density. If such a charge ordering leads to a net increase in the internal energy of the system involved, it will not really occur. This case is shown in Fig. 22(c), with the presence of two regions of (PM+AV) and (AFM+AV) (antiferromagnetic averaged-valence state).

(ii). If $\Delta U^{ch} < \Delta U^{ch}_{crit}$, then $T^{C}_{tran} > T^{S}_{tran}$. Theoretically, a charge ordering does not necessarily involve a spin ordering, that is, it *may* occur when the spins are disordered. Therefore, there may exist two different temperatures of $T^{C}_{tran} > T^{S}_{tran}$, and the T^{S+C}_{tran} line is absent in this case. Correspondingly, as presented in Fig. 22(d), there are three regions in the "phase diagram" which are separated by T^{C}_{tran} and T^{S}_{tran} lines: the regions of (PM+AV), (PM+MV) (paramagnetic mixed-valence) and (AFM+MV) states.

(b) Explanation and discussions for the transition in $Sr_2LaFe_3O_{8.95}$

Since the phase transition in $Sr_2LaFe_3O_{8.95}$ occurs at about 200 K, it can only be represented by Fig. 22(b) with $\Delta U^{ch} > \Delta U^{ch}_{crit}$. That is, the transition is between (PM + AV) and (AFM + MV) phases, as is exactly observed in experiments. In other words, thermodynamically, in $Sr_2LaFe_3O_{8.95}$ system the charge ordering cannot occur in the paramagnetic region because it does not bring about large enough energy decrease ΔU^{ch}.

The charge ordering energy ΔU^{ch} is the sum of two competing energy terms, the Madelung energy and the charge transfer energy (*cf.* formula ***(3)***). We have shown that the charge disproportionation gives rise to a considerable decrease in the Madelung energy. On the other hand, the Hubbard-like energy U_0 in $Sr_2LaFe_3O_{8.95}$ is also expected to be high due to the strong electron correlations between localized *d*-electrons. The small magnitude of $|\Delta U^{ch}| \approx 0$ according to Fig. 22(b) (the possibility of $\Delta U^{ch} > 0$ is not ruled out) indicates that the two effects are almost compensated for each other. However, it is not expected to obtain exact value of ΔU^{ch} from this phase diagram because of the approximations we have made.

For the ideal case where the charge states are completely ordered, the decrease in the Madelung energy was previously given to be $\Delta E_M(\lambda=0) \approx$ - 780 KJ/mol. It leads to a Hubbard-like energy $U_0 \approx 8$ eV for $\Delta U^{ch} \approx 0$ according to ***(2)*** and ***(3)***. In the real situation, the value of Madelung energy can be smaller due to nonintegral charge states $(0 < \lambda < 0.67)$. Correspondingly, the real Hubbard-like energy U_0 may also be lower than 8 eV to some extent. Anyway, such an energy U_0 is not unreasonable [46, 57]. However, an appropriate estimation of energy U_0 depends on the exact knowledge of the Madelung energy ΔE_M.

We have assumed for the phase diagram in Fig. 22 that the volume change during the transition is zero ($\Delta V = 0$), that is, ***no structural transition is involved***. Thus, the above results suggest that this electronic phase transition can be triggered only by the electronic interactions themselves and needs not to be accompanied by a structural distortion with a volume change $\Delta V < 0$ (at decreasing temperature; the effect of that is to increase T_{tran}^{S+C} by $\frac{p \cdot \Delta V}{\Delta S^{tot}}$). This is consistent with the experimental observations.

In addition, according to the result of $\Delta U^{ch} \approx 0$, the observed internal energy change ($\Delta U^{tot} = 4.33$ KJ/mol, *cf.* V-5-3) during the transition is (mainly) due to the spin ordering, *i.e.* $\Delta U^{tot} \approx \Delta U^{spin}$.

(c) Discussions about more general cases with two other examples (CaFeO$_3$ and SrFeO$_3$)

In $CaFe^{4+}O_3$, it was observed that a charge disproportionation [7],

$$Fe^{4+} + Fe^{4+} \Rightarrow Fe^{5+} + Fe^{3+},$$

occurs at 290 K in the paramagnetic region of iron spin state, then follows a paramagnetic-antiferromagnetic transition at a lower temperature $T_N = 116$K [6, 48, 49].

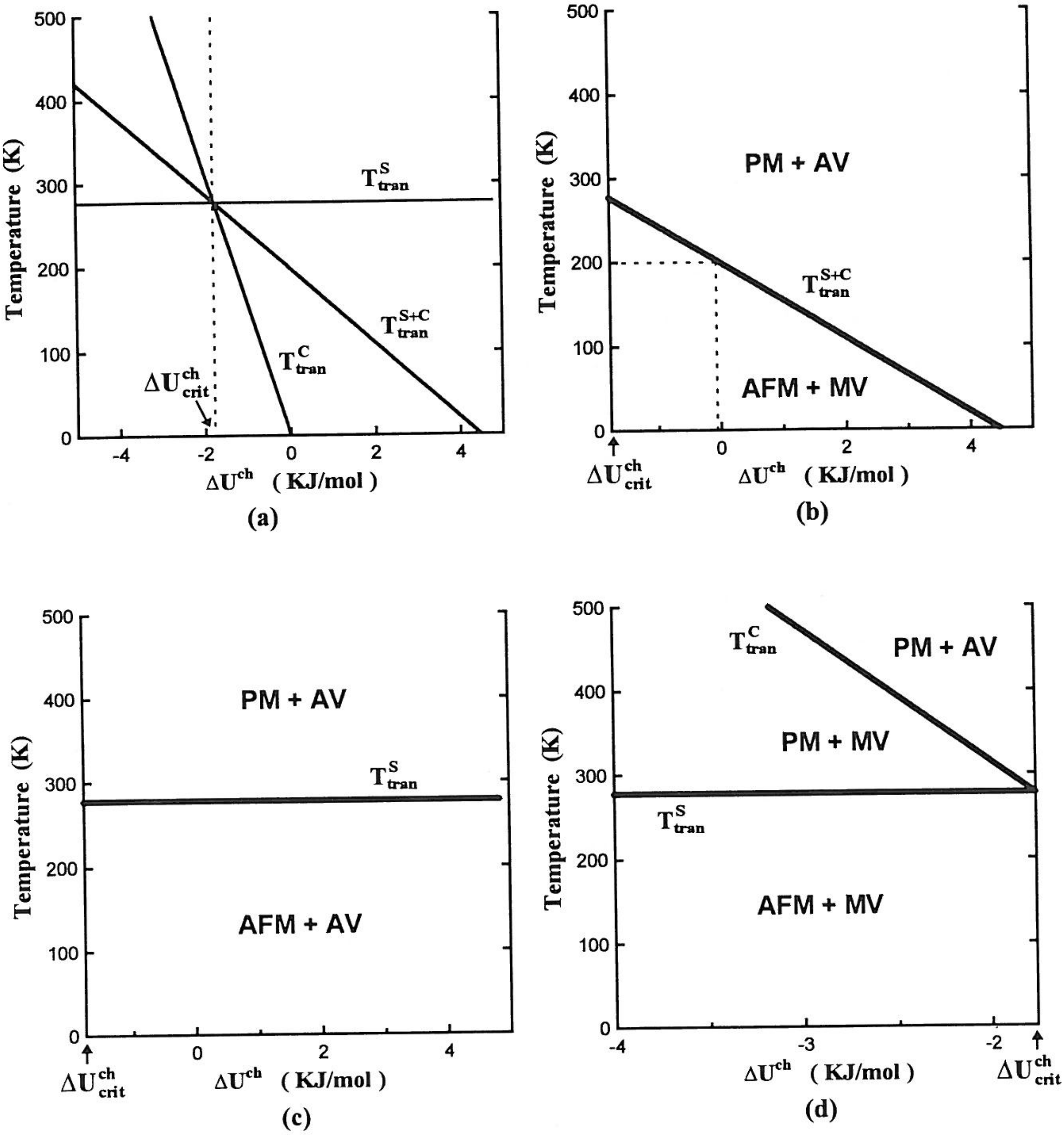

Figure 22

(a). An overall view of possible transition temperatures T^{C}_{tran}, T^{S}_{tran} and T^{S+C}_{tran} of $Sr_2LaFe_3O_{8.95}$ plotted as functions of the charge ordering energy ΔU^{ch}. They inercross at a critical energy ΔU^{ch}_{crit};

(b). The "phase diagram" for $\Delta U^{ch} > \Delta U^{ch}_{crit}$ involving two regions of (PM+AV) and (AFM+MV);

(c). The case for $\Delta U^{ch} > \Delta U^{ch}_{crit}$ involving two regions of (PM+AV) and (AFM+AV);

(d). The case for $\Delta U^{ch} < \Delta U^{ch}_{crit}$ involving three regions of (PM+AV), (PM+MV) and (AFM+MV).

Due to the lack of both experimental and theoretical data, we cannot draw a "phase diagram" for $CaFeO_3$. However, the above observations suggest that the perovskite $CaFeO_3$ belongs to the case with $\Delta U^{ch} < \Delta U^{ch}_{crit}$ ($T^{C}_{tran} > T^{S}_{tran}$). That is, above 290K ($T^{C}_{tran}$, in our notations) the irons are in (PM + AV) state; below 116K (T^{S}_{tran}) they are in (AFM + MV) state; and between 290K and 116K they exist in (PM + MV) state.

The conductivity of $CaFeO_3$ was reported to change from metallic behavior to semiconducting one in the vicinity of the magnetic transition temperature (at about 130 K~140 K) [49]. Since the charge disproportionation in $CaFeO_3$ occurs in the metallic region, it is somewhat different from that in $Sr_2LaFe_3O_{8.95}$. But we believe that a considerable energy decrease arising from the Madelung energy, as in $Sr_2LaFe_3O_{8.95}$, can be present in its ΔU^{ch}. Unfortunately, due to the lack of detailed low-temperature (magnetic) structure data, we cannot verify this by calculation.

Quite differently, in cubic perovskite $SrFeO_3$, its metallic conductivity keeps down to its antiferromagnetic region [9, 50, 51], and the iron valence state remains to be Fe^{4+} at 4.2 K as was evidenced by Mössbauer data [52]. The electronic transition is therefore between (PM + AV) and (AFM + AV) states which occurs at $T_N = 134$ K.

These phenomena reflect that the $SrFeO_3$ system is in $\Delta U^{ch} > \Delta U^{ch}_{crit}$ regime. Such a difference between $SrFeO_3$ and $CaFeO_3$ (where $\Delta U^{ch} < \Delta U^{crit}_{C}$) may result, at least partly, from relatively large interionic distances in $SrFeO_3$. Note that the cell dimension of $SrFeO_3$ is $a_C = 3.845 \sim 3.869$Å [5, 51, 53], which is significantly larger than that of $CaFeO_3$, $a_C \approx 3.770$Å [49, 54], and closer to that for $Sr_2LaFe_3O_{8.95}$, $a_C \approx 3.877$ Å. Therefore, a possible decrease in the Madelung energy in $SrFeO_3$ would be smaller than that in $CaFeO_3$, since the Madelung energy is proportional to $1/a_C$.

It was reported [50, 55] that below T_N $SrFeO_3$ has a helical spin arrangement which is associated with the valence state of Fe^{4+}. Hence, a charge disproportionation is not compatible with such a spin coupling. Among the related oxides, $SrFeO_3$ was referred to as the unique exception showing a single valence state of Fe^{4+} at 4.2 K [6]. It could not be ruled out that a possible charge ordering (*i.e.* when $\Delta U^{ch}_{crit} < \Delta U^{ch} < 0$) in $SrFeO_3$ may be suppressed by the spin ordering.

Finally, we add that an alternative phase diagram may be drawn for a given charge ordering energy ΔU^{ch}. In such a diagram, according to ***(7a)***, ***(7b)*** and ***(7c)***, T^{S}_{tran}

and $T_{\mathrm{tran}}^{\mathrm{S+C}}$ are plotted as linear functions of the spin ordering energy ΔU^{spin}, and $T_{\mathrm{tran}}^{\mathrm{C}}$ appears as a constant (it corresponds to that the $T_{\mathrm{tran}}^{\mathrm{S}}$ line in present phase diagram can move upward and downward for a given ΔU^{ch}). Correspondingly, similar discussions may be made about ***the influence of the variations in ΔU^{spin} on the transition behavior.***

- Conclusions

In a system where both spin coupling and charge disproportionation are possible, its transition behavior, involving the order-disorder of the spin and charge states, depends on the competition and correlation between these two effects:

- If $\dfrac{\Delta U^{\mathrm{ch}}}{\Delta S^{\mathrm{conf}}} > \dfrac{\Delta U^{\mathrm{spin}}}{\Delta S^{\mathrm{spin}}}$, a charge disproportionation will occur at a higher temperature, then follows a spin ordering at a lower temperature. The system $CaFeO_3$ is an example of this case.
- If $\dfrac{\Delta U^{\mathrm{ch}}}{\Delta S^{\mathrm{conf}}} < \dfrac{\Delta U^{\mathrm{spin}}}{\Delta S^{\mathrm{spin}}}$, a spin ordering will definitely occur. The occurrence or non-occurrence of a charge ordering depends on the particular correlation between the spin and charge orderings. The perovskites $Sr_2LaFe_3O_{8.95}$ and $SrFeO_3$ are two different examples.

In the system of $Sr_2LaFe_3O_{8.95}$, due to the compensation between the effects of Hubbard-like energy and Madelung energy, the energy change ΔU^{ch} associated with the charge ordering is greater than the critical value $\Delta U_{\mathrm{crit}}^{\mathrm{ch}} = \dfrac{\Delta S^{\mathrm{conf}}}{\Delta S^{\mathrm{spin}}} \Delta U^{\mathrm{spin}}$ and close to zero, so that the charge ordering cannot occur independently in the paramagnetic region. On the other hand, when the spin ordering occurs, the charge ordering is necessarily involved. As a consequence, the changes in the spin and charge states occur simultaneously at about 200K, which is a temperature intermediate between the hypothetical temperatures for independent spin and charge orderings.

In addition, the electronic phase transition in $Sr_2LaFe_3O_{8.95}$ is an intrinsic behavior of the electronic states, and needs not to be intervened by a structural distortion with a volume change $\Delta V < 0$ (at decreasing temperature). And the observed internal energy change ($\Delta U^{\mathrm{tot}} = 4.33$ KJ/mol) during the transition is mainly contributed by the spin ordering, *i.e.* $\Delta U^{\mathrm{tot}} \approx \Delta U^{\mathrm{spin}}$, since $\Delta U^{\mathrm{ch}} \approx 0$.

V-6-3. Additonal Discussions

- Cause for the Abrupt Behavior of the Magnetic Transition

Below the transition, the magnetic susceptibility of $Sr_2LaFe_3O_{8.95}$ varies only weakly with the temperature, but it shows an abrupt increase in the transition region (from about 180 K to 200 K) (Fig. 9, V-3).

On the other hand, in a theoretical calculation in the mean field approximation (*cf.* Appendix I), we have fitted the magnetic susceptibility using a Hamiltonian containing a biquadratic term in addition to the Heisenberg one, and the abrupt change of the susceptibility during the transition is reproduced. Due to the presence of this non-Heisenberg biquadratic Hamiltonian, the effective exchange integrals, J_a^{eff} and J_f^{eff} (*cf.* relations *(1)* in V-6-1 and *(3)* in appendix I) are then temperature-dependent and diminish with the decrease of the sublattice magnetizations. The resulting spin densities show discontinuities at T_N, which is consistent with the Mössbauer data (*cf.* V-2).

Experimentally, it was also observed that, when temperature rises, the Seebeck coefficient changes its behavior sharply at the onset and finishing temperatures of the transition and it increases more rapidly during the transition; so does the conductivity. These changes in the transport properties are related to the charge transfer (*cf.* V-4-3),

$$e_g^2(\mathrm{Fe}^{3+}) + e_g^0\,(\mathrm{Fe}^{5+}) \Rightarrow 2\,e_g^1(\mathrm{Fe}^{4+})\,,$$

which is just the reverse process of the charge disproportionation and leads to rapid increase in the carrier concentration.

Note that strong superexchange interactions involved in $Sr_2LaFe_3O_{8.95}$ (*cf.* V-3-3) are expected among iron ions of Fe^{3+} and Fe^{5+}, so that the above charge transfer will weaken the spin interactions. Hence, when the magnetic transition sets in, not only the iron spins, but also the effective exchange integrals (J_a^{eff} and J_f^{eff}) can no longer be approximated as constants but will decrease significantly in magnitude due to the simultaneous charge transfer; and such a decrease will in turn reduce the spin couplings and facilitate the charge transfer. This effect of ***"positive feedback"*** can be responsible for the abrupt behavior of the magnetic transition [13].

The good agreement between the theoretical result and the experimental observation of the magnetic transition behavior suggests that the introduction of the biquadratic Hamiltonians well describes the influence of the charge disproportionation on the exchange integrals.

- The Almost Temperature-Independent Magnetic Susceptibility at Low Temperatures

As shown in Fig. 9 (V-3), at low temperatures the magnetic susceptibility (χ_m) of $Sr_2LaFe_3O_{8.95}$ exhibits an unusual almost temperature-independent behavior in a large temperature range until the occurrence of the magnetic transition.

It was argued in V-4 that at low temperatures the electron conduction is via electron hopping between iron Fe^{5+} sites with parallel spins, so that the magnetic couplings can be reinforced due to spin polarization. This can be seen from the fact that, when the conductivity increases with the temperature (Fig. 13), the susceptibility does not increase as usual but remains constant or even decreases slightly for $T < 130K \sim 140$ K, indicating that the spin polarization effect predominates over the thermal agitation of the spin ordering. It can thus be suggested according to Fig. 9 that, at about $T = 130K \sim 140$ K, the two competing effects (the spin polarization and the thermal agitation) become comparable and then change over into the reverse order. As a consequence, the magnetic susceptibility begins to increase slightly with the temperature for $T > 130K \sim 140$ K until the magnetic transition sets in.

In addition, as was previously mentioned, there is a slight break around 134 K in the reduced Seebeck coefficient (α') against 1/T plot (Fig. 13) involving a small increase in the activation energy, which may be a reflection of an increase of the Fermi level due to the thermal agitation of the spin orientation.

- The Absence of a Structural Distortion Which is Expected for the Charge Ordering: the Influence of Magnetic and Pauli Interaction on the Chemical Bonds.

It was previously reported [1] (*cf.* Table 4 in V-1) that the ordered charge states of Fe^{3+} and Fe^{5+} at low temperatures does not lead to a significant structural distortion in $Sr_2LaFe_3O_{8.94}$ and the oxygen ions only shift slightly at 50 K (with Fe–O–Fe bond angle decreasing from ~174° at 300K to 171° at 50K) so that all Fe – O distances remains the same. Our XRD results also confirm that no structural transition and discontinuity in cell dimensions occur in $Sr_2LaFe_3O_{8.95}$ at low temperatures.

This phenomenon is surprising at the first glance, in that a shorter Fe^{5+}–O^{2-} distance than that of Fe^{3+}–O^{2-} is favored by the Coulomb interaction. But note that in this perovskite the interaction between iron spins is also important. We are going to show why it is possible.

Below the ordering temperature, both the σ-type and π-type superexchange interactions involved in Fe^{3+}–O^{2-}–Fe^{3+} pairs are antiferromagnetic in nature [15]. Although a longer Fe^{3+}–O^{2-} bond relative to $Fe^{3.67+}$–O^{2-} bond (for $T > T_N$) is expected due to a weaker Coulomb attraction, it is not favored by the magnetic interactions. This is because an increase in Fe^{3+}–O distance will decrease the effective overlap between oxygen *p*- and iron *d*-orbitals and hence decrease the strength of the superexchange interactions.

As for Fe^{3+}–O^{2-}–Fe^{5+} pairs, the σ-type interaction is that between half-filled and empty iron d_σ-orbitals by the medium of full oxygen p_σ-orbital, *i.e.*

$$d_\sigma^2(e_g^2) \ - \ p_\sigma \ - \ d_\sigma^0(e_g^0)\,,$$

which is ferromagnetic with a moderate strength. The π-type one is that between half-filled iron d_π-orbitals,

$$d_\pi^3(t_{2g}^3) \ - \ p_\pi \ - \ d_\pi^3(t_{2g}^3)\,,$$

which is antiferromagnetic with a weaker strength for a usual Fe – O distance (due to a weak overlapping between the π-type orbitals). Therefore a net ferromagnetic spin coupling results according to Goodenough [15].

The d_π-orbitals are lower-lying ones hence are more localized, so that the electron correlation (the antiferromagnetic spin interaction) may be enhanced considerably at shorter interionic distances.

Moreover, a reduction in Fe – O distance will increase the probability to find electrons with parallel spins at the nominally empty d_σ^0-orbitals on a Fe^{5+} site due to stronger orbital overlappings between the iron and oxygen atoms. The situation involving the $d_{x^2-y^2}$ orbitals is schematically shown in Fig. 23 (note that each Fe^{5+} with empty d_σ^0-orbitals, *i.e.* $d_{x^2-y^2}^0$ and $d_{z^2}^0$ orbitals, is surrounded by six Fe^{3+} irons with half-filled d_σ^2-orbitals and parallel spins; *cf.* Fig. 12 in V-3).

If the densities of these electrons with parallel spins at the d_σ^0-orbitals are significant, according to the Pauli exclusion principle, the interactions between them will give rise to a repulsive force (the Pauli repulsion), and the ferromagnetic σ-type spin coupling will be disturbed.

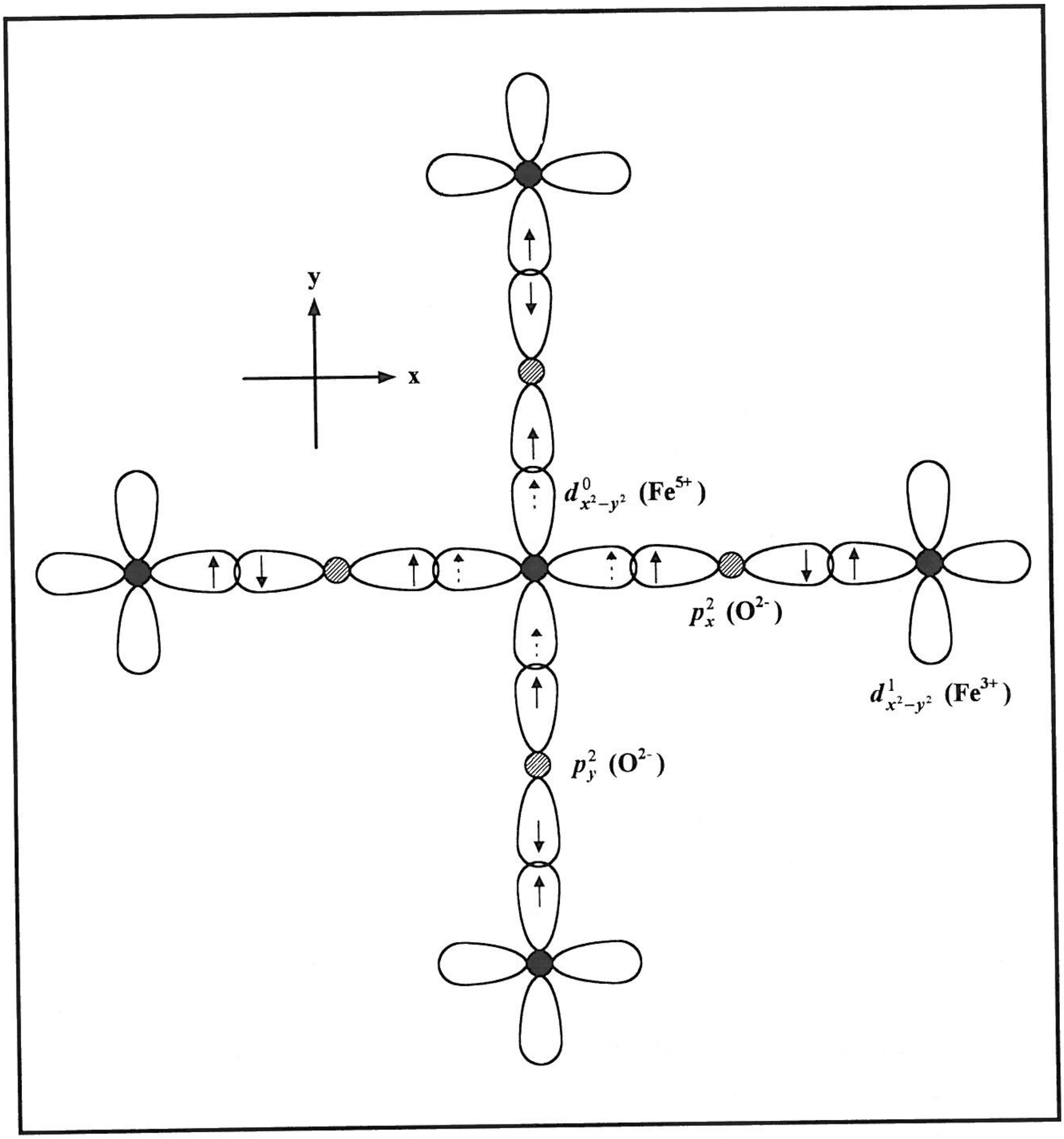

Figure 23

The electronic orbitals associated with a nominally empty $d^0_{x^2-y^2}$ orbital on a Fe^{5+} site. The arrows indicate the relative spin orientations of the electrons occupying the orbitals. Electrons with parallel spins may be transferred, with certain probability, to the $d^0_{x^2-y^2}$ orbital from its neighbors; they are represented by the dashed arrows. With decreases in Fe^{5+} – O^{2-} separations, the probability of such a electron transfer will increase, which may significantly reduce the σ-type ferromagnetic spin interactions and bring about a repulsive energy according to the Pauli principle.

Therefore it is possible that at a shorter Fe^{5+}–O^{2-} separation the effective ferromagnetic (σ-type) spin interaction may be reduced and the Pauli repulsion may become important.

In conclusion: Generally, periodic atomic displacements accompanying a charge ordering may lead to a decrease in the Coulomb energy. However, in the present magnetic system where both the iron spins and charges are ordered, such atomic displacements will reduce the superexchange interactions (which are very sensitive to interatomic distances) and will bring about a repulsive energy according to the Pauli principle. We then suggest that the Coulomb interaction is almost compensated for by these effects. As a consequence, the crystal structure is left undistorted, or distorted by too small an extent to be detected in the diffraction experiments. It is an manifestation of the influence of magnetism and Pauli repulsion on chemical bonds.

In addition, ***the ordered charge densities are not integral*** like Fe^{3+} and Fe^{5+} (at least for the considered temperatures) (*cf.* V-2 and V-5), therefore their effect on the bond lengths is less important than it would be due to a less important Coulomb interaction.

- *Conclusions*

Among the magnetic interactions in $Sr_2LaFe_3O_{8.95}$ below the ordering temperature, contributions of non-Heisenberg type are present. They result in the almost temperature-independent susceptibility at low temperatures (due to the spin-polarization of hopping electrons) and the abrupt magnetic transition (due to the temperature-dependent effective exchange integrals associated with the charge disproportionation).

We show that the absence of a structural distortion (periodic atomic displacements) in this perovskite below the ordering temperature, which is otherwise expected to accompany the charge ordering, may originate mainly from the involved superexchange and Pauli interactions which compete with the Coulomb interactions.

References

[1] Battle, P.D., Gibb, T.C., and Lightfoot, P. (1990). *J. Solid State Chem.* **84**, 271

[2] Battle, P.D., Gibb, T.C., and Nixon, S. (1988). *J. Solid State Chem.* **77**, 124

[3] Hahn, T. (ed.) (1989). *Internat. Tables Crystallogr.*, Vol. A, *Space-Group symmetry*, 2nd rev. edn., Internat. Union of Crystallogr./Kluwer Academic Pub.

[4] Eibschutz, M., Shtrikman, S., and Treves, D. (1967). *Phys. Rev.*, **156**, 562.

[5] Takeda, Y., Kanno, K., Takada, T., Yamamoto, O., Takano, M., Nakayama, N. and Bando, Y. (1986). *J. Solid State Chem.* **63**, 237.

[6] Takano, M., Kawachi, J., Nakanishi, N., and Takeda, Y. (1981). *J. Solid State Chem.* **39**, 75

[7] Takano, M., Nakanishi, N., Takeda, Y., Naka, S., and Takada, T. (1977). *Mat. Res. Bull.* **12**, 923

[8] J-C. Grenier (1976). Ph.D. Thesis, University Bordeaux I

[9] MacChesney, J.B., Sherwood, R.C., and Potter, J.F. (1965). *J. Chem. Phys.* **43**, 1907

[10] Wang, J.T., Lin, C.L. and Mihalisin, T. (1996). *J. Appl. Phys.* **79**, 6608

[11] Morrish, A.H. (1965). *The Physical Principles of Magnetism*, John Wiley & Sons, Inc.

[12] Figgis, B.N. (1966). *Introduction to Ligand Fields*, John Wiley & Sons, Inc.

[13] Nagaev, E.L. (1983). *Physics of Magnetic Semiconductors*, MIR Pub.

[14] West, A.R. (1990). *Solid State Chemistry and its Applications*, John Wiley & Sons, Ltd

[15] Goodenough, J.B. (1963). *Magnetism and the Chemical Bond*, John Wiley & Sons, Inc.

[16] Holstein, T. (1959). *Ann. Phys.* (New York) **8**, 343

[17] Mott, N.F. (1968). *J. Non-cryst. Solids* **1**, 1

[18] Emin, D. (1974). *Phys. Rev. Lett.* **32**, 303

[19] Efros, A.L. and Shklovskii, B.I. (1975). *J. Phys. C: Solid State Phys.* **8**, L49

[20] Efros, A.L. and Shklovskii, B.I. (1985). in *Electron-Electron Interactions in Disordered Systems* (ed. A.L. Efros and M. Pollak), Vol. 10 of *Modern Problems in Condensed Matter Sciences* (Series eds. V.M. Agranovich and A.A. Maradudin), Elsevier Science Pub. B.V.

[21] Mott, N.F. (1993). *Conduction in Non-Crystalline Materials*, Oxford

[22] Zvyagin, I.P. (1991). in *Hopping Transport in Solids* (ed. M. Pollak and B. Shklovskii), Vol. 28 of *Modern Problems in Condensed Matter Sciences* (Series eds. V.M. Agranovich and A.A. Maradudin), Elsevier Science Pub. B.V.

[23] Oversluizen, G., Kuijpers, T.H.J.M. and Metselaar, R. (1984). *Phys. Rev.* **B29**, 4540; and references herein.

[24] Austin, I.G. and Mott, N.F. (1969). *Adv. Phys.* **18**, 41

[25] Böttger, H. and Bryksin, V.V. (1976). *Phys. Stat. Sol.* (b) **78**, 415

[26] Böttger, H. and Bryksin, V.V. (1985). *Hopping Conduction in Solids*, VCH Pub.

[27] Chaikin, P.M. and Beni, G. (1976). *Phys. Rev.* **B13**, 647

[28] Heikes, R.R. (1961). in *Thermoelectricity: Science and Engineering* (ed. R.R. Heikes and R.W. Ure), *Chap. 4*, Interscience Pub.

[29] Culter, M. and Mott, N.F. (1969). *Phys. Rev.* **181**, 1336

[30] Fritzsche, H. (1971). *J. Non-cryst. Solids* **6**, 49

[31] Tuller, H.L. and Nowick, A.S. (1977). *J. Phys. Chem. Solids* **38**, 859

[32] Goodenough, J.B. (1971). in *Progress in Solid State Chem.* (ed. H. Reiss), Vol. 5, Pergamon Press, Ltd

[33] Heikes, R.R. (1963). in *Transition Metal Compounds* (ed. E.R. Schatz), Gordon and Breach

[34] Heikes, R.R., Maradudin, A.A., and Miller, R.C. (1963). *Ann. Phys.* (Paris) **8**, 783

[35] Doumerc, J.P. (1994). *J. Solid State Chem.* **110**, 419

[36] Marsh, D.B. and Parris, P.E. (1996). *Phys. Rev.* **B54**, 7720

[37] Goodenough, J.B. (1970). *Mat. Res. Bull.* **5**, 621

[38] Liu, N.-L. H. and Emin, D. (1984). *Phys. Rev.* **B30**, 3250

[39] Zvyagin, I.P. (1973). *Phys. Stat. Sol.* (b) **58**, 443

[40] Shafarman, W.N., Koon, D.W., and Castner, T.G. (1989). *Phys. Rev.* **B40**, 1216

[41] Castner, T.G. (1991). in *Hopping Transport in Solids* (ed. M. Pollak and B. Shklovskii), Vol. 28 of *Modern Problems in Condensed Matter Sciences* (Series eds. V.M. Agranovich and A.A. Maradudin), Elsevier Science Pub. B.V.

[42] Anderson, P.W. (1958). *Phys. Rev.* **109**, 1492

[43] Mott, N.F. (1990). *Metal-Insulator Transitions*, 2nd edn., Taylor & Francis Ltd

[44] Levine, I.N. (1988). *Physical Chemistry*, McGraw-Hill Book Co.

[45] Kachkachi, H., Kornilovitch, P., Meurdesoif, Y., Grenier, J.C., and Zhou, F. (1997). *J. Mag. Magnetic Materials*, accepted for publication

[46] Cox, P.A. (1992). *Transition Metal Oxides: An Introduction to their Electronic Structure and Properties*, Oxford

[47] Lide, D.R. and Frederikse, H.P.R. (Eds.) (1994). *CRC Handbook of Chemistry and Physics*, 75th edn., p. 10-205, CRC Press, Inc.

[48] Takano, M., Nakanishi, N., Takeda, Y. and Naka, S. (1979). *J. Phys. Colloq.* **40**, C2-313

[49] Takeda, Y., Naka, S., Takano, M., Shinjo, T., Takada, T., and Shimada, M. (1978). *Mat. Res. Bull.* **13**, 61

[50] Takeda, T., Yamaguchi, Y, and Watanabe, H. (1972). *J. Phys. Soc. Japan* **33**, 967

[51] Demourgues, A. (1992). Ph.D. Thesis, University Bordeaux I

[52] Gallagher, P.K., MacChesney, J.B., and Buchanan, D.N.E. (1964). *J. Chem. Phys.* **41**, 2429

[53] Wyckoff, R.W.G. (1964). *Crystal Structures*, 2nd edn., Vol. 2, p 394, John Wiley & Sons, Inc.

[54] Kanamaru, F., Miyamoto, H., Mimura, Y., and Koizumi, M. (1970). *Mat. Res. Bull.* **5**, 257

[55] Oda, H., Yamaguchi, Y, Takei, H. and Watanabe, H. (1977). *J. Phys. Soc. Japan* **42**, 101 and *J. Phys. Colloq.* C1, **38**, C1-121

[56] Smart, J.S. (1966). *Effective Field Theories of Magnetism*, W.B. Saunders Company

[57] Torrance, J.B., Lacorre, P., Asavaroengchai, C., and Metzger, R.M. (1991). *Physica C* **182**, 351

[58] Torrance, J.B., Lacorre, P., Asavaroengchai, C., and Metzger, R.M. (1991). *J. Solid State Chem.* **90**, 168

[59] Smith, G.S. and Snyder, R.L. (1979). *J. Appl. Crystallogr.* **12**, 60

[60] Battle, P.D., Gibb, T.C., and Nixon, S. (1989). *J. Solid State Chem.* **79**, 75

General Conclusions

Conclusion Générale

Ce travail avait pour but d'étudier le comportement électrochimique sous potentiel anodique de quelques ferrites de structures dérivées de la perovskite, déficitaires en oxygène. Les précurseurs sont les ferrites $SrFeO_{2.5}$ et $CaFeO_{2.5}$ de structure brownmillerite et $Sr_2LaFe_3O_8$ et $Ca_2LaFe_3O_8$ de type G appartenant à la série $AMO_{3-1/n}$ ($n = 2, 3, \cdots$, ou ∞). Leur aptitude à l'intercalation de l'oxygène a été systématiquement étudiée. Les phases contenant du strontium peuvent être oxydées, $SrFeO_3$ et $Sr_2LaFe_3O_{8.95}$ ont pu être ainsi préparées. En revanche, celles contenant du calcium ne présentaient aucune aptitude à l'oxydation électrochimique.

L'intercalation de l'oxygène est possible grâce à la présence de chemins de diffusion dans les plans de tétraèdres. Nous avons montré que trois types de fenêtres existaient : des fenêtres triangulaires, trapézoïdales et rectangulaires. Les études des interactions à courte et longue distance sur la base d'un modèle ionique ont montré que l'énergie totale nécessaire à la diffusion au sein des canaux dans $CaFeO_{2.5}$ était de façon significative la plus élevée. Une étude comparative a permis de corroborer ces études théoriques aux résultats expérimentaux, notamment à la difficulté d'oxyder les phases du calcium. Nous avons aussi émis l'hypothèse que les espèces O^- formées par transfert électroniques de l'oxygène vers le métal étaient les espèces diffusantes, car susceptibles d'abaisser les barrières de potentiels.

Utilisant la méthode électrochimique, nous avons préparé notamment $Sr_2LaFe_3O_{8.95}$ qui a été ensuite caractérisé en détail. D'un point de vue structural, le désordre Sr-La a été confirmé et la symétrie $R\overline{3}c$ adoptée.

L'évolution thermique de la susceptibilité magnétique de ce composé montre une transition brutale autour de 200 K qui a fait l'objet de toute notre attention. Elle est due à une coïncidence de la température d'ordre magnétique et de la dismutation du fer tétravalent selon la schéma suivant :

$$3\,Fe^{3.67+} \Leftrightarrow Fe^{(5-2\lambda)+} + 2\,Fe^{(3+\lambda)+} \qquad (\text{avec } 0 < \lambda < 0.67)\,.$$

valence moyenne paramagnétique	valence mixte antiferromagnétique

Cette dismutation de Fe^{4+} a été clairement mise en évidence par une étude de spectroscopie Mössbauer à basse température.

Dans l'état paramagnétique, les électrons d sont dans un état localisé, spin fort : $\mu_{Fe} = 5.46\ \mu_B$, valeur très proche de la valeur calculée ($\mu_{Fe}^{spin} = 5.30\ \mu_B$).

Les propriétés de transport caractérisent une semi-conduction de type hopping (petits polarons) dont l'énergie d'activation (0.13 eV) est due à l'activation de la mobilité des porteurs. Ce hopping électronique conduit à une valence moyenne du fer au delà de 200 K comme cela est confirmé par résonance Mössbauer.

Dans l'état antiferromagnétique, la susceptibilité magnétique varie peu : ceci a pu être modélisé sur la base de la structure magnétique particulière de ce matériau et les interactions d'échange ont été calculées.

La conductivité électrique suit une loi de Mott en $T^{-1/4}$ (variable-range hopping) en deçà de 100 K. Entre 100 et 195 K, le mécanisme de conduction est plus complexe, il implique à la fois une activation du nombre de porteurs et de leur mobilité.

La transition de phase électronique à 200 K a été étudiée en détail. Nous suggérons que la dismutation de charge se produit en même temps que la transition magnétique.

Les mesures de chaleur spécifique montrent que le changement d'entropie est $\Delta S_{exp} \approx 22.5$ J/mol·K, valeur sensiblement inférieure à celle calculée en supposant des valeurs entières Fe^{3+} et Fe^{5+} : ceci laisse supposer, comme le confirme la spectroscopie Mössbauer, que les charges ne sont pas entières ($Fe^{(5-\lambda)+}$ et $Fe^{(3+\lambda)}$).

Enfin nous avons montré que la variation d'énergie interne lors de la transition ($\Delta U \approx \Delta H = 4.33$ kJ/mol) était essentiellement due à l'ordre des spins. Les calculs thermodynamiques montrent aussi que la transition de phase est un phénomène intrinsèque qui ne nécessite pas une transition structurale qui par ailleurs n'est pas observée.

General Conclusions

The orthorhombic brownmillerite phases $SrFeO_{2.5}$, $CaFeO_{2.5}$ and G-type phases $Sr_2LaFe_3O_8$, $Ca_2LaFe_3O_8$ are, respectively, the n = 2 and n = 3 members in the series of $AMO_{3-1/n}$ (n = 2, 3,···, or ∞). The main structural features of these phases are the arrangement of (n-1) sheets of MO_6 octahedra (**O**) alternating with one sheet of MO_4 tetrahedra (T), as well as the ordered oxygen vacancy rows in their tetrahedral layers which are along the $[101]_C$ direction of related cubic perovskite cells (*i.e.* the ***a***-direction of their proper lattices for the setting used in this thesis). That results in **OTOT'** and **OOT** polyhedral stacking sequences for the brownmillerite structure and the G-type structure, respectively, and the characteristic cell dimensions which are related to the cubic one (a_c) as $a_n \approx \sqrt{2} \cdot a_c$, $b_n \approx (6\text{-n}) \cdot a_c$, and $c_n \approx \sqrt{2} \cdot a_c$. The experimental observation of $c_n > a_n$ can be attributed to the presence of the oxygen vacancy rows.

In this thesis work, (I) the electrochemical behaviors (under oxidation conditions) of these oxygen-deficient ferrites (the precursors) are systematically studied, (II) their different capabilities of oxygen intercalation are analyzed and explained, and (III) some physical properties of perovskite phase $Sr_2LaFe_3O_{8.95}$ (obtained by electrochemical oxidation) are investigated. The main conclusions are given in the following.

(I). Using electrochemical method (of both potentiostatic and galvanostatic modes under ambient conditions), the perovskite phase $Sr_2LaFe_3O_{8+\delta}$ (δ up to ~0.90, the averaged value according to chemical analysis) is prepared by intercalating oxygen into its precursor $Sr_2LaFe_3O_8$ (G-type phase). Increasing temperature (T < 90°C) makes the intercalation more rapid at lower oxygen concentrations but not at higher ones, and it does not increase the oxidation degree.

At a given temperature, the highest intercalation rate (indicated by the highest oxidation current) is observed at intermediate oxygen concentrations. It seems that, at lower oxygen concentrations, the intercalation rate is limited by the high electrical resistivity of the precursor which decreases with oxygen intercalation, so that the intercalation rate increases with the concentration; while at higher oxygen concentrations it is diffusion-determined, so that the intercalation rate decreases with increasing oxygen concentration.

Similarly, the cubic perovskite phase $SrFeO_{2.5+\delta}$ ($\delta = 0.34 \sim 0.40$) can also be obtained from the orthorhombic precursor $SrFeO_{2.5}$ (brownmillerite phase) by electrochemical oxygen intercalation.

Results show that the electrochemical method is also efficient for intercalating oxygen into some precursors having high resistivity (~ 10^8 Ω·cm), provided that their resistivity would decrease considerably with oxygen intercalation.

However, our attempts were not successful to oxidize, using this electrochemical method, the Ca-containing brownmillerite phase $CaFeO_{2.5}$ and G-type phase $Ca_2LaFe_3O_8$, although their structures are similar to those of the Sr-containing ferrites.

(II). For the ionic crystal structures of the brownmillerite and G-type phases, the oxygen intercalation is via their oxygen vacancy rows (the diffusing channels). We show that the widths of these diffusing channels can be described by the radii of three periodic polygonal "windows" along the channels, they are so-called trapezoid window, triangular window and rectangular window. Among them, the triangular window is the narrowest for each phase.

In the initial stage of the oxygen intercalation, effects such as interactions between diffusing oxygen atoms and variations in the host lattices are not important. From a viewpoint of ionic structure, the interaction energy involved in the oxygen diffusion in this stage depends mainly on two kinds of interactions between diffusing oxygen anion and ions in the host lattices of the precursors :

- One is ***the short-range Pauli interaction*** which involves mainly the lattice ions forming the channel "windows" and becomes important when the diffusing oxygen squeezes between them. The narrower the windows (the channels), the stronger the interaction (the Pauli repulsion).
- Another is ***the long-range Coulomb interaction*** between the electric charges of the diffusing oxygen anion and of the lattice ions. It is related to the ionic arrangement in the structures of the precursors.

Based on available crystallographic data and ionic model, the interaction energies of the above origin are estimated and calculated for brownmillerite $Ca_2Fe_2O_5$, $Sr_2Fe_2O_5$ and G-type $Sr_2LaFe_3O_8$ phases. The results show that the oxygen intercalation capabilities of the three phases are determined by these two interactions at the triangular or the trapezoid window centers, and that ***the total interaction energy experienced by an oxygen anion diffusing along the channels in $Ca_2Fe_2O_5$ structure is significantly higher than the corresponding energies in the other two structures.***

The difference in the interaction energies involved in the three ferrites explains why they exhibit different oxygen intercalation capabilities under electrochemical conditions as well as, to a certain extent, under high oxygen pressures. The situation of $Ca_2LaFe_3O_8$ may be assumed to be similar to that of $Ca_2Fe_2O_5$.

It is suggested that the oxygen species involved in the diffusion process may be O^- but not O^{2-}, in the sense that a lower energy barrier (of both the Coulomb and the Pauli interaction origin) is expected for O^-, so that its diffusion may be facilitated.

(III). Some physical properties of perovskite phase $Sr_2LaFe_3O_{8.95}$

We have confirmed by powder XRD analysis that the A-site Sr^{2+} and La^{3+} ions in this phase are disorderly distributed and that no structural transition and discontinuity in the cell dimensions occur from 300 K down to 80 K. According to previous report, the $R\bar{3}c$ symmetry is adopted for the structure, which is viewed as distorted from the cubic perovskite structure (having $Pm\bar{3}m$ symmetry) by coordinate shifts of oxygen atoms, although the XRD data are not sufficient to decide between the $Pm\bar{3}m$ and $R\bar{3}c$ symmetries in this case (the reason is analyzed).

This perovskite exhibits an abrupt magnetic transition (paramagnetic ⇔ antiferromagnetic) over a narrow temperature range of about 180 K to 200 K, which is associated with a simultaneous disproportionation of iron charge (averaged-valence ⇔ mixed-valence), *i.e.*, referring to $Sr_2LaFe_3O_9$ for simplicity, $3\ Fe^{3.67+} \Leftrightarrow Fe^{(5-2\lambda)+} + 2\ Fe^{(3+\lambda)+}$ (with $0 < \lambda < 0.67$). The two critical temperatures (the Néel and disproportionation temperatures) coincide at $T_N = T_D = 196$ K based on various measurements.

(a) in the paramagnetic region, iron *d*-electrons are in localized high-spin states. The magnetic moment per iron obtained according to the Curie-Weiss law is $\mu_{Fe} = 5.46\ \mu_B$, which, being close to the estimated spin-only value ($\mu_{Fe}^{spin} = 5.30\ \mu_B$), reflects the quenching of the orbital moment of ${}^5E_g$ (Fe^{4+}) state by the chemical environment as theoretically predicted. In the vicinity of the Néel temperature, however, the Curie-Weiss law is somewhat deviated due to short-range spin ordering.

The electron transport (with a constant carrier concentration $n_e = n_{Fe^{3+}} = 6.29\times10^{21}\ cm^{-3}$) is by hopping of e_g-electrons localized on Fe^{3+} sites (small polarons) to nearest-neighboring Fe^{4+} sites, *i.e.* $\underset{Fe^{3+}}{(Fe^{4+}+e^-)} + Fe^{4+} \Leftrightarrow Fe^{4+} + \underset{Fe^{3+}}{(Fe^{4+}+e^-)}$; the activation energy associated with the hopping mobility is 0.13 eV according to conductivity data. This electron hopping results in the averaged valence state intermediate between Fe^{3+} and Fe^{4+}, as is observed in Mössbauer experiments.

The corresponding Seebeck coefficient, which decreases slightly with rising temperature, can be well accounted for by combined contributions of configurational and vibrational entropies, electronic spin and orbital degeneracies, as well as spin polarization effect.

(b) in the antiferromagnetic region , the conductivity obeys Mott $T^{-1/4}$ law for T = 60 K ~ 100 K, which is related to the variable-range hopping at partially occupied e_g-levels of the nominal Fe^{5+} states where the Fermi level is pinned; while the Seebeck coefficient is proportional to 1/T (but not to $T^{1/2}$, the reason is given). Between 100 K and 195 K, the conductivity behavior cannot be described by a single mechanism – both the carrier concentration and carrier mobility contribute significantly to the temperature dependence of the conductivity.

We show that, if the temperature dependence of the Seebeck coefficient $\alpha(T)$ is determined by the dependence of the site ratio $c(T)$, the reduced Seebeck coefficient α' ($= \frac{\alpha}{(k_B/e)\ln 10}$) will generally exhibit the same temperature dependence as the logarithm of carrier concentration ($\log[n(T)]$).

At temperatures below the transition region, e_g-electrons are considered to hop via nominal iron Fe^{5+} sites with parallel spins, giving rise to a spin polarization effect. As a consequence, the magnetic susceptibility displays an unusual almost temperature-independent behavior. Upon entering the transition region, however, the susceptibility increases abruptly with temperature. This abrupt behavior of the magnetic transition can be attributed to temperature-dependent effective exchange integrals which are associated with the charge disproportionation. Theoretically, this phenomenon can be well described by using a non-Heisenberg biquadratic Hamiltonian in addition to the Heisenberg one, as it is shown by our calculations in the mean field approximation (a cooperative work).

Magnetic measurements also reveal that the susceptibility increases with the field for $H > \sim 7000$ Oe. It could be explained by the effect of anisotropy, being consistent with the previously reported magnetic structure model.

(c) about the electronic phase transition. We suggest that, when temperature rises, the electronic phase transition first occurs in defective regions (where the magnetic and/or the crystal structure are mismatched and disturbed) just before the whole system is transformed. This mechanism accounts for the two-peak anomaly (at 189K and 196K) in the specific heat data and the coexistence of the two electronic phases over the transition temperature range.

The entropy change of the transition obtained from the specific heat data is $\Delta S_{exp} \approx 22.5$ J/mol·K, which is much smaller than that calculated using Boltzmann formula for the ideal cases. It confirms that, at least in the measured temperature range below the ordering temperature, the valence states of Fe^{3+} and Fe^{5+} and the spin densities of $S_{Fe^{3+}}=5/2$ and $S_{Fe^{5+}}=3/2$ are more nominal than real (*i.e.* the charges and the spins are not ideally ordered), which is in agreement with the Mössbauer data.

From the specific heat data, the internal energy and enthalpy changes associated with the electronic phase transition are obtained to be $\Delta U \approx \Delta H = 4.33$ KJ/mol. The internal energy change is the sum of three contributions: the superexchange interaction energy (ΔU^{spin}), the change in the Madelung energy (ΔE_M) and the energy arising from Hubbard-like iron-to-iron charge transfer (ΔE_{CT}). The first two effects lower the energy, the last one increases the energy. The energy change only involved in the charge disproportionation is given by $\Delta U^{ch} = \Delta E_M + \Delta E_{CT}$.

We show that, from a general thermodynamic point of view, in a system where both spin coupling and charge disproportionation are possible, its transition behavior, involving order-disorder of the spin and charge states, depends on the competition and correlation between these two effects:

- If the charge disproportionation energy $\Delta U^{ch} < \Delta U^{ch}_{crit}$ ($= \frac{\Delta S^{conf}}{\Delta S^{spin}} \cdot \Delta U^{spin}$, a critical value), the disproportionation will occur at a higher temperature, then follows a spin ordering at a lower temperature. The system $CaFeO_3$ is an example for this case.
- If $\Delta U^{ch} > \Delta U^{ch}_{crit}$, a spin ordering will definitely occur. The occurrence or non-occurrence of a charge ordering depends on the particular correlation between the spin and charge orderings. The perovskites $Sr_2LaFe_3O_{8.95}$ and $SrFeO_3$ are two different examples.

In the system of $Sr_2LaFe_3O_{8.95}$, due to the compensation between the effects of Hubbard-like energy and Madelung energy, the energy change ΔU^{ch} associated with the charge ordering is greater than the critical value ΔU^{ch}_{crit} and close to zero, so that the charge ordering cannot occur independently in the paramagnetic region. On the other hand, when the spin ordering occurs, the charge ordering is necessarily involved. As a consequence, the changes in the spin and charge states occur simultaneously at about 200K, which is a temperature intermediate between the hypothetical temperatures for independent spin and charge orderings.

Since the charge disproportionation energy $\Delta U^{ch} \approx 0$, the observed internal energy change ($\Delta U = 4.33$ KJ/mol) during the transition in $Sr_2LaFe_3O_{8.95}$ is mainly contributed by the spin ordering, *i.e.* $\Delta U \approx \Delta U^{spin}$.

The thermodynamic calculation also suggests that the electronic phase transition in $Sr_2LaFe_3O_{8.95}$ is an intrinsic behavior of the electronic states, and needs not to be intervened by a structural distortion with a volume change $\Delta V < 0$ (at decreasing temperature).

However, it is all the same surprising that no periodic atomic displacements accompany the charge ordering in this perovskite. We show that this phenomenon may originate mainly from the involved superexchange and Pauli interactions which compete with the Coulomb interactions.

In addition, the electron localization observed in $Sr_2LaFe_3O_{8.95}$ can be explained by combined effects such as the Anderson localization caused by a random field arising from the disorder of Sr^{2+} and La^{3+} ions, the self-trapping due to small polaron formation (for $T > T_N$) and the spin and charge orderings (for $T < T_N$).

From the specific heat data, the Debye temperature Θ_D of $Sr_2LaFe_3O_{8.95}$ is estimated to be around 300 K.

Appendix I

Magnetic and Thermodynamic Properties of $Sr_2LaFe_3O_9$ (theoretical calculations)

Magnetic and thermodynamic properties of $Sr_2LaFe_3O_9$*

H.Kachkachi[a], P.Kornilovitch[b], and Y.Meurdesoif[a]

[a]*CPTMB, CNRS-URA 1537, University Bordeaux I, Rue du Solarium, 33174 Gradignan Cedex, France*

[b]*King's College, Strand, London WC2R 2LS, UK.*

J.-C. Grenier, and F. Zhou

ICMCB, CNRS, Avenue du Docteur A. Schweitzer, 33608 Pessac Cedex France

We use a Dirac-Heisenberg Hamiltonian with biquadratic exchange interactions to describe the first-order magnetic transition occurring in the perovskite $Sr_2LaFe_3O_9$. Up on fitting the experimental curve for the magnetic susceptibility below and above the Néel temperature, we give an estimate of the exchange integrals for the antiferromagntic and ferromagnetic interactions in this compound. Within linear spin-wave theory we find that the magnon spectrum comprises a gapless antiferromagnetic mode together with two gapped ferromagnetic ones.

PACS numbers: 75.10Jm, 75.50Ee

keywords : antiferromagnetic-ferromagnetic ordering, biquadratic interactions, first-order magnetic transition.

Corresponding author: kachkach@bortibm4.in2p3.fr

***To appear in Journal of Magnetism and Magnetic Materials**

I. INTRODUCTION

Since the discovery of high-T_c copper-oxide superconductors [1], investigations of superconductivity and magnetism of d-electron based oxides with perovskite structure have gained new interest. Iron based oxides are not superconducting, but exhibit interesting electronic properties such as disproportionation as in $CaFeO_3$ or metalic properties as in $SrFeO_3$. In addition, these ferrites often shown very peculiar magnetic properties.

Almost stoichiometric $Sr_2LaFe_3O_{9-\delta}$, ($\delta \simeq 0$) can be prepared under air by long annealing at $200°C$ or using electrochemical oxidation in alkaline solution [2], [3], [4]. All reported data of structural and physical properties show very similar features.

The low-temperature Mossbauer data for the perovskite $Sr_2LaFe_3O_{8.94}$ studied in [2] are consistent with a $2:1$ ratio of the two types of Fe cation with electronic characteristics fairly close to Fe^{3+} and Fe^{5+}, respectively. The Neutron-Powder-Diffraction data at $50K$, show clear evidence that the low temperature phase exhibits an antiferromagnetic ordering [2]. More precisely, there is antiferromagnetic ordering among subcells of ferromagnetically-ordered spins. At room temperature only is observed an average value of the charge, which demonstrates the existence of a fast electron transfer.

So, upon heating the compound passes from a mixed-valence phase through a first-order transition to the paramagnetic average-valence phase. Experimental data [3] for the specific heat show two peaks, the highest of which seems to be related to a first-order phase transition. The smaller peak, on the other hand, disappears as one fills in more oxygen vacancies in the sample, as was shown by the data of ref. [4] for the sample $Sr_2LaFe_3O_9$, where the specific heat only shows one (large) peak at about the same temperature as in [3].

The inverse magnetic susceptibility for $Sr_2LaFe_3O_{8.94}$ shows [2] an abrupt change at about $200K$ with a minimum indicative of a transition to antiferromagnetic ordering; and above this temperature the susceptibility is almost field-independent; while below there is a pronounced dependence on the magnetic field which appears to be an intrinsic property of the phase, and suggests the possibility of a (weak) ferromagnetism, probably due to spin mis-alignment. The same sharp jump in the magnetic susceptibility is reported in refs. [3] and [4].

According to previous structural studies [2], this compound exhibits an almost cubic perovskite structure, the rhombohedral distortion being very small and not detectable by X-Ray Diffraction analysis. The magnetic structure was determined from the Neutron-Diffraction data [2] and is shown in figure 1.

The coupling between iron cations is of a superexchange-type via oxygen anions. However, the usual approximation consists in treating the system as that of iron cations interacting via an effective exchange integral. More precisely, in our case the coupling between two Fe^{3+} ions is antiferromagnetic with the exchange constant denoted henceforth by[1] J_a, while that between Fe^{3+} and Fe^{5+} is ferromagnetic with the constant J_f, while there is no coupling between two cations Fe^{5+}, as this would occur along the diagonal of the (slightly deformed) elementary cube, and thus would be negligible in comparison with the other two couplings (see figure 1). In our particular case, these exchange integrals are obtained by fitting the experimental data with a model of localized spins with two kinds of nearest-neighbor interactions.

Accordingly, we consider a model that describes a system of 6 localized spins, four of $\frac{5}{2}$ and two of $\frac{3}{2}$, based on a Dirac-Heisenberg Hamiltonian with antiferromagnetic and ferromagnetic couplings J_a, J_f, respectively and taking into account the corresponding biquadratic interactions, denoted by j_a, j_f. The latter are known [5] to induce a first-order transition because of the strong change of the exchange interactions as a function of the interatomic distances, and also the associated change in the elastic energy of the material. The characteristic and very significant feature of such magnetic-transformation mechanism is the sharp change of the elastic constants of the crystal in the absence of any volume changes in the region of the antiferromagnetic transformation [5]. In our case, the exchange-induced dis-

---

[1] The subscripts a and f refer to antiferromagnetic and ferromagntic orderings, respectively.

tortion of the crystal is of an order of magnitude too small [2], [3] to be responsible for the change of the order of the magnetic transition. In fact, it was pointed out in [6] and then shown in [7] that the usual superexchange mechanism is fully capable of explaining the origin and magnitude of the biquadratic exchange interaction. Also Nagaev ([8], section 2.7) studied the interplay between Dirac-Heisenberg and different kinds of non-Dirac-Heisenberg interactions and the role of the latter in changing the order of the magnetic transition viz in MgO, MnO and NiO. Moreover, since the spins in our case are much larger than $\frac{1}{2}$, more excited spin states start to participate in increasing the entropy of the system, and the two-level-system approximation no longer holds as the temperature increases. Therefore, in order to account for this effect, we must add higher-order terms to the Dirac–Heisenberg Hamiltonian. Accordingly, we shall add nearest-neighbor biquadratic interactions which, from the physical point of view could account for the effect of charge disproportionation occurring in our compound. Next, we show that indeed the biquadratic contributions to the exchange energy account for the first-order magnetic transition occurring in $Sr_2LaFe_3O_9$, and which is reflected by a sharp jump in the magnetic susceptibility and large peak in the specific heat. Consistently, we also predict an anomalous behavior for the sublattice magnetizations, i.e. the jump down to zero in the vicinity of the Néel temperature. Indeed, we obtain a good fit of the experimental data on the specific heat and the magnetic susceptibility in both the ordered and disordered phases for the exchange interactions $\frac{J_a}{k_B} \simeq 26K$, $\frac{J_f}{k_B} \simeq 6.5K$; and the corresponding biquadratic exchange integrals $j_a \simeq 0.11 \times J_a$ and $j_f \simeq 0.08 \times J_f$.

Note that the antiferromagnetic exchange integral J_a between two iron ions Fe^{3+} in perovskite compounds such as $LaFeO_3$ was also estimated by Anderson [10] who found $J_a \simeq 26K$, and a close value, $24K$, was also found by Grenier et al. [11] in $Ca_2Fe_2O_5$ with similar perovskite structure.

Next, we compute the magnon spectrum within the approach of linear spin-wave theory. The spectrum contains a gapless antiferromagnetic mode and two gapped ferromagnetic branches. Unfortunately, to the best of our knowledge, there are so far no experimental data on the Inelastic-Neutron Scattering for the present powder sample. However, to account for the anomalous behavior of the sublattice magnetizations near the transition point, it turns out that non-linear spin-wave corrections are necessary.

II. THEORY

a. Hamiltonian The unit cell of our system is sketched in figure 1, and the Dirac-Heisenberg Hamiltonian for such system can be written as

$$H_{DH} = -J_f \sum_{\langle i,j \rangle} \sum_{\alpha,\beta} \mathbf{s}_{i\alpha} \cdot \mathbf{S}_{j\beta} + J_a \sum_{\langle i,j \rangle} \sum_{\alpha,\beta} \mathbf{S}_{i\alpha} \cdot \mathbf{S}_{j\beta} \tag{1}$$

where henceforth $\mathbf{S}, \mathbf{s}$ denote the spins $\frac{5}{2}$ of Fe^{3+}, and $\frac{3}{2}$ of Fe^{5+}, respectively. $\sum_{\langle i,j \rangle}$ denotes the sum over all pairs of nearest-neighbor sites i, j; each Fe^{5+} ion having six Fe^{3+} ions as nearest-neighbors, while the nearest-neighbors of each Fe^{3+} ion are three Fe^{3+} and three Fe^{5+}. The sum $\sum_{\alpha,\beta}$ runs over the six different atoms in the unit cell, see figure 1.

Then to the Hamiltonian (1) we add the following non-Dirac-Heisenberg Hamiltonian of nearest-neighbor biquadratic interactions

$$H_{NDH} = -j_f \sum_{\langle i,j \rangle} \sum_{\alpha,\beta} (\mathbf{s}_{i\alpha} \cdot \mathbf{S}_{j\beta})^2 - j_a \sum_{\langle i,j \rangle} \sum_{\alpha,\beta} (\mathbf{S}_{i\alpha} \cdot \mathbf{S}_{j\beta})^2 \tag{2}$$

Note that we have adopted the convention that all exchange couplings J_a, J_f, j_a, j_f are positive.

Within the mean-field (MF) approximation it turns out that in fact the effect of adding these biquadratic interactions is to redefine the exchange integrals J_a and J_f, into temperature-dependent effective ones as follows

$$\begin{aligned} J_a &\longrightarrow J_a^{eff} = J_a + 2j_a \langle S \rangle^2 \\ J_f &\longrightarrow J_f^{eff} = J_f + 2j_f \langle S \rangle \langle s \rangle \end{aligned} \tag{3}$$

where $\langle S \rangle$ and $\langle s \rangle$ are the spontaneous sublattice magnetizations on the sites Fe^{3+} and Fe^{5+}, respectively. The same is also true within spin-wave theory, see sect.4. However within the linear-spin-wave approximation the effective couplings J_a^{eff}, J_f^{eff} are independent of temperature since in this case the spins S and s are respectively substituted for the sublattice magnetizations $\langle S\rangle$ and $\langle s\rangle$.

As was demonstrated by Nagaev [8], all non-Dirac-Heisenberg interactions, biquadratic in our case, change the order of the magnetic transition from second to first. It is readily seen in (3) that the effective exchange integrals decrease in magnitude with decreasing magnetizations because of a decrease in the order parameters $\langle S\rangle$ and $\langle s\rangle$. Inversely, a decrease in the effective exchange integrals in turn leads to a decrease in the magnetizations, i.e. there is a positive feedback effect. This brings about the change in the order of the transition as the ratio, $\frac{j}{J}$ in the present case, between the non-Dirac-Heisenberg and the Dirac-Heisenberg interaction reaches a certain critical value.

Henceforth, to avoid writing cumbersome formulae, we shall only give the expressions for physical quantities derived from the Hamiltonian (1), but keeping in mind that all calculations are done using the effective exchange integrals J_a^{eff}, J_f^{eff} defined in (3).

b. Spontaneous magnetizations Within the MF approximation the order parameters $\langle S\rangle$, $\langle s\rangle$ are found to satisfy the following coupled self-consistent equations

$$\begin{aligned} \langle S\rangle &= B_S\left(z\beta\left[J_a\langle S\rangle + J_f\langle s\rangle\right]\right) \\ \langle s\rangle &= B_s\left(2z\beta J_f\ \langle S\rangle\right) \end{aligned} \tag{4}$$

where $\beta = \frac{1}{k_B T}$, and $B_j(x)$ is the usual Brillouin function

$$B_j(x) = (j+\frac{1}{2})\coth(j+\frac{1}{2})x - \frac{1}{2}\coth\frac{x}{2}$$

and $z = 3$, i.e. half the number of nearest neighbors of an atom.

Upon making the substitutions (3) the self-consistent equations (4) become more complicated and then they can be solved only numerically. The corresponding solution is shown in solid lines in figure 2, for the values of the exchange integrals obtained by fitting the experimental data on the specific heat and magnetic susceptibility, see sect.3 below.

c. Susceptibility We have computed the magnetic susceptibility both in the ordered and paramagnetic phases following the generalized mean-field approach of Smart [9]. For this purpose, we use the fact that the spontaneous magnetizations given by eqs.(4) exhibit the following antiferromagnetic-ferromagnetic arrangement at $T < T_N$ (see figure 1)

$$\langle \mathbf{S}_2 \rangle = -\langle \mathbf{S}_3 \rangle = -\langle \mathbf{S}_5 \rangle = \langle \mathbf{S}_6 \rangle\,, \quad \langle \mathbf{s}_1 \rangle = -\langle \mathbf{s}_4 \rangle \tag{5}$$

Thereby we obtain the following expressions for the transverse magnetic susceptibility,

$$\chi_{\perp} = \alpha \times \frac{J_f \left(2\langle S\rangle + \langle s\rangle\right)^2 + 2J_a \langle S\rangle \langle s\rangle}{2zJ_f J_a \ \langle S\rangle^2} \tag{6}$$

and parallel susceptibility[2]

$$\chi_{||} = \alpha \times \frac{2T \cdot \left(2B_S'(y_0^S) + B_s'(y_0^s)\right) + 2z \cdot \left(J_a + 4J_f\right) B_s'(y_0^s) B_S'(y_0^S)}{T^2 + zJ_a T \cdot B_S'(y_0^S) - 2z^2 J_f^2 \ \cdot B_s'(y_0^s) B_S'(y_0^S)} \tag{7}$$

where

$$y_0^s = \left(2zJ_f \langle S\rangle\right)\beta, \qquad y_0^S = z\left(J_f \langle s\rangle + J_a \langle S\rangle\right)\beta$$

and have introduced the conversion coefficient $\alpha = \mu_0 (g\mu_B)^2 N_c / k_B$. With $g = 2$, and $N_c = \frac{N_A}{2}$, N_A being the Avogadro number, as there are two molecules of the sample in the unit cell.

It is worthwhile to note that the transverse susceptibility (6) is a decreasing function of temperature.

Now, as we are dealing with powder sample, the total magnetic susceptibility below the Néel temperature is given by

$$\chi(T) = \frac{1}{3}\chi_{||} + \frac{2}{3}\chi_{\perp}$$

Next, in the paramagnetic phase the total magnetic susceptibility is found to be

$$\chi_{PM} = \alpha \times \frac{2}{z} \cdot \frac{y + 2x + J_a - 4J_f}{xy + J_a x - 2J_f^2} \tag{8}$$

where

---

[2] Here the prime stands for the derivative of the Brillouin function $B(x)$with respect to x.

$$x=\frac{3k_BT}{z}\frac{1}{s(s+1)},\qquad y=\frac{3k_BT}{z}\frac{1}{S(S+1)}$$

One can check that as $T\to T_N$, $B_j'(x)\to\frac{j(j+1)}{3}$, so that eq.(7) reduces to eq.(8), and at $T=T_N$, we get $\chi_\perp=\chi_\parallel=\chi_{PM}$.

d. Entropy Within the foregoing approach the entropy (per atom) of the system reads

$$\frac{S(T)}{N_c}=2\left[\log\left(C_\sigma(\beta A)\right)-\beta A\left\langle s\right\rangle\right]+4\left[\log\left(C_S(\beta B)\right)-\beta B\left\langle S\right\rangle\right] \tag{9}$$

where $A=2zJ_f\left\langle S\right\rangle$, $B=z\left[J_a\left\langle S\right\rangle+J_f\left\langle\sigma\right\rangle\right]$, and $C_j(x)=\frac{\sinh\left[(2j+1)\frac{x}{2}\right]}{\sinh(\frac{x}{2})}$.

When plotted as a function of temperature, for the exchange couplings obtained below, the entropy (9) increases with increasing temperature up to the Néel point where it exhibits an abrupt jump characteristic of a first-order transition, and then it saturates to a constant given by the configurational entropy in the paramagnetic phase.

e. Specific heat The specific heat within the same approximation is given by[3]

$$\frac{C_v}{N_c}=-2z\cdot\left(J_a\cdot\left\langle S\right\rangle\partial_T\left\langle S\right\rangle+J_f\cdot\left[\left\langle s\right\rangle\partial_T\left\langle S\right\rangle+\left\langle S\right\rangle\partial_T\left\langle s\right\rangle\right]\right) \tag{10}$$

for $T\lesssim T_N$.

Above T_N the mean-field approximation yields a zero specific heat since in this temperature range the order parameters and thereby the free energy vanish, see figure 4.

III. RESULTS AND DISCUSSION

The Dirac-Heisenberg model including the biquadratic interactions studied here has been written for the ideal compound $Sr_2LaFe_3O_9$ with no oxygen vacancies. On the other hand, the compound with the closest composition to the latter was studied experimentally by Wang et al. in [4]. Therefore, we believe that our theory is more suitable for fitting the experimental data of ref. [4] than those of [2] or [3], especially from the quantitative point

---

[3] ∂_T stands for the derivative with respect to temperature.

of view. However, we also obtain good qualitative agreement with the authors of refs. [2], [3].

A reasonable (numerical) fit to the experimental data [4] on the magnetic susceptibility and specific heat given in figures 3 and 4, led to the following values of the exchange integrals and biquadratic interactions

$$\frac{J_a}{k_B} \simeq 26K, \qquad \frac{J_f}{k_B} \simeq 6.5K \tag{11}$$
$$j_a \simeq 0.11 \times J_a, \quad j_f \simeq 0.08 \times J_f$$

As was mentioned in the introduction, the value of the antiferromagnetic exchange integral J_a found here is in agreement with the ones obtained by Anderson [10], i.e. $J_a \simeq 26K$ in $LaFeO_3$, or by Grenier et al. [11], that is $24K$ in $Ca_2Fe_2O_5$.

For these couplings we find that the sublattice magnetizations exhibit a sharp drop at the Néel temperature indicating that the transition is of first order, see figure 2. This behavior is also reflected in the magnetic susceptibility, which exhibits a sharp jump at the transition, in agreement with the susceptibility measured by Wang et al. [4] and also with the one reported by Zhou et al. [3], see figure 3. We see that the susceptibility curve obtained within the mean-field theory fits both qualitatively and quantitatively to the one measured by Wang et al. [4], however the authors of ref. [3] obtain a larger jump at the critical temperature.

In addition, the jump in the entropy (9) is indicative of a first-order transition, and yields the latent heat released by the system at the transition. Accordingly, for the exchange integrals found above, we find that the contribution of magnetic excitations to the latent heat is given by the product of the jump in the corresponding entropy at the critical temperature and the latter, i.e. $Q(T_N) = T_N \times \Delta S \simeq 2.9\ KJ/mole$. The experimental enthalpy found by Zhou et al. [3] is $\Delta H \simeq 3.7\ KJ/mole$, which is the total enthalpy of the system.

Consequently, the specific heat obtained within the mean-field approximation (10) diverges at the Néel temperature. In the magnetically ordered phase and around the transition we obtain a good fit of this to the experimental curve obtained by Wang et al. [4], see figure 4. As is well known the mean-field theory cannot be correct above the Néel temperature, for it predicts the absence of short-range order. In particular, in our case the specific heat computed within mean-field approximation drops to zero for $T > T_N$, since then the order parameters vanish, i.e. $\langle S \rangle = \langle s \rangle = 0$. Alternatively we have computed the contribution to the specific heat (10) in the paramagnetic phase using the appraoch of high-temperature expansion, but this does not yield a significant contribution. We have also taken into account that we are only dealing with the contribution of magnetic excitations to the transition while leaving out the lattice component.

To derive the Curie-Weiss law for the magnetic susceptibility in the paramagnetic phase, we note that the denominator in (8) is quadratic in temperature, and thus leads to a hyperbolic function of temperature, as in the case of a ferrimagnet. However the high temperature asymptote to the hyperbola does have the Curie-Weiss law form, that is

$$\chi = \frac{C_a}{T - \theta_a} \tag{12}$$

with

$$C_a \simeq 12, \quad \theta_a \simeq -228K$$

in fair agreement with the experimental result [2], [3]

$$C = 11.4, \qquad \theta = -250K$$

In the paramagnetic phase, we can also estimate the average magnetic moment corresponding to the average valence of iron. Indeed, the relationship between the magnetic moment per atom and susceptibility

$$\mu = \sqrt{8 \times \chi(T - \theta_a)} = 2.83 \times \sqrt{\frac{C_a}{3}}$$

yields for iron

$$\mu(Fe) = 2.83 \times \sqrt{\frac{C_a(Fe)}{3}} \simeq 5.66\mu_B$$

which agrees with the value found by Battle et al. [2], that is $5.55\mu_B$.

IV. SPIN WAVE THEORY

f. Spectrum Within the linear spin-wave theory based on the Holstein-Primakoff representation [12] of spin operators ($\frac{1}{S}$ expansion), we find three doubly-degenerate magnon branches, as shown in figure 5. The explicit expressions of the corresponding magnon energies are rather messy and we omit writing them here. Nonetheless, around the point $\Gamma, k = (0,0,0)$, located at the center of the Brillouin zone we can write,

$$\begin{aligned}
\hbar\omega_1(k) &= \sqrt{\rho^1_{xy} \cdot (k_x^2 + k_y^2) + \rho^1_z \cdot k_z^2} \\
\hbar\omega_2(k) &= \sqrt{\Delta_1 + \rho^2_{xy} \cdot (k_x^2 + k_y^2) + \rho^2_z \cdot k_z^2} \\
\hbar\omega_3(k) &= \sqrt{\Delta_2 + \rho^3_{xy} \cdot (k_x^2 + k_y^2) - \rho^3_z \cdot k_z^2}
\end{aligned} \tag{13}$$

where the gaps Δ_1 and Δ_2 are given by

$$\begin{aligned}
\Delta_1 &= \frac{9J_f}{4}\left[2J_a\, sS + J_f(2S + s)^2\right] \\
\Delta_2 &= \frac{9J_f}{4}\left(2J_a sS + J_f s^2\right)
\end{aligned}$$

and the spin stiffness coefficients ρ^1_{xy}, ρ^1_z, etc., are (cumbersome) functions of the exchange integrals. Recall that the exchange integrals J_a and J_f must be redefined using eq.(3) and taking into account the fact that in the linear-spin-wave approximation the sublattice magnetizations $\langle S \rangle$ and $\langle s \rangle$ are replaced by their nominative values $S = \frac{5}{2}$ and $s = \frac{3}{2}$, respectively.

It is seen in figure 5 that the first of the spectrum branches, the lowest curve, is gapless and of antiferromagnetic type. Whereas, the second and third branches, the upper ones, represent gapped ferromagnetic modes. We have assumed here that the anisotropy is too small to produce a gap in the magnon spetrum at temperatures the latter is obtained.

Therefore, the spectrum above shows that we have antiferromagnetic ordering at low temperature, together with a "weak ferromagnetic ordering" that starts propagating upon heating. As discussed in the introduction, it should be interesting to compare our results for the magnon spectrum with the experimental data, were Inelastic-Neutron Scattering measurements possible on the compound $Sr_2LaFe_3O_9$. This would also allow us to compare the spin stiffiness coefficients we have found here with the experimental ones, and then determine the effective magnetic moments of Fe^{3+} and Fe^{5+} at zero temperature, and thereby estimate their reduction by quantum fluctuations.

g. Brillouin zone The Brillouin zone is a $3D-$hexagon (see figure 5) whose edges are defined by

$$\frac{-\pi}{\sqrt{6}} \le k_z \le \frac{\pi}{\sqrt{6}}, \ \frac{-2\pi}{\sqrt{3}} \le k_y \le \frac{2\pi}{\sqrt{3}}, \ -\left|\frac{4\pi}{3} - \frac{|k_y|}{\sqrt{3}}\right| \le k_x \le \left|\frac{4\pi}{3} - \frac{|k_y|}{\sqrt{3}}\right|.$$

h. Thermodynamic quantities The ground-state energy per site is given by

$$\frac{E_g}{N_c} = H_0 + \frac{1}{N_c}\frac{\sqrt{18}}{2}\sum_{\nu=1}^{3}\int_{B.Z.} \frac{d^3k}{(2\pi)^3}\,\hbar\omega_\nu(k) \tag{14}$$

where

$$H_0 = -zJ_a \cdot S(S+1) - zJ_f \cdot [S(s+1) + s(S+1)] \simeq -0.16\ eV$$

and $\frac{E_g}{N_c} \simeq -0.12\ eV$.

Next, within linear spin-wave theory we have studied the temperature dependence of the internal energy, specific heat, and sublattice magnetizations. We have found that at low temperatures, the internal energy behaves as T^4, and that the specific heat behaves as T^3, which is consistent with an antiferromagnetic ordering at low temperatures.

On the other hand, as discussed in the introduction, the linear spin-wave theory turns out to be a poor approximation in the vicinity of the transition, as long as sublattice magnetizations are concerned. Indeed we find that $\langle S\rangle$ and $\langle s\rangle$ decrease linearly with temperature as this approaches the Néel point, and vanish at different temperatures, see figure 2. There we also see that the linear-spin-wave theory yields, at zero temperature, quantum corrections to the magnetic moments of Fe^{3+} ions but no corrections to those of Fe^{5+} ions. Therefore, we think that further non-linear corrections should be taken into account so as to obtain the correct temperature dependence of the sublattice magnetizations especially as the temperature approaches the Néel point.

V. CONCLUSION

We have modelled the first-order magnetic transition occurring in the perovskite $Sr_2LaFe_3O_9$ using a Dirac-Heisenberg Hamiltonian including (nearest-neighbor) biquadratic interactions, whose origin could be related with the disproportionation of iron. We have been able, by fitting the experimental magnetic susceptibility and specific heat, to estimate the superexchange integrals for the antiferromagnetic and ferromagnetic interactions, as well as the biquadratic ones. The first of these integrals is consistent with the results of previous work on kindred compounds.

Elastic-Neutron Scattering will be performed on this compound for checking the anomalous behavior of the sublattice magnetizations predicted here. Unfortunately, it is difficult to check up on the magnon spectrum we have computed. Nevertheless, the latter does confirm the magnetic structure determined from Neutron-Diffraction data by Battle et al. [2] in the compound $Sr_2LaFe_3O_{8.94}$.

Non-linear spin-wave calculations and Monte Carlo simulations are still under investigation. Finally, it should be very instructive to understand more in detail the effect of iron disproportionation, or more generally the charge redistribution, on the magnetic ordering.

VI. ACKNOWLEDGMENTS

P.K. would like to acknowledge the kind hospitality extended to him by the Laboratoire de Physique Théorique during his stay. We would like to thank M.L. Kulic, A.I.Buzdin, J.P.Brison and D.Foerster for helpful discussions; and J.Leandri for checking our fit of the exchange constants using the MINUIT algorithm.

---

[1] J.G. Bednorz and K.A. Muller, Z. Phys. **B64** (1986) 189.

[2] P.D.Battle, T.C.Gibb, and S.Nixon, *J. Sol. State Chem.*, **77** (1988) 124; P.D.Battle, T.C.Gibb, and P.Lightfoot, *ibid*, **84** (1990) 271.

[3] F. Zhou, A. Wattiaux, and J.C. Grenier ICMCB, to be submitted for publication.

[4] J.T.Wang, C.L.Lin, and T.Mihalisin, J. Appl. Phys. **79** (1996) 6608.

[5] C.Kittel, Phys.Rev.**120** (1960) 335; C.P.Bean and D.S.Rodbell, Phys. Rev. **126** (1962) 104; D.S.Rodbell, I.S.Jacobs, J.Owen, and E.A.Harris, Phys. Rev.Lett. **11** (1963) 10; N.P. Grazhdankina, Sov. Phys. Uspekhi **11** (1969) 727.

[6] P.W. Anderson, Phys. Rev. **115** (1959) 2.

[7] N.L. Huang and R. Orbach, Phys. Rev.Lett. **11** (1964) 275.

[8] E.L. Nagaev, *Physics of magnetic semiconductors,* MIR Publishers, 1983.

[9] J. S. Smart, *Effective field theories of magnetism*, W.B.Saunders Company, 1966.

[10] P.W. Anderson, " *Theory of magnetic exchange interactions: exchange in insulators and semiconductors*", in F.Seitz and D.Turnbull (eds.), Solid State Physics: Advances in Research and Applications, Academic Press, Vol. **14** (1963) 99.

[11] J.C. Grenier, M. Pouchard, and P. Hagenmuller, Mat. Res. Bull. **11** (1976) 721.

[12] T.Holstein, H.Primakoff, Phys. Rev. **58** (1940) 1098; A.I.Akhiezer, V.G.Bar'yakhtar and S.V.Peletminskii, *Spin Waves*, North-Holland Pub. Company, 1968.

Figure captions

- Figure 1: The crystal and magnetic structure of $Sr_2LaFe_3O_9$ [2]. The large circles represent Fe^{3+} and the medium ones represent Fe^{5+}, with the arrows indicating the size and orientation of their spins; the smallest circles stand for intermediate oxygen atoms. The $2Sr^{2+} : La^{3+}$ cations which are disorderly located in the cubic centers have been omitted for clarity. The hexagonal unit cells of the two structures are commensurate, but the unit cell of the crystal structure is a triple one, while that of the magnetic structure is a primitive one, for the rhombohedral translations are absent in the magnetic structure. Each unit cell contains two formulae of $Sr_2LaFe_3O_9$, hence six iron ions, which form six magnetic sublattices below the ordering temperature.

- Figure 2: The solid curves represent the temperature dependence of the sublattice magnetizations predicted by mean-field theory including biquadratic interactions. The upper (solid) curve represents the magnetization $\langle S \rangle$ of the Fe^{3+} ions of spin $\frac{5}{2}$, and the lower curve is the magnetization $\langle s \rangle$ of Fe^{5+} of spin $\frac{3}{2}$, obtained for the exchange integrals given in eq.(11) in the text.

  The dashed curves represent the corresponding sublattice magnetizations predicted by the linear-spin-wave theory, up to a temperature of $120K$.

- Figure 3: The curve in balls represents the experimental magnetic susceptibility of ref. [4], and the one in triangles is the suscpetibility measured by Zhou et al. [3]. The solid line is the magnetic susceptibility obtained from MF theory including biquadratic interactions.

- Figure 4: The curve in balls is the experimental specific heat of ref. [4], and the solid line is our theoretical result of MF theory including biquadratic interactions.

- Figure 5: Plot of the magnon spectrum along the path $Z\Gamma X M \Gamma Y$ indicated in the Brillouin zone shown as inset.

Fig. 1 The crystal and magnetic structure of $Sr_2LaFe_3O_9$

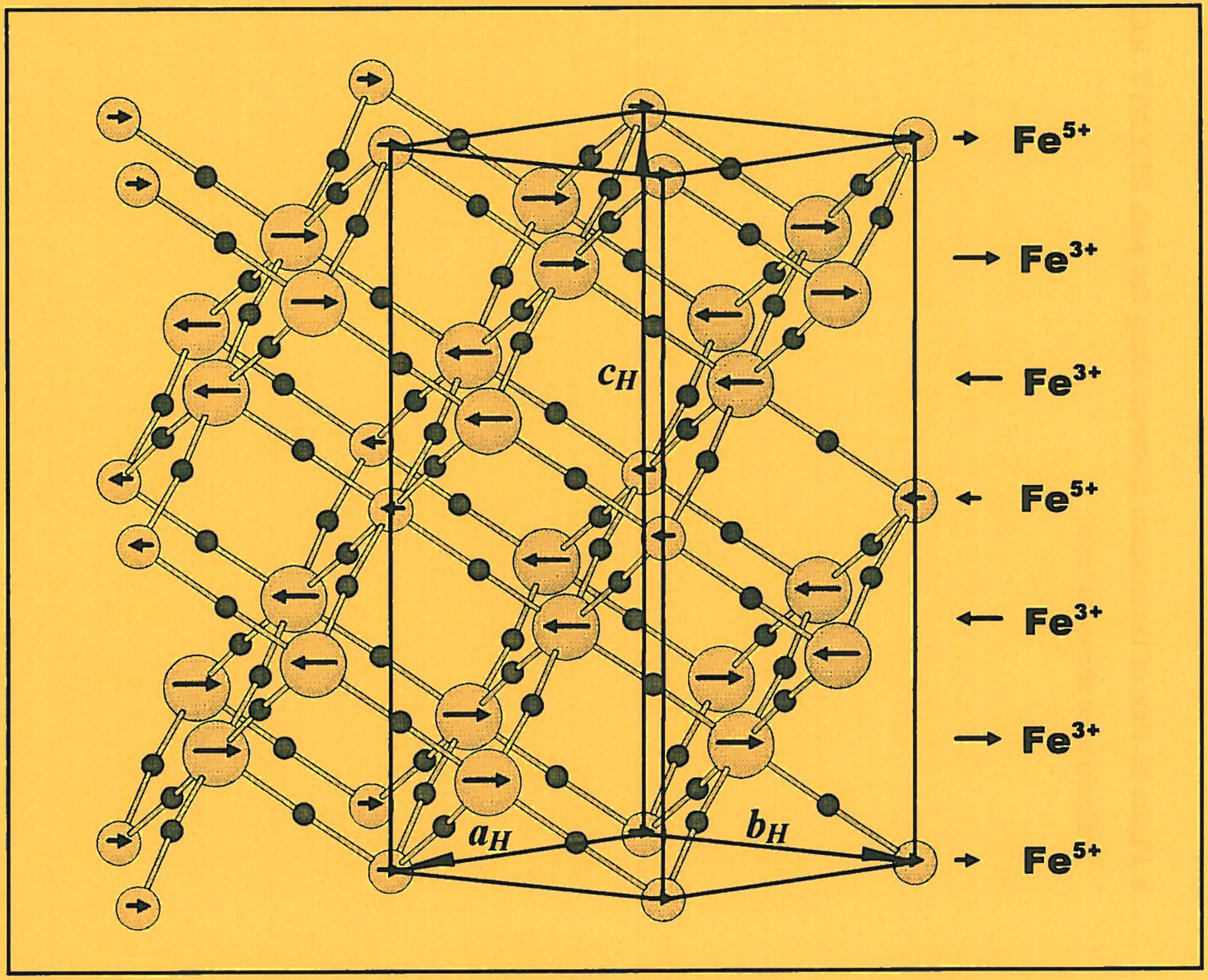

Fig.2

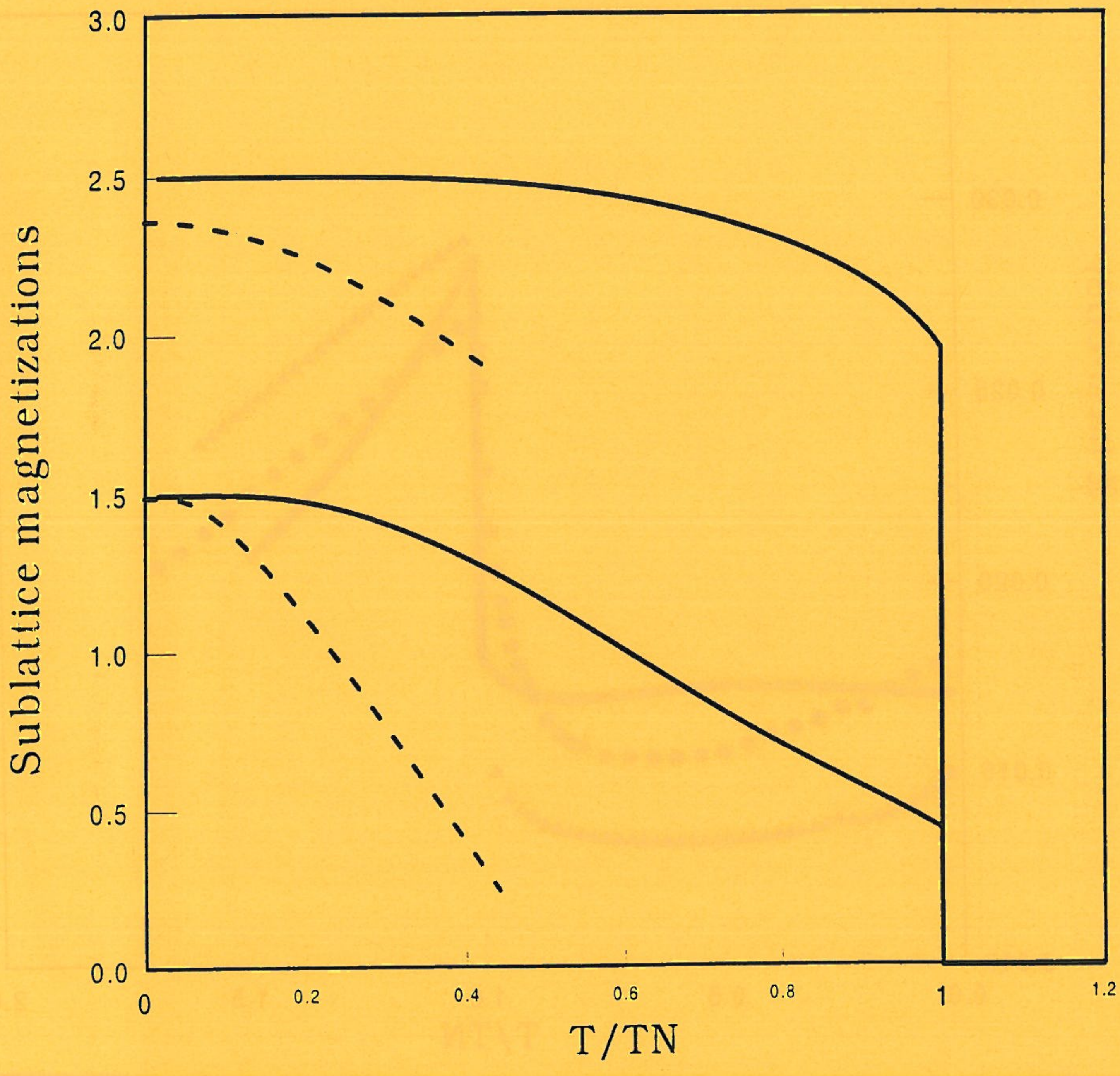

3.0
2.5
2.0
1.5
1.0
0.5
0.0
0
0.2
0.4
0.6
0.8
1
1.2
Sublattice magnetizations
T/TN

Fig.3

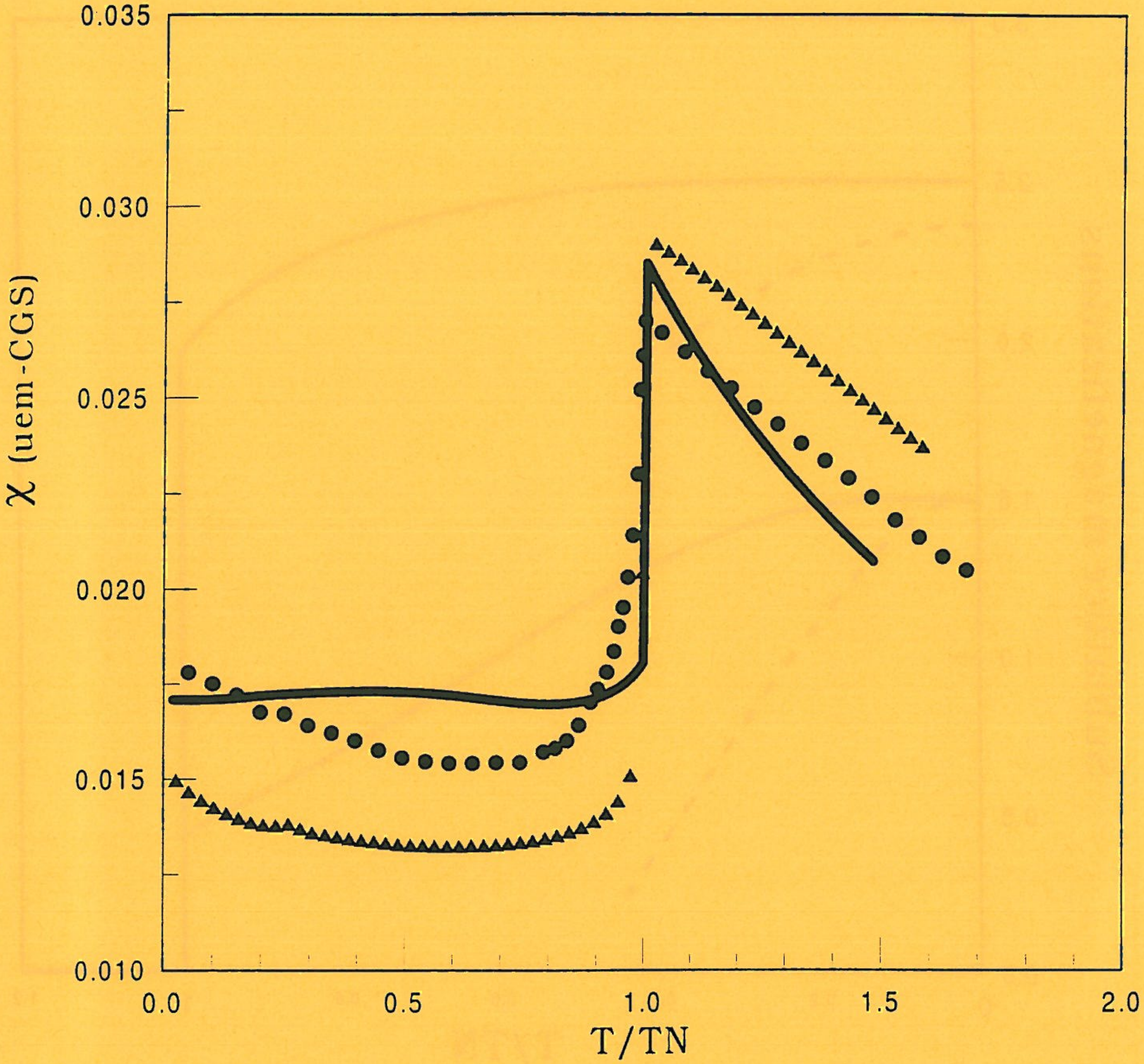

Fig.4

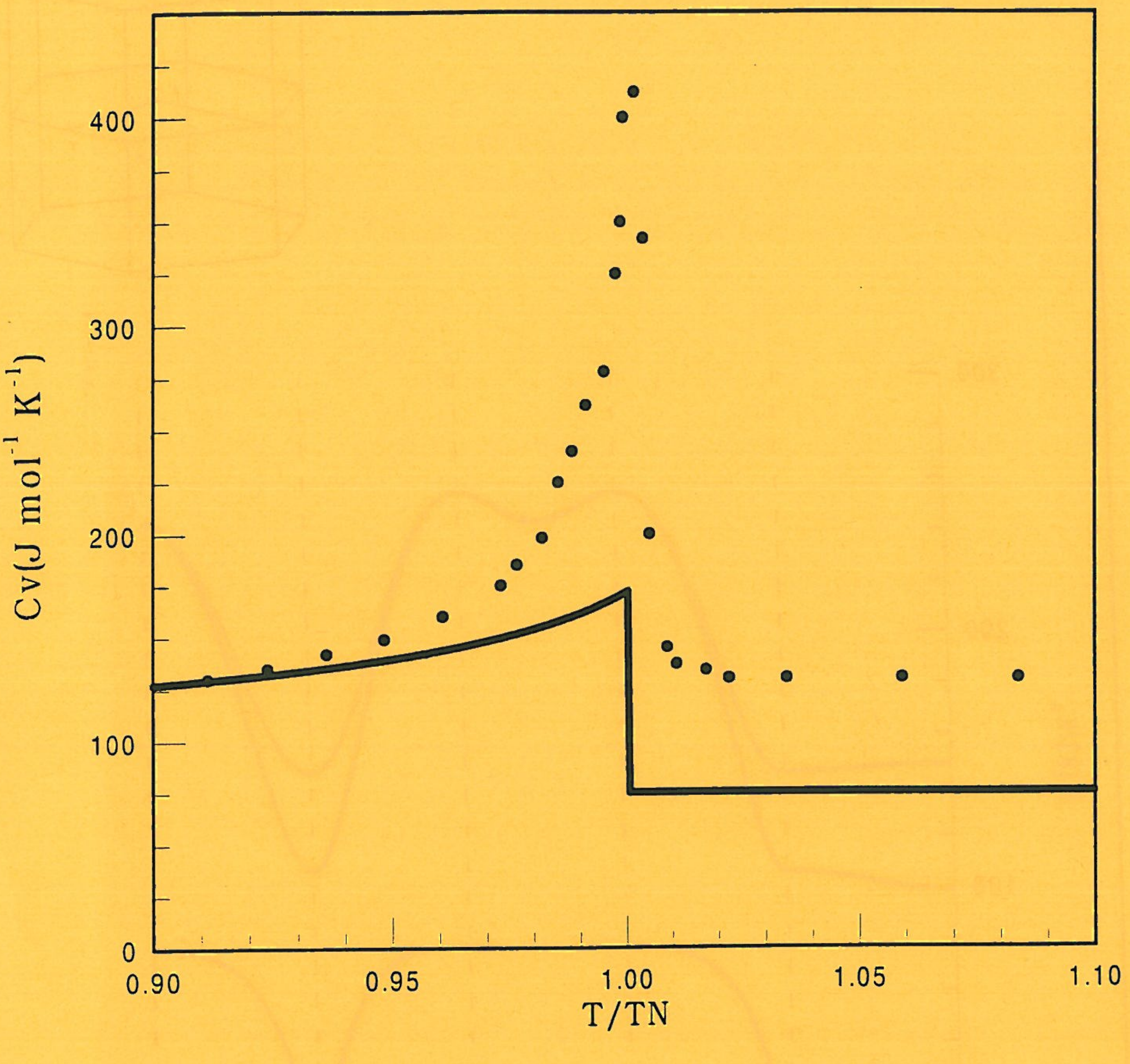

Fig. 5

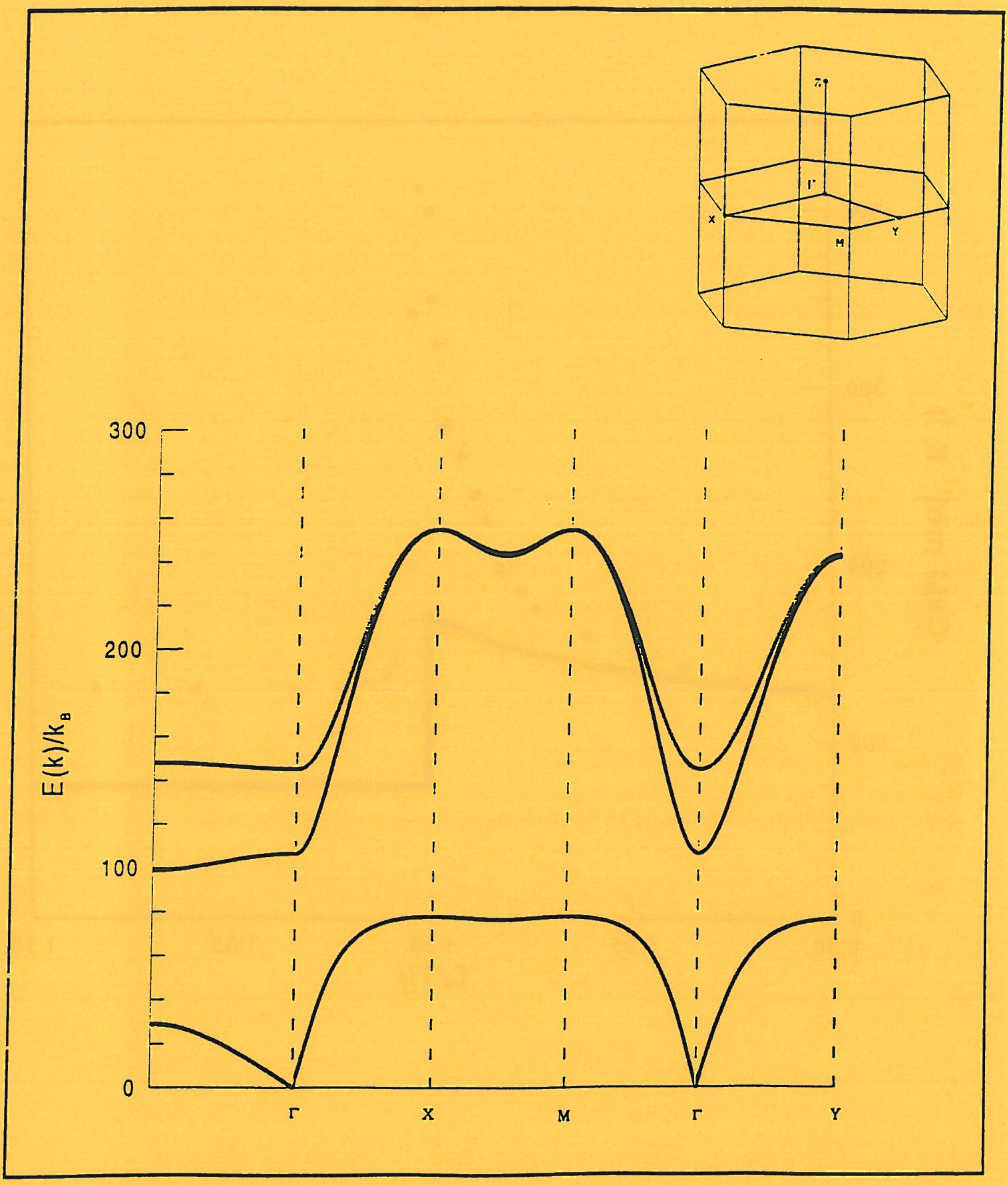

Appendix II

The Calculation Formula for the Trapezoid Window Radii of the Oxygen Diffusing Channels

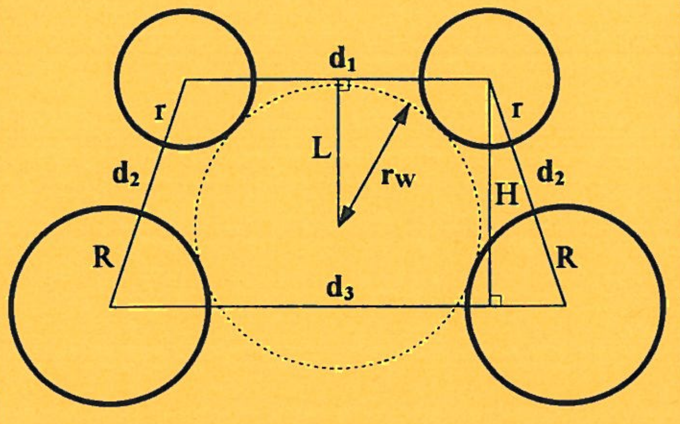

A general trapezoid window

The geometry of a "trapezoid window" in the brownmillerite and G-type structures (*cf.* IV-1 and IV-2) may be generally represented as in the figure.

Atomic radii of R, r and interatomic distances of d_1, d_2, d_3 in the problem are given (here d_1, d_2 , d_3 are defined as the same as in Fig. 8 of section IV-2-1). The formula given in IV-2-1 for calculating the "window radius" r_W can be derived as follows.

According to the figure, we have

$$\left(\frac{d_1}{2}\right)^2 + L^2 = (r_W + r)^2 \tag{1}$$

and

$$\begin{aligned}(H - L)^2 + \left(\frac{d_3}{2}\right)^2 &= (r_W + R)^2 \\ &= (r_W + r)^2 + (R - r)^2 + 2(R - r)(r_W + r).\end{aligned} \tag{2}$$

Subtracting (1) and (2) leads to

$$2LH = H^2 - \left(\frac{d_1}{2}\right)^2 + \left(\frac{d_3}{2}\right)^2 - (R - r)^2 - 2(R - r)(r_W + r). \tag{3}$$

Now set

$$M = H^2 - \left(\frac{d_1}{2}\right)^2 + \left(\frac{d_3}{2}\right)^2 - (R - r)^2 = \frac{2d_2^2 - d_1^2 + d_1 d_2}{2} - (R - r)^2, \tag{4}$$

where

$$H^2 = d_2^2 - \left(\frac{d_3 - d_1}{2}\right)^2. \tag{5}$$

Then from (1) and (3), (4) we obtain

$$4L^2H^2 = 4H^2(r_W + r)^2 - H^2 d_1^2 \tag{6}$$

and

$$4L^2H^2 = M^2 - 4M(R - r)(r_W + r) + 4(R - r)^2(r_W + r)^2, \tag{7}$$

respectively, which give the following quadratic equation :

$$[4H^2 - 4(R - r)^2](r_W + r)^2 + 4M(R - r)(r_W + r) - (M^2 + H^2 d_1^2) = 0. \tag{8}$$

The solution to (8) is :

$$r_W + r = \frac{-4M(R-r) + \sqrt{\Delta}}{2[4H^2 - 4(R-r)^2]} \quad ,$$

where
$$\Delta = [4M(R-r)]^2 + 4[4H^2 - 4(R-r)^2](M^2 + H^2 d_1^2)$$
$$= 16H^2 \left\{[d_2^2 - (R-r)^2][d_2^2 + d_1 d_3 - (R-r)^2]\right\} .$$

Therefore, the value of the trapezoid window radius r_W is given by

$$\left\{ \begin{array}{l} r_W + r = \dfrac{-M(R-r) + H\sqrt{[d_2^2 - (R-r)^2][d_2^2 + d_1 d_3 - (R-r)^2]}}{2[H^2 - (R-r)^2]} , \\ \text{with } H^2 = d_2^2 - \left(\dfrac{d_3 - d_1}{2}\right)^2 , \\ \text{and } M = \dfrac{2d_2^2 - d_1^2 + d_1 d_3}{2} - (R-r)^2 . \end{array} \right.$$

Appendix III

Experimental Techniques

AIII-1. X-ray Powder Diffraction Analysis

The instrumental conditions and data collection are described below:

Instrument:	For room-temperature experiments: Philips PW 1050 For low-temperature experiments: Philips PW 1965
Radiation:	Cu K_{α}; wavelengths used: 1.54187Å (K_{α}) for $2\theta < 50°$ and 1.54060Å ($K_{\alpha 1}$) for $2\theta > 50°$
Generator power:	40KV, 30mA
Monochromator:	Curved graphite
Detector:	Proportional counter (Xe)
Soller slit:	2 sets (in incoming and diffracted beam)
Divergence angle:	1°
Receiving slit width:	0.2 mm
2θ range:	5° ~ 80°
Step size:	0.02°
Counting time/step:	4s or 5s for experiments at RT; 2s for those at LT
Temperature:	80K ~ 300K
2θ error correction:	Interpolation from fitted quadratic error function of internal standard (Si, 99.999%)
Intensity measurement:	Approximated by areas of FWHM×h
Cell refinement method:	Least-squares refinement program PIRUM [1]

AIII-2. Mössbauer Spectroscopy

Mössbauer resonance spectra were recorded in the temperature range from 4.2 K to 293 K on a spectrometer at constant acceleration using a ^{57}Co (Rh) source held at room temperature. Fittings of spectra were done by least-squares refinement using the sum of Lorentzians. Isomer shifts were determined relative to metallic iron (α-Fe) at 293 K.

AIII-3. Magnetic Measurements

The magnetization and magnetic susceptibility were measured from 5K to 350K in applied magnetic fields up to 2T using a SQUID magnetometer (MPMS-5S, Quantum Design) and a susceptometer (DSM8, Manics).

AIII-4. Conductivity and Seebeck Coefficient

The DC conductivity data were obtained using the four-probe method. Detailed descriptions for the conductivity and Seebeck coefficient measurements were given elsewhere [2, 3].

AIII-5. Specific Heat and Enthalpy

The specific heat and enthalpy data were determined from 115 K to 330 K using a differential scanning calorimeter (DSC7, PERKIN-ELMER) in helium atmosphere at a scanning speed of 10 K/min. The sample mass used for the measurement was about 10 ~ 15 mg. The instrument was calibrated for enthalpy measurement against an indium (In) standard and for temperature measurement against standards of both indium and mercury (Hg) at the above scanning speed. The error in the temperature measurement is smaller than ±0.2 K. The specific heat measurement was verified with a sapphire standard.

AIII-6. Chemical Analysis of Fe^{4+} Content

Concentrations of Fe^{4+} ions, τ, in the ferrites (such as $Sr_2LaFe^{3+}_{3-\tau}Fe^{4+}_{\tau}O_{8+\delta}$ or $Sr_2Fe^{3+}_{2-\tau}Fe^{4+}_{\tau}O_{5+\delta}$ etc.) were determined by redox process using solutions of Mohr salt ($(NH_4)_2Fe^{2+}(SO_4)_2 \cdot 6H_2O$) and potassium dichromate ($K_2Cr_2O_7$) in the presence of barium diphenylamine sulfonate as indicator. The contents of oxygen species O^{2-} of the phases were then obtained according to the relation $\delta = \tau/2$.

Redox Reactions Involved:

In acid solution, the Fe^{2+} ions (in excess) from the Mohr salt react with Fe^{4+} ions from the sample according to

$$Fe^{2+} + Fe^{4+} \Rightarrow 2\ Fe^{3+}\ .$$

The remaining Fe^{2+} in the solution is titrated by 0.1N $K_2Cr_2O_7$ following the reaction

$$6Fe^{2+} + (Cr_2O_7)^{2-} + 14H^{+} \Rightarrow 6Fe^{3+} + 2Cr^{3+} + 7H_2O\ .$$

Operation Procedures:

1. Accurately weigh two or three aliquots of finely powdered sample (~100 mg for each) in beaker flasks;
2. Accurately add into one of the beaker flasks 10ml of 0.1N Mohr salt (the Mohr salt is dissolved in 0.1N H_2SO_4 solution);
3. Add 20ml HCl solution (its concentration is about HCl (37%):H_2O = 1:1 or 1:2, in volume portion);
4. Heat (if necessary) the solution over a sand-bath to well dissolve the sample powder (it's better to control the temperature and the time at their lowest possible values);
5. Add 50ml H_2O, then cool the solution in flowing water to room temperature;
6. Add 10ml of 9N H_2SO_4 (to stabilize the Mohr salt);
7. Add 5ml of 85% H_3PO_4 (to eliminate the yellow color due to the presence of Fe^{3+}, which will otherwise interfere with the observation of the final point);
8. Add 5 ~ 6 drops of the indicator (0.2% or $2g{\cdot}l^{-1}$ solution of barium diphenylamine sulfonate);
9. Titrate the solution with 0.1N $K_2Cr_2O_7$ until to the final point as indicated by the just occurrence of light violet color;
10. Do a blank test (without the sample powder) under the same conditions (same quantities of the solutions, same heating temperature and time, etc.);
11. Repeat the procedures 2 ~ 10 for the rest aliquots of the sample.

Calculation Formula:

$$\tau = \frac{M \cdot N \cdot \Delta V}{m - 8 \cdot N \cdot \Delta V},$$

with:

M: the molar mass (in g) of non-oxidized phase ($Sr_2LaFe_3^{3+}O_8$ or $Sr_2Fe_2^{3+}O_5$ etc.);

m: the mass of the sample (in mg);

N: the normality of $K_2Cr_2O_7$ solution (it is 0.1N here);

ΔV: $\Delta V = V_0 - V$, with V being the volume of the $K_2Cr_2O_7$ solution consumed during the titration and V_0 the corresponding volume for the blank test (they are all in ml).

References

[1]. Werner, P.-E. (1969). *Ark. Kemi.* **31**, 513

[2]. Dordor, P., Marquestaut, E., Salducci, C. and Hagenmuller, P. (1985). *Revue Phys. Appl.* **20**, 795

[3]. Dordor, P., Marquestaut, E. and Villeneuve, G. (1980). *Revue Phys. Appl.* **15**, 1607